CRANFIELD UNIVERSITY

IBRAHIM NURUDDIN KATSINA

EFFECT OF WELDING THERMAL CYCLES ON THE HEAT AFFECTED ZONE MICROSTRUCTURE AND TOUGHNESS OF MULTI-PASS WELDED PIPELINE STEELS

SCHOOL OF APPLIED SCIENCES
WELDING ENGINEERING

PhD THESIS
Academic Year: 2011 - 2012

Supervisor: Dr Supriyo Ganguly and Mr David Yapp
September 2012

CRANFIELD UNIVERSITY

SCHOOL OF APPLIED SCIENCES
WELDING ENGINEERING

PhD

Academic Year 2011 - 2012

IBRAHIM NURUDDIN KATSINA

Effect of welding thermal cycles on the heat affected zone microstructure and toughness of multi-pass welded pipeline steels

Supervisor: Dr Supriyo Ganguly and Mr David Yapp
September 2012

This thesis is submitted in fulfilment of the requirements for the degree of PhD

ABSTRACT

This research is aimed at understanding the effect of thermal cycles on the metallurgical and microstructural characteristics of the heat affected zone of a multi-pass pipeline weld.

Continuous Cooling Transformation (CCT) diagrams of the pipeline steel grades studied (X65, X70 and X100) were generated using a thermo mechanical simulator (Gleeble 3500) and 10 mm diameter by 100 mm length samples. The volume change during phase transformation was studied by a dilatometer, this is to understand the thermodynamics and kinetics of phase formation when subjected to such varying cooling rates. Samples were heated rapidly at a rate of 400°C/s and the cooling rates were varied between $t_{8/5}$ of 5.34°C/s to 1000°C/s. The transformation lines were identified using the dilatometric data, metallographic analysis and the micro hardness of the heat treated samples.

Two welding processes, submerged arc welding (SAW) and tandem Metal Inert Gas (MIG) Welding, with vastly different heat inputs were studied. An API-5L grades X65, X70 and X100 pipeline steels with a narrow groove bevel were experimented with both welding processes. The welding thermal cycles during multi-pass welding were recorded using thermocouples.

The microstructural characteristics and metallurgical phase formation was studied and correlated with the fracture toughness behaviour as determined through the Crack Tip Opening Displacement (CTOD) tests on the welded specimens. It was observed that SAW process is more susceptible to generate undesirable martensite-austenite (M-A) phase which induce formation of localised brittle zones (LBZ) which can adversely affect the CTOD performance. Superimposition of the multiple thermal cycles, measured in-situ from the different welding processes on the derived CCTs, helped in understanding the mechanism of formation of localised brittle zones.

Charpy impact samples were machined from the two X65 and X70 grades, for use in thermal simulation experiments using thermo mechanical simulator (Gleeble). The real thermal cycles recorded from the HAZ of the SAW were

used for the thermal simulations, in terms of heating and cooling rates. This is to reproduce the microstructures of the welds HAZ in bulk on a charpy impact sample which was used for impact toughness testing, hardness and metallurgical characterisation.

The three materials used were showing different response in terms of the applied thermal cycles and the corresponding toughness behaviours. The X65 (a) i.e. the seamless pipe was showing a complete loss of toughness when subjected to the single, double and triple thermal cycles, while the X65 (b), which is a TMCP material was showing excellent toughness in most cases when subjected to the same thermal cycles at different test temperatures. The X70 TMCP as well was showing a loss of toughness as compared to the X65 (b).

From the continuous cooling transformation diagrams and the thermally simulated samples results it could be established that different materials subjected to similar thermal cycle can produce different metallurgical phases depending on the composition, processing route and the starting microstructure.

Keywords:

Thermal simulations, Gleeble 3500, submerged arc welding, Tandem MIG welding, Continuous Cooling Transformation diagrams, Dilatometry, Phase transformations, Charpy impact toughness, CTOD.

ACKNOWLEDGEMENTS

In the name of Allah the beneficent the merciful. I wish to express my profound gratitude to Allah (SWT) for his grace and mercy granted to me right form birth to date, "Alhamdulillah."

My heartfelt gratitude goes to my parents, Alhaji Nuruddin Ibrahim and Hajiya Binta Na'iya, and my wife Fadila and children Ja'afar and Muhammad Noor for their support both morally and spiritually, and for their patience, love, guidance, encouragement and prayers during this research period. May Allah have mercy on them as they have mercy on me Ameen. Same goes to my brothers and sisters for whose love, guidance, encouragement and prayers have seen me through all the good and bad times.

My heartfelt gratitude goes to the Petroleum Technology Development Fund (PTDF) and my employers Hassan Usman Katsina Polytechnic, Katsina for the opportunity awarded to me to pursue a PhD at Cranfield University.

I wish to render my unreserved gratitude to my project supervisors Dr Supriyo Ganguly and Mr David Yapp for their patience, care, guidance, and time given to me during this research work. I will never forget it, thank you and God bless you.

I will also like to show my appreciation to our technical staffs that have helped me through the practical work, especially Mr Brian Brooks, Flemming Nielsen, Andrew Dyer, Mathew Kershaw and Stuart Morse of University of Manchester for his help with all the Gleeble machine experiments. I will also want to acknowledge the help of Mr Alan Denney of Saipem UK, for his support during this research.

My profound gratitude goes to my review chair, Dr Philip Longhurst and my subject adviser Dr Paul Colegrove, and finally Professor Stewart Williams for their care concern and support during the course of my research.

I wish to acknowledge the support and encouragement of my colleagues in the office, especially Harry for his help with all the Matlab programs and Daniel for

his help with office suite. Similar goes to Wojciech, Eurico, Mathew, Stephan, Usani, Filomeno, Tamas, Craig, Isidro, Wang, Jibrin, Anthony, Adam, Fude, Pedro, Goncalo and Sonia.

During the course of my stay at Cranfield I have met a lot of wonderful people, some of whom I have shared my joys and sorrow with, noticeable among them are Nuhu, Abdulkarim, B. Muneer, Muammer, Bello, Abba, Shinkafi, Murtala, Sanusi, Sani, Abu, Abdussalam, Saif, Abu-Abdullah, Sami, Abdulmajid, Sulaiman, Mubarak, Muhammad and Furjani (Rigima) among others numerous to mention. I say to you all thank you very much and God bless you.

Finally, I am grateful to my lord Once again who has created me and makes it possible with his mercy to witness this day and time, and to see the fruits of my hard work and dedication.

"Alhamdu lillahil lazi bi ni’imatihi tatimmus-salihat".

TABLE OF CONTENTS

LIST OF FIGURES

LIST OF TABLES

LIST OF EQUATIONS

LIST OF ABBREVIATIONS

a	crack length
a_c	critical crack extension
B	thickness of CTOD test specimen
CEV	carbon equivalent
CR	cooling rate
CTOD	crack tip opening displacement
CTOA	crack tip opening angle
CVN	charpy V notch test
CGHAZ	coarse grain heat affected zone
DJ	double joint
FAD	failure assessment diagram
FCGR	fatigue crack growth rate
FGHAZ	fine grain heat affected zone
GMAW	gas metal arc welding
GTAW	gas tungsten arc welding
HI	heat input
HAZ	heat affected zone
IR	infrared
ICHAZ	intercritical heat affected zone
ICRCGHAZ	intercritically reheated coarse grain heat affected zone
J	crack tip J-integral
J_c	critical J at the onset of brittle crack extension when $\Delta_a < 0.2$ mm

J_{Ic}	critical J near the onset of stable crack extension
J_m	J at first attainment of maximum F plateau for full plastic behavior
J_u	critical J at the onset of brittle crack extension when $\Delta_a \geq 0.2$ mm
K	stress intensity factor
K_{Ic}	plane strain fracture toughness
LBZ	local brittle zone
LM	lamellar martensite
LVDT	linear variable differential transducers
M-A	martensite-austenite
MIG	metal inert gas
RICC	roughness induced crack closure
SAW	submerged arc welding
SBCCGHAZ	subcritical coarse grain heat affected zone
SCRCGHAZ	supercritically reheated coarse grain heat affected zone
SENB	single edge notched bend specimen
SPCCGHAZ	supercritical coarse grain heat affected zone
SRXRD	spatially resolved X-ray diffraction
$t_{8/5}$	cooling time from 800°C to 500°C
TC	thermocouples
TMCP	thermo-mechanically controlled processing
TRXRD	time resolved X-ray diffraction
UACGHAZ	unaltered coarse grain heat affected zone
UFAF	ultrafine acicular ferrite

VHN	vickers hardness number
V	notch opening displacement
V_p	plastic component of V
W	CTOD specimen width
WM	weld metal
XRD	X-ray diffraction
δ	crack tip opening displacement (CTOD)
δ_c	critical δ at the onset of brittle crack extension when Δ_a < 0.2 mm
δ_m	δ at the first attainment of maximum F plateau for fully plastic behavior
δ_u	critical δ at the onset of brittle crack extension when $\Delta_a \geq$ 0.2 mm

1 INTRODUCTION

The quest for an efficient and reliable source of energy has been on going in the world for the past centuries. It is booming even more in the twenty first century.[1] Fossil fuel has been and is still one of the most widely used natural resource around the globe for the generation of electricity, especially in the modern high efficiency combined cycle power plants and for domestic uses.[2] Several researchers[3; 4] have detailed the use of natural gas as one of the most efficient and effective, coupled with its abundance. Natural gas is intrinsically cleaner (less CO_2) than other fossil fuels.[5; 6]

However, worldwide the large reserves of natural gas are remotely located and therefore, they are required to be transported from the source to the consumers as shown in figure 1-1. Fossil fuels are nowadays transported from the origin to several other countries across the border.[7] The most efficient way of transporting them is by high-pressure long distant pipelines.[3; 4; 8]

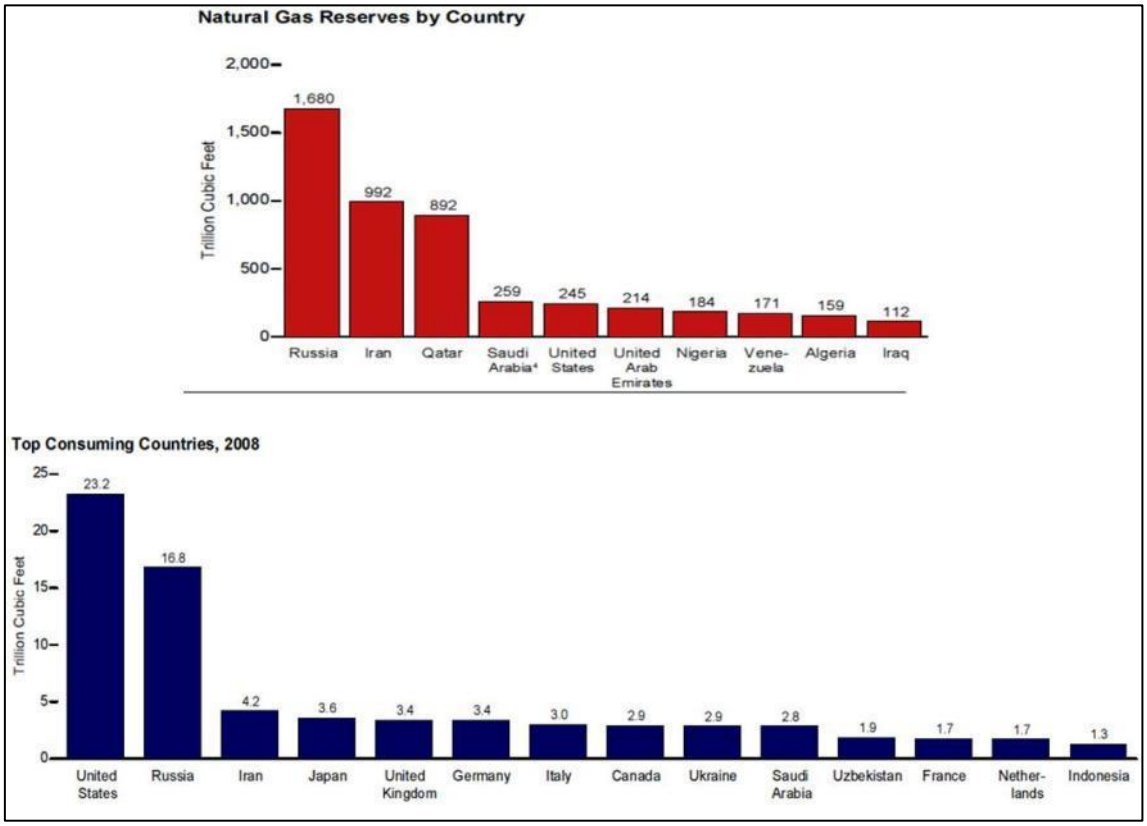

Figure 1-1 Natural Gas reserves and consumption around the world [9]

Welding is the most preferred and productive of all the joining process, to join these long distant cross-country pipelines. However, unlike other joining techniques, it produces an integrated structure with newly formed fusion and heat affected zones. The metallurgical characteristics of the fusion and heat affected zones are completely different from the parent material. This is due to the heat from the process which causes grain growth, precipitates formation and dissociation of carbides. This leads to formation of a graded structure.

The thermo mechanical controlled processing (TMCP) route, presents a cheaper and more effective means of producing these pipeline steel. Therefore, it was commonly adopted by pipeline manufactures, as a strengthening technique.[10; 11] The strength is achieved by producing very fine grains,[12; 13] and various carbides and nitrides or a combination of both within the microstructure. These precipitates tend to reduce the grain size by hindering the grain boundary movement, thereby making grain growth almost impossible.[14]

However, welding changes the microstructure of these steels due to the formation of heat affected zone. Thermal cycles exceeding the transformation temperatures in the HAZ, lead to a significant loss of toughness. This is due to grain growth as a result of carbides dissolution, forming the coarse grain HAZ. While in multi-pass welds, the intercritically re-heated coarse grain HAZ is formed. The re-heated zones produce some unwanted islands, so called martensite austenite (M-A) constituents, leading to the formation of local brittle zones (LBZ). [15-19]

Due to criticality (onshore, offshore, high pressures, natural and manmade disasters etc.) of the application, it is required to understand how a crack or defect will interact with the microstructure and propagate.[20] The welded structure has to undergo a stringent toughness, crack tip opening displacement (CTOD) test. A small localised brittle zone in the entire weld can result in failure to qualification of a weldment and in turn a welding process. To meet the set standards, repairs are normally carried out on defective welds. This is costing the industries both time and money.

In this research, we are trying to understand how the thermal cycles from a real weld, can results in the formation of M-A phase, and its effect. Apprehend its effect on the fracture toughness of the welds. Then simulate those thermal cycles on charpy samples. This will produce a bulk microstructure with similar properties for fracture toughness testing, and for both mechanical and microstructural characterisations.

This thesis contains a total of nine chapters, where chapter 1 is the introduction. Chapter 2 is the literature review, where the findings in this research area have been discussed critically. Chapter 3 presents the aims and objectives of this research work. This has been derived after synthesizing the data obtained from the literature review.

Chapter 4 contains all the materials and equipments used in this research. The experimental set-ups and how they were carried out was presented in chapter 5. The results were presented in chapter 6, and it contains the results obtained from the experiments only. Chapter 7 presents a full discussion about the results.

The conclusions and recommendations for future work are presented in chapters 8 and 9 respectively. Finally the references and appendices are presented at the end of the thesis.

2 LITERATURE REVIEW

2.1 **Background**

The search for even more efficient, reliable and cleaner source of energy has been on for decades.[21] Improvements through research and development have been the main factor in achieving the desired results. A lot of research[6; 22] has taken place with regards to finding an economical and productive way of transporting these natural resources. Pipelines have been the crucial answer to the problem. They must be welded to one another and laid either onshore or offshore to be able to transport these resources.[23-25]

The welding processes have been optimized in many respects such as process parameters, shielding gas, consumables, weld preparation or bevel etc, in order to get the most productive and cost effective means of joining these pipes.[26-29]

Modern steel manufacturing techniques has made it possible to optimize the production routes. This requires changing the microstructures to obtain an excellent combination of strength and toughness.[30-35]

There are certain problems associated with welding these pipeline steels, especially the modern high strength low alloy steels (HSLA) or the thermo-mechanically controlled processed steels (TMCP).[6; 15; 36-40 41] This is due to their production sequence which results in to very fine grains. It causes some deleterious effects on the HAZ properties when welded.

Research papers[15-19] over years have recognized that the loss in toughness of the HAZ can be due to the following reasons.

(i) Formation of CGHAZ (Coarse grained heat affected zone)
(ii) Formation of ICCGHAZ (Intercritical coarse grained heat affected zone)
(iii) Reheated ICCGHAZ (Reheated intercritical coarse grained HAZ)

These have been related to local brittle zone formation, and will be explained in detail later in this review.

2.2 **Multi-pass welds, thermal cycles and microstructures**

The thermal cycles of multi-pass welds have a significant influence on the mechanical and the metallurgical properties of the welded joints.[42] They are usually the cause of local brittle zones, which were believed to be due to the presence of M-A islands.[43; 44]

Zalazar et al.[45] evaluate the metallurgical phases that originate from pipeline steel welds by using multi-pass welds at low heat inputs. Despite using low heat input in their studies, local brittle zones could not be avoided. This is as a result of the complex mechanism involving thermal cycles and compositional effects.

Haze and Aihara[46] conducted a study on the microstructural changes taking place in a multi-pass weld as shown schematically in figure 2-1. The first thermal cycle represents the first weld bead, which has once heated all the figures A, B, C and D to about 1400°C, coarse grain microstructure was formed.

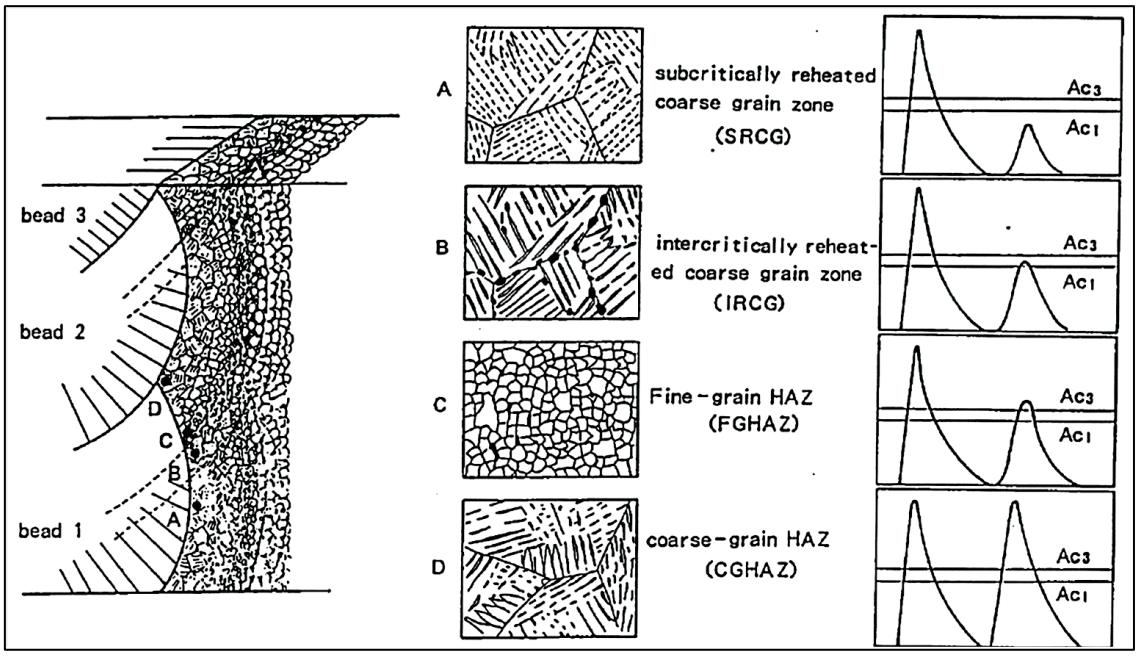

Figure 2-1 various microstructures produced by welding heat cycles[45-47]

Figure A has been reheated just below the A_{C1} and is called the subcritically reheated coarse grain (SRCG) zone. The base structure remains, but the second phase may decompose, i.e. the microstructure is annealed.

In figure B the reheating temperature was between the inter-critical temperature regions i.e. A_{C1} and A_{C3}. It is called the intercritically reheated coarse grain (IRCG) zone. Partial re-austenitization occurs at local regions with high carbon contents, and there is a high tendency of forming brittle microstructures (M-A island). This critical region normally exists at about 3 mm from the fusion line of the first pass,[45] depending on the welding process.

When the temperature crosses the A_{C3} line as seen in figure C, it is referred to as supercritically reheated fine grain (SCFG) zone. Complete re-austenitization occurs, but the peak temperature is not high enough to promote grain growth. Therefore, the microstructure becomes normalised or refined.

At figure D, the reheating has gone well above A_{C3} line; the high temperature promotes grain growth. This region is called the coarse grain (CG) zone, and produces a coarse grained microstructure.

Adams[48] proposed the use of a two-dimensional heat flow analysis using equation (2-1), to identify the metallurgical microstructures in the HAZ of a multi-pass weld. Eight distinct regions that have been subjected to different heat cycles were identified from the heat flow analysis as in figure 2-2.

$$\{1/(T_{max} - T_0) = 4.13C \times \rho \times \upsilon \times y/q + 1/(T_m - T_0)\} \quad \textbf{(2-1)}$$

Where:

T_{max} = maximum temperature attained (K)

T_m = melting temperature (K)

T_o = initial temperature (K)

°C = specific heat (J/g.K)

q = heat input per unit plate thickness (J/mm)

υ = welding speed (mm/s)

ρ = density (f/mm^3)

y = distance from fusion line (mm)

Equation (2-1) was simplified to

$$\{1/\,(T_{max} - T_0) \;=\; \mathrm{A} \times \mathrm{y} \;+\; 1/(T_m - T_0)\} \qquad \textbf{(2-2)}$$

Where A is a constant, determined using T_{max} = 1173K, T_m =1823K, and *y* is the HAZ width.[47; 48] The following regions were classified as local brittle zones (LBZ) sites:

1. The coarse grain HAZ (CGHAZ)
2. Subcritically reheated coarse grain HAZ (SRCG HAZ)
3. Intercritically reheated coarse grain HAZ (IRCG HAZ)
4. Tempered intercritically reheated coarse grain HAZ (TIRCG HAZ)

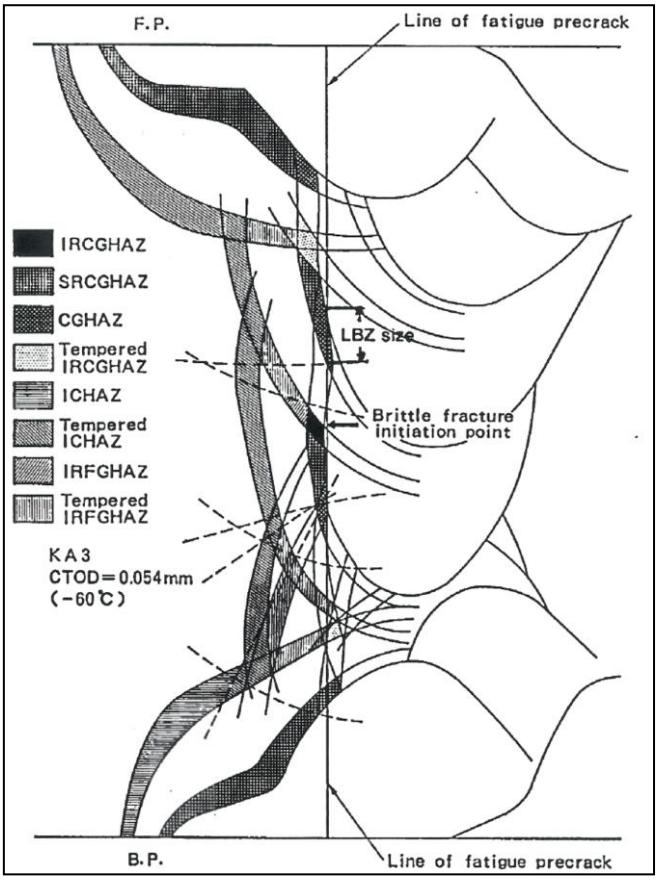

Figure 2-2 Identification of microstructures of CTOD specimen (K-joint) [47]

Multi-pass weld holds some excellent properties such as microstructural refinement, better toughness and less residual stresses compared to single pass weld. This is because: [49]

- The thermal cycle from subsequent passes refine the grains from the previous pass
- Total heat input per weld pass is reduced, therefore grain growth is effectively reduced
- Previous passes provide some preheating effect that tends to extend the critical cooling time of $\Delta t_{8/5}$
- The subsequent passes has an annealing effect on the previous one, thereby relieving residual stresses from the previous passes

Figure 2-3 is a schematic comparison between a single pass weld and a multi pass weld.

The correct prediction of microstructure and hardness of the HAZ in multi-pass welds of high strength steels are very important in optimizing the design of a pipeline project with respect to weldability. The development of thermo-microstructural models such as TENWELD© have been a welcome development.[50]

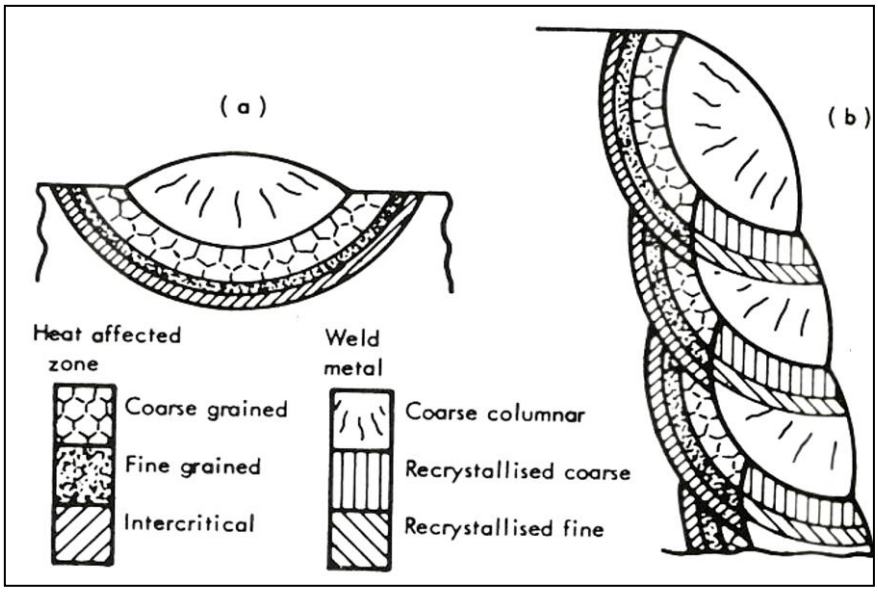

Figure 2-3 Schematic comparison of the microstructures of (a) single run and (b) multi-run welds[49]

2.3 **Martensite-Austenite constituents**

The basis of M-A constituents can be related to the martensitic reaction. This normally occurs when austenite is transformed by rapid cooling or quenching to room temperature. Martensite is a very hard phase and forms one of the constituents of normal hardened steels (i.e. steels that are quenched and tempered to improve their strength). It consists of a much finer plates of super-saturated form of ferrite, with a body centred tetragonal (BCT) crystal structure.[12; 51-53]

Martensite formation is extremely rapid mainly because it is diffusion-less process occurring at the lower temperature level. The temperature where diffusion-less transformation starts is referred to as Martensite start temperature designated as M_s, which is above room temperature. The transformation normally continues in a displacive mode, until it reaches the martensite finish temperature known as M_f. Normally some small amount of austenite is retained.[51; 53]

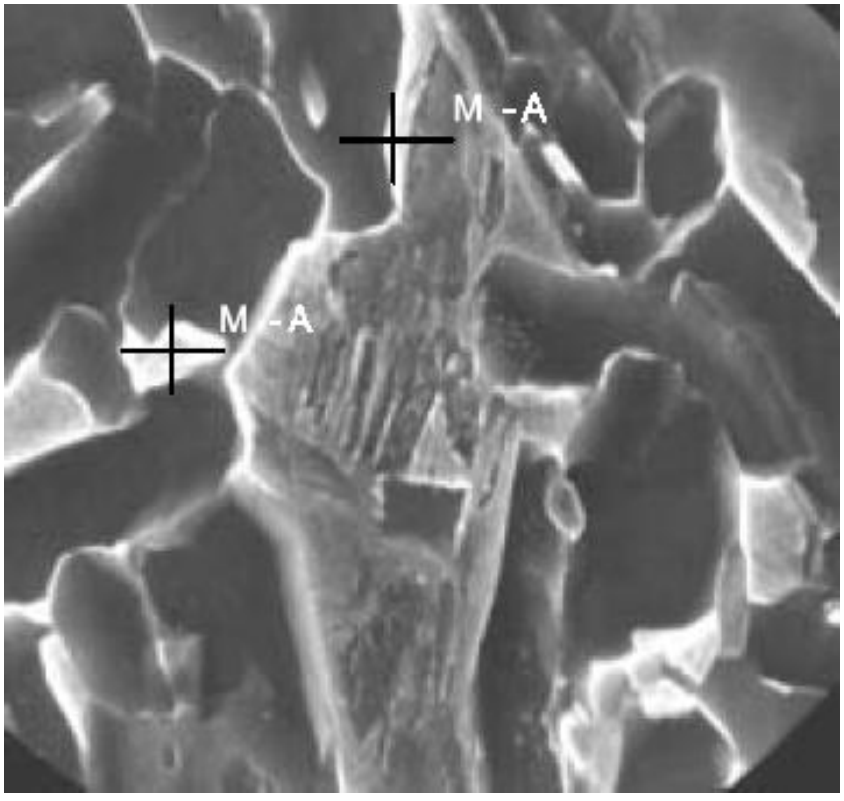

Figure 2-4 SEM of an M-A constituent on the grain boundaries, 10,000×[42]

In welding, there is rapid cooling due to heat sink by the surrounding material and the environment. Depending on the thermal cycles, formation of martensite in the HAZ might be inevitable. This also varies from one material to another, and depends on grain size, cooling rate, carbon equivalent and hardenability among others. In the case of high strength steels their fine grained structure has an influence on the transformation when subjected to different thermal cycles.

The mode by which martensite and bainite are formed has been found to affect mechanical properties of materials. This has been explored by Bhadeshia.[54] High magnification SEM micrograph with M-A phase identified on it is shown in figure 2-4.

2.3.1 M-A formation during multi-pass welding

There has been an intensive research[6; 38; 55; 56] which looked at the problems of welding high strength steels. Emphasis was given to the formation of these deleterious phase i.e. M-A phase or constituents. There are several theories of formation and effects of M-A on the HAZ of pipeline welds.

For the past three decades, Ikawa et al.[52] have made a scrupulous research in identifying the theory behind the formation of M-A constituents. They come up with an acceptable explanation of how the M-A phases are being formed upon cooling of the material from austenitic state. Bainitic ferrite is obtained first, while the remaining austenite becomes stable due to carbon enrichment.[57; 58] This takes place at about 400-350°C, with a carbon content of about 0.5 - 0.8%.

Upon continuous cooling, at the range of 350-300°C part of the austenite tends to transform in to ferrite and carbides. But under instantaneous cooling, this process will never take place, whereby the un-decomposed austenite transform in to twin and lath martensite at a lower temperature, while diminutive amount of austenite is retained. Part of the reason been the compressive stresses imposed by the surrounding acicular ferrite.[42] In other words, the remaining austenite is strained as the transformation induces volume change (increase in volume). Therefore, the remaining austenite becomes strained. This is generally referred to as the M-A constituents. [52; 59]

Lambert et al.[20] also explain the formation of M-A constituents in similar manner, agreeing with the above theory, i.e. upon continuous cooling, there was a partial transformation of the austenite in to martensite, leading to the formation of M-A islands.

Chunming et al.[5] investigate the formation of M-A islands in X70 pipeline steel by using TEM. The result of their thermo-mechanical simulation test shows that M-A islands were formed during the continuous cooling phase.

The unchanged austenite during ferritic transformation becomes enriched with carbon and eventually transformed in to M-A islands upon further continuous cooling. These M-A islands are made-up of retained austenite flakes and a number of micro-twinned martensite plates with various size and orientation as shown in figure 2-5.[5] While figure 2-6 is a TEM bright field image of M-A phase.

All the theories agree on the mode of formation of M-A islands. The major difference is from one material to another with different compositions which normally alter the transformation temperatures and durations.

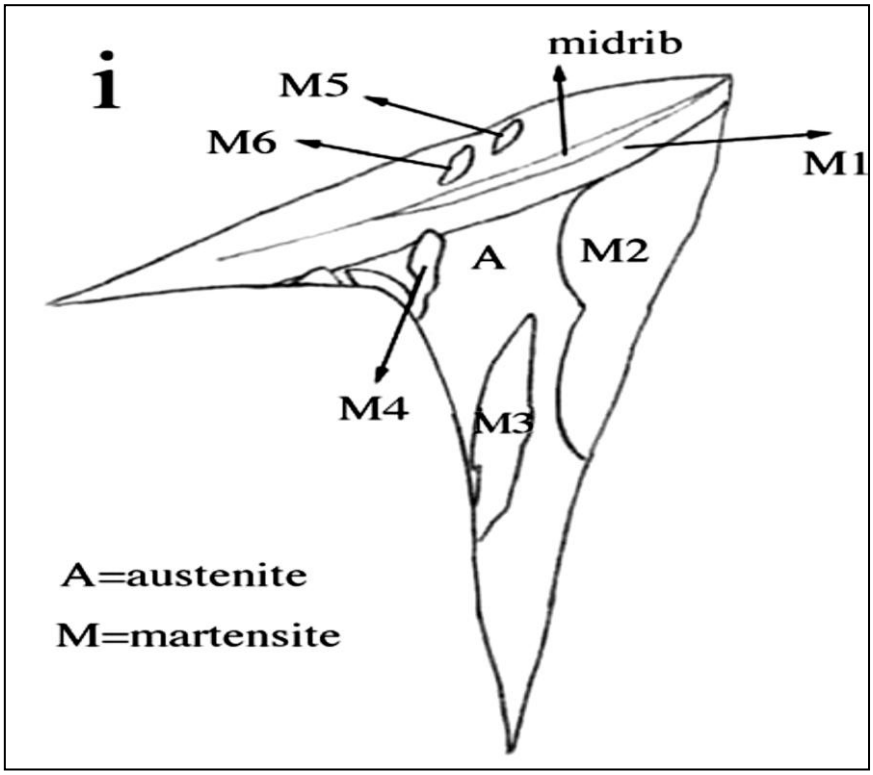

Figure 2-5 Illustration of fine structure of M-A island.[5]

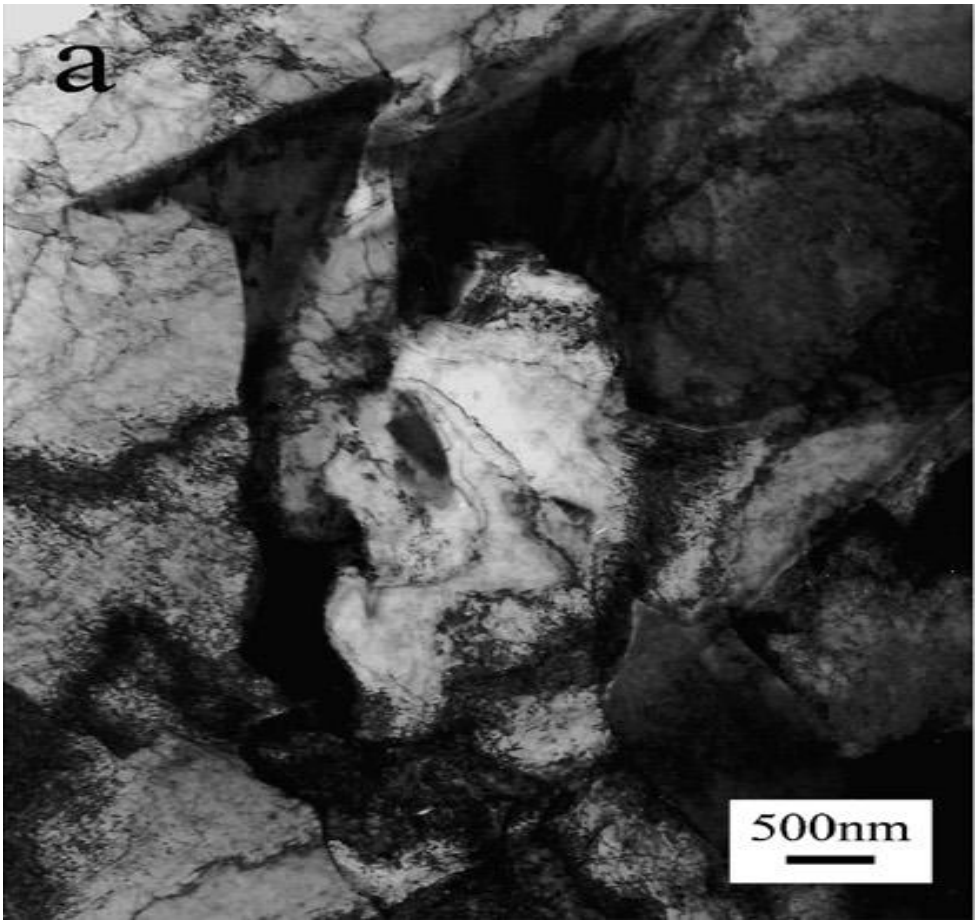

Figure 2-6 TEM bright image of M-A island.[5]

2.3.2 Identifying the M-A constituents

This debatable phase, the M-A constituents is not easily identifiable as they are frequently misinterpreted with other microstructures such as carbides or ferrite-carbides, especially when etched with conventional nital solution. This applies to both optical and scanning electron microscopic examinations. [59]

Therefore, a number of researchers[5; 20; 52; 59-61] have focused in understanding the most effective ways to identify and characterise such phases by using several techniques. These include creating new and effective etchants that gives different orientations from the normal etchants, also by using several etching and microscopic techniques such as SEM, TEM, XRD, EBSD and so on in the characterisation.

2.3.2.1 Etching techniques

Two step electrolytic etching

Some of the researchers [52; 59] have demonstrated the possibility of using two-step Metallographic etching technique in order to characterise between M-A constituents and carbides. Ikawa et al.[52] explained the technique behind the two step electrolytic etching.

Ethylene diamine tetra acetic acid (EDTA) 5 g, sodium fluoride (NaF) 0.5 g and distilled water 100 ml was used as the first etchant. 3 volts and 3 seconds were used as the etching conditions. This method is excellent in etching the ferrite while leaving the M-A constituents and carbides unetched.

Subsequently, picric acid 5 g, sodium hydroxide (NaOH) 25 g and distilled water 100 ml were used as electrolytes for the second stage etching, with 6 volts and 30 seconds etching conditions.

This second stage tends to etch carbides preferentially, such that after the two stage etching, the M-A constituents are embossed and carbides are depressed in a ferritic matrix. This makes it easier to distinguish between M-A constituents and carbides when inspected in SEM as shown in figure 2-7.

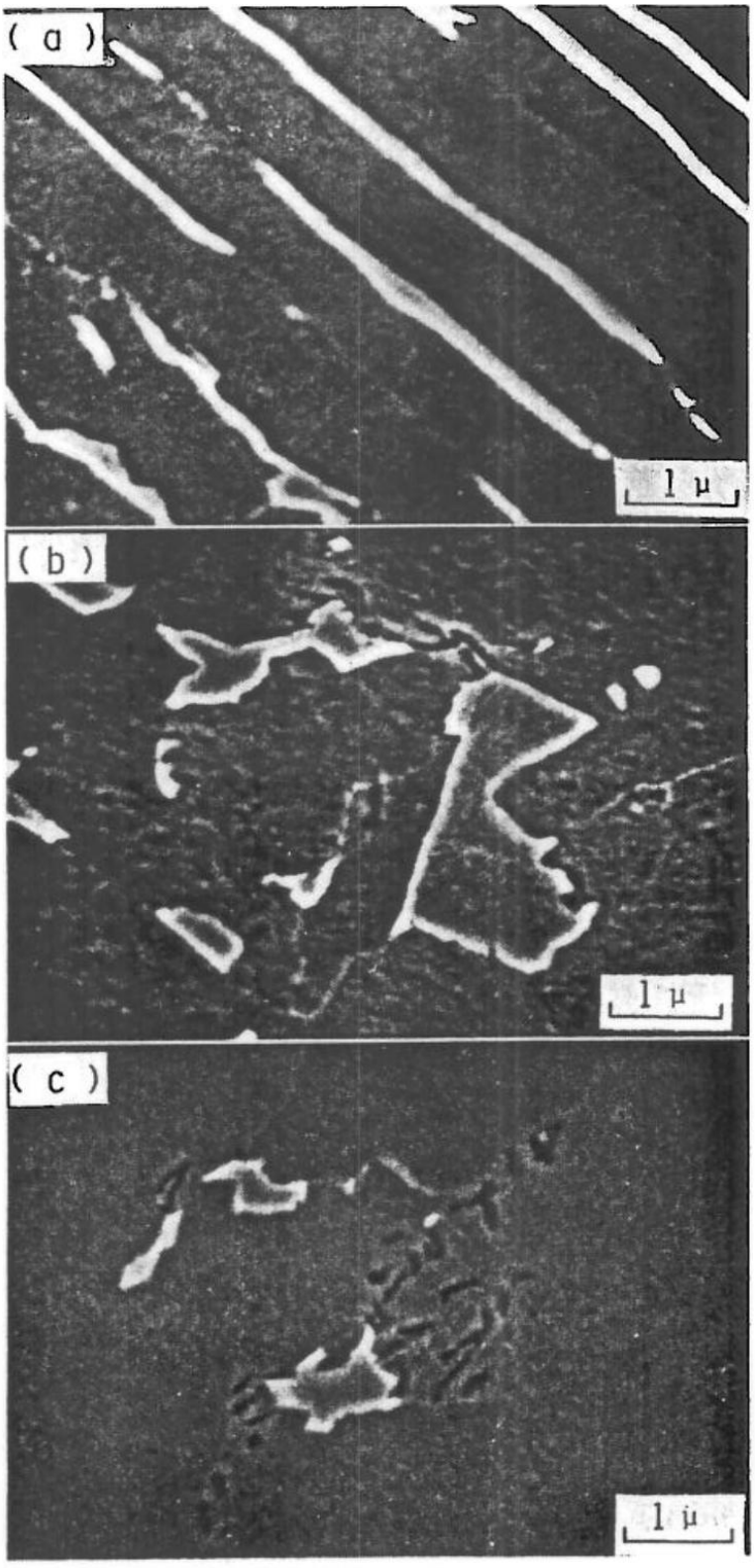

Figure 2-7 SEM micrograph after two step electrolytic etching showing (a) elongated M-A constituent, (b) Massive M-A constituent and (c) decomposed structure[52]

Villela's reagent

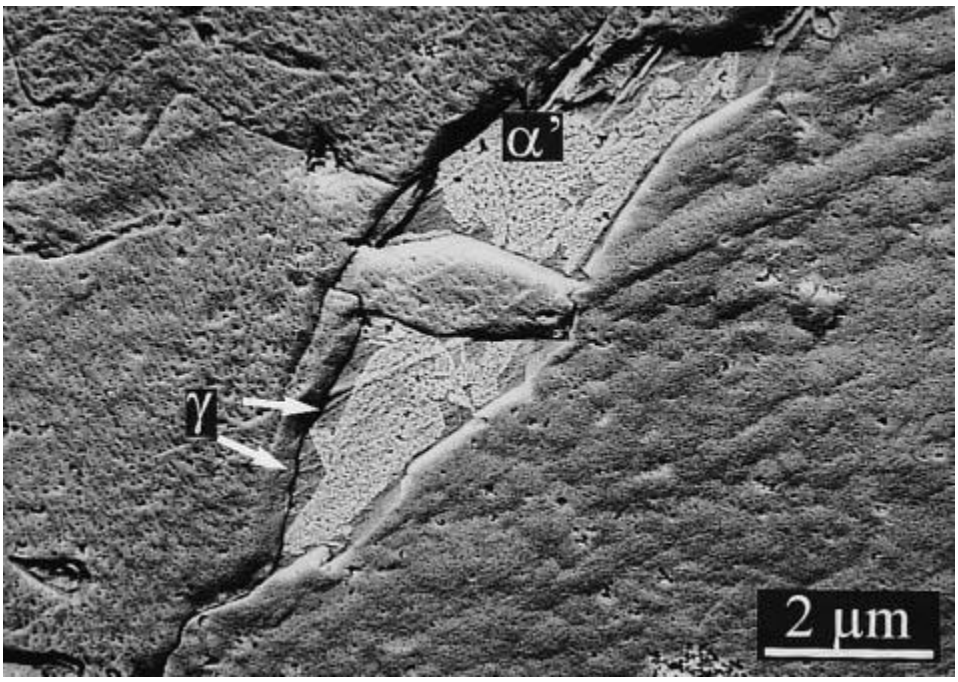

Figure 2-8 Typical mixed M-A island observed (after Villela etching) using FEG equipped scanning electron microscope operated at 1 kV.[20]

Villela's reagent (ethyl alcohol 95 ml, hydrochloric acid 5 ml and picric acid 1 g) was used on SEM samples. It makes martensite and austenite in the M-A constituents to be characterised accurately as reported by Lambert et al.[20] Figure 2-8 is showing SEM micrograph taken after etching with Villela reagent.

1% sodium bisulphate etchant

Lambert et al.[20] use 1% sodium bisulphate etchant which results into very distinctive colouration of the different phases. That makes them easily identifiable. It is such that bainite appears light brown, retained austenite appears white, martensite as brown and carbides as black under optical microscope.

LePèra etchant

LePèra[60] also comes up with a new improved etchant and a method for characterizing the various phases in high-strength dual-phase steels.

Conventional techniques and etching procedures have certain limitations when micrographs were taken for electronic image analysis. In such circumstances, often, specimens are tempered or over etched in order to get sufficient contrast during image analysis. This may cause some of the phase constituents e.g. bainite and grain boundaries to look similar (assume same shade) during micrograph observation.

It was found that using 1% aqueous sodium-meta-bisulfite (Na_2S_2O) and 4% picric acid in ethyl alcohol in a 1:1 ratio produced excellent contrast. This eliminates the need for tempering or over etching.

The technique for preparing the specimen is such that the normal grinding methods are used. But the final polishing is done in a series of polishing and short etching treatments (5-7 sec) with 2% nital to remove any deformed metal.

Caution has to be taken to remove completely the nital etch before using LePèra etchant. This is because any traces of the nital on the specimen appears passive to the etchant. Therefore the final polishing needs to be done twice longer to ensure there is no more nital on the specimen. The etchant is then mixed and used immediately by immersing the sample for 7-12 seconds at room temperature. This shows a kind of effervescent reaction at the surface during the etching process. Finally the specimen is rinsed with ethyl alcohol and blown dry. The surface should appear as blue-orange.

Figure 2-9 and figure 2-10 are showing optical micrographs of a high strength dual phase steel etched with both nital and LePèra etchants. The same position was etched with the two reagents for comparison.

Modified LePèra reagent

The quest for characterizing these phases leads Clark et al.[62] to modify the LePèra reagent. They use a new mixing formula with a volume ratio of 1:2 (4% picral: 1% aqueous sodium-meta-bisulfite). This differs from LePèra with a mixing ratio of 1:1. They found it to be more effective for HSLA 100 steel. The mixture must be prepared just before etching, and discarded after, i.e. not to be

re-used again. The suggested etching time is between 30 – 60 seconds, until the samples turn in to a uniform golden-tan colour.

A three dimensional optical micrograph of the same samples etched with 2% nital and modified LePèra agent is shown in figure 2-11.

(a) 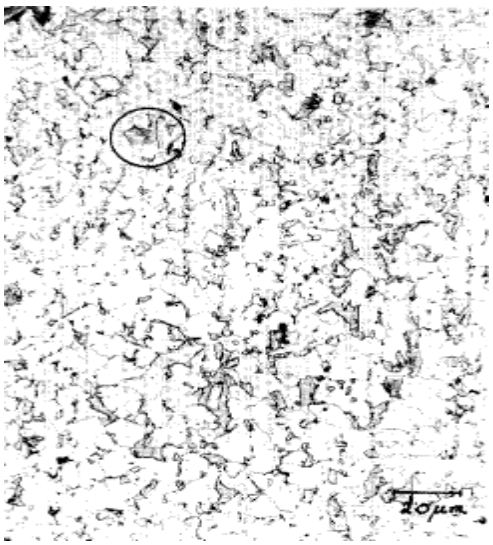 (b) 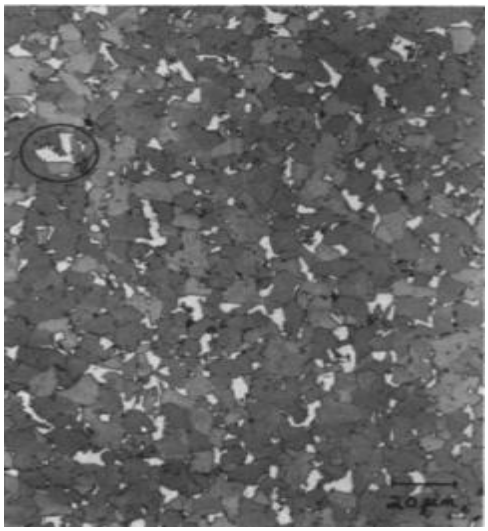

Figure 2-9 (a) High-strength dual-phase steel. 2% nital (b) same field as a, improved etchant.[60]

(a) 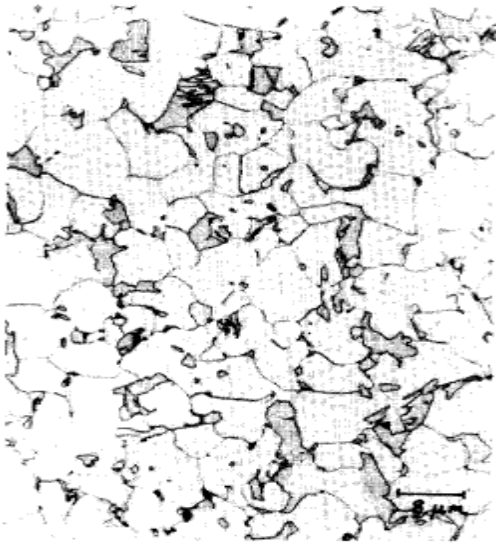 (b) 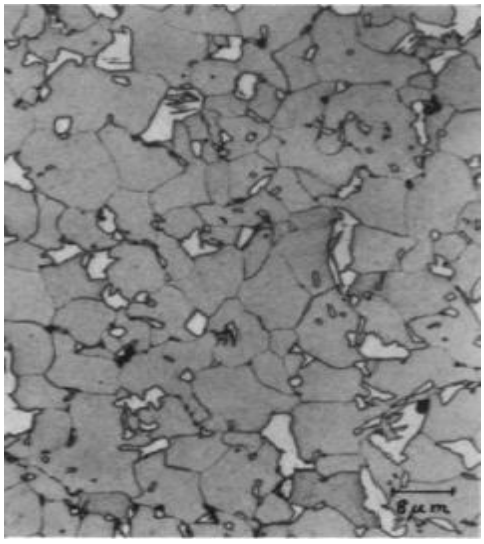

Figure 2-10 (a) same sample as above 2% nital (b) same field as a, improved etchant.[60]

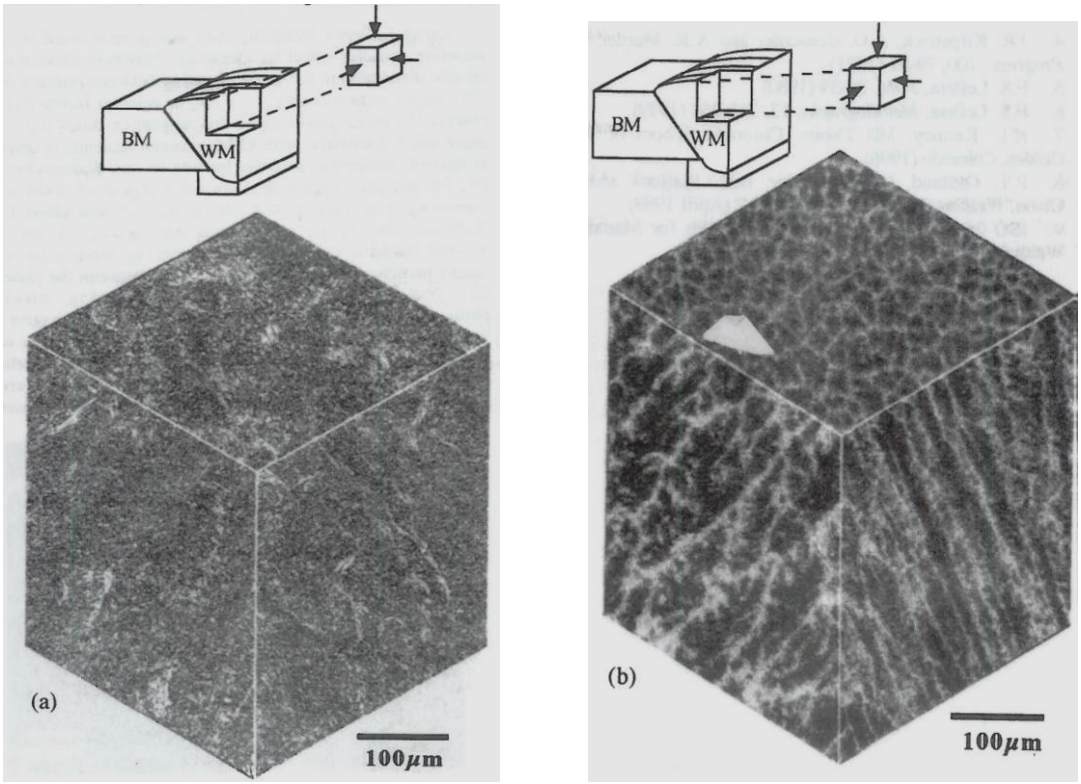

Figure 2-11 Three-dimensional optical micrograph showing, (a) as-deposited microstructure as revealed by 2% nital and (b) solidification segregation as revealed by modified LePèra Reagent.[62]

2.3.2.2 Microscopy

Optical microscopy has by far been the oldest and most widely used means of identifying microstructures. With the advent of the electron microscopy both scanning and the transmission, more detailed information can be generated from the samples, following a meticulous preparation. The recent EBSD[63; 64] and XRD[65] techniques also contribute immensely in microstructural characterization and metallurgical phases determination respectively.

Many researchers [5; 52; 61; 66] have employed one or more of these techniques to determine the so called M-A constituents, understand its appearance, mode of formation and favourable sites or locations.

These techniques have also been employed in characterizing other defects.[67] Li et al.[68] makes extensive use of EBSD to investigate fracture separation, while

Chunming et al.[5] have researched in to this unexploited area, by using the TEM to characterise the M-A islands in X70 pipeline steel, as discussed earlier.

Zhong et al.[61] use the TEM technique to study in-situ the effect of these M-A island on the crack propagation in an ultrafine acicular ferritic pipeline steel (UFAF). Their result indicates that grain-boundary-film structure comprising of Martensite/Austenite, could have a significant effect on the crack propagation behaviour in UFAF steel. Presence of such structure results in lowering of fatigue-crack-growth-rate (FCGR), because of roughness induced crack closure (RICC) during cyclic loading.

The enhancement of this RICC by the M-A film structure has been considered as a novel discovery, which can play a role in the development of new pipeline steels with both high fatigue properties and high strength.[61]

In recent advances, Komizo and Terasaki[69] developed a new Time Resolved X-Ray Diffraction (TRXRD) system, which is a very useful kit for the development of high strength steel weld metal with martensitic phase. Their recent work was an in-situ study of the solidification behaviour for a GTAW welding of super-martensitic steel using the developed system. They were able to catch the peritectic reaction during solidification of the weld, within a time resolution of 0.01 seconds. Figure 2-12 is a schematic representation of the TRXRD.

Earlier work by Babu et al.[70-72] was based on observing the phase evolution in Fe-C-Mn-Al steel welds under rapid and slow cooling conditions. They made use of the in-situ TRXRD technique with synchrotron radiation, at a resolution of 0.05 seconds. The metallurgical phase evolution in both the HAZ and the WM was observed. Figure 2-13 shows the experimental set-up used for the TRXRD, while figure 2-14 is a schematic representation of the slow and fast cooling experiments.

Zhao et al.[73] made use of XRD technique to observe the lath boundary thin film martensite, in acicular ferritic ultralow carbon pipeline steels. They were able to find a relation between the increase in toughness of the ultralow carbon steel and the presence of the lath boundary thin film. This is due to the change in

fracture grain to smaller size, and inhibition of crack propagation or change in its direction.

Electron microscopy techniques, e.g. SEM, TEM and EBSD have been employed in characterizing the microstructures of X80 and X100 pipeline steels.[74] The results revealed the metallurgical phases of X80 to principally consists of acicular ferrite containing M-A phase. The phases in X100 are bainitic ferrite, in lath and granular morphologies as the main phase, with some M-A as a second phase.[74]

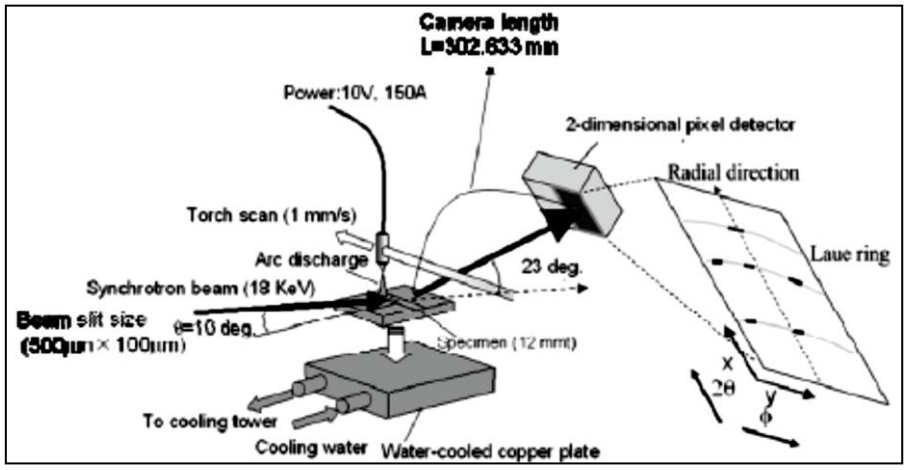

Figure 2-12 Schematic illustration of Time-Resolved X-Ray Diffraction system set in the 46XU beam line in Spring-8.[69]

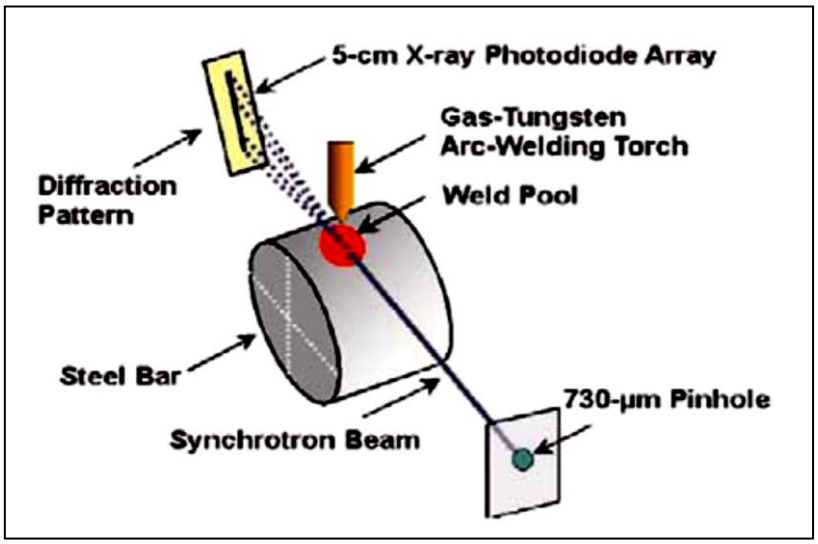

Figure 2-13 Experimental setup for TRXRD experiments.[72]

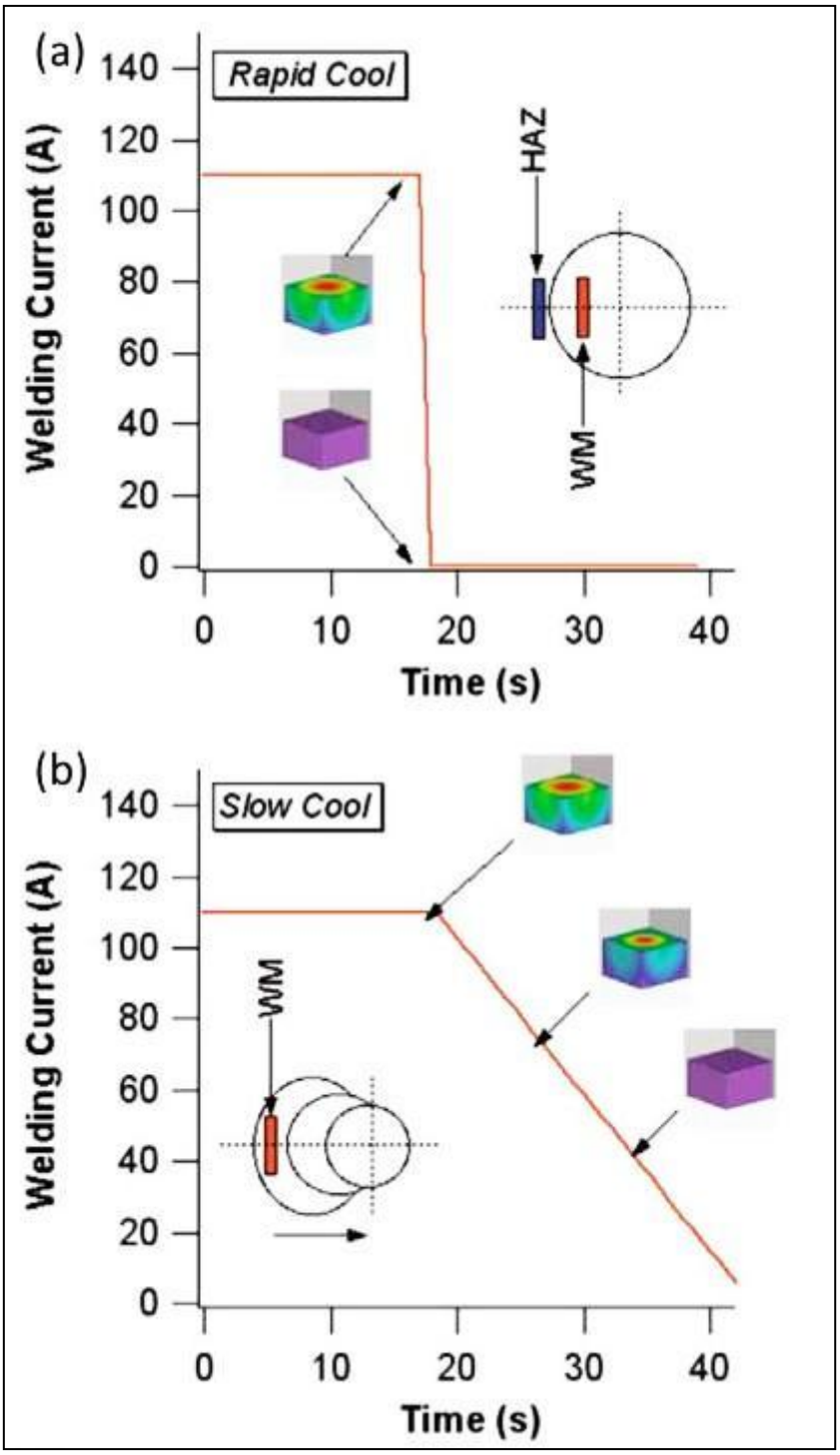

Figure 2-14 (a) is the schematic representation of static weld experiment where the arc was extinguished instantaneously, and (b) slope-down experiment where the arc current was reduced slowly from maximum value to zero in 25 s. Due to the decreasing current, arc movement took place and the weld pool shifted as shown in the inset.[72]

Elmer et al.[75] presents the Spatially Resolved X-Ray Diffraction (SRXRD) as a novel and unique experimental procedure. It was used to characterise the microstructural evolution, by directly mapping the existing phases in the HAZ during arc welding. Carbon-manganese steels were investigated in their research. Different phase transformation regions such as; α-ferrite, partial and/or complete transformation to α-Fe, γ-Fe, and δ-Fe phases were among the transformations identified using the system.

A study conducted by Nobuaki et al.[76] in-situ observation of austenite to ferrite transformation in low carbon steels was explored by using a laser scanning confocal microscope, as shown in figure 2-15. This is another novel method of studying the transformation behaviour of different materials.

Most of these researches could be used as an input towards pipeline welds, for fundamental understanding about the reasons of M-A phase formation. More knowledge about the In-situ transformation during the arc welding of these pipeline steels could be gathered.

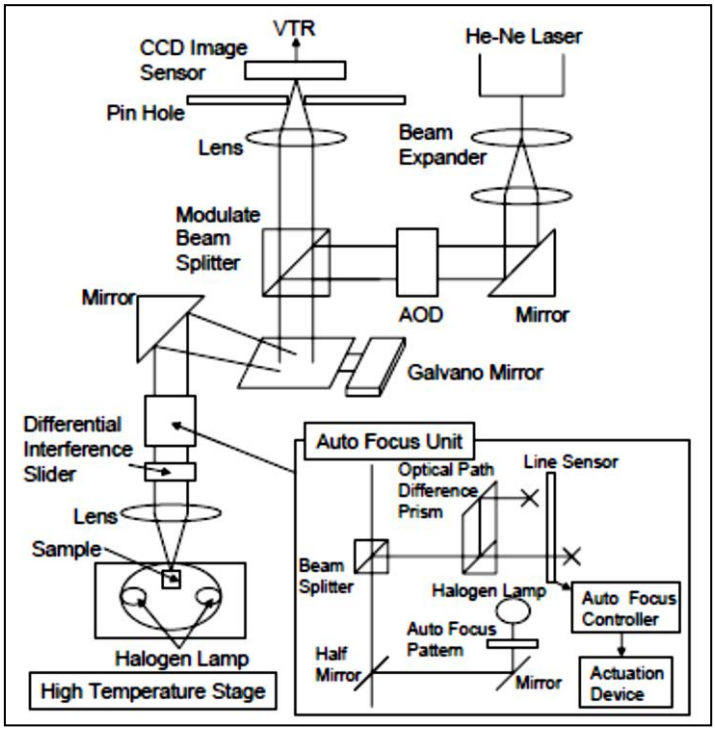

Figure 2-15 Schematic diagram of high-temperature laser confocal microscope system.[76]

2.4 **Phase transformation in pipeline steels**

The understanding of phase transformation in pipeline steels is vital.[77] Due to the nature of their applications, i.e. under different terrains and operational conditions, pipeline steels requires a matching combination of strength and toughness. These properties are achieved through various processing and heat treatment routes, which gives different phase combinations and microstructural condition. Therefore a sound knowledge of phase transformation is necessary to understand the effect of welding heat on these pipeline steels.[42; 78; 79]

Knowledge of grain growth and nucleation during phase transformations help to develop materials with excellent mechanical properties.[57] Due to the nature of welding thermal cycle, the weld metal cools very fast, losing heat to the environment and the neighbouring base metal. This leads to the formation of heat affected zones.

This rapid cooling leads to non-equilibrium conditions, resulting in strain induced solid state phase transformation.[70] In pipeline steels welds, the condition is like normal solidification of a cast metal.[80] A cellular-dendritic structure is obtained, which consist of coarse and columnar austenitic grains that curve into the weld centre line, with a fine cellular network within the grains.[49]

Grain nucleation and growth are very important in polycrystalline materials, i.e. metals. During processing, they control the kinetics of different phase transformations and recrystallization processes.

The final grain size determines the strength of the material. Generally smaller average grain sizes results in a stronger material, such as these high strength steels.[57] This has been explained by equation (2-3) termed as Hall- Petch equation. Where d is the average grain diameter, σ_o and k_y are constants for a particular material.[81]

$$\sigma_{yield} = \sigma_0 + k_y d^{-1/2} \quad \textbf{(2-3)}$$

Phase transformation during welding is generally controlled by a number of factors which include, the composition of both the base and filler metals, metallurgical processes occurring at different interfaces, and the thermo-mechanical histories during the welding process.[49]

The general approaches for investigating phase transformations in welding have been classified into two: In-vitro and In-situ.[82]

In-vitro, which simply means simulation of the welding thermal cycles on some standard specimens that could be used for further mechanical and microstructural analysis, have been in use since the late 40's by Nippes and Savage.[83]

While in-situ means using a real weld to measure the thermal history at a particular point, with the use of thermocouples or other non-contact methods such as infrared[84] and/or thermal cameras. Accurate capturing of thermal cycles (temperature vs. time) and differential analysis of the same are used in determination of start and finish of the phase transformation.[82]

On-going researches have shown the viability of other thermal analysis methods in determining the phase transformation temperatures in welding, such as single sensor differential thermal analysis.[85]

2.4.1 Cooling rates during multi-pass welding and its effects on metallurgical characteristics

Phase transformations are influenced by the cooling rates experienced by the weld metal and associated HAZ from the different welding process variables.[70]

Given the wide range of cooling rates taking place during the solidification of steel welds, it is likely that the first phase to form is not in an equilibrium condition.[70] This leads to the formation of different kinds of phases and thus affects the mechanical properties.

Studies[78; 86-90] have been carried out to understand the effect of different cooling rates on metallurgical and mechanical properties of pipeline steel welds.

Recent work by Keehan et al.[91] explores the effect of cooling rate on microstructure and properties of high strength steel welds.

Shi and Han[92] used simulated thermal cycle specimens to show the effect of cooling time and peak temperatures on fracture toughness and microstructure. They found in their work that the best toughness was obtained at a cooling time $t_{8/5}$ of 18 s. Also the volume fraction of M-A constituent increases with increase in cooling time, while that of martensite decreases with increase in cooling time.

The microstructural characterisation of API 5L X80 pipeline steels subjected to different thermal cycles was evaluated by Bott et al.[93] they subjected the steels samples to an austenitization temperature of 900°C for an hour, then cooled at three different rates of 1.5°C/s, 30°C/s and 115°C/s using air, oil and water respectively. They looked at the effects of these thermal cycles on the hardness, tensile strength, grain size and phases.

2.5 **Inter-pass temperature**

Inter-pass temperature can be referred to as the temperature both minimum and maximum, of the preceding pass and adjacent base metal just before the successive pass during a multi-pass weld.[94] It has a very strong relation with the mechanical and metallurgical properties of a weld, it also influences the distortions. Inter-pass temperature depends on the composition of the material and the cooling rate of the weld.[95]

As explained by Jones and Luo[96] the preheating range is based on various factors such as; chemical composition and physical properties of the weld piece, the thickness of the weld pieces, electrode type, heat input and the level of standards needed. The control of preheat and inter-pass temperatures reduces the effect of residual stress and cooling rates imposed by the welding process, and thus the metallurgical phases formed.[97] Preheating temperature can be calculated using the carbon equivalent, which shows the possibility of martensite formation in a particular material.[98]

Lord et al.[99; 100] reported the results from using artificial neural network to predict the inter-pass temperature and its effect on the various mechanical properties and microstructural constituents.

2.6 **Continuous cooling transformation (CCT) curve**

A CCT diagram is a tool that can be used to design the processing routes for steel with specific composition and microstructure so as to get the desired metallurgical and microstructural properties. This has significant application in pipeline steels and materials in general. CCT describes the degree of phase transformation as a function of time for an incessantly decreasing temperature. The various lines in the diagram shows the start and finish temperatures for each metallurgical phase change.[101] Figure 2-16 is a typical CCT diagram.

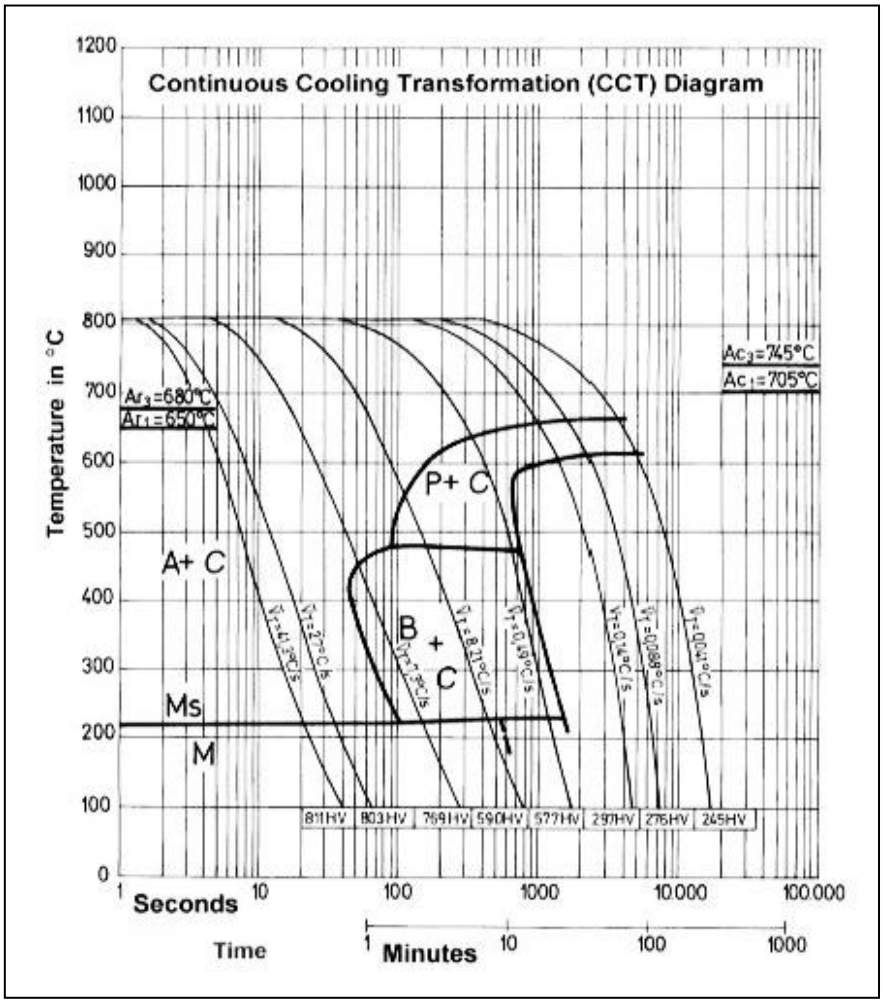

Figure 2-16 Continuous cooling transformation diagram[102]

In the early days, CCT diagrams were produced in the laboratories using conventional experiments (heating furnace). This need a lot of work to be carried out and thus very labour intensive and took a long period of time to complete one.[87]

However, with the advent of new computational techniques and more sophisticated equipment that allows the simulation of the cooling rates in materials. Coupled with the huge amount of data available at the moment, it has therefore becomes easier and faster to produce these CCT diagrams.[103; 104]

Equipment's such as Dilatometer and Gleeble thermo mechanical simulator are increasingly used. A lot of research is being conducted using these machines to simulate the effect of thermal cycle on pipeline steel. [88; 89; 105-108] CCT diagrams and their applications on the heat affected zone[78; 109] and microstructural development of micro alloyed steels[110-112] have been investigated.

Onsoien et al.[109] developed a CCT diagram for X70 grade pipeline steel HAZ by the means of a dilatometer and metallographic analysis. The diagram is said to be valid for the HAZ in welding operations. The martensite starts and finish temperatures, together with A_{C1} and A_{C3} were determined. They found out that at a relatively low cooling time of about 10 s, the metallurgical phases are basically bainitic and martensitic, a fully martensitic structure was obtained at the shortest cooling time. While longer cooling times i.e. 20 to 109 seconds produces a 100% bainitic microstructure.

Earlier, Shome and Mohanty[78] tried to work out the CCT diagrams for the HAZ in HSLA-80 and HSLA-100 steels. The HAZ simulations were carried out using a Gleeble-1500 thermo-mechanical simulator and a dilatometer. They were able to establish CCT diagrams for the entire HAZ in the two pipeline steels. The metallurgical phases mainly consist of acicular ferrite (AF) and lamellar martensite (LM) phases. Their proportions and morphologies were changing with the peak temperatures and cooling conditions of the weld thermal cycles.

In agreement with Onsoien et al.[109], they[78] also found out that a full martensitic structure was obtained under low heat input, which means that the weld was

cooled faster under a shorter period of time. This was observed in the HSLA-80 steel, while the HSLA-100 presents a mixed structure.

Guang et al.[87] proposed a new method of plotting CCT curves for some steels by using differential scanning calorimetry in addition to conventional dilatometer and metallographic analysis, to accurately plot the CCT diagrams. Figure 2-17 to figure 2-19 are showing more on that.[87]

Fonda et al.[113] developed CCT diagrams for two ultra-low carbon welding consumables using a dilatometer. They record the transformation start and finish temperatures by using a large range of $\Delta t_{8/5}$ (1 - 4000 sec) as cooling rates.

2.7 **Dilatometric analysis**

Dilatometry has been an effective way or technique of determining the transformation behaviour of steels.[114] The procedure is based on change in length or expansion of the sample during heating, cooling or isothermal holding.

It has been termed as the most powerful method of studying the solid to solid phase transformations in steels and a wonderful way of determining the phase transformation temperatures in steel during continuous heating and/or cooling.[107]

The basic theory behind the use of dilatometric analysis for phase transformation is that, during phase transformation the lattice structure of a material changes, which is followed by a change in specific volume.[107]

These techniques are valuable in determining and recording the time-temperature and the dilatation curves of a material. These curves are used to extract the relevant information needed to construct CCT diagrams for different materials, by using the differential thermal analysis of the curves and the quantitative analysis of the microstructures of the samples used.

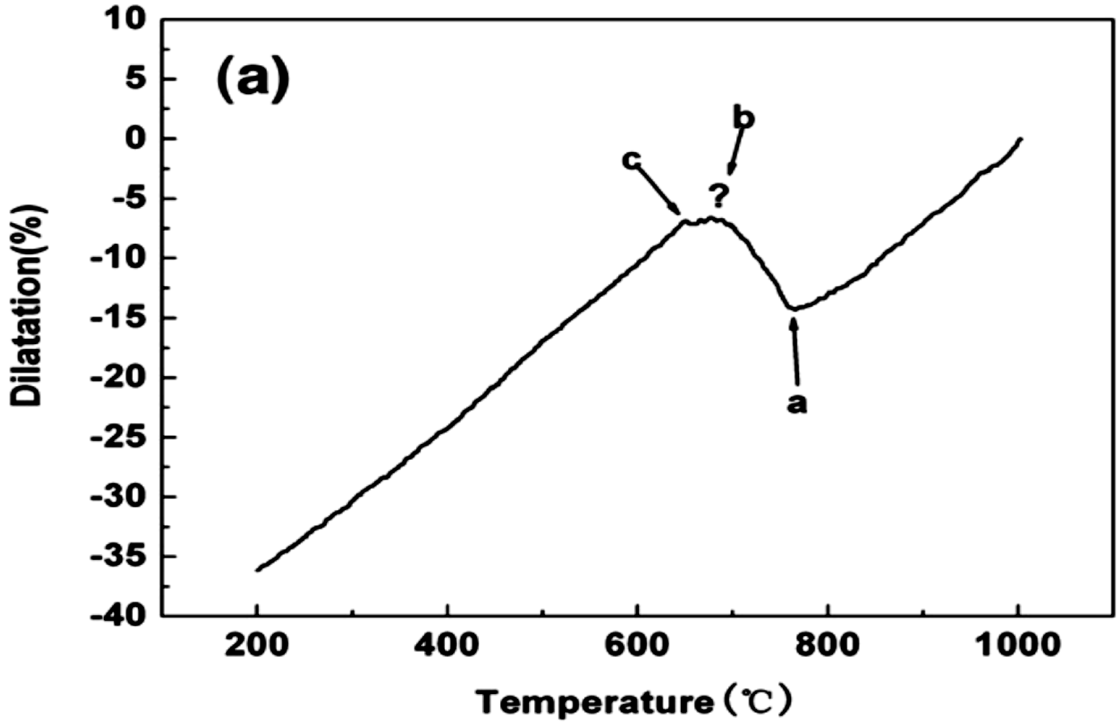

Figure 2-17 A typical dilation curve at a cooling rate of 0.1°C/s with no clear vertices.[87]

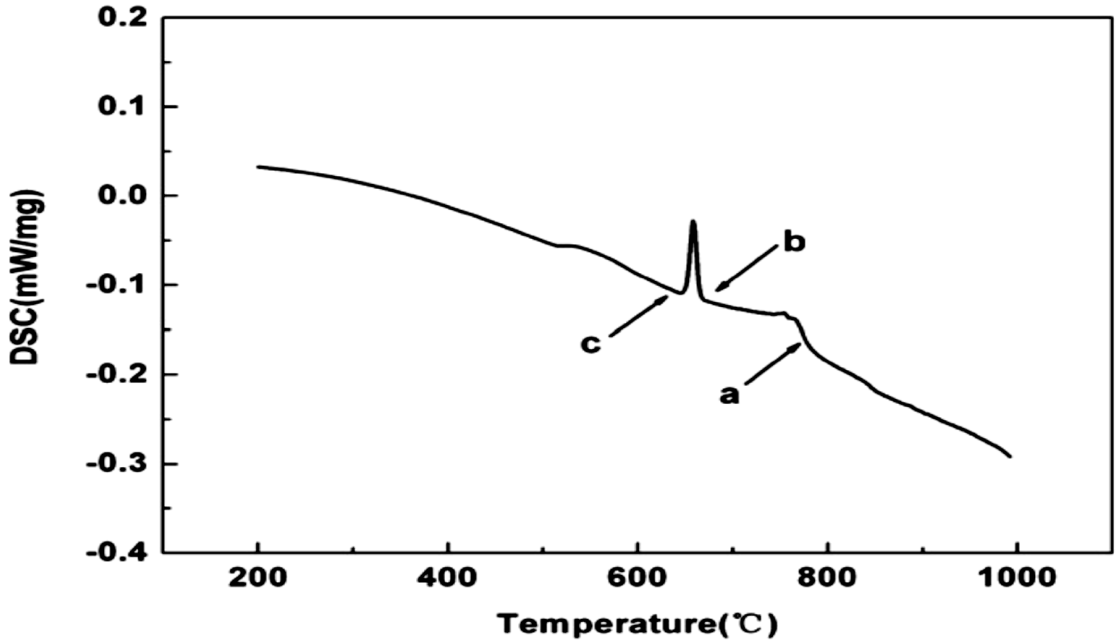

Figure 2-18 A DSC diagram at a cooling rate of 0.1°C/s showing clear transformation points.[87]

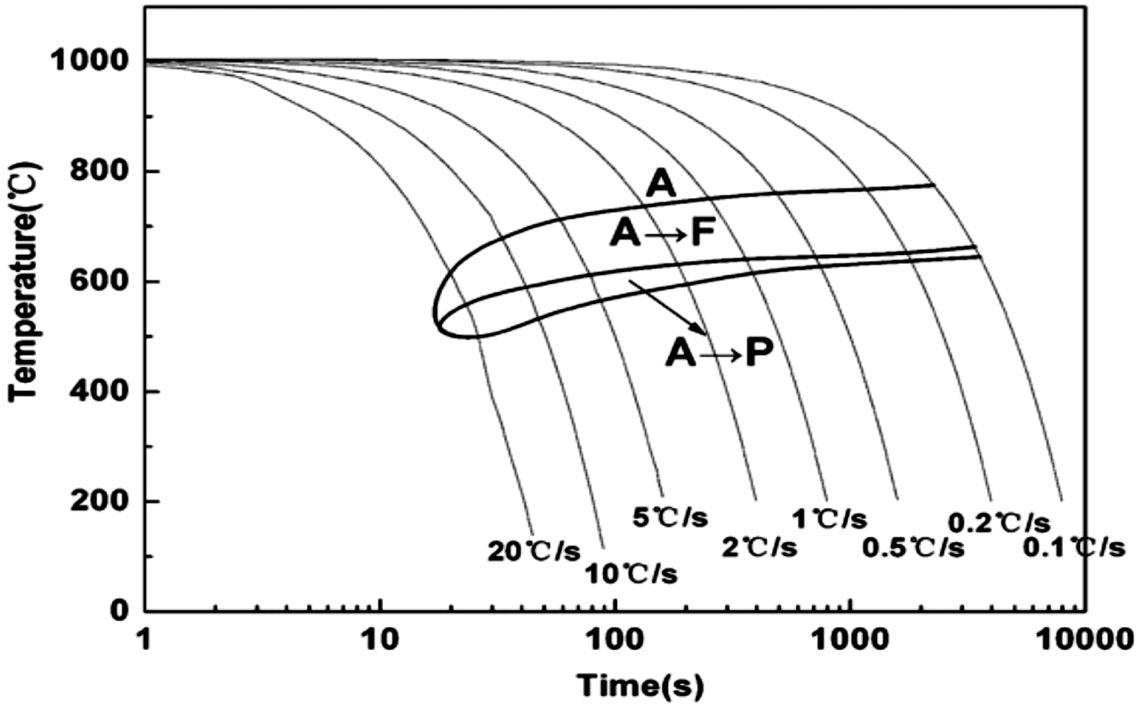

Figure 2-19 A CCT diagram made by the use of dilatometric test, microstructural examination and DSC analyses.[87]

Interestingly, the question raised by Guang et al.[87] on the clarity of the dilatation curves, has been explained rather more clearly and convincing by Garcia et al.[107] and Lee et al.[89] as discussed below.

Lee et al.[89] investigated the use of dilatometric analysis to understand the transformation pattern of carbon manganese steel. Figure 2-20 indicates the five possible transformations obtainable from the dilatational changes recorded at different cooling rates. The arrows indicates the transformation start temperatures of polygonal ferrite (F), acicular ferrite (AF), pearlite (P), pseudo pearlite (PP), martensite (M) and the martensite start temperature (M_s).

They showed the resulting microstructure and transformation products obtained from the different cooling conditions. An interrupted heating and quenching test was carried out to define the exact microstructures that forms at various temperatures, these was how the arrows in figure 2-20 were identified.

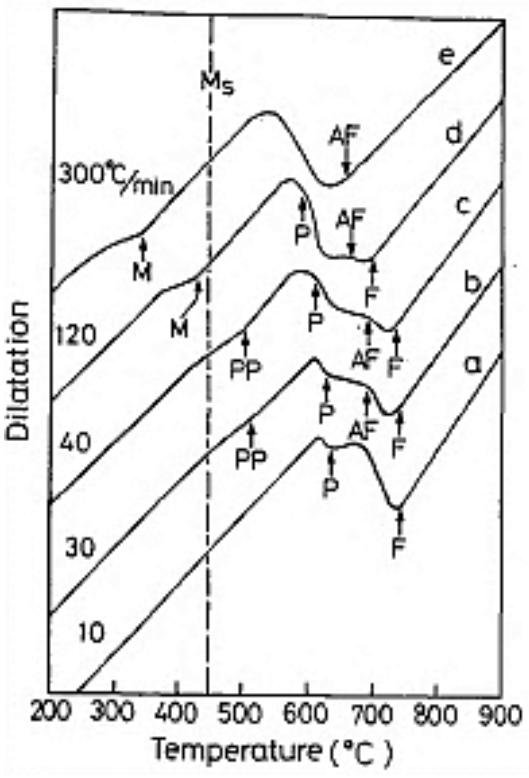

Figure 2-20 Dilatation curves of various cooling rates.[89]

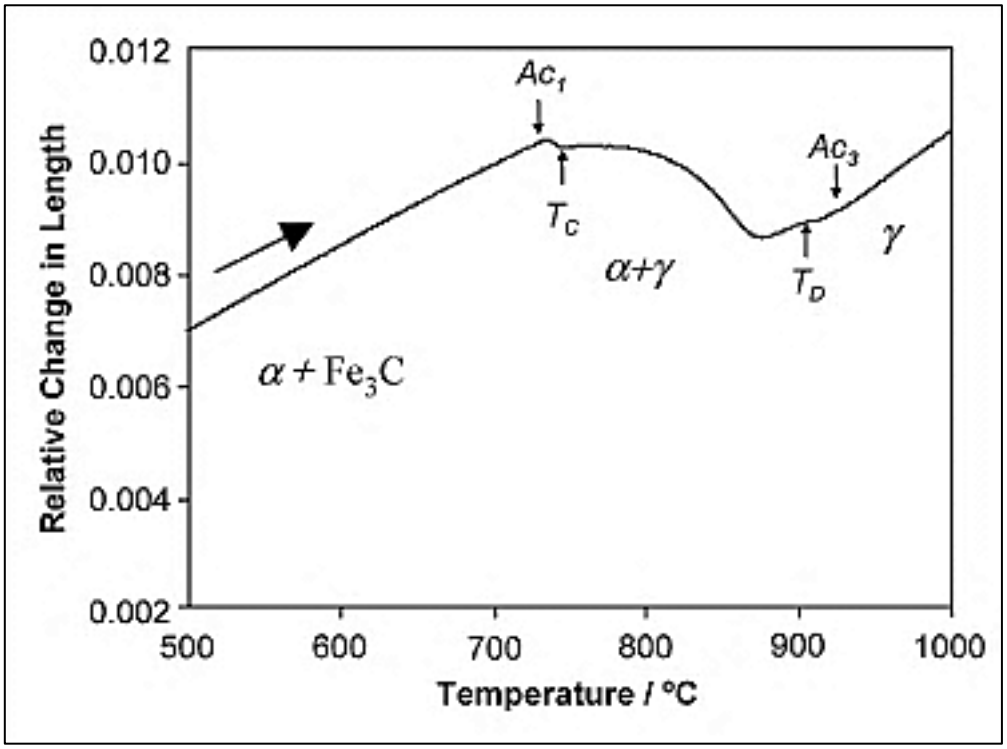

Figure 2-21 Heating dilatation curve of a low carbon steel at a very slow heating rate (0.05 K s^{-1})[107]

Garcia et al.[115] used high resolution dilatometry and the interrupted heating process at 10°C above and below the A_{C1} temperature to clarify the anomaly referred to as T_C and T_D in figure 2-21. It was found that the A_{C1} is the pearlite to austenite transformation point, while T_C corresponds to the ferrite to austenite transformation start temperature.[115]

The deviation observed at T_D corresponds to the austenite formation from the residual untransformed ferrite grains remaining in the microstructure. Datta and Gokhale[116] found out that these residual ferrite grains transforms almost instantaneously at T_D under isothermal conditions. This is due to change in ferrite to austenite transformation kinetics.[116]

High resolution dilatometry was also used to detect the splitting phenomena of martensitic transformation in some stainless steels.[117] They explained that in these materials, the non-isothermal transformation of austenite in to martensite is not continuous within a certain range of temperatures. It sometimes splits in to different stages as shown in figure 2-22.

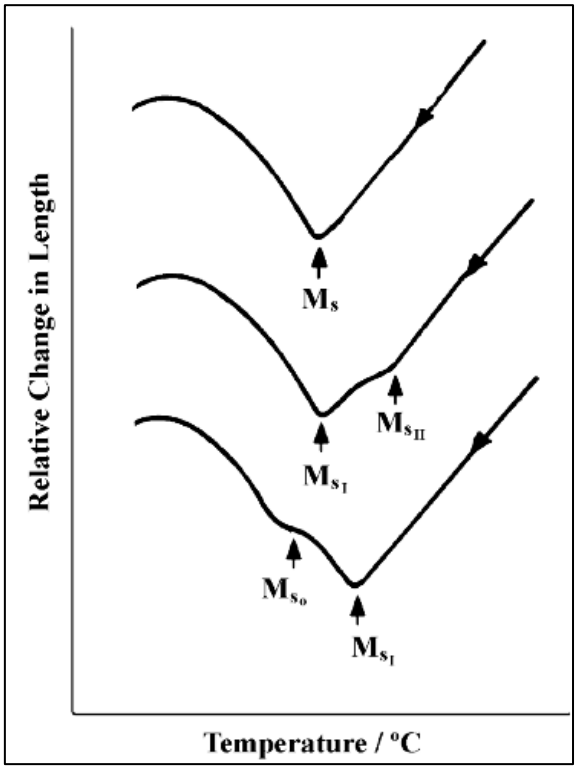

Figure 2-22 Dilatometric representation of the splitting phenomena on the martensitic transformation of Cr13 and CrMoV14 stainless steels.[107]

2.8 **HAZ simulation using Gleeble thermo mechanical simulator**

As far back as the 1950's, Nippes et al.[118] developed a device for testing the temperature effects and thermal histories of structural alloys. This gives the art and science of HAZ simulation a new face, since the size of the HAZ is normally very small to machine out specimens for mechanical testing. A fairly close temperature peaks and microstructures could be achieved by using thermo-mechanical simulators such as Gleeble.[119] Figure 2-23 is showing a schematic representation of a weld simulator.

Knorovsky et al.[119] explores the pros and cons of dilatometry in the Gleeble, which they describe as a sophisticated piece of equipment. The Gleeble is used in producing specimens with the required time, temperature and deformation histories. Though it was invented for producing bulk samples of simulated localised HAZ regions, it has found more applications such as the study of kinetics behind solid state reactions using dilatometry, among others.

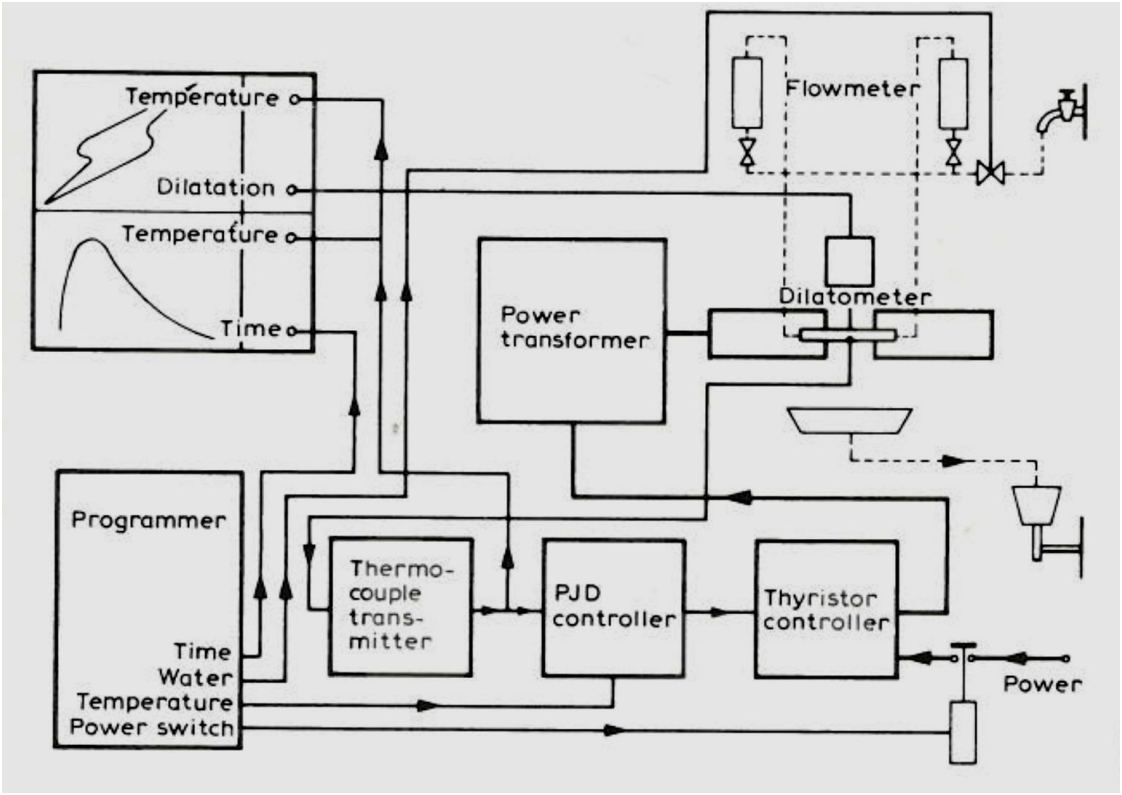

Figure 2-23 Schematic layout of weld simulator equipment[49]

They[119] also outlined the common errors as bad laboratory practice, inadequate personnel training and equipment condition (i.e. calibration, functionality and general maintenance). The non-uniformity generally occurring in the material and thermal distribution within the samples are other areas of concern.

2.8.1 Modelling of weld simulation

Models have been developed to simulate the thermal cycles, cooling rates and phase transformation in both weld metal and HAZ, using various welding processes such as GMAW tandem and dual tandem processes. These models were developed to predict the mechanical properties of girth welds on pipelines steels.[120]

Garcia et al.[121] modelled the pearlite-to-austenite transformation in eutectoid steel. They apply a mathematical model using the Avrami equation, which successfully reproduce the kinetics involved in pearlite-to-austenite transformation, during continuous heating. The Experimental transformation temperatures A_{C1} and A_{C3}, and the overall dilatometric behaviour due to austenite formation were in good agreement with their predicted results. On the other hand, austenite to ferrite phase transformation in low alloy steels was also investigated by Gamsjager et al.[122]

Other researchers[123-125] have also looked at the phase transformation kinetics in relation to dilatation curves and the isothermal decomposition of austenite.

2.9 **Effect of different welding procedures on HAZ toughness**

The use of modern efficient and highly productive welding procedures has become inevitable for the pipeline construction companies. High strength and toughness is essential in both girth weld metal and the neighbouring heat affected zones (HAZ). Especially in the application of strain based design, the requirements for strength and toughness is becoming more stringent.[126]

Hamad et al.[127] have looked at the effect of different GMAW procedures, including dual, single and tandem torches on the HAZ toughness of X80 grade.

They use both crack tip opening displacement (CTOD) and Charpy impact test to evaluate the HAZ toughness. Finally they conclude that lower heat input coupled with lower $t_{8/5}$ cooling times results in a considerable improvement of the CTOD values.

2.10 **Effect of composition**

It has been established[128; 129] long ago that chemical composition[130] determines the martensitic substructure, by influencing the M_s temperature and the strength of the martensite formed. Due to the role of most alloying elements as solid solution strengtheners in austenite, the thermodynamic driving force for initiating martensitic shear transformation is increased, while the M_s temperature is lowered.[58]

The results of McMahon and Thomas[58] showed thin sheets of highly deformed retained austenite surrounding some of the martensite laths in all the as-quenched samples. Upon heating to a tempering temperature of about 200ºC, the interlath austenite was reduced, while upon tempering at 400ºC, the interlath disappears completely. This indicates that the tempering process has transformed the retained austenite into ferrite, followed by precipitation of interlath carbides, this leads to a loss in toughness.

The influence of niobium on the microstructure, mechanical properties and the transformation kinetics of the coarse grain heat affected zone (CGHAZ), in high strength low alloy steels (HSLA) using different heat inputs has been investigated.[131]

Their results showed that the addition of 0.026% niobium decreased the transformation start temperature of the steel by about 15°C to 30°C, when compared with steel without niobium. They also showed that 0.026% niobium addition can lead to a very significant deterioration of CGHAZ toughness, when welded at high heat inputs. This was related to the formation of substantial amount of granular bainite. But at low heat inputs the toughness decreases a little.

The simulated HAZ of some HSLA steels containing four different levels of vanadium have been studied, in order to evaluate the effect on mechanical properties and microstructure. The work affirm that the addition of not more than 0.05% vanadium in to these low carbon low alloy steels, gives a balance in the desired strength and toughness of the HAZ, while the addition of more than 0.10% the reverse was the case.[132]

Beidokhti et al.[133] explores the effect of titanium addition on mechanical properties and microstructure of HSLA pipeline steel. They established that within a range of (0.02% to 0.05%) titanium, the best possible combination of microstructure and impact properties were obtained. The effects of other chemical elements such as carbon and nitrogen have been evaluated.[134]

In a similar research by Calvo et al.[135] they found out that residual Cu content improves the hardenability, by decreasing both A_{C3} and A_{C1} temperatures, while increasing Nb content raises the non-recrystallization temperature by accelerating niobium (C, N) precipitation. However, Si addition to Nb micro-alloyed steels decreases the non-recrystallization temperature.

Ishida[136] has carried out a thermodynamic calculation to predict the effect of alloying elements on the M_s temperature in iron-based alloys. He showed that the changes in M_s temperature due to the alloying elements addition, is because of the chemical and mechanical effects on the reactions. Finally he combined the effects of these alloying elements on the M_s temperature of iron in the following equations.

$$Ms\ ^{o}C, at.\% = 545 - 71C + Al + 7Co - 14Cr - 15Cu - 23Mn - 8Mo - 6Nb - 13Ni - 4Si + 13Ti - 4V + 0W \quad \textbf{(2-4)}$$

$$Ms\ ^{o}C, wt.\% = 545 - 330C + 2Al + 7Co - 14Cr - 13Cu - 23Mn - 5Mo - 4Nb - 13Ni - 7Si + 3Ti + 4V + 0W \quad \textbf{(2-5)}$$

Where equation (2-4) is for atomic percentage and equation (2-5) is for weight percentage. The M_s temperature of pure iron was reported by Gilbert and Owen[137] as 545°C. It was estimated by extrapolating the M_s temperatures from a series of iron-carbon alloys to zero carbon, as carried out in their experiments.

A new empirical formula for the calculation of M_s temperature for pure iron and super-low carbon alloy steels was also developed by Liu et al.[138]

$$Ms\ ^{o}C = 795 - 25{,}000C_1 - 45Mn - 35V\ \ Nb + Zr + Ti\ - 30Cr - 20Ni - 16Mo - 8W - 5Si + 6Co + 15Al \quad \textbf{(2-6)}$$

$$Ms\ ^{o}C = 525 - 350\ C_2 - 0.005\ - 45Mn - 35V\ \ Nb + Zr + Ti - 30Cr - 20Ni\ - 16Mo - 8W - 5Si + 6Co + 15Al \quad \textbf{(2-7)}$$

Equation (2-6) is for $C_1 < 0.005$ and equation (2-7) is for $0.005 \leq C_2 < 0.02$, where C_1 and C_2 are carbon contents respectively.[138]

2.11 **Recent advances**

The idea of identifying the M-A constituents and its effect on pipeline steels have grown in recent time, the influence of different processes and especially their thermal effects or thermal cycles have been investigated.

Moeinifar et al. has conducted some relevant research[139-141] in relation to the thermal cycles of submerged arc welding. The effect of second peak temperature and the simulation of the HAZ for SAW have been explored.

They looked at the effect of the second peak temperature on the subcritical, intercritical and supercritical HAZ of a double pass weld, with the help of a Gleeble thermo mechanical simulator and standard charpy size samples. Three different temperatures were used as second peak; they are 700, 800 and 900°C, while keeping the cooling rates constant. They explore the morphology of the martensite austenite (M-A) constituents using field emission scanning electron microscope, and established that the M-A particles acts as crack initiation sites for fracture, during determination of fracture toughness.[139]

Influence of thermal cycles on the properties of CGHAZ has been examined, it was established that increase in hardness of the CGHAZ was because of the fractional area of the M-A particles due to different cooling rates.[140]

Suzuki et al.[142] made use of oversize charpy samples (11 × 11 mm) for thermal simulation to check the influence of M-A islands on HAZ fracture due to high heat input. The calculated and simulated thermal cycles used in their research indicated that, the higher the heat input the longer it takes to reach the peak temperature, this is far from the reality of a real weld thermal cycle, because in a real weld, the heating is very fast.

It might be more logical to infer that during welding with a higher heat input the heating will be more rapid when compared to lower heat input, where the rise in temperature is less rapid.[142]

In another research conducted by Zhang et al.[131] by using similar sample size as used by Suzuki et al.[142] very fast heating rate (500 °C/sec) was used. This was a similar heating rate observed in a real weld, but a holding time of 3 seconds was used. This was not the case when compared to a real weld thermal cycle.

Li et al. [143] also use oversized charpy samples (10.5 × 10.5 × 80 mm) to thermally simulate the CGHAZ of X70 grade pipeline steel welds, made by manual metal arc welding with a heat input of 1.2 kJ/mm. They use a heating rate of 200 °C/sec and a peak temperature of 1350°C, they also hold at the peak temperature for 1.2 seconds.

2.12 **Summary**

This literature review has critically looked in to the formation of local brittle zones in the heat affected zone of a multi-pass weld. The theories behind the formation of the M-A constituents and the techniques used in order to identify the M-A phase was also reviewed. The inter-relationship between phase transformation, inter-pass temperature and continuous cooling of a multi-pass weld and their influence on formation of M-A phase was also discussed.

Techniques such as dilatometric analysis, heat affected zone simulation, different etching techniques, optical and scanning electron microscopy techniques has also been reviewed.

A substantial amount of research have gone in to identifying and characterizing the M-A phase, which has been linked to the formation of local brittle zones. There is a good understanding of the M-A phase formation in general and especially on multi-pass welds, the theories supporting it are quite elaborate. A good number of techniques have been developed for this purpose, but there is no certainty in the mode of formation of the local brittle zones in a real weld, in terms of phase transformation kinetics.

There is no comprehensive understanding of the thermal cycles responsible for the formation of these brittle phases in a real weld. Most of the researches were making some reasonable extrapolations of the simulated results on to the real welds.

On the other hand, simulation of the various heat affected zones on charpy impact samples in order characterize the effect of the various thermal cycles on the HAZ toughness have been extensively researched. However, the thermal cycles used in terms of heating and cooling are significantly different from a real weld situation. Most of the researchers generate their simulated thermal cycles from computer simulation and welding software.

In this research CCT diagrams were constructed using dilatometric analysis techniques. Understanding welding thermal cycles through instrumented welds, leads to precise knowledge of phase transformation products from the constructed CCT diagrams.

It was shown that combining all these aspects of research would lead to the understanding of M-A phase formation in real life multi-pass weld.

3 AIMS AND OBJECTIVES

3.1 **Aim**

The aim of this research is to develop fundamental understanding on the underpinning process factors that lead to the formation of brittle phases in the heat affected zones (HAZ) of multi-pass pipeline steels welds.

The research will try to derive a simpler methodology to characterise the effect of multiple thermal cycle on the toughness of the high strength low alloy pipeline steels. Derivation of CCT diagrams of the same steels composition would aid in understanding the metallurgical phase formation in the HAZ.

Therefore, a correlation between the metallurgical phase formation and toughness characteristics can be drawn for different multiple thermal cycles representing different welding processes.

3.2 **Specific research objectives**

This research has been narrowed down to four pipeline steels some of which are susceptible to LBZ formation. The following are the research objectives:

1. To record the real HAZ thermal cycles from submerged arc and tandem MIG welds.

2. Carry out CTOD testing of the welds HAZ to check the presence of LBZ.

3. Simulate those thermal cycles in a thermo-mechanical simulator (Gleeble Machine) using standard charpy samples.

4. Impact toughness determination of the thermally simulated specimens.

5. Mechanical and metallurgical characterisation of the welds mentioned in bullet 1 above and the thermal simulation samples mentioned in bullet 3.

6. Identify the thermal cycles which lead to the formation of brittle metallurgical phases resulting in loss of toughness.

7. Recommendations on how to avoid loss of toughness in the heat affected zones (through formation of LBZ).

The flow chart shown in figure 3-1 is a schematic representation of the research programme. The problem of low toughness will be investigated by understanding the welding thermal cycles, thermal simulation using a thermo-mechanical simulator (Gleeble machine) and driving continuous cooling transformation diagrams. Capturing of HAZ thermal cycles in a multi-pass weld and simulation of the thermal cycle will lead to simulation of phase formation and subsequent CCT analysis will indicate phase constituents.

The samples are then characterised both mechanically and metallurgically, and the results were analysed. From the findings, corrections are then proposed on how loss of toughness can be reduced or avoided where necessary.

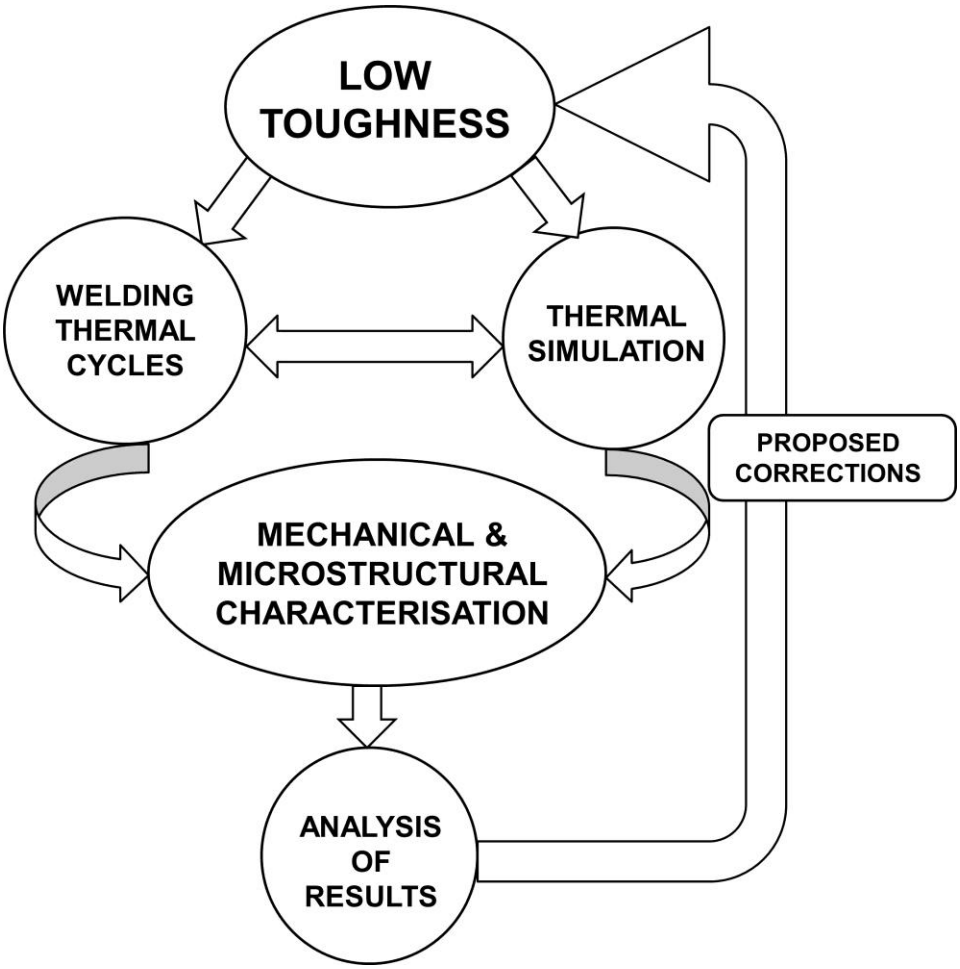

Figure 3-1 Research flow chart

4 MATERIALS AND EQUIPMENTS

The materials used in this work are presented in this chapter. They comprise of pipeline steels and consumables among others. Equipments used for welding processes, weld instrumentation, thermal simulation and characterisation (metallurgical and mechanical) are also presented.

Each of the above mentioned categories is presented as an independent heading below. Only the most important materials and instruments used are presented and discussed.

4.1 **Materials**

4.1.1 Pipeline steels

Three different grades of high-strength pipeline steels were used in this project. They were X65, X70 and X100 grades, the chemical compositions are given in table 4-1.

The X65 (a) is a seamless pipe, while the X65 (b) is a thermo-mechanically controlled processed (TMCP) material, both materials have specified minimum yield strength of 450 MPa.[98; 144]

The X70 and X100 pipes are thermo-mechanically controlled processed (TMCP) materials. They both have specified minimum yield strengths of 485 MPa and 690 MPa respectively.[98; 144] The outside diameters and wall thicknesses of all the steel grades are given in table 4-1.

DNV-OS-F101 recommends that for pipes with carbon content ≤ 0.12%, the carbon equivalent should be calculated using the P_{cm} formula, while for carbon content > 0.12% the *CE* formula should be used.[144]

Table 4-1 Chemical composition of the pipeline steel grades.

Materials	OD/WT. (mm)	Chemical analysis in wt.%														Carbon equivalent	
		C	Mn	Cr	Ni	Cu	V	Al	Mo	Si	S	P	B	Nb	Ti	CE_{IIW}[(a)]	P_{cm}[(b)]
X65 (a)	324/25.4	0.08	1.65	0.11	0.16	0.17	<0.004	0.03	0.08	0.22	<0.003	0.014	<0.0005	0.02	<0.01	0.40	0.18
X65 (b)	1210/31.0	0.07	1.62	0.03	0.22	0.21	<0.01	0.03	0.02	0.11	<0.003	0.012	<0.0005	0.04	<0.01	0.39	0.17
X70	1210/31.0	0.06	1.77	0.08	0.26	0.27	<0.01	0.042	0.02	0.14	<0.005	0.013	<0.0005	0.03	0.01	0.41	0.19[(c)]
X100	1321/22.9	0.06	1.88	0.02	0.39	0.40	<0.01	<0.01	0.25	0.29	<0.003	0.010	<0.0005	0.04	0.01	0.53	0.21

(a) CE_{IIW} = C + (Mn + Si)/6 + (Cr + Mo + V)/5 + (Ni + Cu)/15

(b) P_{cm} = C + Si/30 + Mn/20 + Cu/20 + Ni/60 + Cr/20 + Mo/15 + V/10 + 5B

(c) For nominal wall thickness t > 25 mm the carbon equivalent may be increased by 0.01

(d) OD is outside diameter, and WT is wall thickness.

4.1.2 Filler wires

The filler wires used for the narrow groove tandem MIG welds were all having a nominal diameter of 1.0 mm. They are Union MoNi and OK Autrod 12.22.

For the submerged arc welds, 3.2 mm diameter wires were used, which include; ESAB OK Autrod 12.22 and the Lincoln LNS164. Table 4-2 gives the chemical compositions of all the wires used.

Table 4-2 Chemical composition of the filler wires

Wire Grade	Dia. (mm)	C [%]	Mn [%]	Cr [%]	Ni [%]	Cu [%]	V [%]	Al [%]	Mo [%]	Si [%]	*CEV*
Union MoNi	1	0.1	1.46	-	1.05	0.14	0.01	-	0.39	0.66	0.5
OK Autrod 12.22	1	0.09	1.7	0.15	0.15	0.35	0.03	0.02	0.15	1.0	0.64
OK Autrod 12.22	3.2	0.1	1.0	-	-	0.25	-	-	-	0.2	0.32
LNS164	3.2	0.11	1.7	0.01	0.84	<0.01	<0.01	<0.01	0.49	0.2	0.59

CEV_{IIW} = C + (Mn + Si)/6 + (Cr + Mo + V)/5 + (Ni + Cu)/15

4.1.3 Shielding gas

Shielding gases were used for the narrow groove tandem MIG welds, both during trials and the real welds. The gasses include:

- 80% Ar and 20% $Co_{2.}$
- 92% Ar and 8% CO_2.
- 75% Ar, 20% CO_2, 5% O_2 (Argo shield heavy).

4.1.4 Flux

An OERLIKON OP 121TT and Lincoln 888 welding fluxes were used throughout the experiments. Their chemical analyses as provided by the manufactures are given in table 4-3 and table 4-4.

Table 4-3 Composition of Lincoln 888 flux from the manufacturer

888 Flux	% Comp.
Si	9.81
Mn	1.00
Cr	0.11
Ni	0.07
Mo	0.16
Al	8.63
Ti	0.46
V	0.07
Zr	0.10
Mg	14.54
Fe	1.42
Ca	18.71
K	1.00

Table 4-4 Composition of OP 121TT flux from the manufacturer

FLUX OP 121TT Composition	
Calcium Fluoride	20-30%
Magnesium Oxide	27 – 36%
Aluminium Oxide	17-25%
Quartz (SiO_2)	0.1-1%
Wollastonite ($Ca(SiO_3)$)	7-15%
Potassium Silicate	2-5%
Sodium Silicate	2-5%
GRAIN SIZE	0.1 – 2 mm

4.2 **Welding equipments**

The equipments used for the welding processes will be presented here.

4.2.1 Welding rig

The linear welding rig shown in figure 4-1 was used for both the tandem MIG and submerged arc welds. It has a movable bed where samples are mounted, and can move left or right at a set speed. The welding torches were kept stationary in all cases, while the bed moves the samples along the torch.

A calibration chart has been made by Liratzis[145] to achieve the required travel speed for the tandem MIG welds. The submerged arc welding requires a slower travel speed compared to the MIG process. Therefore, a new calibration chart for slower speed was made for the SAW as shown in figure 4-2. Travel speed in (mm/min) is plotted against the dial numbers of the control panel.

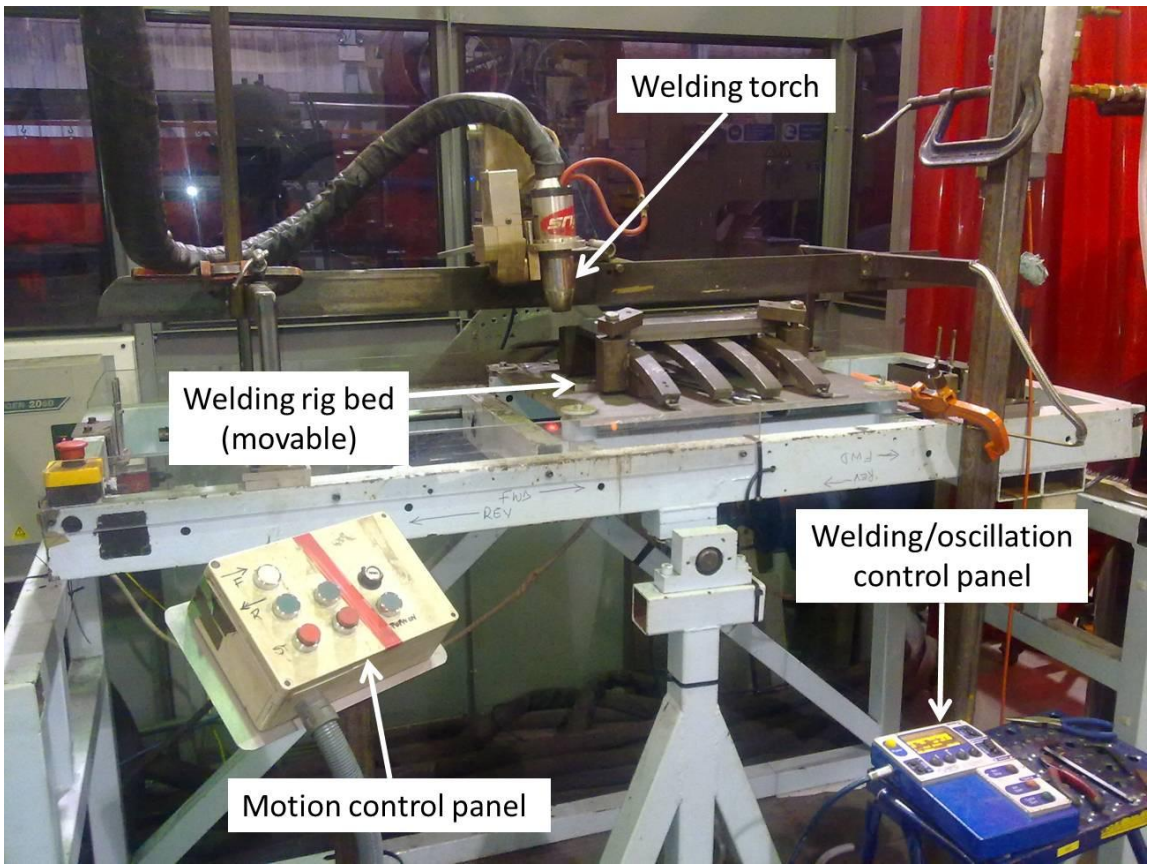

Figure 4-1 Linear welding rig with an RMS welding head oscillator

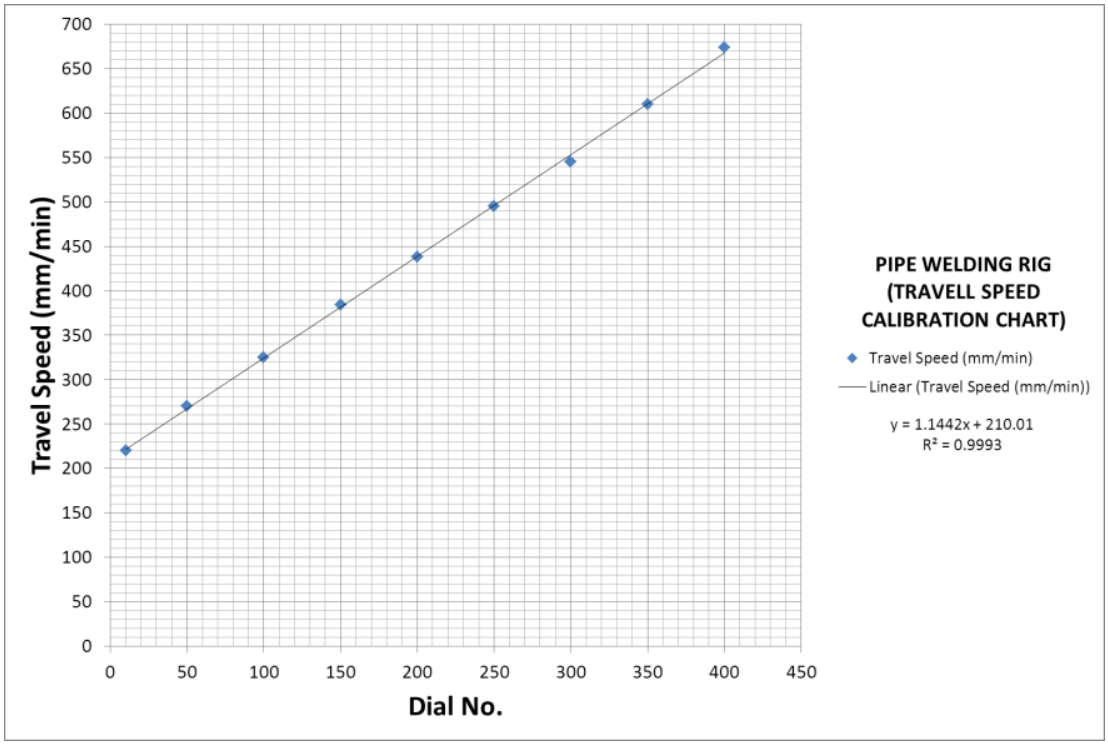

Figure 4-2 Travel speed calibration used for submerged arc welding

4.2.2 Submerged arc welding power source

STARMATIC 1300 DC welding machine, with SUBARC 5 and MECACYCLE S controllers were used for the submerged arc welds as shown in figure 4-3.

The Starmatic 1300 DC has a maximum open circuit voltage of 80 V and 1000 A duty cycle at 100%, and operated in DC mode. It is a very rugged welding machine that can achieve high welding currents without any problem. It can be used for drooping and constant voltage welding processes, particularly designed for automatic submerged arc welding process.

Subarc 5 controller is used to set the welding parameters i.e. current and voltage before welding. It also has the controls for the wire feed and has the arc start and stop buttons situated on it. It is equipped with a microprocessor, therefore, it can capture and display real time current, voltage and wire feed speed during welding.

The Mecacycle S unit allows the manual or automatic controls of motion and movement of the mecasaf 15.10 welding boom, which holds the welding torch.

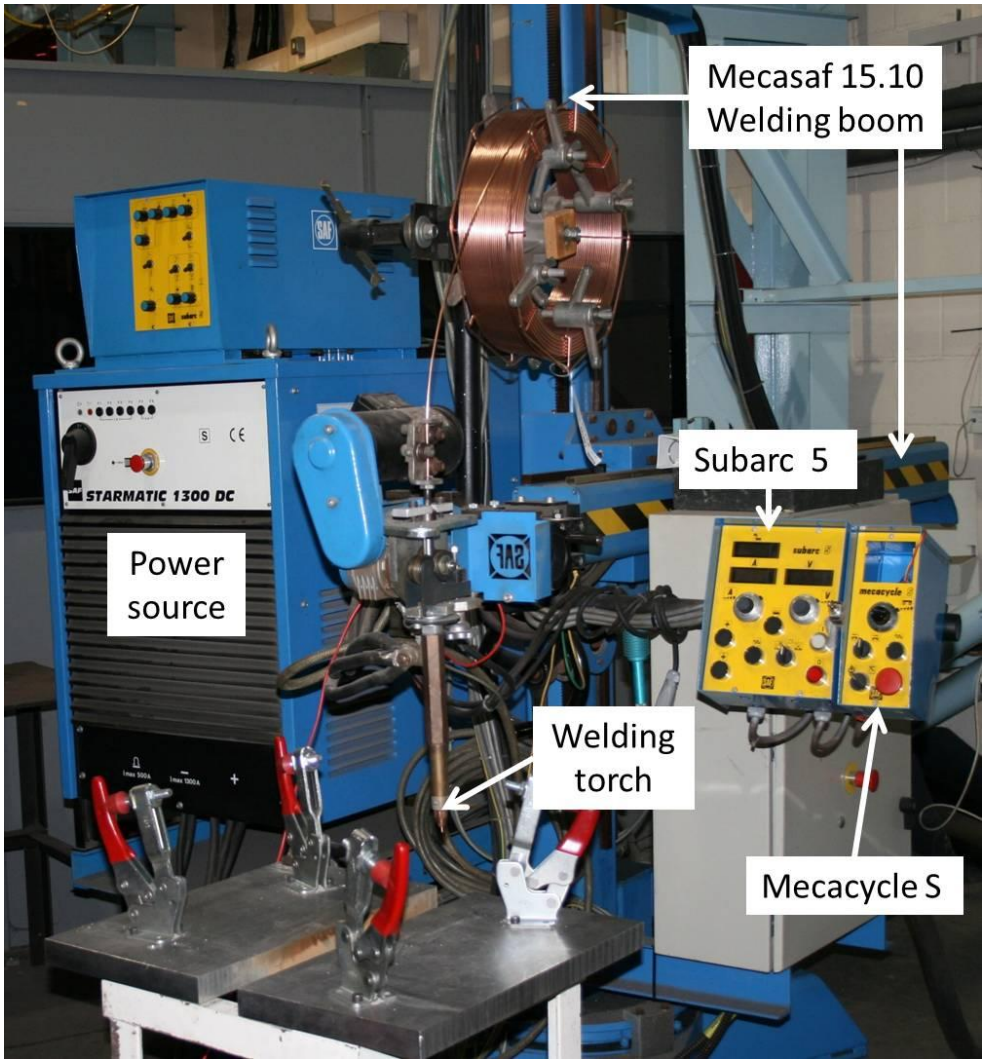

Figure 4-3 STARMATIC 1300 DC submerged arc welding machine with a Subarc 5 and Mecacycle S controllers.

4.2.3 Tandem MIG power source

Two sets of Fronius TPS 4000 power sources (TransPuls Synergic) fully synchronised in a tandem (lead and trail) mode as shown in figure 4-4, were used for the narrow groove tandem MIG welds. They can deliver 300 A at 100% duty cycle. The welding sets are fitted with a control panel at their top front face, where parameters such as voltage, wire feed speed, wire diameter, welding mode (e.g. pulsed transfer mode) can be selected and adjusted. The machines are equipped with microprocessors and fully digitalised. During welding they display the actual current and voltages, while the average values are shown after welding.

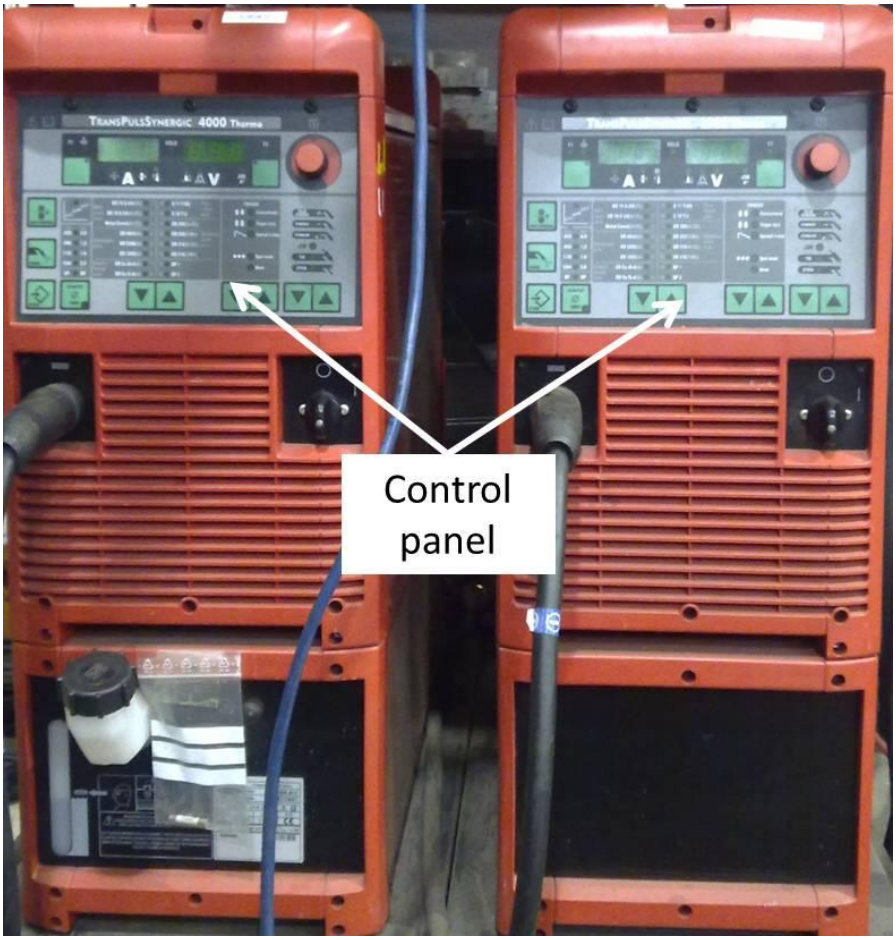

Figure 4-4 Fronius TPS 4000 thermo power welding machines

4.3 **Weld Instrumentation**

The instruments used in capturing the thermal cycles and the welding parameters i.e. current, voltage and wire feed speed for the SAW and Narrow groove tandem MIG welds are presented here.

4.3.1 Thermal cycles acquisition during welding processes

A data acquisition device was developed for the purpose of this research. This was a modification to what Hudson[146] built and used earlier at Cranfield University. Standard office desktop computer and thermocouple data acquisition device (NI PCIE-6351, X Series Multifunction DAQ) with a maximum frequency of 100 MHz were used. They give the flexibility of capturing data at a very high sampling rate. A SHC68-68-EPM Shielded cable was used to minimise the noise. Figure 4-5 is a picture of the equipment. K-type (NiCr/Ni) thermocouples

were used in this research. Because the area of interest was the HAZ, and the K-type thermocouples can accurately capture temperatures up to 1370°C.[146]

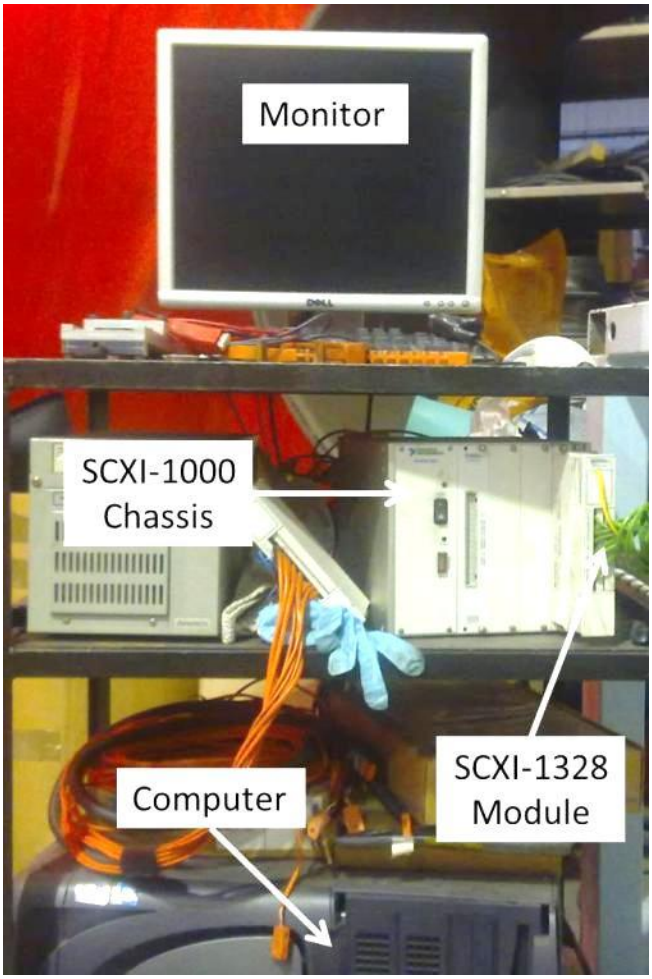

Figure 4-5 Thermocouple data acquisition device

Figure 4-6 Capacitance discharge welder SR-48

4.3.2 Capacitance discharge welder

Capacitance discharge welder SR-48 was used to make a hot junction or a ball end at the thermocouple tips. It was also used to attach the thermocouples to the samples. The equipment is shown in figure 4-6.

4.3.3 Measurement of welding parameters

AMV 4000 series was used for the welding parameters acquisition, it has eight channels as standard, and is capable of acquiring data at 100 kHz per channel, and it is shown in figure 4-7.

The first three channels were used in this research, and they were set to measure current, voltage and wire feed speed respectively. Probes were used for current and wire feed speed measurements, the probes were connected to the earth wire and welding wire to measure current and wire feed speed respectively. Clamps were connected to the negative and positive terminals for the voltage, which are the welding torch and the welding plate.

Figure 4-7 AMV 4000 welding data logger

4.4 **Thermal simulation**

The equipments used in the thermal simulations will be presented here.

4.4.1 Gleeble machine

Gleeble 3500 is a fully integrated digital controlled thermo-mechanical simulator as shown in figure 4-8, it has a direct resistance heating sysytem capable of heating samples up to 10,000°C/s, and can achieve similar cooling rate at the surface of the sample with an optimum quenching system.[147; 148]

It has high thermal conductivity clamps (used as grip to hold specimens) made from copper as shown in figure 4-9. The copper clamps are water cooled and it helps in achieving very high degree of uniformity in cooling rates, which is one of the most important features of the system.

The Gleeble 3500 is operated and controlled by computer interface in a windows based workstation. A purpose built software (QuikSim), controls the heating and cooling simulation profiles of the experiments. A pictorial view of the QuikSim window is shown in figure 4-10. Data captured during the experiments are displayed in Origin software for processing and analysis.

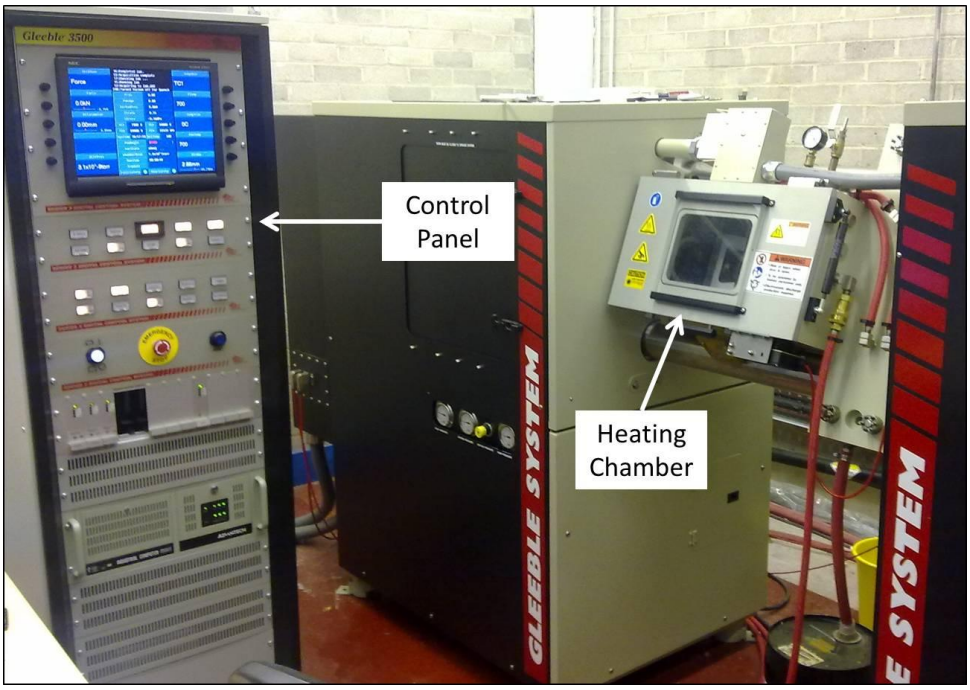

Figure 4-8 Gleeble 3500 thermal mechanical simulator

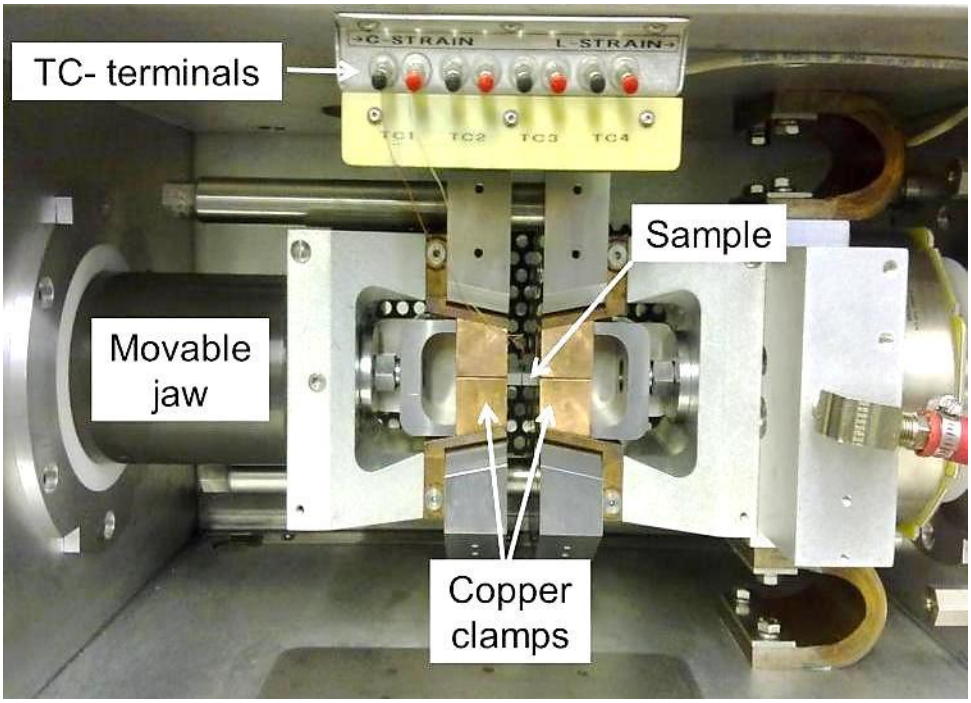

Figure 4-9 the heating chamber of the Gleeble 3500 simulator

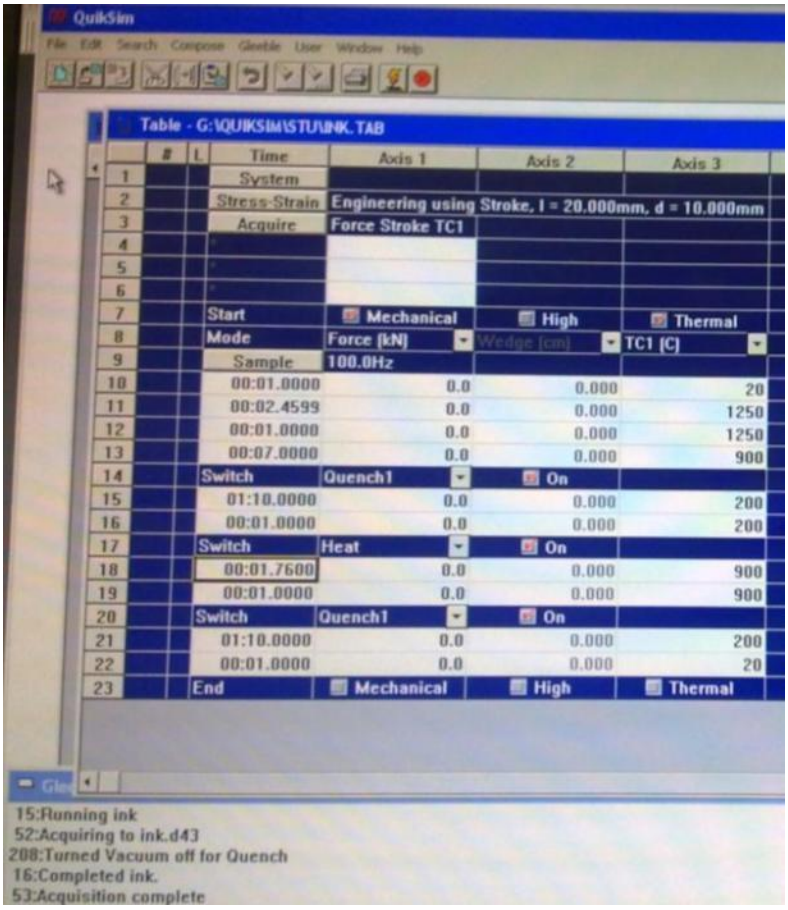

Figure 4-10 QuickSim software window

Figure 4-11 High resolution dilatometer with a range of ± 2.5 mm

4.4.2 Dilatometer

A CCT dilatometer model 39018 which has a Linear Variable Differential Transducer (LVDT) was used for the dilatometric experiments.[149] This model has fine adjustments for quartz measurement tip pressure, which helps to maintain accuracy in high temperature experiments. It has a linear range within ± 2.5 mm and a linearity of ± 0.25% full scale, and can hold specimens of 5 mm to 16 mm diameter. It has a resolution of ± 0.4 µm, which is based on the electronic signal conditioning used. Figure 4-11 is showing a high resolution dilatometer.

4.5 **Characterisation**

The instruments used for the metallurgical and mechanical characterisations will be presented under this heading.

4.5.1 Metallographic examination

The welded and simulated samples were prepared for metallography on the Buehler metaserv 2000 and motopol automatic grinding machines. Using 120, 240, 1200, 2500 grit papers, 6 µ diamond paste and 0.05 micron colloidal silica for final polishing.

Three different etchants were used as follows;

- 2% Nital (2% nitric acid in ethyl alcohol) for micrographs.
- 10%Nital (10% nitric acid in ethyl alcohol) for Macrographs.

- LePèra (1% aqueous sodium metabisulfite and 4% picric acid in ethyl alcohol in a 1:1 ratio) for identifying M-A phases in optical microscopy.

The etched samples were examined using an optical microscope and an XL30 ESEM (environmental scanning electron microscope) for microstructural evaluation and fractography.

4.5.2 Micro hardness measurements

A Zwick Roell micro hardness testing machine was used in measuring the hardness of the samples. It is an automatic hardness testing machine that makes use of a diamond indenter and has two lenses of 10 and 40 magnifications. It is equipped with a table that moves in the x, y and z directions as shown in figure 4-12.

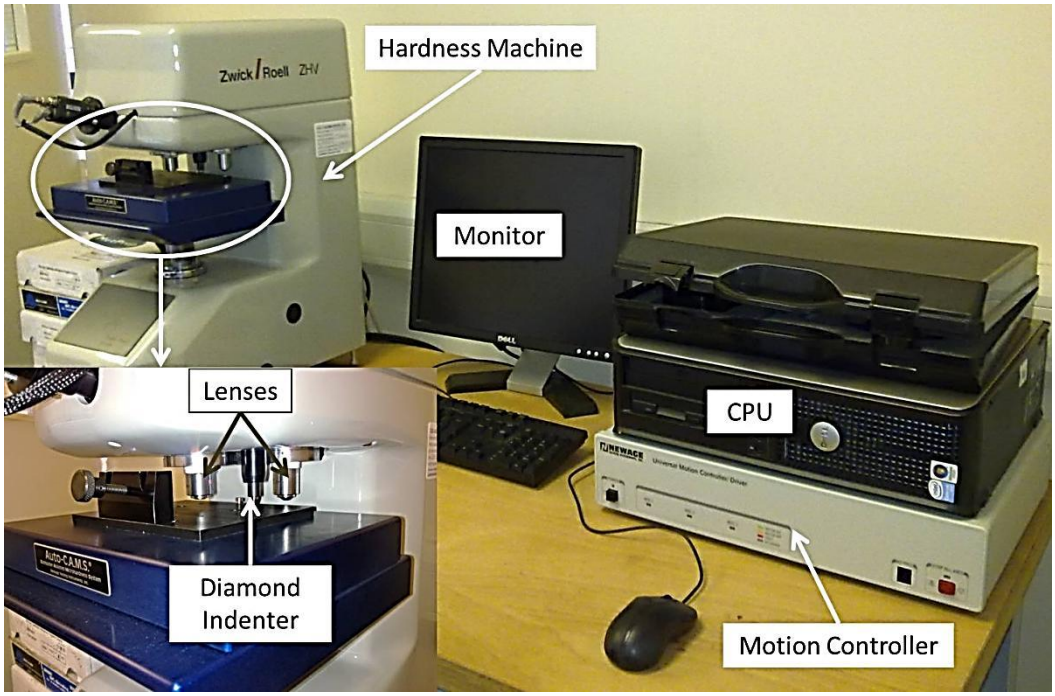

Figure 4-12 Zwick Roell micro hardness testing machine

5 EXPERIMENTAL METHODS

Figure 5-1 is an outline of the materials used for the various experiments carried out in this research. This is to give a general overview of what material was used for what experiment, and to serve as a summary of the research in terms of experiments and material usage.

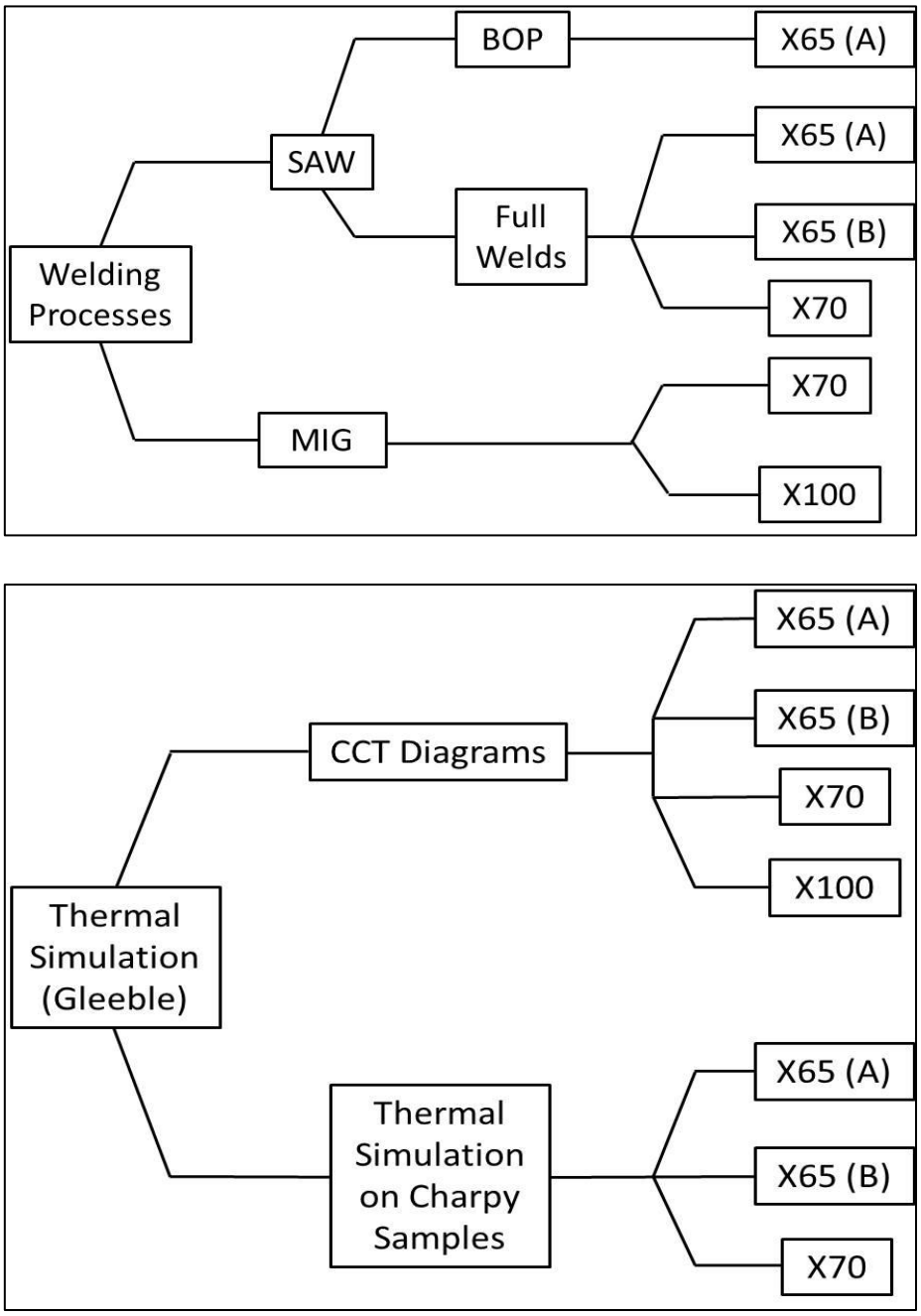

Figure 5-1 Outline of materials used for the various experiments

5.1 **Dilatometric experiments (CCT Diagrams)**

CCT diagrams of all the pipeline steels listed in table 4-1 were constructed by thermal simulation and dilatometric analysis of volume change during heating and cooling.

Samples were machined along the longitudinal axis of the pipes, in to circular bars of 100 mm length by 10 mm diameter.

The samples were divided into three, 30 mm on both sides, and 40 mm was left at the middle for the dilatometric experiments. This region was then marked out into two and the thermocouples were attached at the centre of the samples as described in figure 5-2. The dilatometer was attached to the sample as shown in figure 5-3.

In order to generate the thermal cycles, a simple heating and cooling pattern was used. Samples were heated to 950°C at a heating rate of 400°C/s, held at that temperature for 300 seconds. Samples were then cooled at various cooling rates ranging from 56.3°C/s to 0.3°C/s and corresponding $t_{8/5}$ of 5.34 seconds to 1000 seconds respectively. Figure 5-4 is a graphic representation of the thermal cycles used.

This sequence was repeated for all the different grades of steel. The same ranges of cooling rates were studied for all the different grades. The thermal cycles and the dilatation curves were analysed, the transformation points were determined by the tangential method, and it will be explained in details in chapter 7.

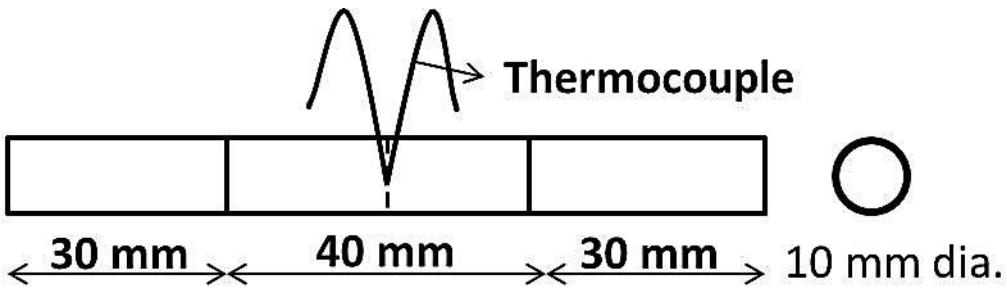

Figure 5-2 Schematic of the dilatometric samples

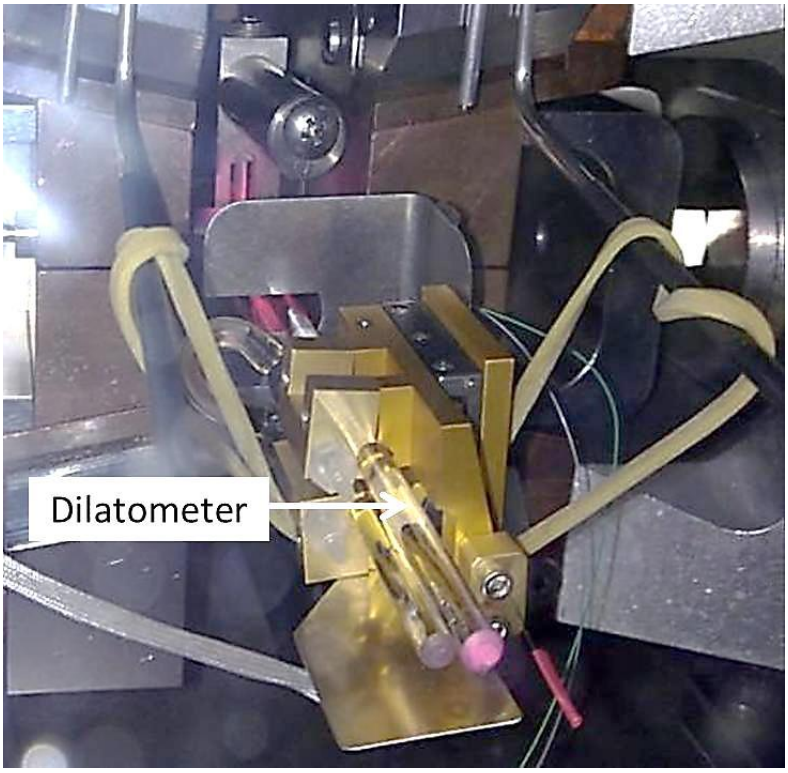

Figure 5-3 Dilatometer attached to the sample

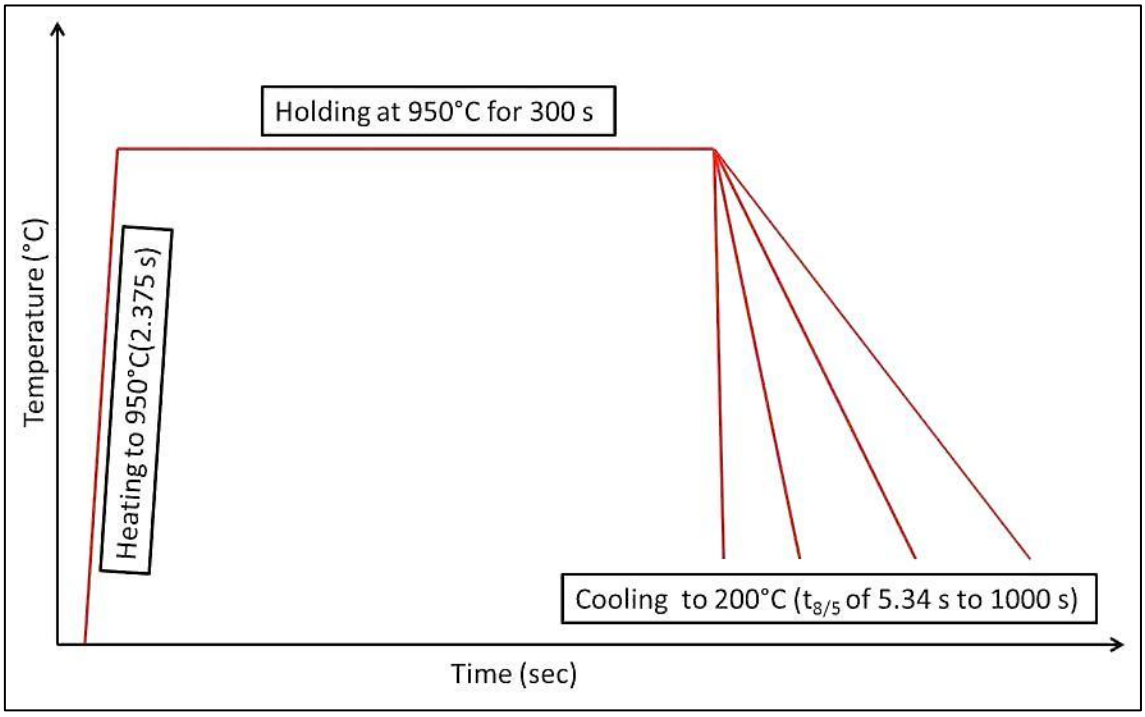

Figure 5-4 Graphic representation of the dilatometric experiments

5.2 **Submerged arc welds**

Submerged arc welding was carried out on X65 (A), X65 (B) and X70 pipeline materials as given in table 4-1. The process was carried out in two different categories, i.e. Bead on Plates (BOP) and full Welds. The following sections explain the different experiments carried out using SAW process.

5.2.1 Bead on plate welds

An experiment was designed consisting of four welds, from weld 1 to weld 4, having one, two, three and four passes respectively as given in table 5-1.

Seamless X65 (A) pipe was cut longitudinally on a band saw. The pieces (samples) were ground off using a hand held grinder to remove all the oxides from the surface. The bead on plate (BOP) welds were made with the sole aim of capturing the thermal cycles of the HAZ during a multi pass weld, and to understand the effect of the subsequent passes on the previous ones. It also helps in identifying suitable parameters that were used during the full welds.

Thermocouples were attached to see the viability of using them to capture the thermal cycles of the heat affected zones.

As given in table 5-2, OK Autrod 12.22 wire and an OP 121TT flux were used for the BOP welds. These consumables are designed for multi-pass welds, tailored towards good toughness for high strength applications.[150] The flux is a basic agglomerated flux, with excellent characteristics of up to a 1000 Amps, and has low hydrogen content of less than 5 ml H_2/100 g.

OP 121TT reacts neutrally to silicon and manganese, therefore, can be used with different wire compositions, while still maintaining high weld metal charpy impact and CTOD toughness. The slag freezes quit fast after welding. Damp flux needs to be re-dried to about 300-350°C for at least an hour to remove the moisture.[150]

Table 5-1 BOP weld names and number of passes on each weld

Weld Name	Number of Passes
Weld 1	1 pass
Weld 2	2 passes
Weld 3	3 passes
Weld 4	4 passes

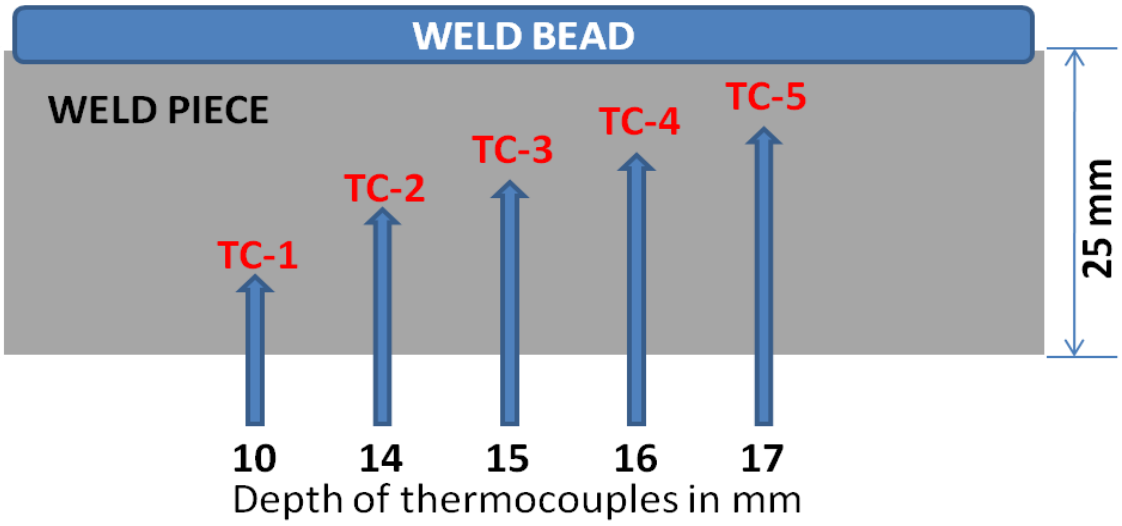

Figure 5-5 Submerged arc welds bead on plate thermocouples positioning

Holes were drilled at the bottom surface of the samples and thermocouples were attached at different depths from the bottom of the samples with respect to the HAZ as shown in figure 5-5, so as to capture the thermal cycles at different part of the HAZ. Five thermocouples were inserted through the drilled holes, constant welding parameters were maintained throughout the experiment, and they are given in table 5-2.

Centre line of the thermocouple holes was first inscribed on the bottom of the samples. Reference holes were drilled on both ends of the weld piece, penetrating all through. These two holes were joined together to form the centre line of the weld bead. Therefore, the same centre line was maintained for the weld beads and the thermocouples.

The samples were then placed on the welding rig in a manner so that the thermocouple wires can move freely underneath. Using the parameters in table 5-2, the welding torch was aligned with the centre line. Clamps were used to hold the sample firmly in position, maintaining the centre line. Flux holder was put in place, and flux taken from the oven was spread within the flux holder. An amount just enough to cover the arc was used, as shown in figure 5-11.

Thermocouple lids from the weld piece were connected to the logger and each thermocouple was checked to ensure they are ready to collect data.

The arc was then started, followed by the travel. The data acquisition was also started. In this experiment, it was the torch that was mounted on the welding boom which does the travel along the plate.

Table 5-2 Submerged arc welds bead on plate welding parameters

SAW BOP WELDING PARAMETERS	
Welding wire	ESAB OK Autrod 12.22 (3.2 mm diameter)
Welding flux	OERLIKON OP 121TT
Current	500 Amps
Voltage	33 Volts
CTWD	22 mm
Travel speed	520 mm/min
Wire feed speed	1.43 m/min
DAQ-Sampling rate	100Hz
AMV Settings	1KHz, 1024 samples

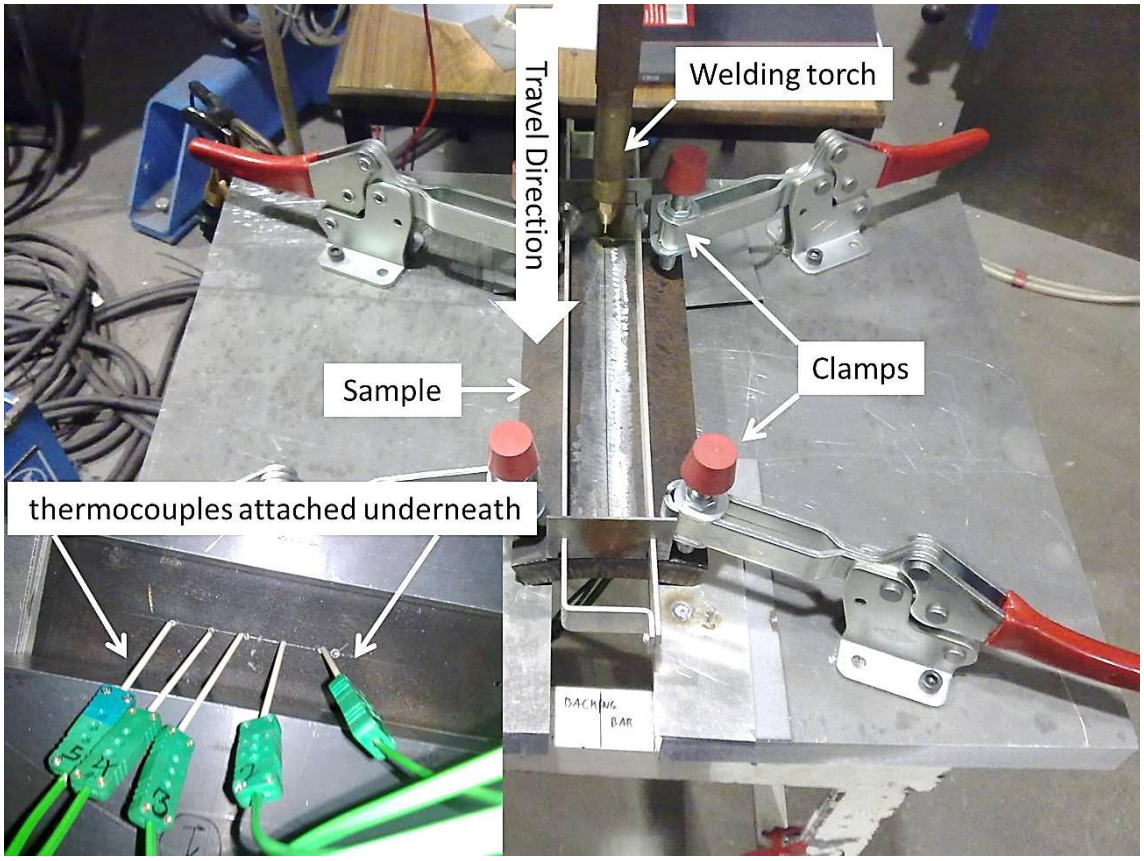

Figure 5-6 Bead on plate welds set-up

5.2.2 Full submerged arc welds

Narrow groove bevel design was used for the full welds as shown in figure 5-7. Two different types of X65 and X70 grades were used for this experiment as shown in figure 5-1. The properties and the compositions of the pipeline materials have been given in chapter 4.

Samples were cut in the longitudinal direction of the pipes, suitable samples (350 mm × 90 mm) were removed and machined (bevelling) to the required bevel design. Two pieces from the machined samples were tacked together with the help of a specially cut piece from the same material grade, to form a full sample of 350 mm × 180 mm. Run-out plates from a 12 mm thick plain carbon steel (S355) were also tacked to both ends of the sample using MIG welding, as shown in figure 5-8.

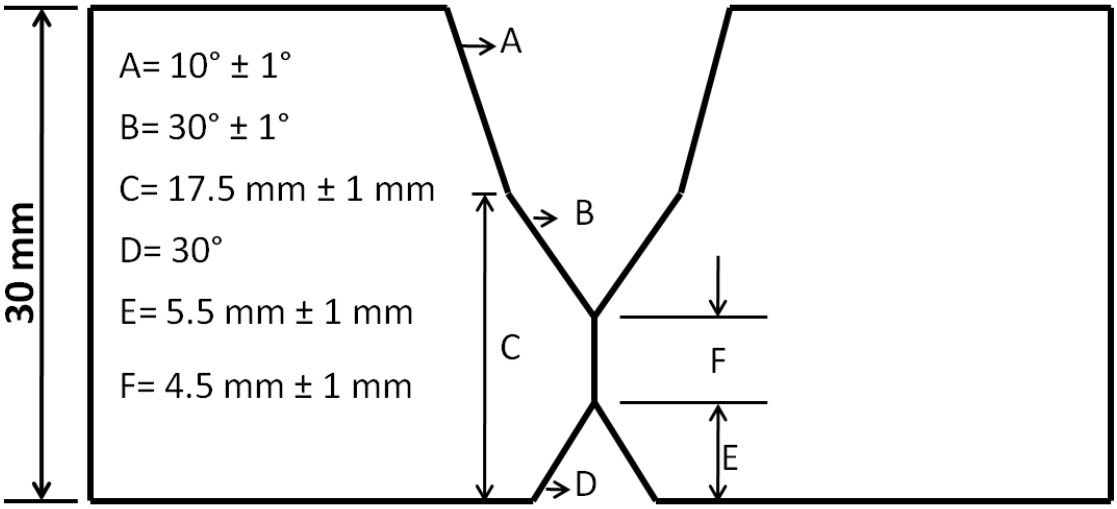

Figure 5-7 Submerged arc welds narrow bevel design

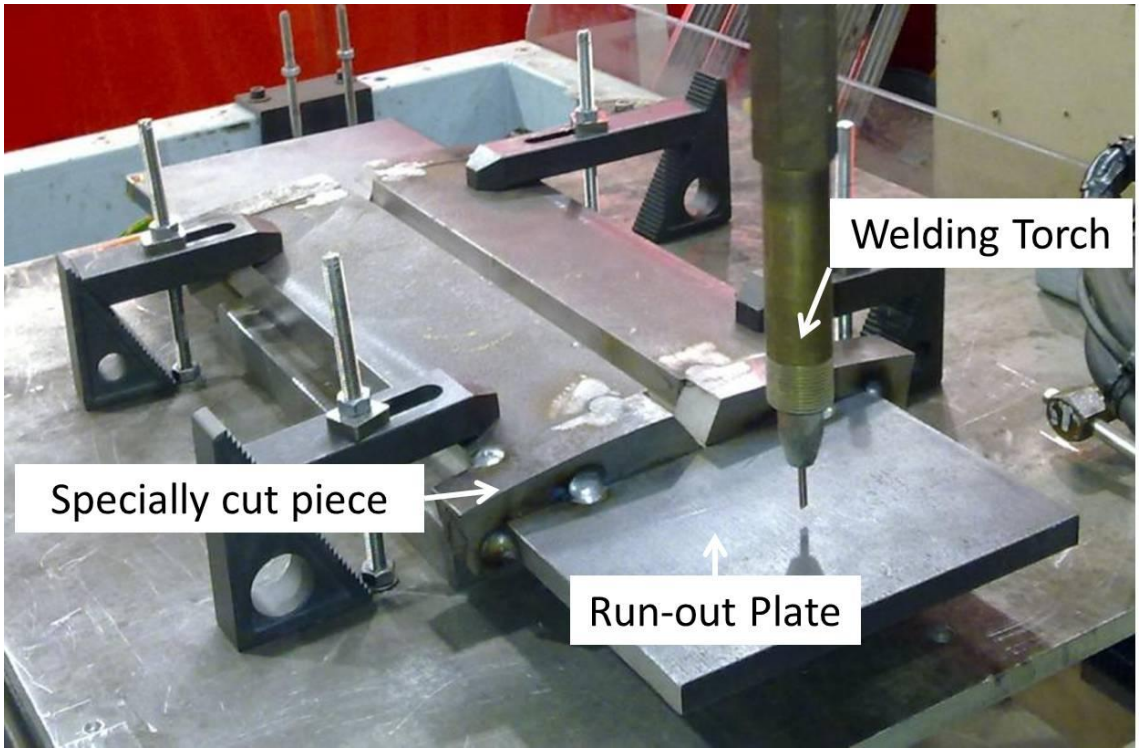

Figure 5-8 Submerged arc welds set-up

After been tacked together, the thermocouples holes were drilled on a milling machine. The thermocouples were attached using a capacitance discharge welder through the drilled holes.

Six thermocouples were used on each of the welds, two at a depth of 10 mm from the bottom and four at 15 mm from the bottom. The thermocouples were positioned at various distances to cover the areas of interest as indicated in figure 5-9.

K-type thermocouples were used to capture the thermal cycles of the heat affected zones. Ceramic sheaths of about 3 mm in diameter were used, it has two holes where the thermocouples wires pass through. The ceramic protect the thermocouple wires from the welding heat and from touching the sample to avoid capturing of unwanted data. Capacitance discharge welder was used to join the tips of the two wires to form a ball end. The wires were then welded to the bottom of the holes firmly to avoid any unwanted temperature recording (fluctuations).

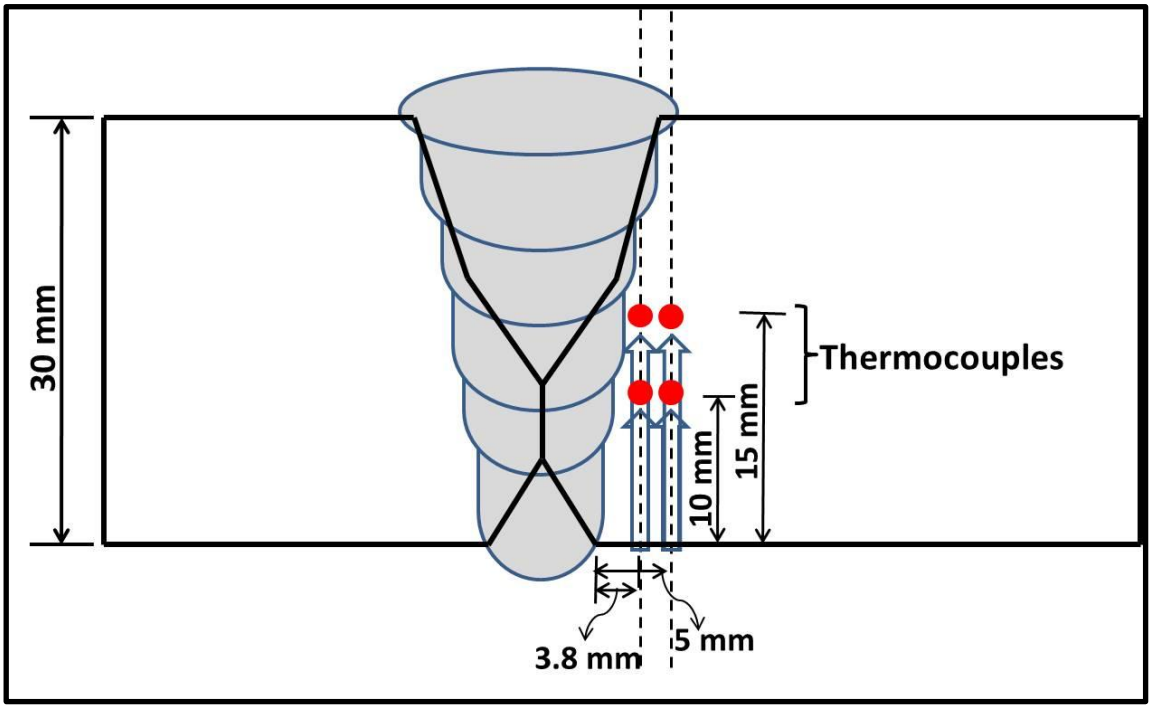

Figure 5-9 Submerged arc full welds thermocouples positioning

In some cases, thermocouples with a fibre glass protective covering were used, which eliminates the need for a ceramic sheath, as the fibre glass can protect the thermocouple wires at high temperatures without any damage or fluctuations in data acquisition. In the case of the ceramic sheath, fibre glass tape was used to protect the covering of the thermocouple wires from heat to avoid melting, as shown in figure 5-10.

Prepared samples were then mounted on the welding rig and clamped. The jig was designed to allow the thermocouples to pass underneath unhindered. The thermocouples were then connected to the data logger, and the sampling rate was set. For this research, the sampling rate was 100 Hz (samples/second) throughout.

The current and voltage were pre-set on the welding machine, a constant CTWD of 22 mm was kept, while the AMV was connected to record the data, which was used to calculate the actual heat input. The welding parameters are given in Appendix A.1.

A purposely made flux holder was used to hold the flux before and during the welding process. The flux was reheated to and maintained at 80°-100°C to drive away moisture. It was constantly left in the oven. Small amount was taken and spread within the flux holder just before welding as shown in figure 5-11.

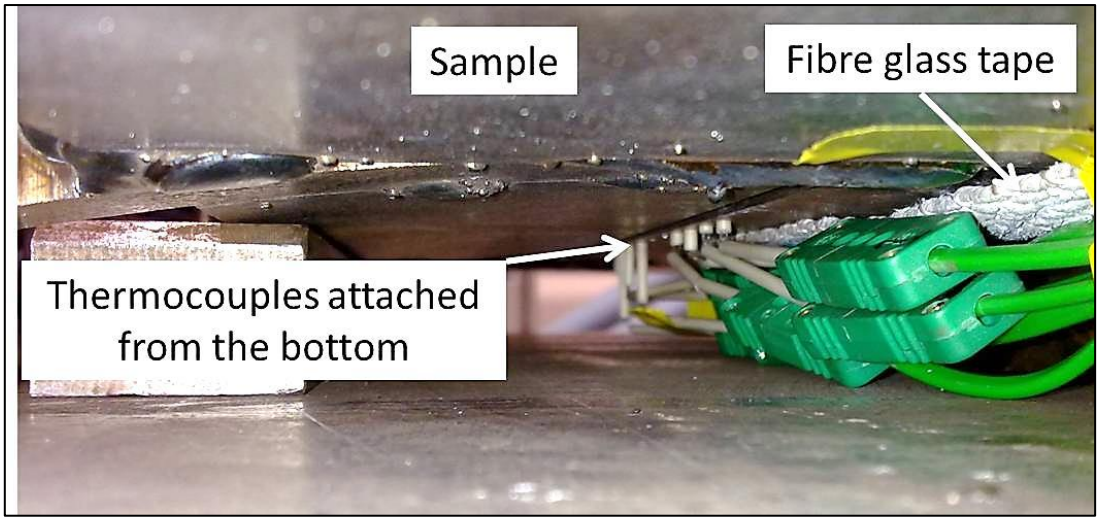

Figure 5-10 Thermocouples arrangements before submerged arc welding

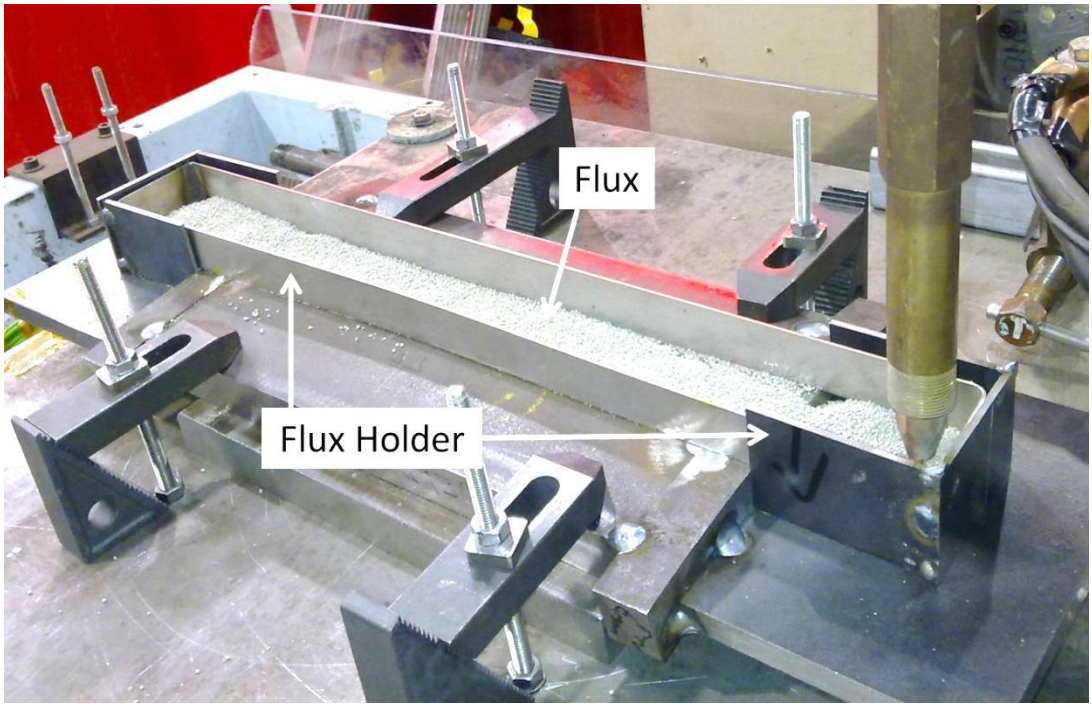

Figure 5-11 Flux holder

During the trial welding, there was problem with slag removal in all the passes, especially the root pass. This was later found out to be due to high voltage and too much flux in the holder. After a very useful discussion about submerged arc welding with the manufacturers of the wire and flux (Lincoln Electric) representative Alan Bewick[151], the following advices were given;

- Little amount of flux should be used, the flux pile should be just enough to cover the arc.
- Lower voltage should be used for the root pass, 26 V – 28 V is enough.

5.3 **Tandem MIG welds**

X70 and X100 pipeline steels were used for the tandem MIG welds as shown in figure 5-1. Suitable samples (350 mm × 300 mm) to match the welding rig were cut longitudinally. The 5° bevel was cut on the band saw with the help of a custom made jig. Backing bar cut from the same materials were then welded to the weld pieces, with a 4 mm gap left at the bottom as shown in figure 5-12.

A specially designed jig was used on a milling machine to drill a 3.5 mm diameter hole for attaching thermocouples. The jig was constructed to pre-determine the drilling angle as calculated from the AutoCAD design shown in figure 5-13.

Thermocouples were attached using the capacitance discharge welder, they were firmly secured to the base of the holes as indicated in figure 5-14.

Prepared samples were then mounted on to the welding rig and clamped to the jig. Welding parameters used are as given in Appendix A.2.

Welding was started after making sure that all the welding parameters and oscillation were ok. After each pass the parameters and oscillation were checked, while the thermocouple logger records the thermal cycles.

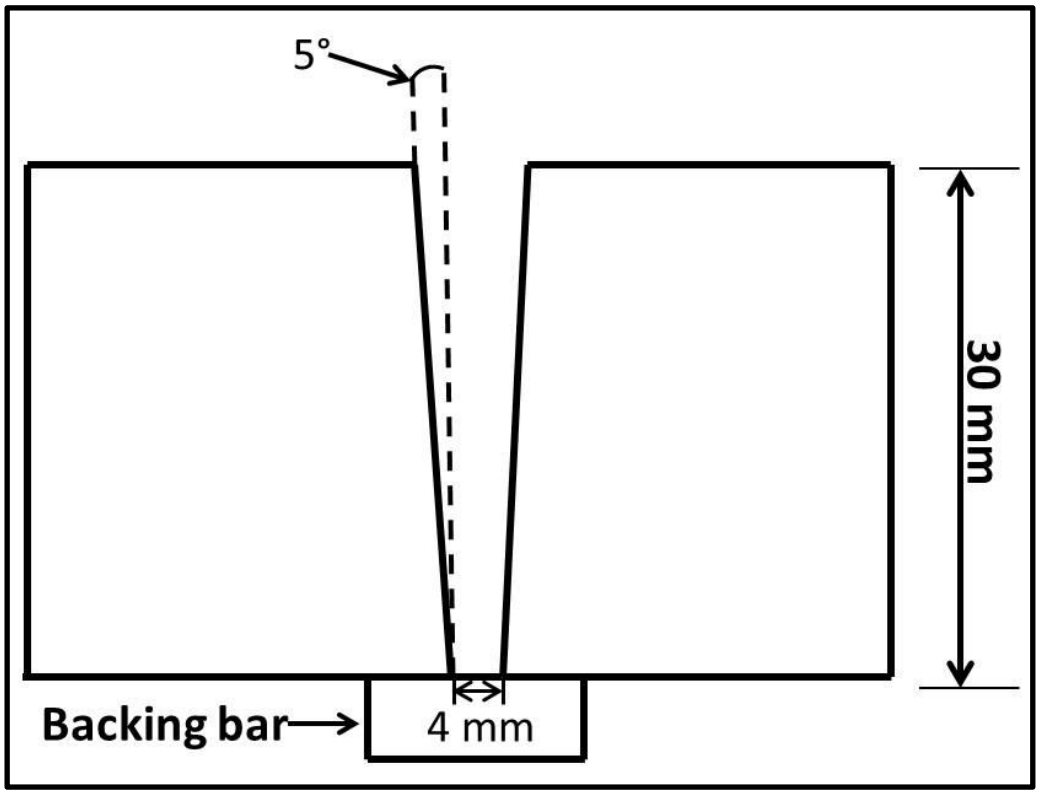

Figure 5-12 Narrow groove (tandem MIG) bevel design

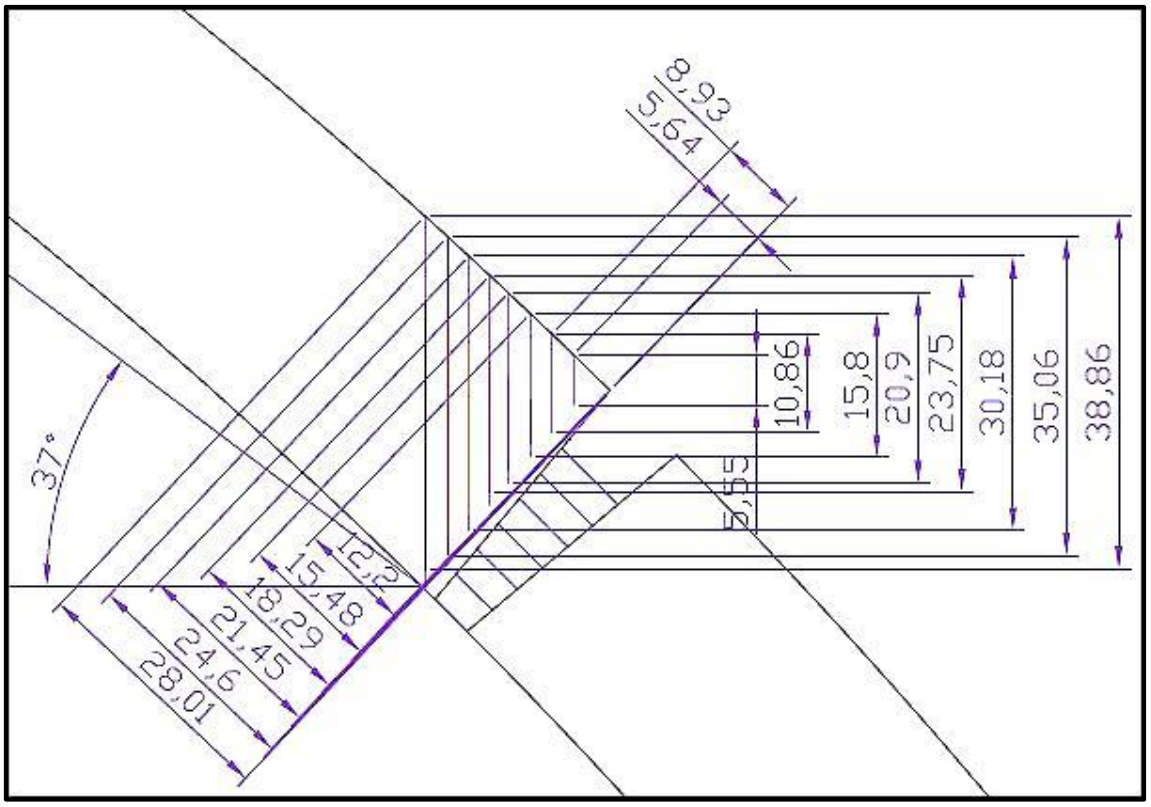

Figure 5-13 AutoCAD drawing of the tandem MIG welds thermocouple placement

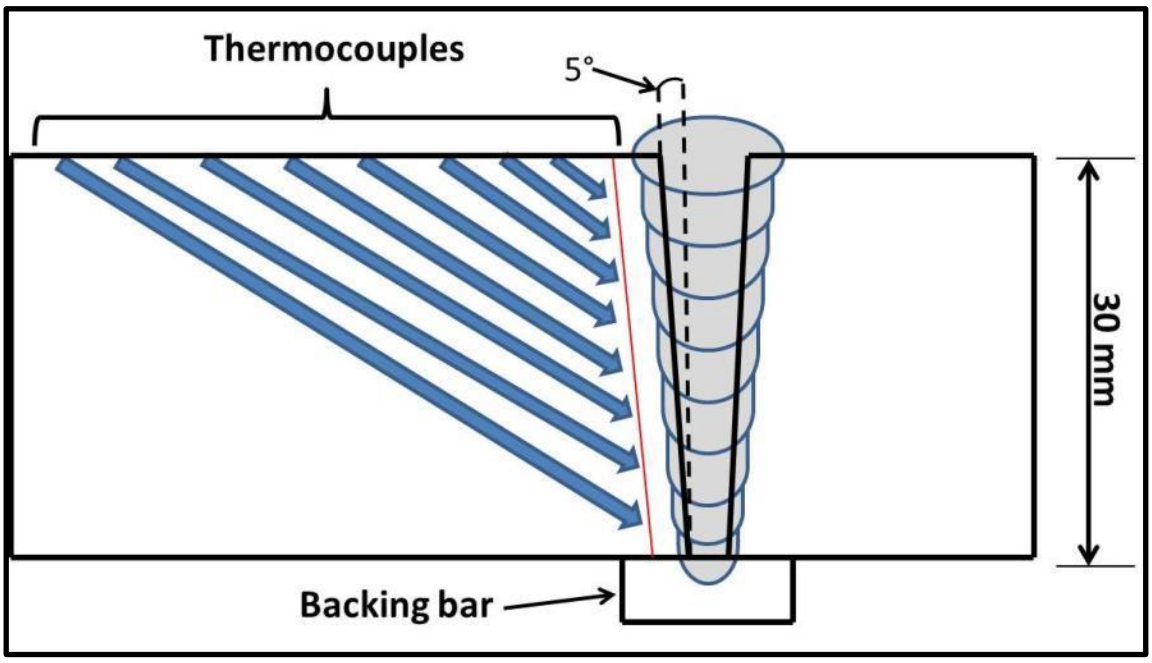

Figure 5-14 Tandem MIG welds thermocouple arrangement

5.4 **Thermal simulation (Gleeble) experiments**

Gleeble experiments were performed using 10 × 10 × 55 mm charpy impact samples, on X65 (A), X65 (B) and X70 pipeline steels with compositions as given in table 4-1. Using standard charpy impact samples helps to eliminate the need of a conversion factor that has to be used when sub-size charpy impact samples were used. [174]

Plates were cut from these three materials for machining. Standard charpy samples were machined longitudinally from the plates and sent back to us in an un-notched condition for the heat treatments. The samples were notched and charpy impact tested after the heat treatments. Figure 5-15 is a schematic representation of the samples orientation with respect to the plates.

The edges of the samples were used for clamping and the middle for the heat treatment, as shown in figure 5-16. K-type thermocouples were used and they were attached in the middle of the samples as indicated by the dashed lines. The thermocouples were welded with the aid of a special thermocouple welder made for the gleeble machine as shown in figure 5-17.

Samples with attached thermocouples were then placed in the heating chamber of the gleeble machine. Using the copper clamps, samples were securely fixed between a movable and a fixed arm.

A quenching device was screwed on to the fixed arm. The quench device was adjusted to purge the quench medium at the centre of the samples i.e. where the thermocouple were placed.

Two C-clamps were used to hold the copper clamps in place, which secures the samples firmly. Then the thermocouples were connected to the lids located on top of the chamber.

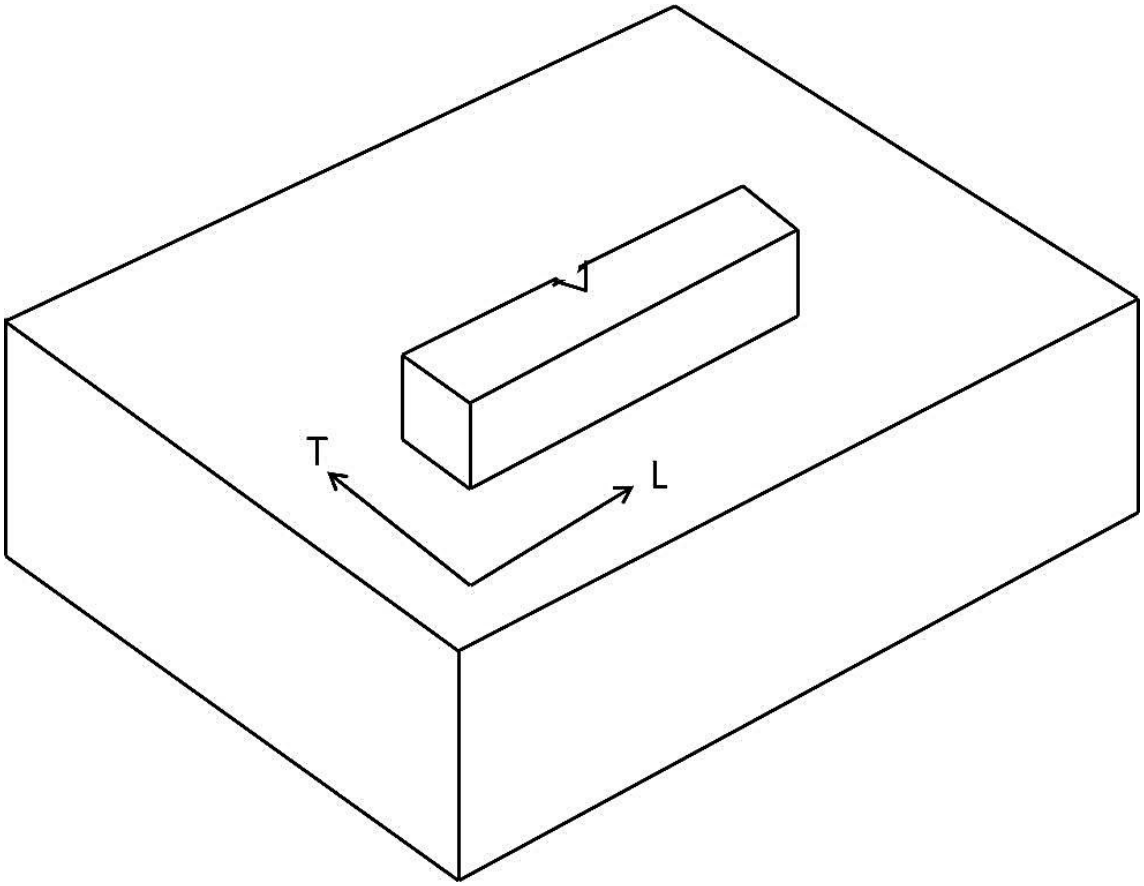

Figure 5-15 Schematic of the relative orientation of the samples with respect to the plates

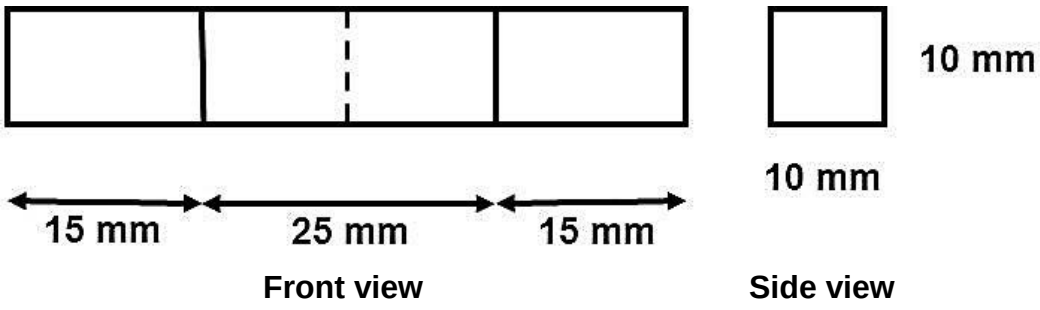

Figure 5-16 Schematic of the gleeble samples

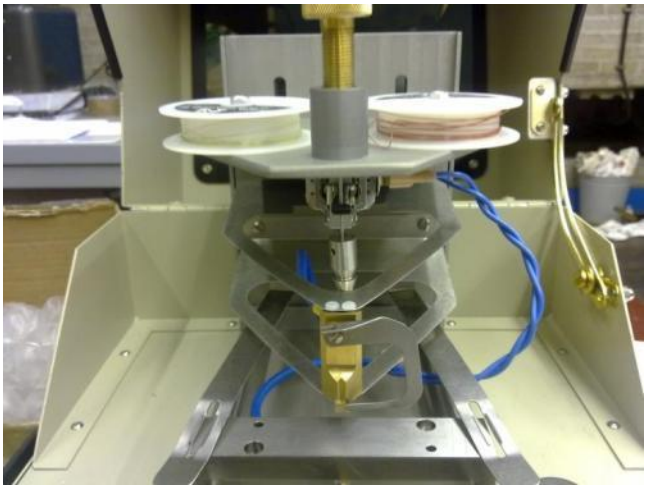

Figure 5-17 Gleeble thermocouple welder

5.4.1 Gleeble machine operation

The Gleeble machine was set and a new file was created. This allows writing of the programme to be executed, (i.e. the rate of heating and cooling). A graphic representation of the thermal cycles used for the single, double and triple thermal cycles on all the materials is shown in figure 5-18.

The machine has capabilities of using air and water quench, which comes from a small pressurized tank connected to the quenching device via a hose. For this experiments air quench was used and in some cases no quench was used.

A trial experiment was first set up using X70 grade to understand how the Gleeble machine works. The final sets of heat treatments were designed for all the three materials, i.e. X65 (A), X65 (B) and X70 grades as shown in figure 5-1. Heat treated samples were notched and tested on the charpy impact machine at various test temperatures (-40°C, -60°C and -80°C).

The heat treatments used and the corresponding charpy impact values are given in Appendix B.

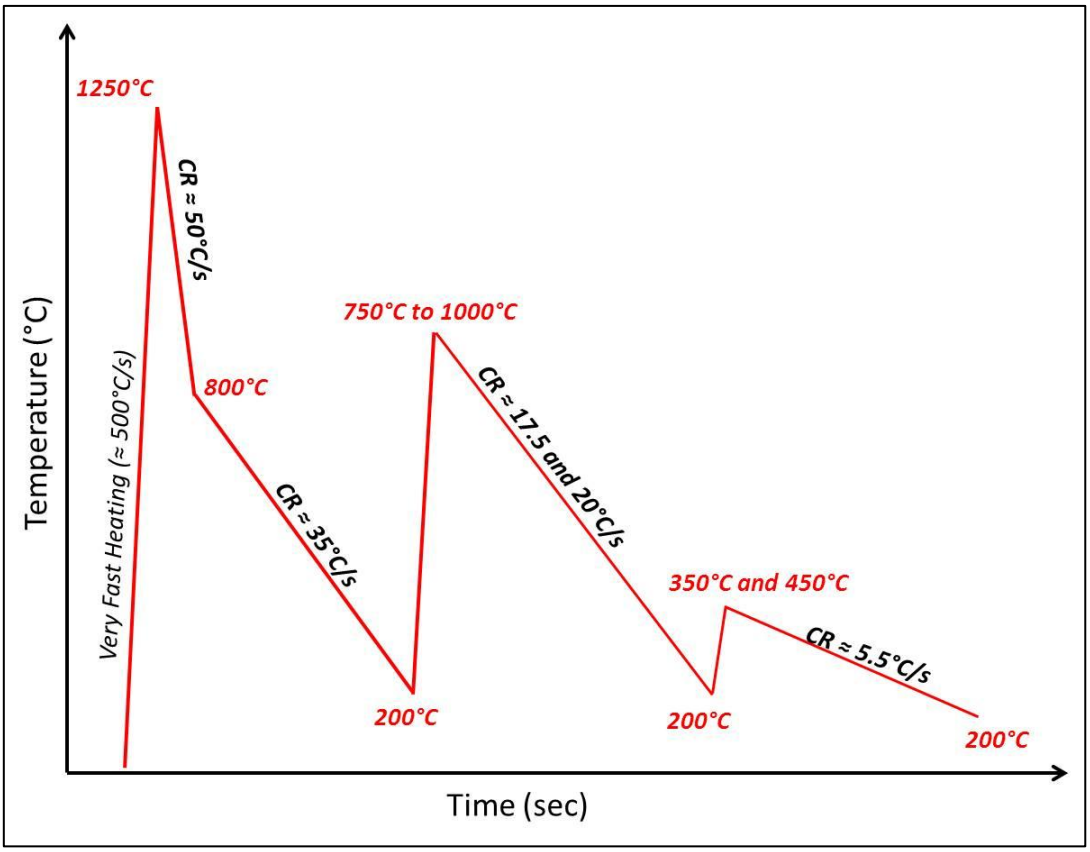

Figure 5-18 Graphic representation of the gleeble experiments

5.5 **Metallographic examination**

Welded samples were cut across the welds using the cut off saw. Handable samples were removed and ground manually on the Metaserv 2000 grinding machine.

10% nital was used to etch the samples for macrographs, while 2% nital was used for the micrographs, SEM and micro hardness samples. LePèra etchant was used to characterise the M-A phase in some of the welds and the thermally (Gleeble) simulated samples.

The broken charpy impact samples from the gleeble experiments were sectioned in to two, across the broken face (i.e. perpendicular to the notch) as shown figure 5-19.

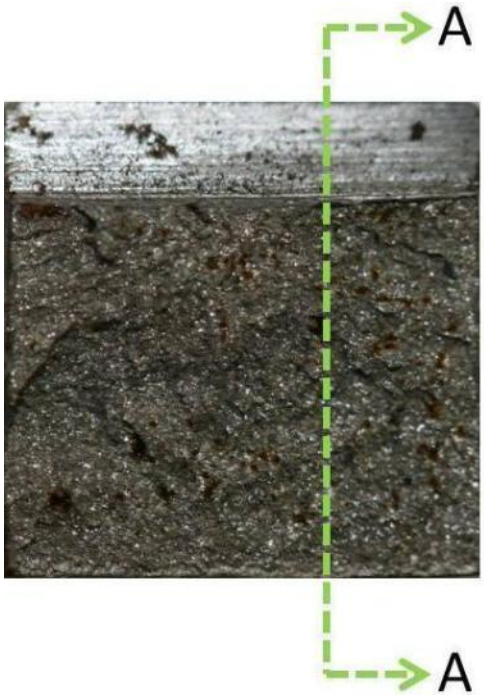

Figure 5-19 Broken charpy sample showing where the metallographic samples were taken across section A – A

Section A – A was taken so as to avoid the uneven surface from the outer face. Samples from A – A were mounted in bakelite, in to 30 mm diameter moulds, using the automatic mounting machine.

While for the dilatometric experiments, metallographic samples were cut from the middle of the samples (at the thermocouples position). Small pieces were then cut off and mounted on the middle face in bakelite.

Mounted samples were then arranged on to the grinding wheel of the Motopol automatic grinder for grinding and polishing. Coarse diamond wheel was first used for lapping, so as to get even and flat surface on all the samples.

Grit papers from 1200 and 2500 grades were used for the grinding. Then a 6µ diamond paste on a silk cloth was used for the final grinding. Colloidal silica gel of a 0.05µ grade was used for the polishing.

Finally samples were washed under running water and soap to remove any stain from the silica. They were then washed with isopropanol and dried up before etching. All the samples were etched using 2% Nital.

5.6 **Hardness measurements**

Micro hardness tests were carried out using the Zwick Roell hardness tester. The micrographic samples were used for the hardness testing.

The submerged arc welds and tandem MIG welds hardness traverses were carried out according to figure 5-20. While for the X65 (A) and X100 which are 25 mm and 22.9 mm thick respectively, the same pattern was used but instead of 5 mm gap at the edges, 2 mm was used.

During CTOD test, a fatigue crack is propagated along the test samples up to mid-thickness, where the notch is placed. Therefore, a hardness map was designed to cover the notch and its surroundings, as shown in figure 5-21.

Figure 5-22 is a schematic of the gleeble samples hardness traverse used for all the samples. While for the dilatometric samples (10 mm diameter in size), eight indents were placed along the centre line of the samples. 1 mm gaps were left in-between the indents.

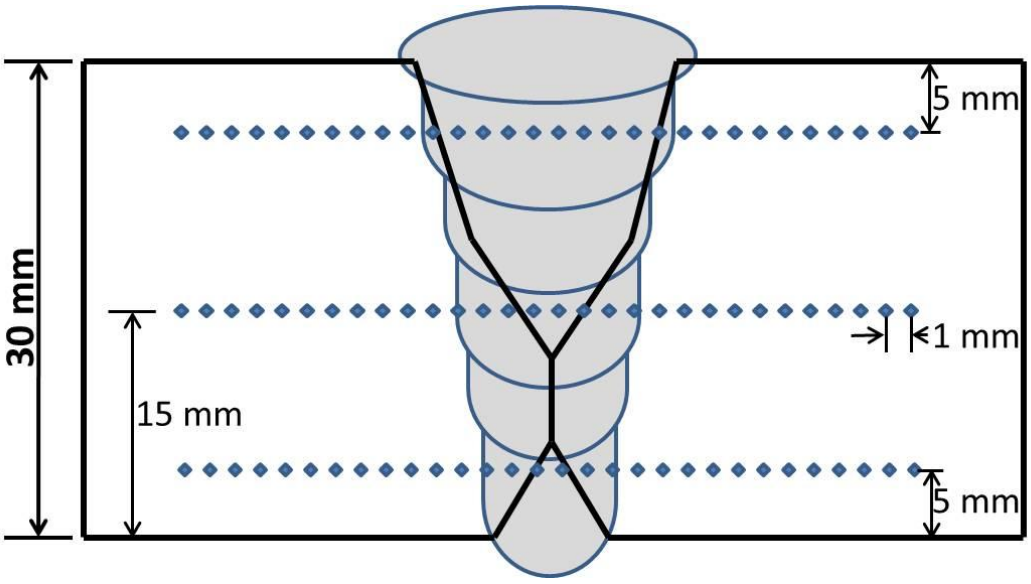

Figure 5-20 Schematic of full welds hardness traverse

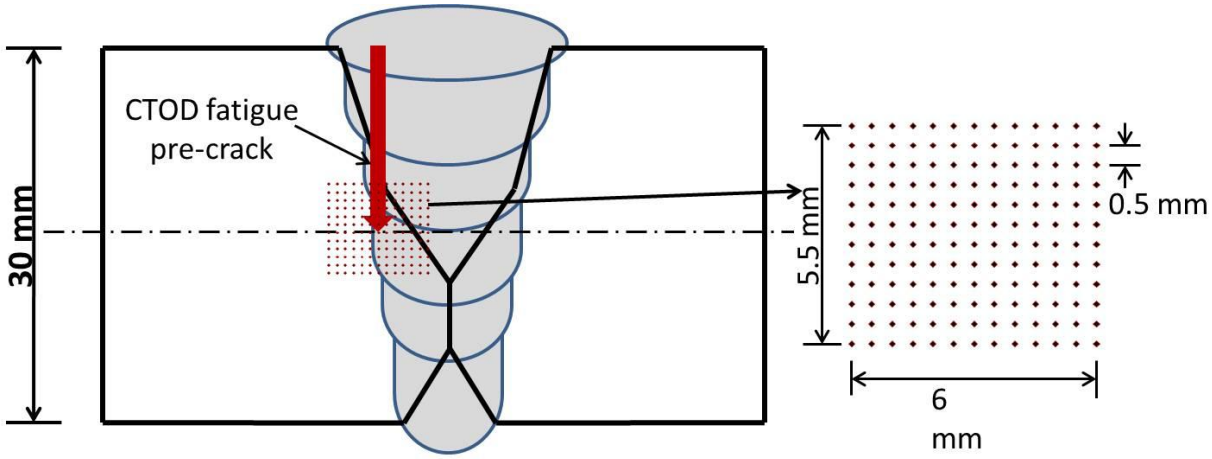

Figure 5-21 Schematic of the full weld hardness map

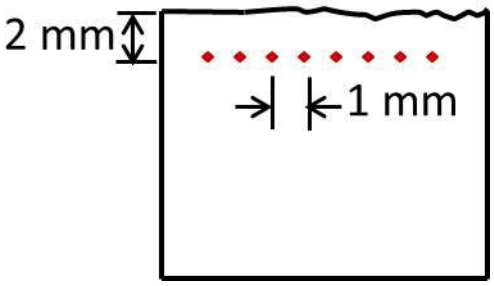

Figure 5-22 Gleeble sample hardness traverse

For the gleeble samples, hardness traverse of the outer surface was taken to compare the hardness values at mid thickness and outer surface of the heat treated samples. This comparison was made to validate the consistency in heating and cooling properties of the Gleeble 3500. In all the hardness traverses for gleeble and dilatometric samples, the average values were taken as the hardness values of the samples.

5.7 **Tensile test**

Parent metal tensile tests were conducted on all the four pipeline steels used in this research, i.e. X65 (A), X65 (B), X70 and X100.

Samples were cut in the longitudinal direction of the pipes, and tested in accordance with ASTM E8/E8M:2011[152].

5.8 **Charpy impact test**

All the samples used in the gleeble experiments were charpy impact tested afterwards.

Heat treated charpy impact samples were first notched with a 2 mm V notch. Notched through thickness test was carried out in accordance to ASTM E23-07[153], charpy machine with a nominal energy of striker 300J ± 10J was used.

The samples were tested at -40°C, -60°C and -80°C. With the exception of a few samples that were tested at 0°C and -20°C.

5.9 **Crack tip opening displacement test (CTOD)**

Two welds each from the submerged arc full welds on X65 (A), X65 (B) and X70 were sent out for the CTOD test. While for the tandem narrow groove welds, only the X70 was tested.

CTOD testing was conducted at -10°C, in accordance with BS 7448 Pt1:1991-02[154]. In all the samples the notch was located on the HAZ of the welds. This is to check for the presence of any localized brittle zone within the HAZ.

6 EXPERIMENTAL RESULTS

Results from the experiments conducted in this research are presented in this chapter. There will be no discussion, it will follow in the next chapter.

This chapter has been divided in to five major parts, under which the results are presented in a comparative manner where ever possible.

Heading 6.1 will comprises the parent materials properties, heading 6.2 entails the dilatometric experiments i.e. CCT diagrams. Results from the submerged arc welding are presented in heading 6.3, while the tandem MIG welding results are given in heading 6.4. Thermal simulations (Gleeble) experimental results are presented under heading 6.5, more details are given under each heading.

6.1 **Parent materials**

The parent materials mechanical and microstructural analyses are presented here, they include the hardness, charpy impact toughness, and tensile tests, optical and scanning electron micrographs.

6.1.1 Parent materials mechanical properties

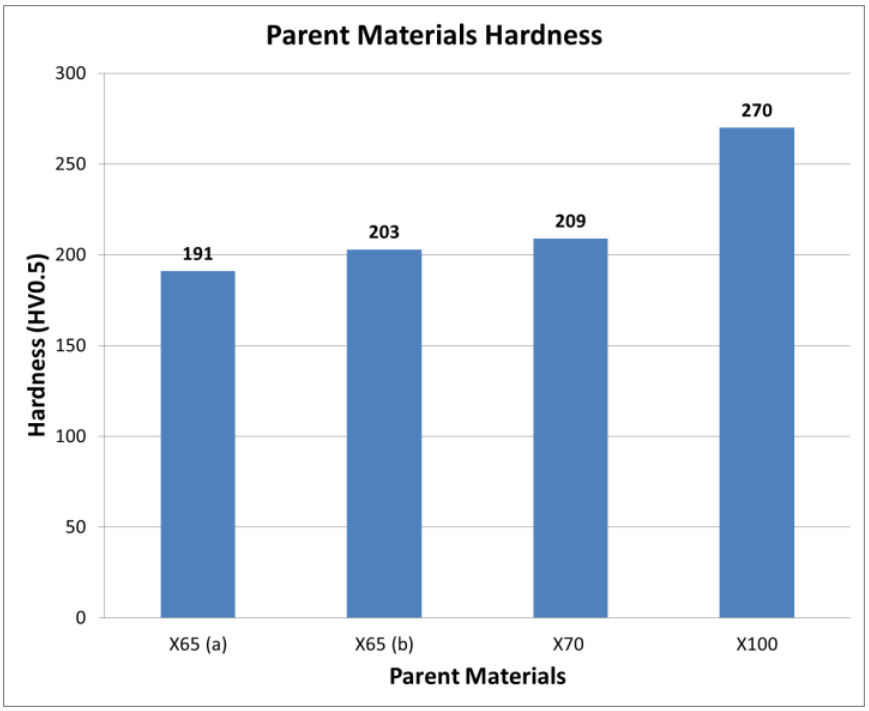

Figure 6-1 Parent materials hardness values (HV0.5)

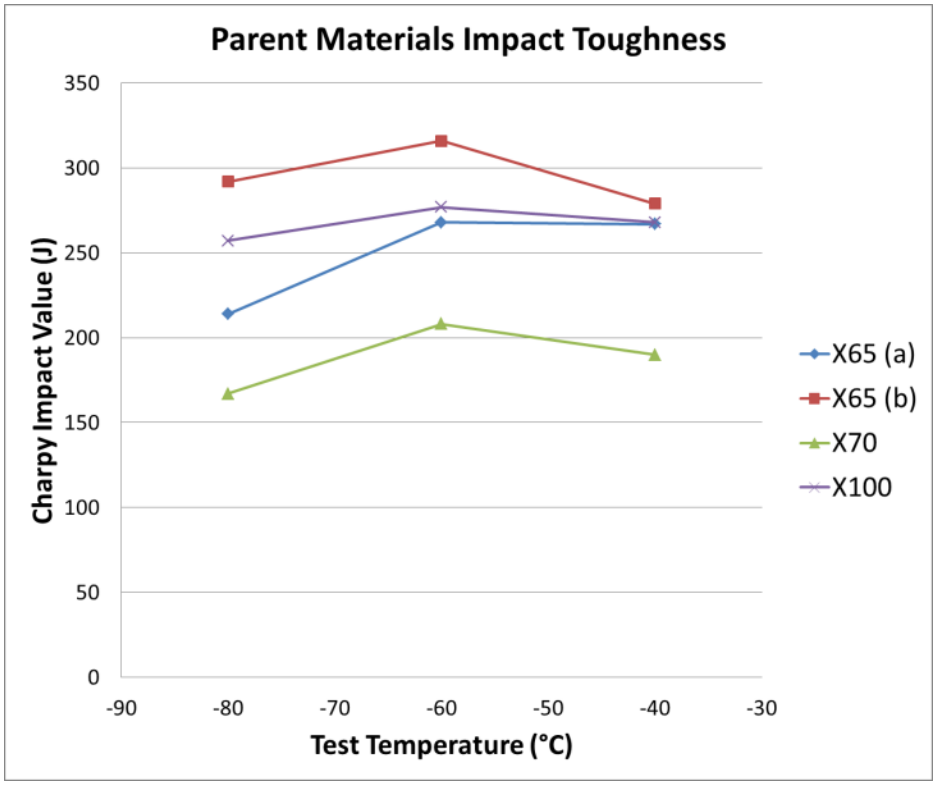

Figure 6-2 Parent materials charpy impact toughness

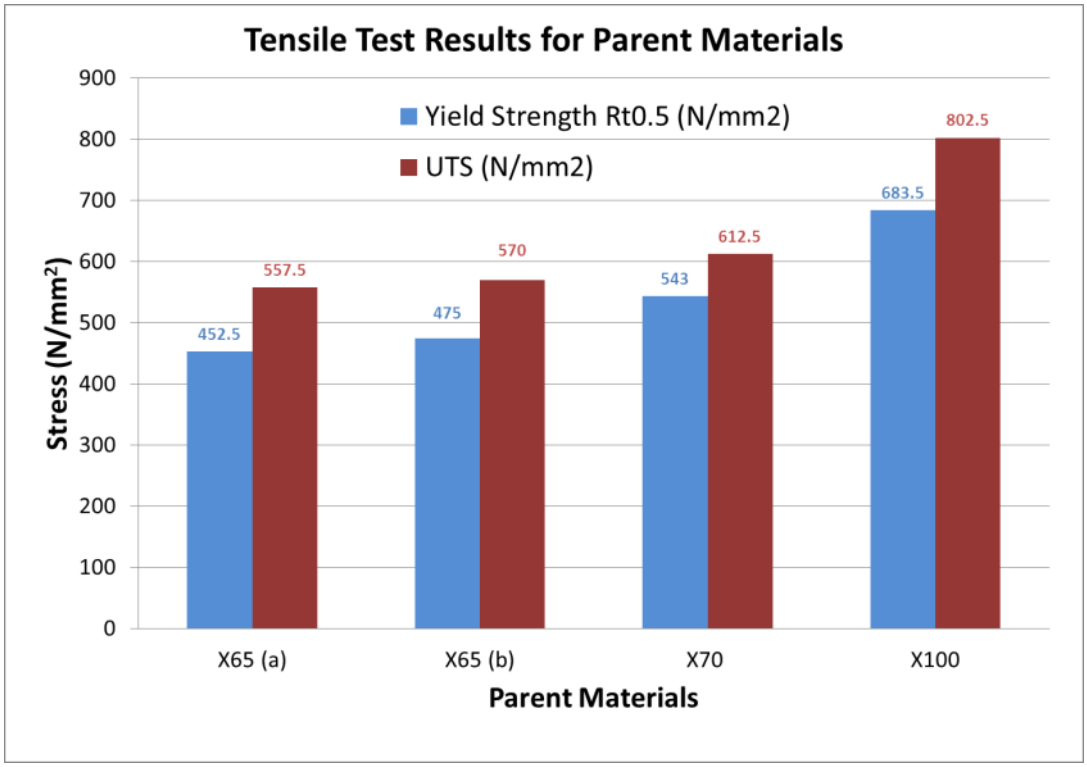

Figure 6-3 Parent materials tensile properties

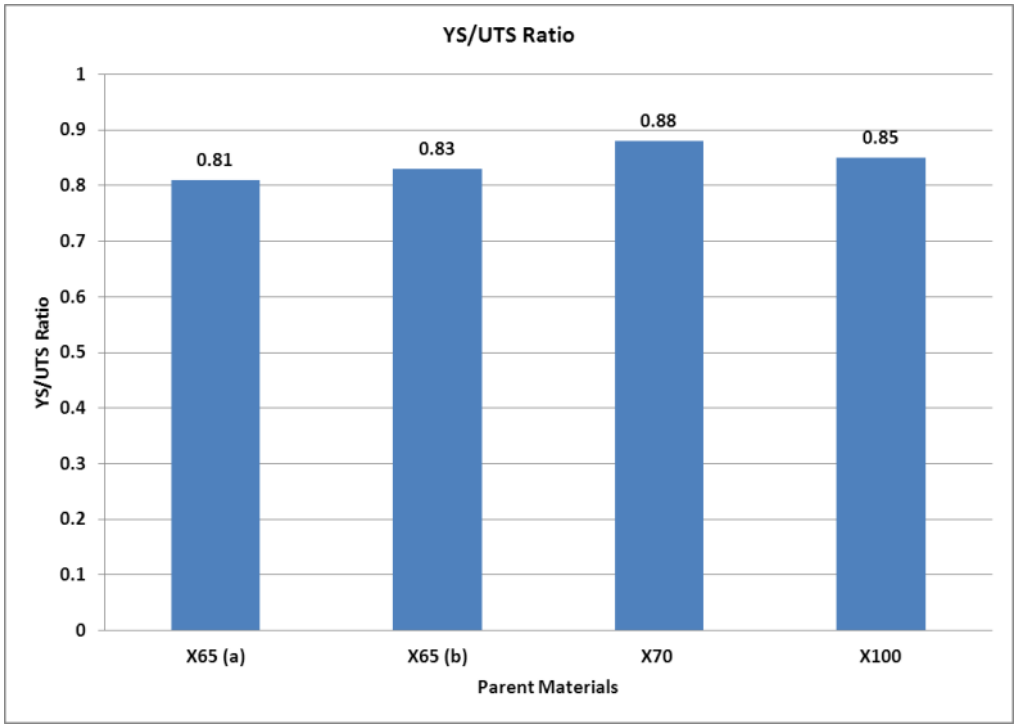

Figure 6-4 YS/UTS ratio of the parent materials

6.1.2 Parent materials microstructure

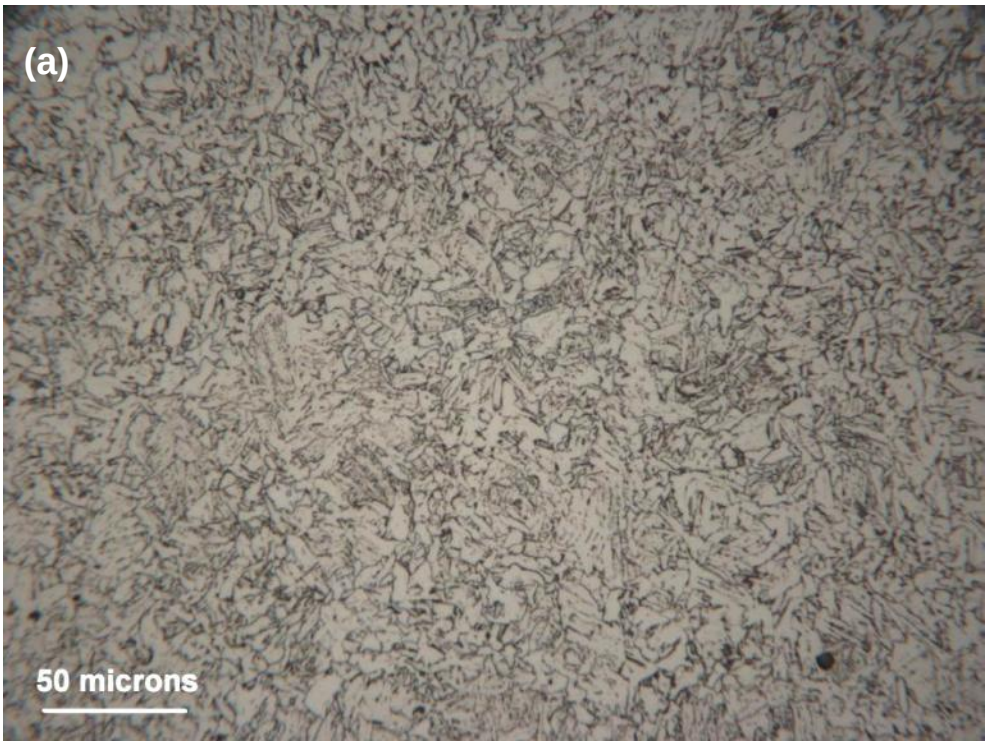

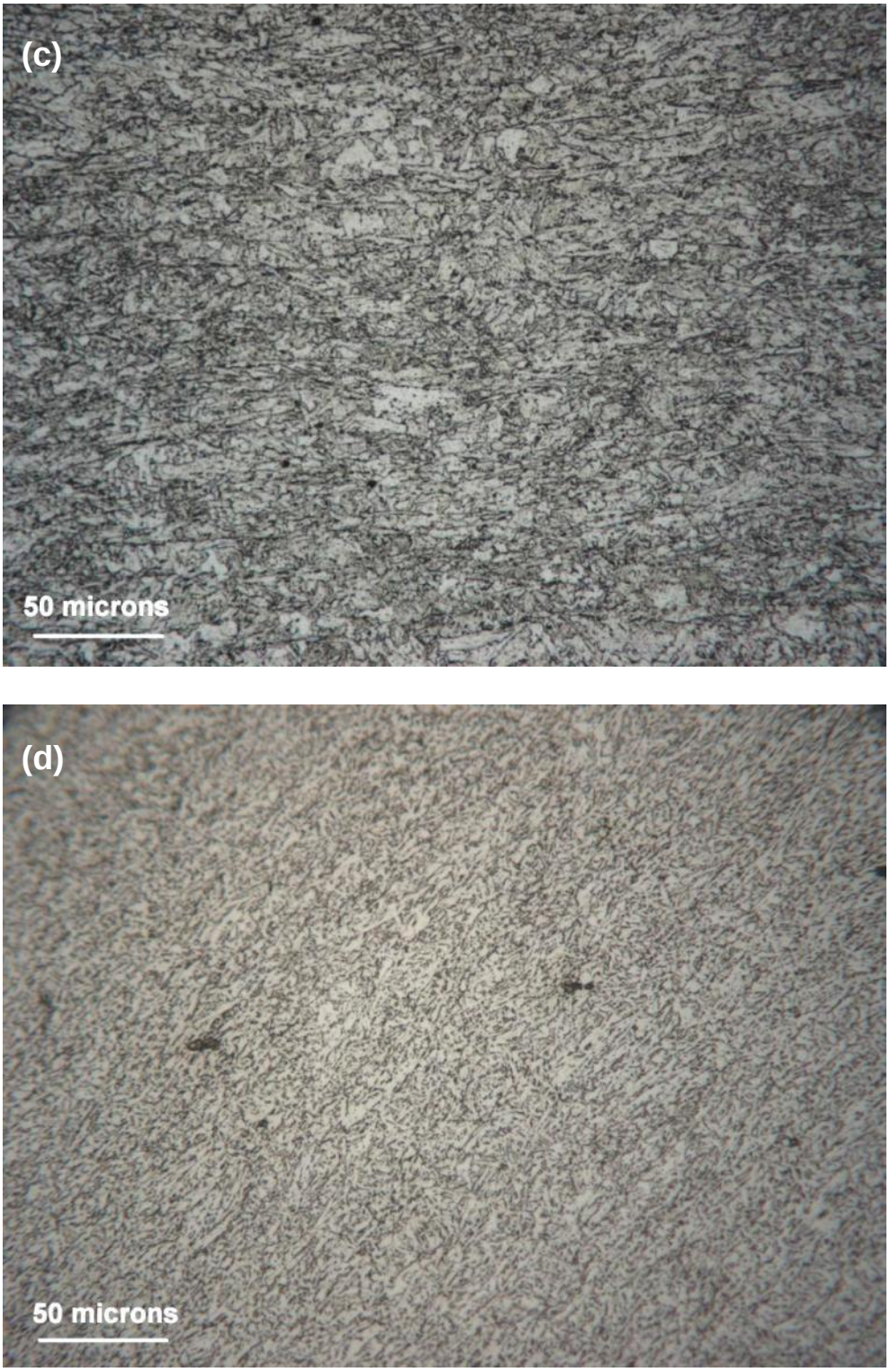

Figure 6-5 Optical micrographs of all the parent materials (a) X65 (A), (b) X65 (B), (c) X70 and (d) X100 pipeline materials

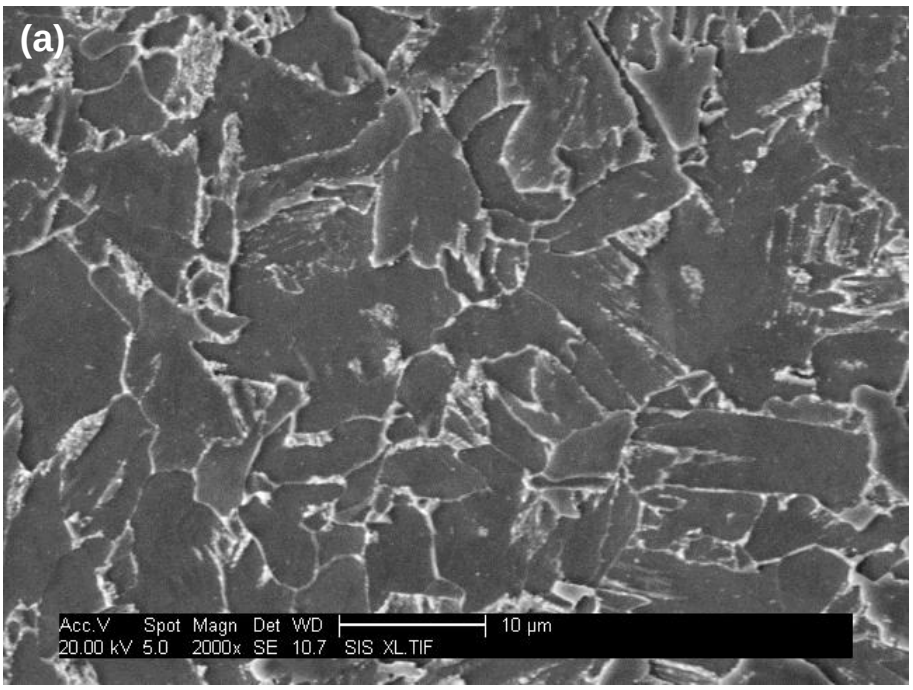
(a)
Acc.V Spot Magn Det WD 10 µm
20.00 kV 5.0 2000x SE 10.7 SIS XL.TIF

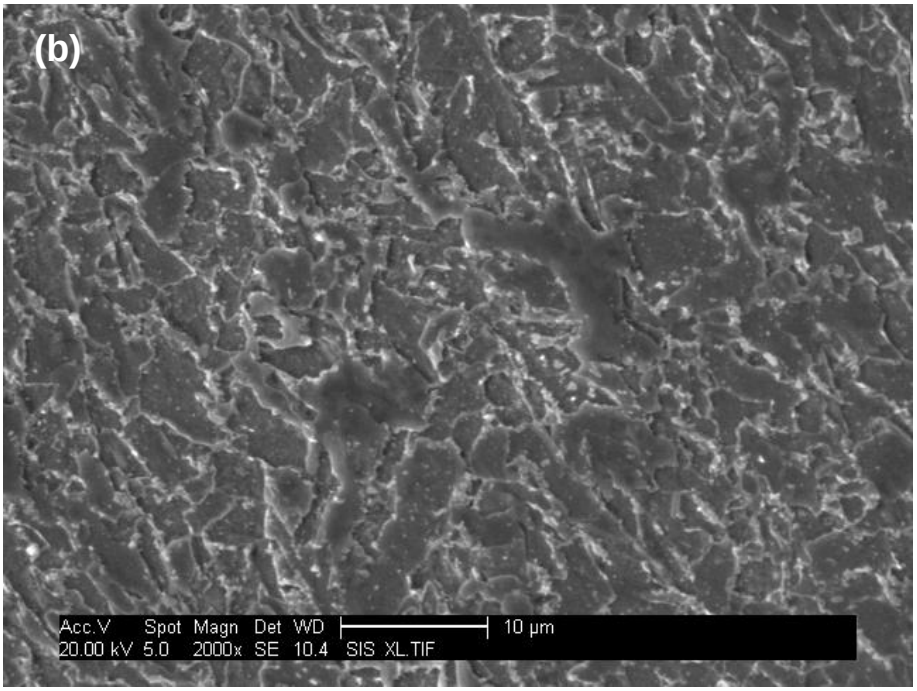
(b)
Acc.V Spot Magn Det WD 10 µm
20.00 kV 5.0 2000x SE 10.4 SIS XL.TIF

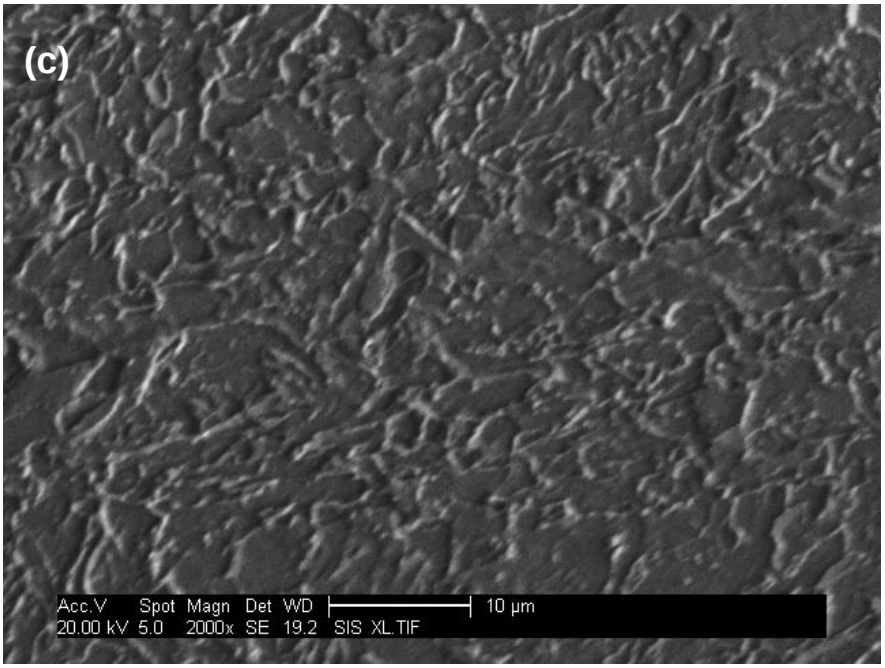

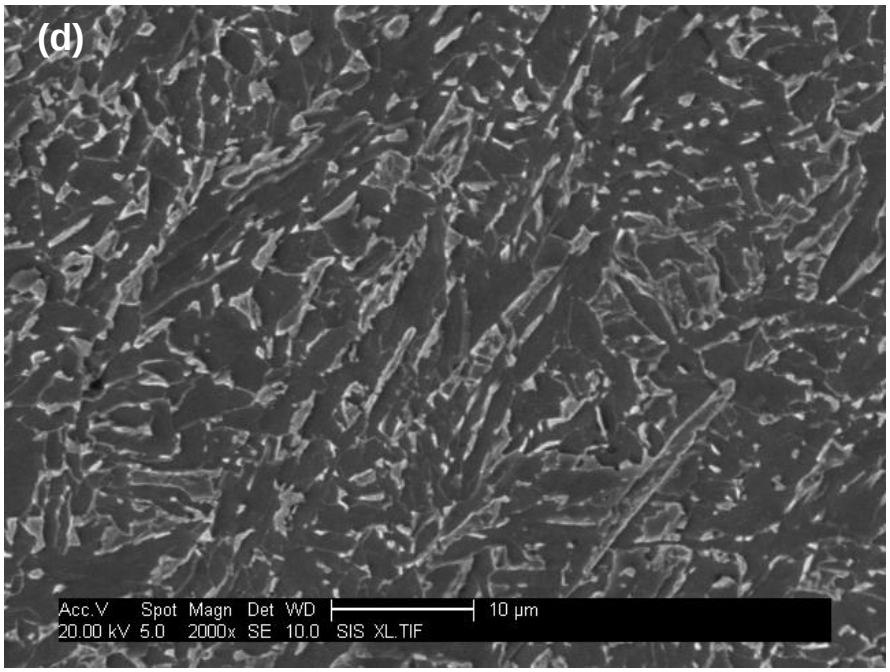

Figure 6-6 SEM Micrographs of all the parent materials (a) X65 (A), (b) X65 (B), (c) X70 and (d) X100 pipeline material

6.2 **Dilatometric experiments (CCT Diagrams)**

Results from the dilatometric experiments are presented under this heading, they are representation of the thermal cycles used for the heat treatments and the corresponding dilatation curves. A schematic on how the dilatation curves were used to extract the transformation start and finish temperatures and the A_{C1} and A_{C3} temperatures is presented.

The CCT diagrams are presented as plots of the cooling curves on a log scale, with the transformation points superimposed on them. Representative microstructures from some of the thermal cycles are presented. Some microstructures from the four materials will be presented side by side for comparison, so as to see the influence of the same cooling rates on different materials.

The effect of the cooling rates on transformation start and finish temperatures on different materials is also presented.

The hardness values will be presented, and some plots of the hardness against the cooling rates ($t_{8/5}$) will be presented.

6.2.1 Thermal cycles and dilatation curves

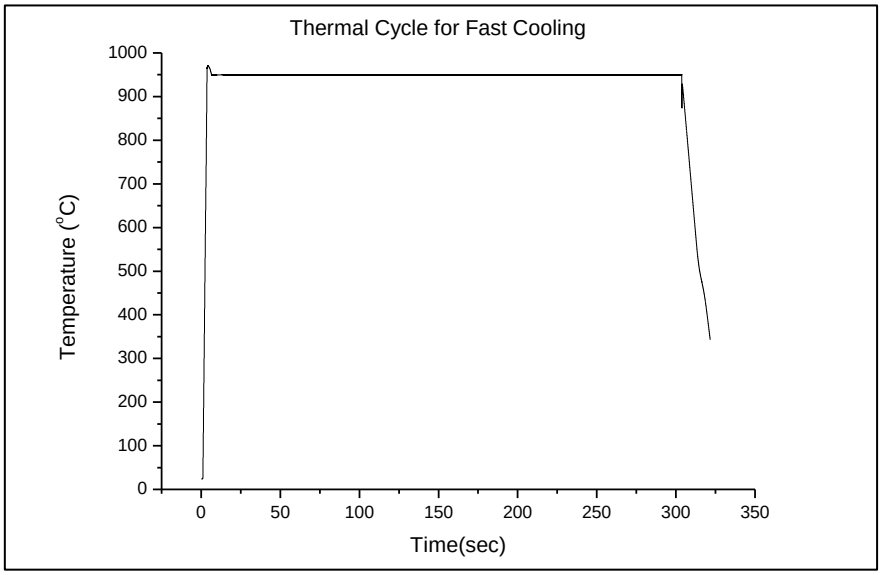

Figure 6-7 Thermal cycle recorded from the Gleeble machine for a fast cooling rate

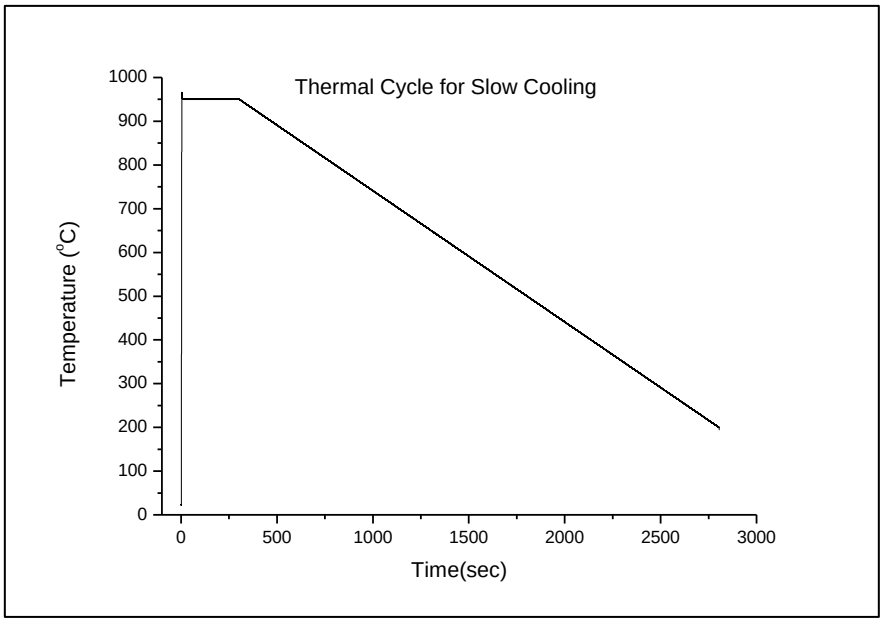

Figure 6-8 Thermal cycle recorded from the Gleeble machine for a slow cooling rate

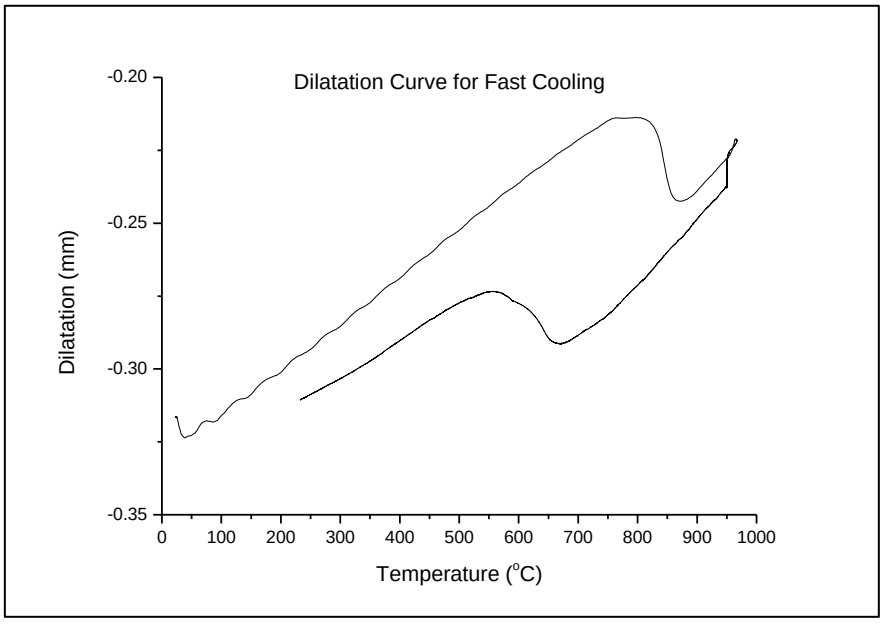

Figure 6-9 Dilatation curve recorded by a dilatometer for a fast cooling rate

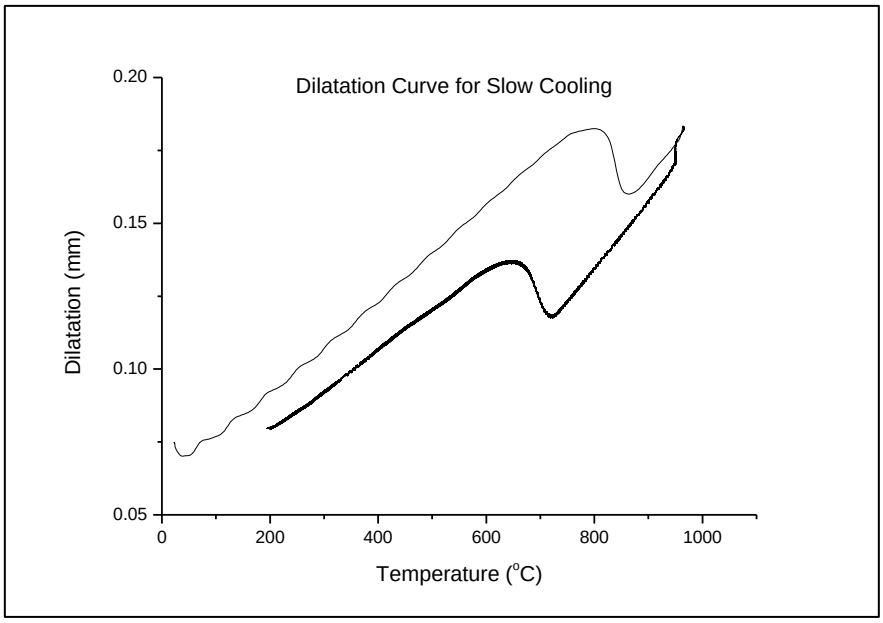

Figure 6-10 Dilatation curve recorded by a dilatometer for a slow cooling rate

Table 6-1 Cooling rates, $t_{8/5}$ and hardness values recorded from the CCT samples

X65 (A)			X65 (B)			X70			X100		
CR (°C/s)	$t_{8/5}$ (s)	HV 0.5	CR (°C/s)	$t_{8/5}$ (s)	HV 0.5	CR (°C/s)	$t_{8/5}$ (s)	HV 0.5	CR (°C/s)	$t_{8/5}$ (s)	HV 0.5
50	6	252	56.2	5.34	244	42.8	7	235	56.2	5.34	293
47.6	6.3	270	46.4	6.47	232	38.6	7.8	253	47.7	6.29	283
46.8	6.4	271	42.2	7.1	235	30	10	238	29.7	10.09	290
28.8	10.4	233	39.5	7.59	235	20	15	240	20	15	297
20	15	264	30	10	237	12	25	221	12	25	274
12	25	196	20	15	218	6	50	204	6	50	260
6	50	199	12	25	196	3.33	90	205	3.33	90	238
3.33	90	174	6	50	185	1.2	250	184	1.2	250	228
1.2	250	154	3.33	90	174	0.75	400	177	0.75	400	220
0.75	400	147	1.2	250	165	0.5	600	176	0.5	600	220
0.5	600	147	0.75	400	158	0.3	1000	165	0.3	1000	211
0.3	1000	157	0.5	600	154						
			0.3	1000	146						

Table 6-2 Experimental and calculated transformation temperatures [136; 165]

Materials	Exp. A_{C1} (°C)	Cal. A_{C1} (°C)	Exp. A_{C3} (°C)	Cal. A_{C3} (°C)	Cal. M_S (°C)	PM (HV5)
X65 (A)	742	706	888	845	480	191
X65 (B)	720	707	877	862	515	203
X70	757	708	875	858	475	209
X100	750	710	884	870	468	270

6.2.2 Transformation start and finish temperatures

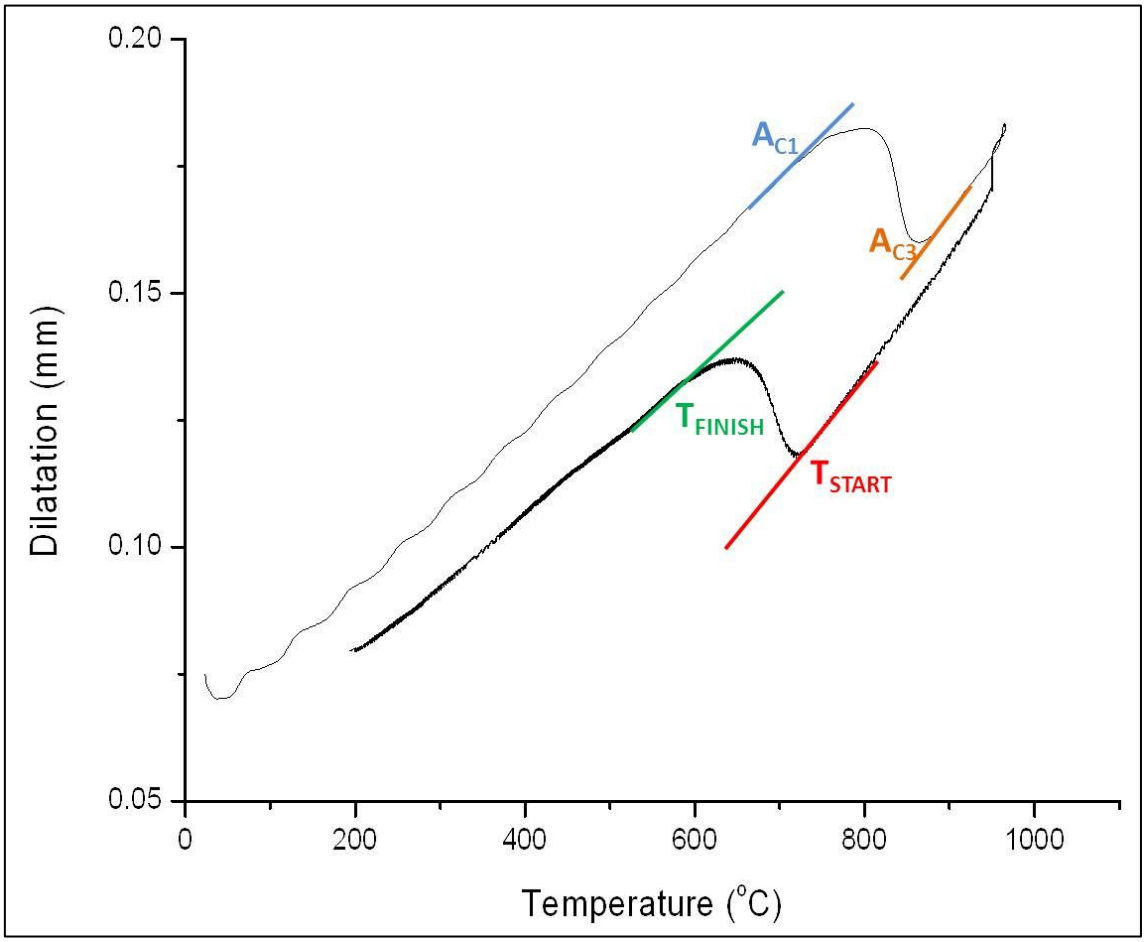

Figure 6-11 A dilatation curve indicating the transformation start and finish, the A_{C1} and A_{C3} temperatures

6.2.3 CCT Diagrams

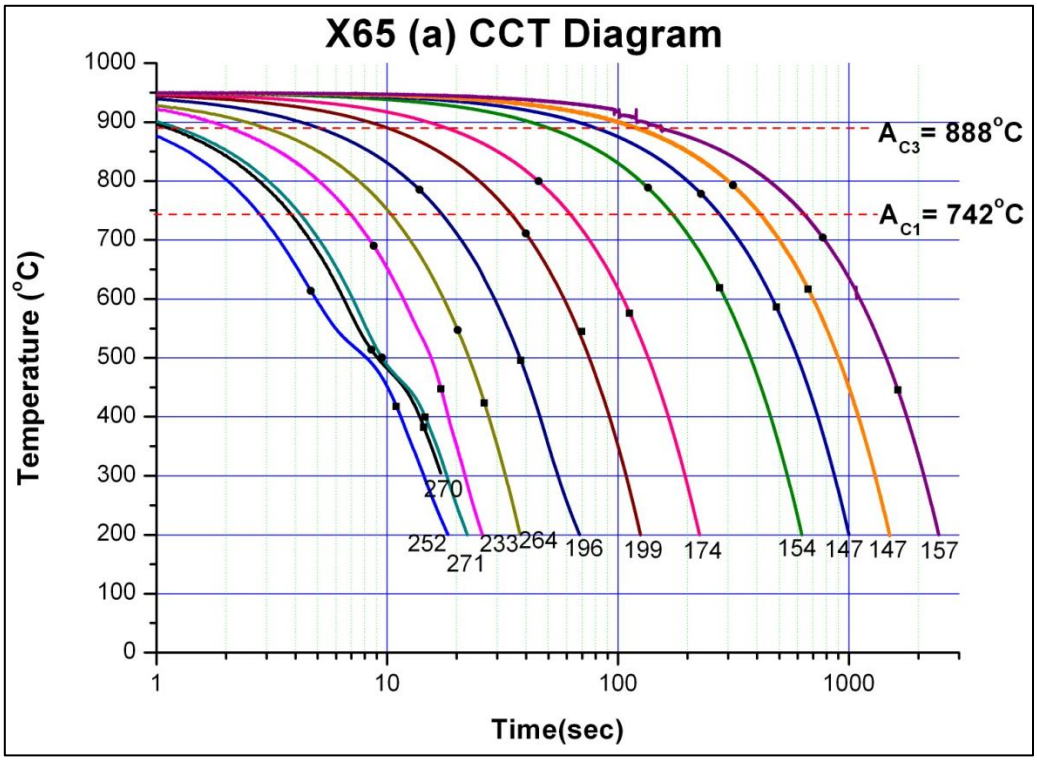

Figure 6-12 CCT diagram of X65 (A)

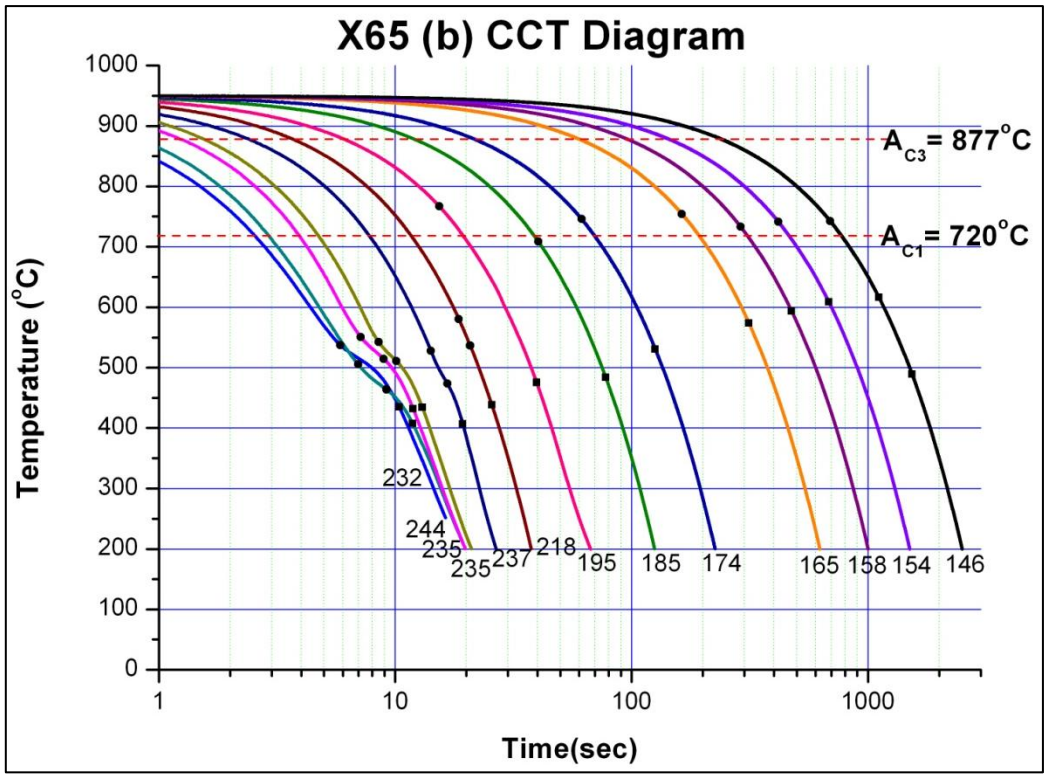

Figure 6-13 CCT diagram of X65 (B)

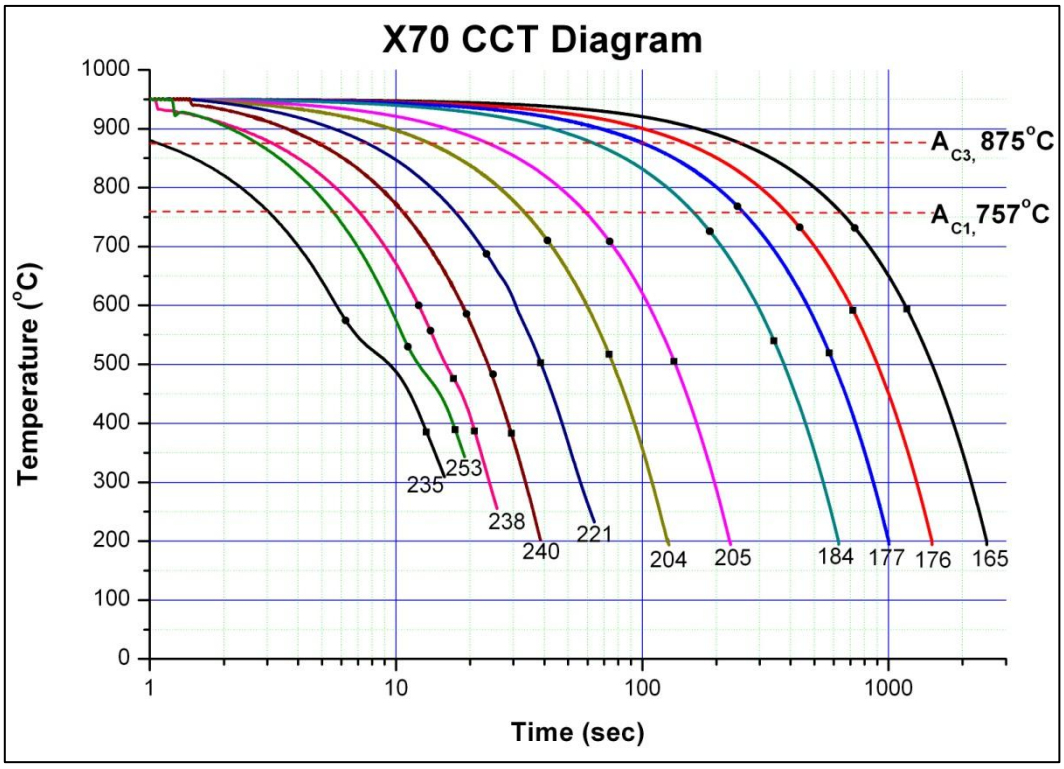

Figure 6-14 CCT diagram of X70

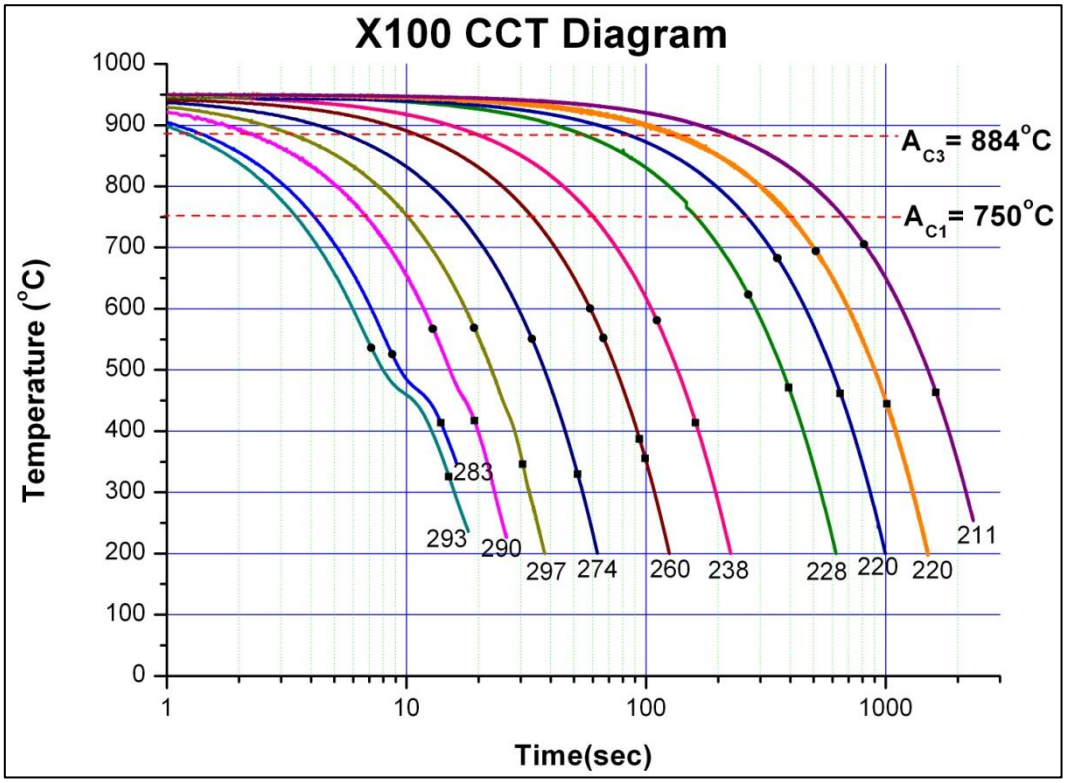

Figure 6-15 CCT diagram of X100

6.2.4 Microstructural characterisation of dilatometric samples

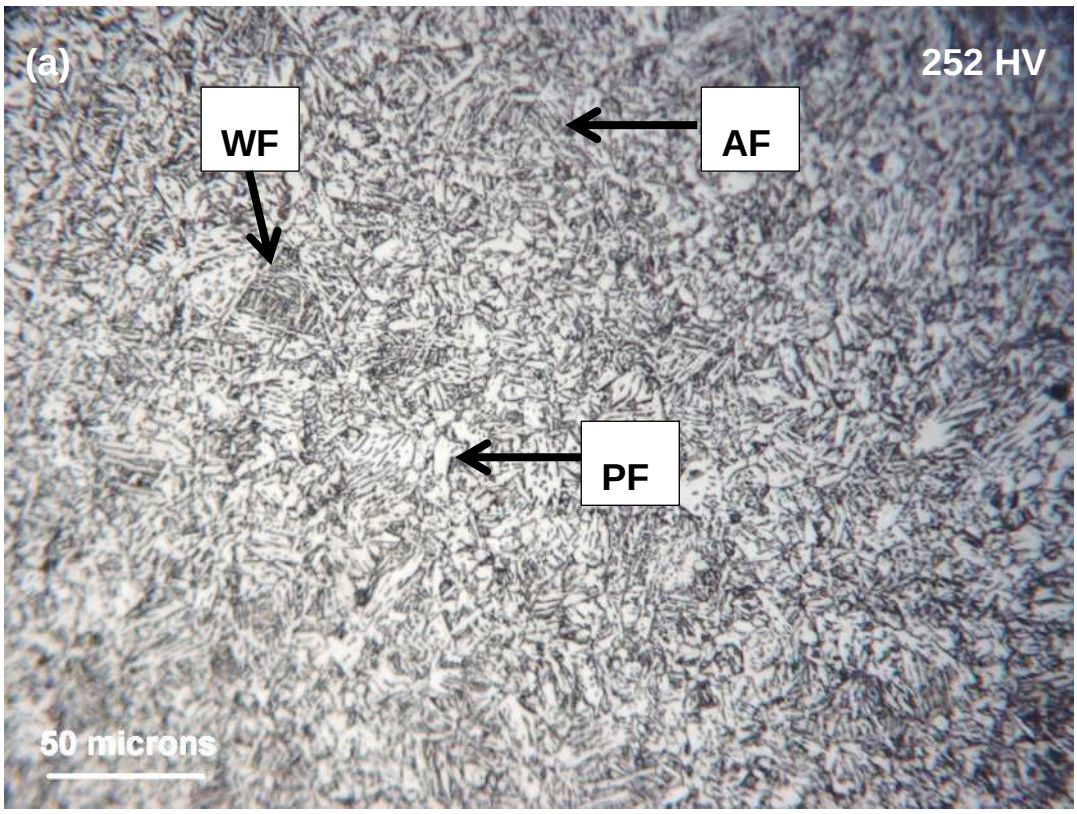

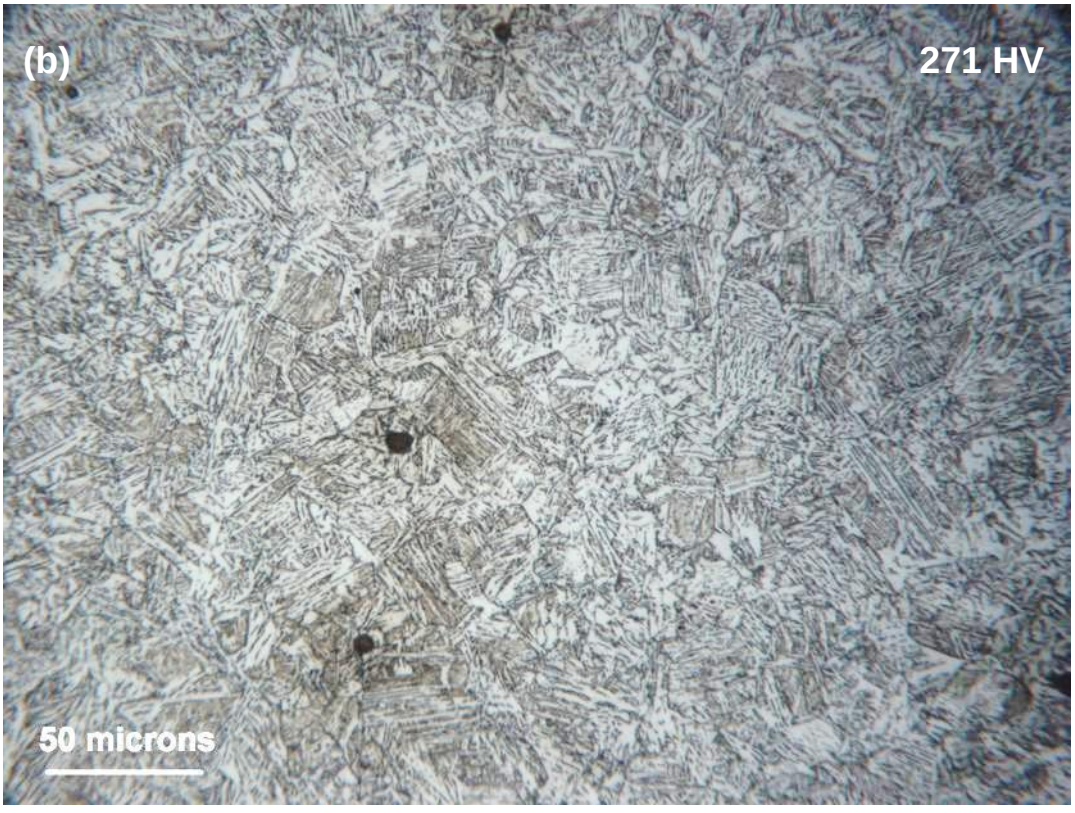

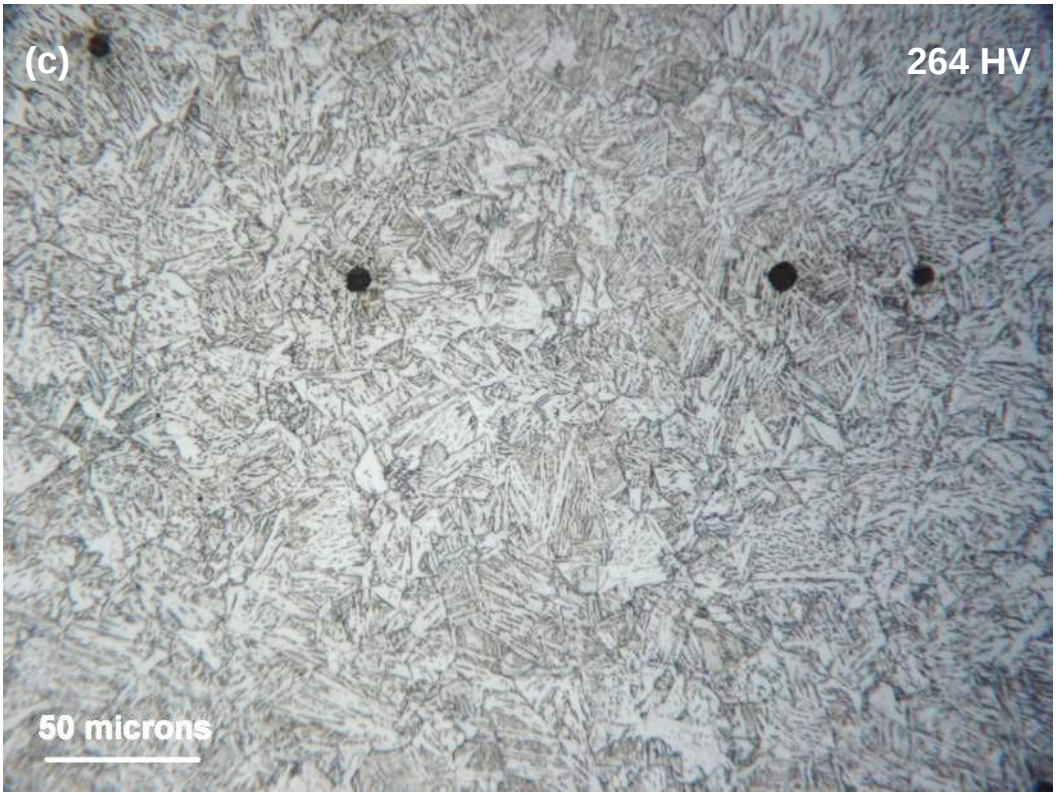
(c)
264 HV
50 microns

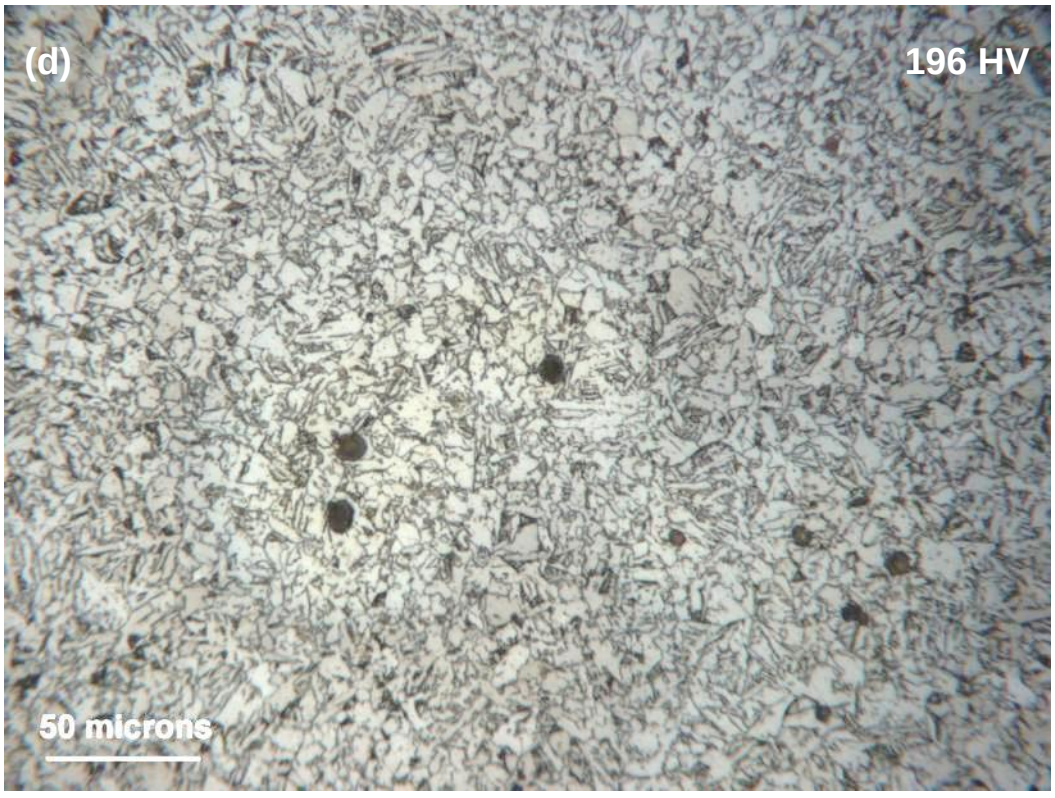
(d)
196 HV
50 microns

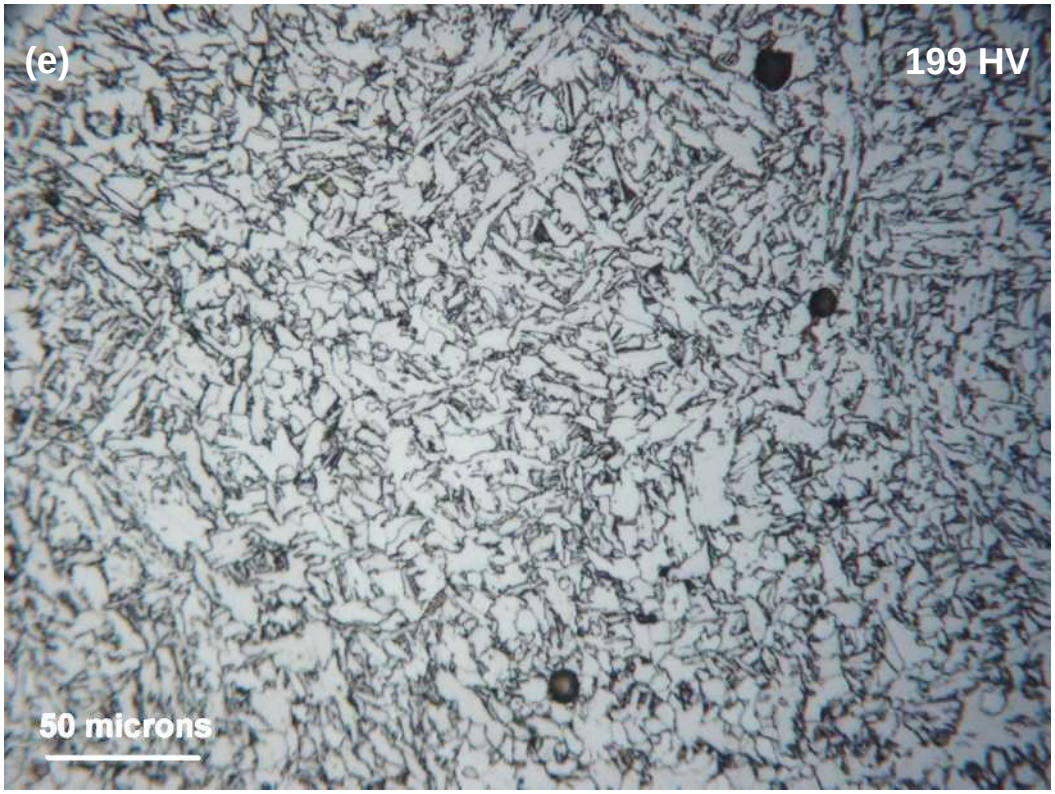
(e)
199 HV
50 microns

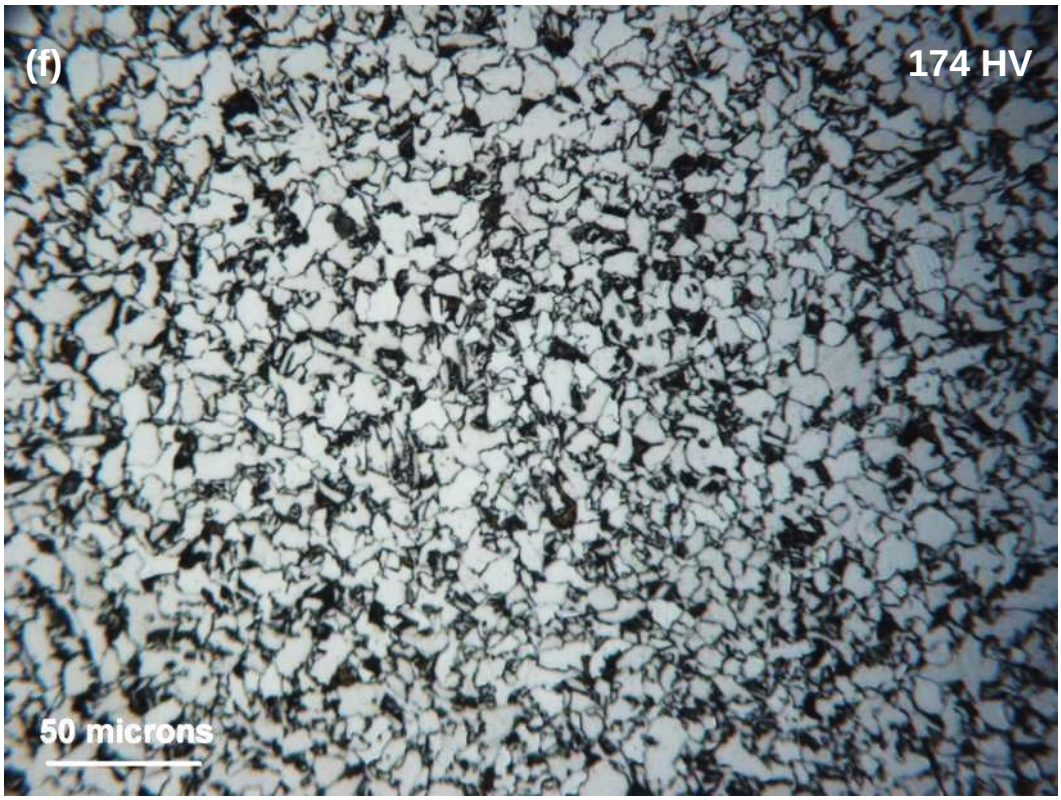
(f)
174 HV
50 microns

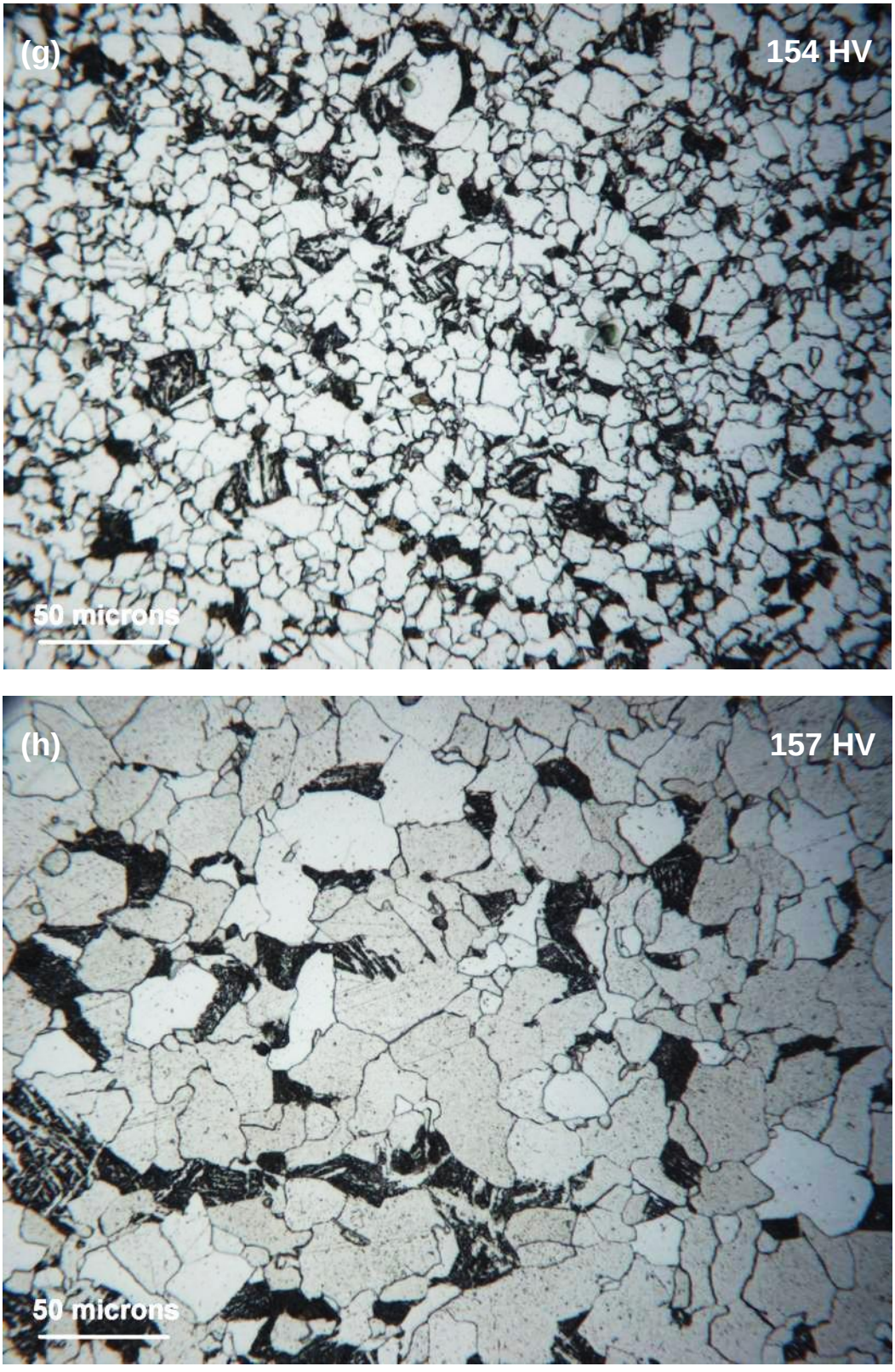

Figure 6-16 Optical micrographs of X65 (A) steel after dilatometric cycles, cooled at $t_{8/5}$ of (a) 6 s, (b) 6.4 s, (c) 15 s, (d) 25 s, (e) 50 s, (f) 90 s, (g) 250 s, (h) 1000 s, and their respective hardness HV0.5


(a)
244 HV
50 microns

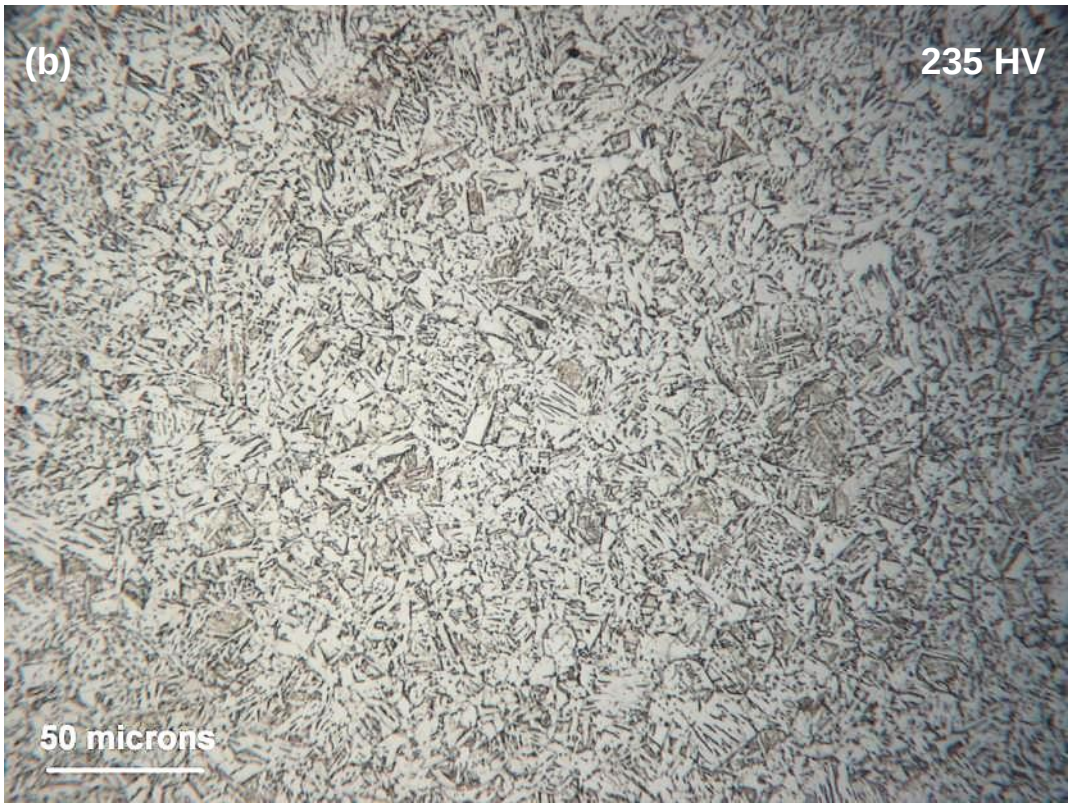
(b)
235 HV
50 microns

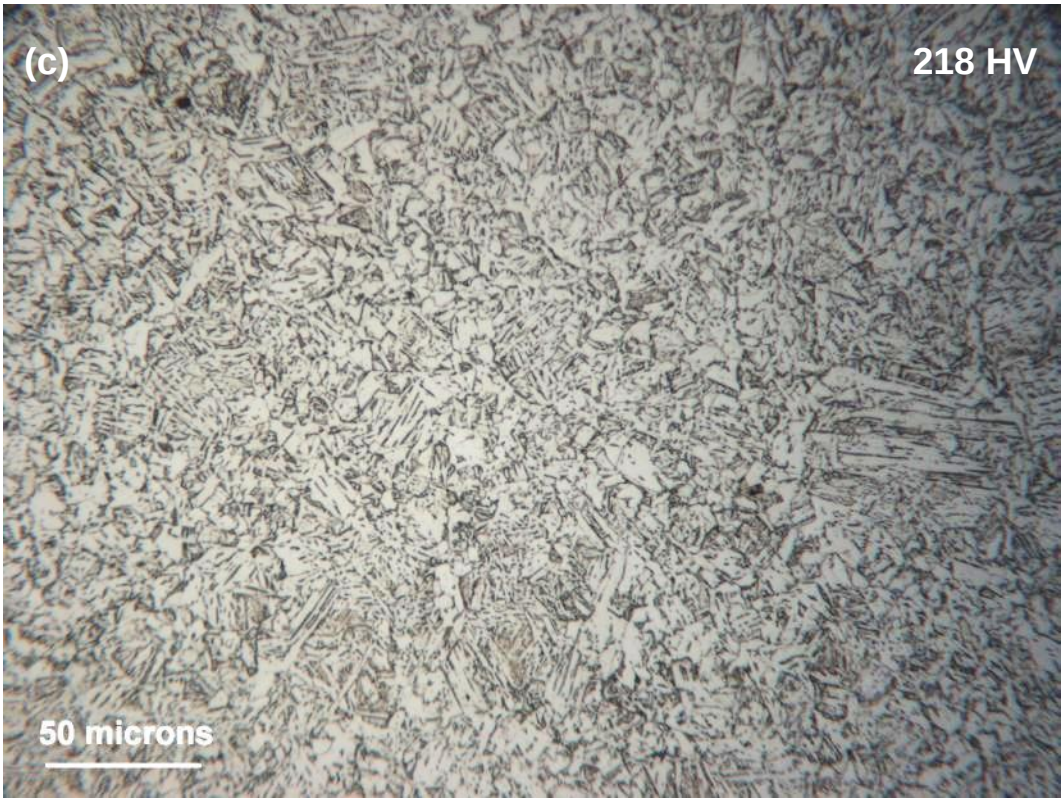
(c)
218 HV
50 microns


(d)
195 HV
50 microns

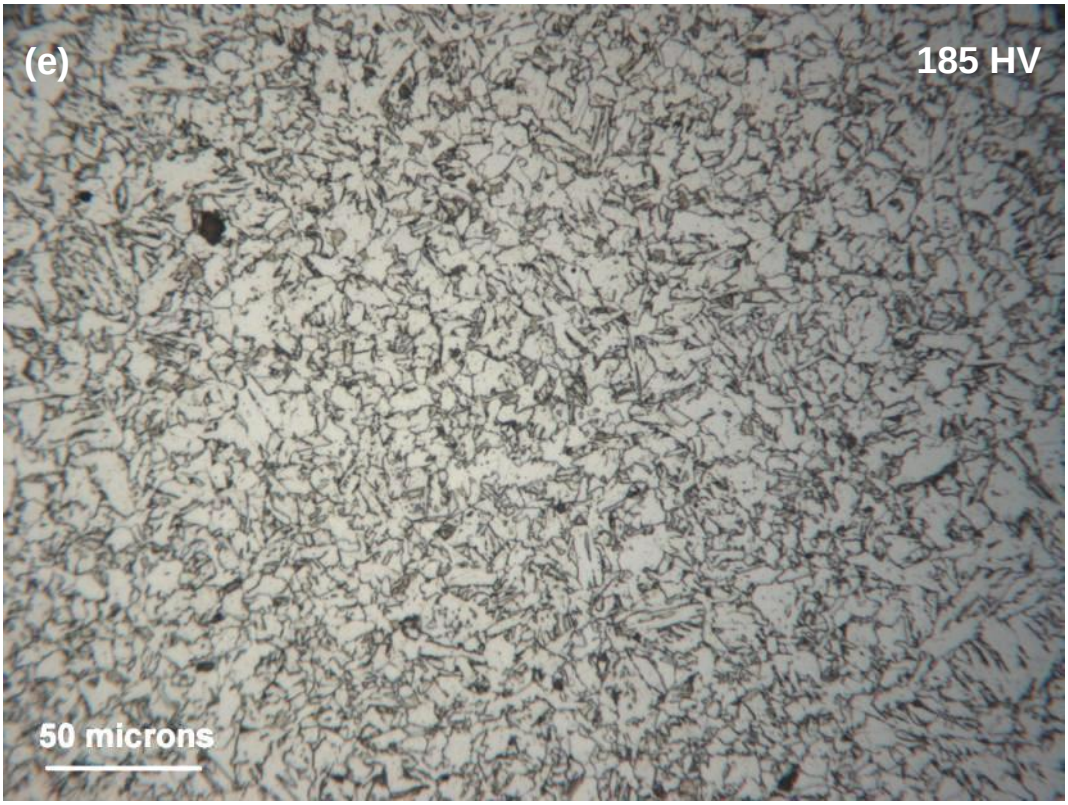
(e)
185 HV
50 microns

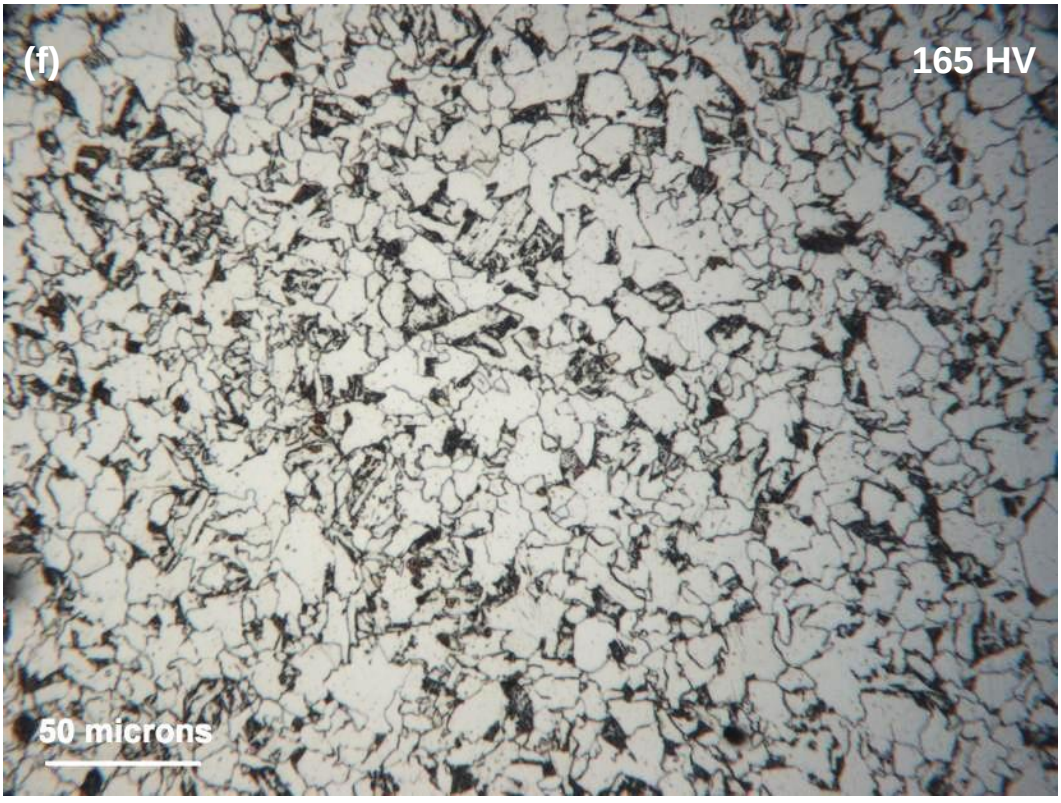
(f)
165 HV
50 microns

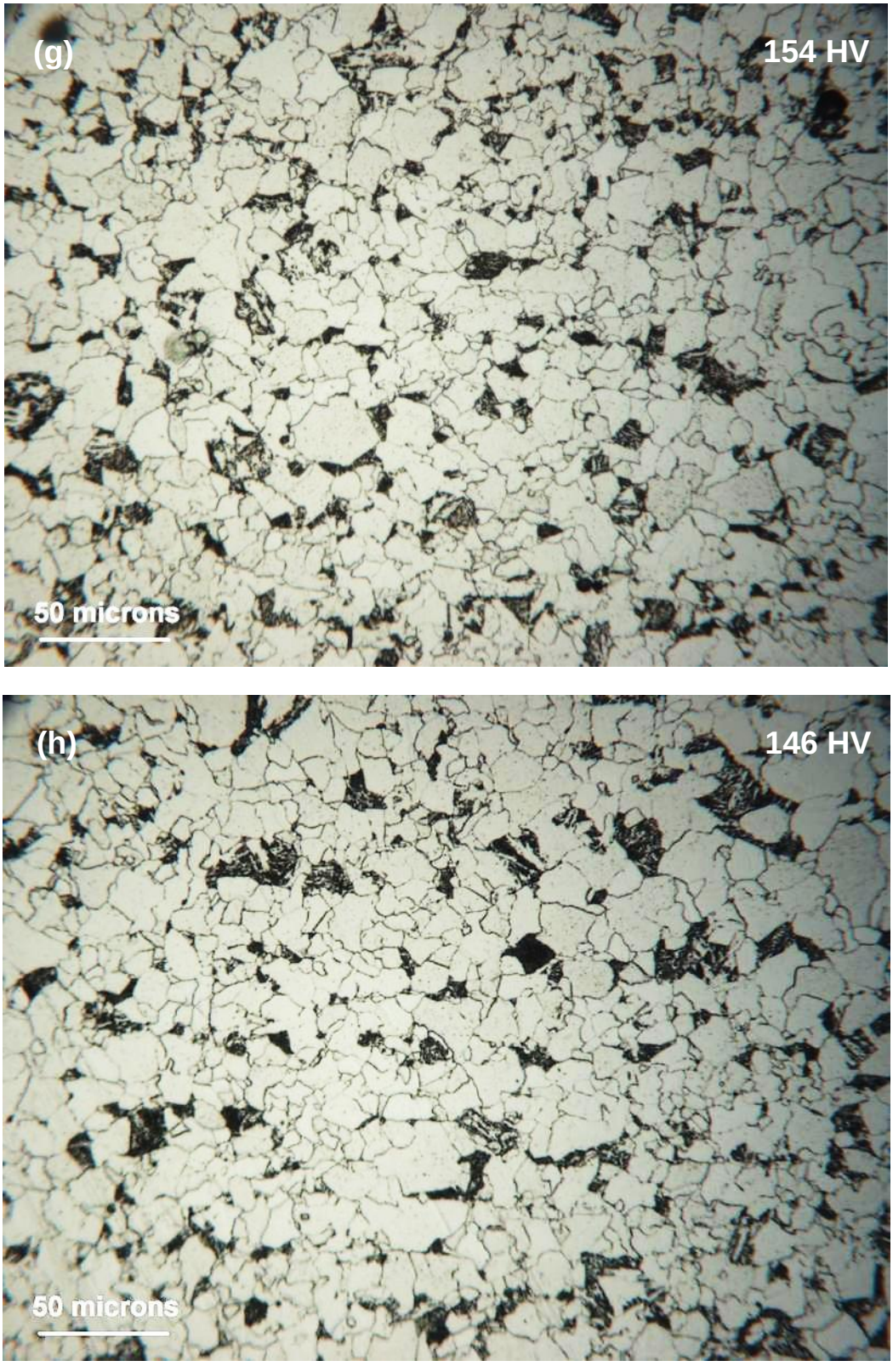

Figure 6-17 Optical micrographs of X65 (B) steel after dilatometric cycles, cooled at $t_{8/5}$ of (a) 5.34 s, (b) 7.59 s, (c) 15 s, (d) 25 s, (e) 50 s, (f) 250 s, (g) 600 s, (h) 1000 s, and their respective hardness HV0.5

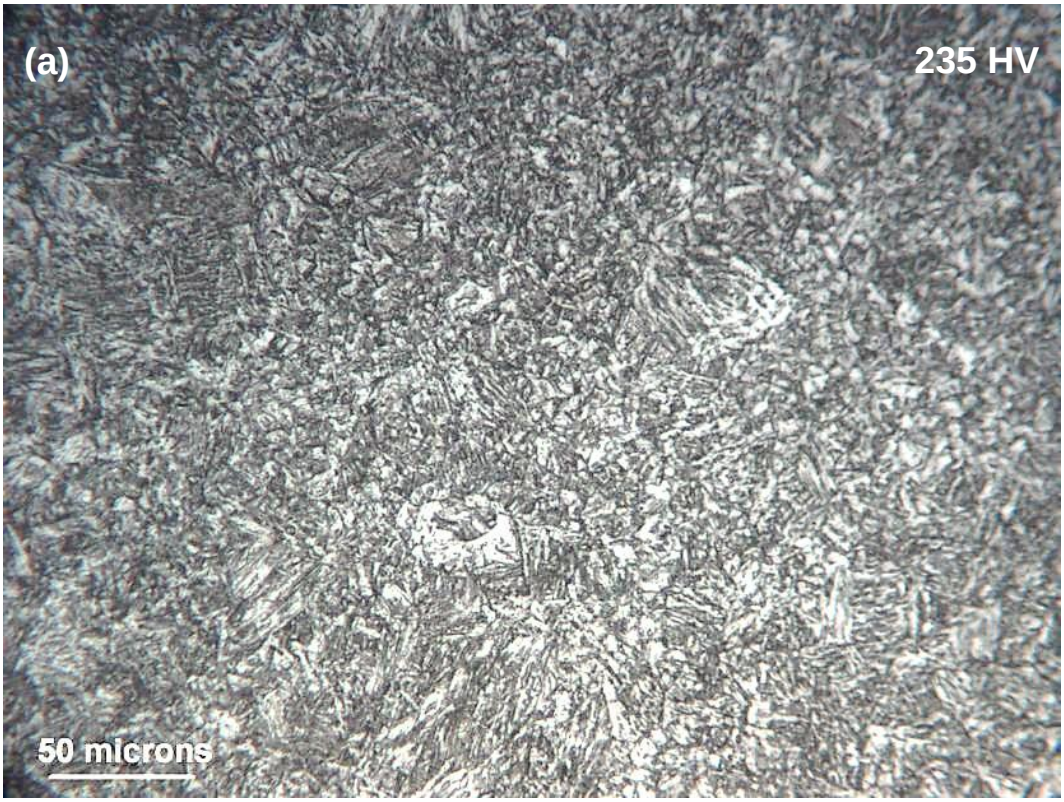
(a)
235 HV
50 microns

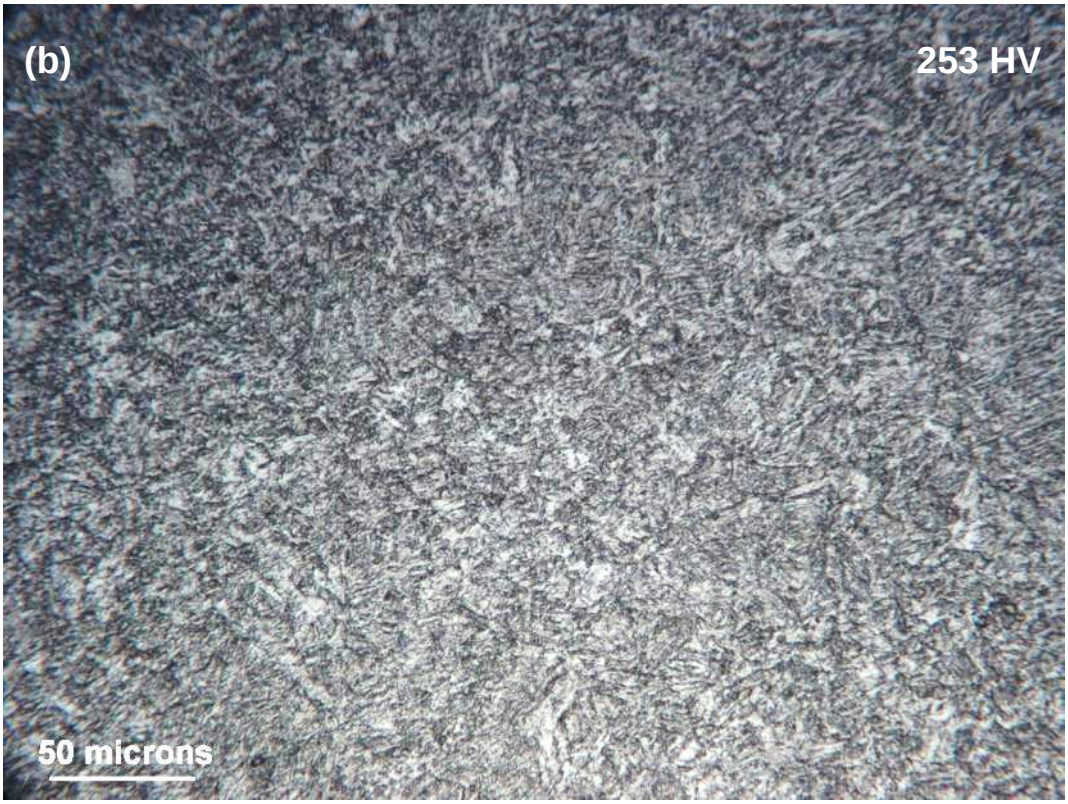
(b)
253 HV
50 microns

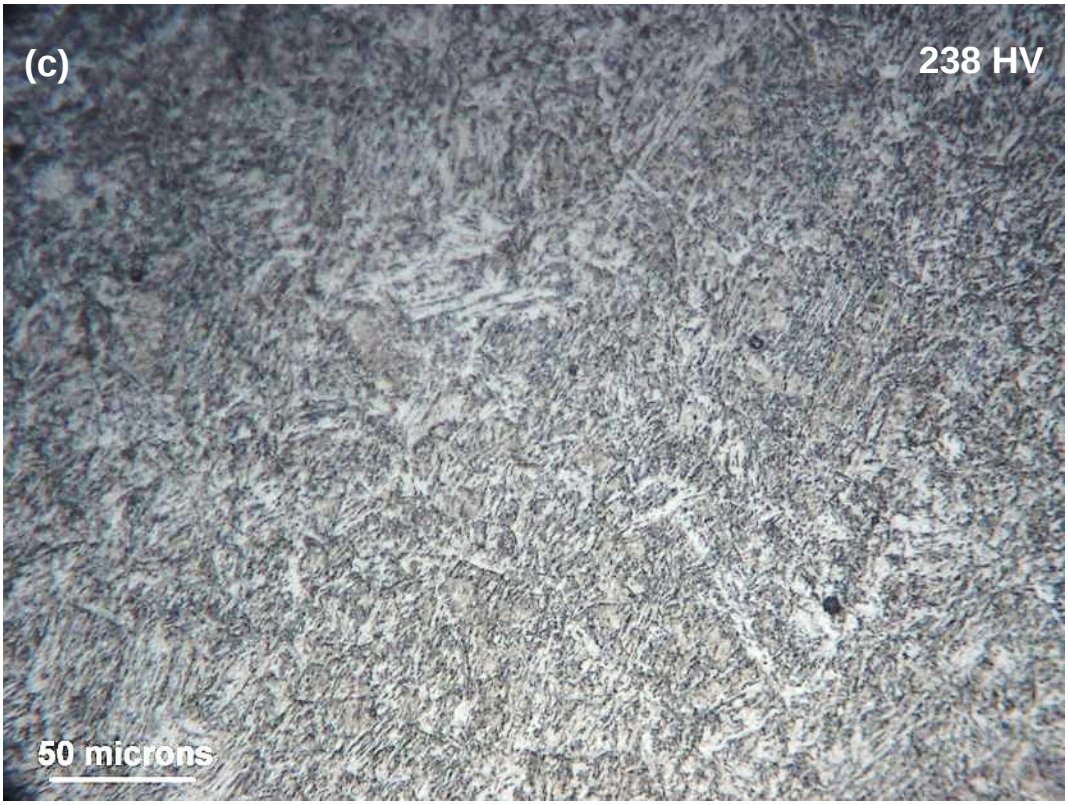
(c)
238 HV
50 microns

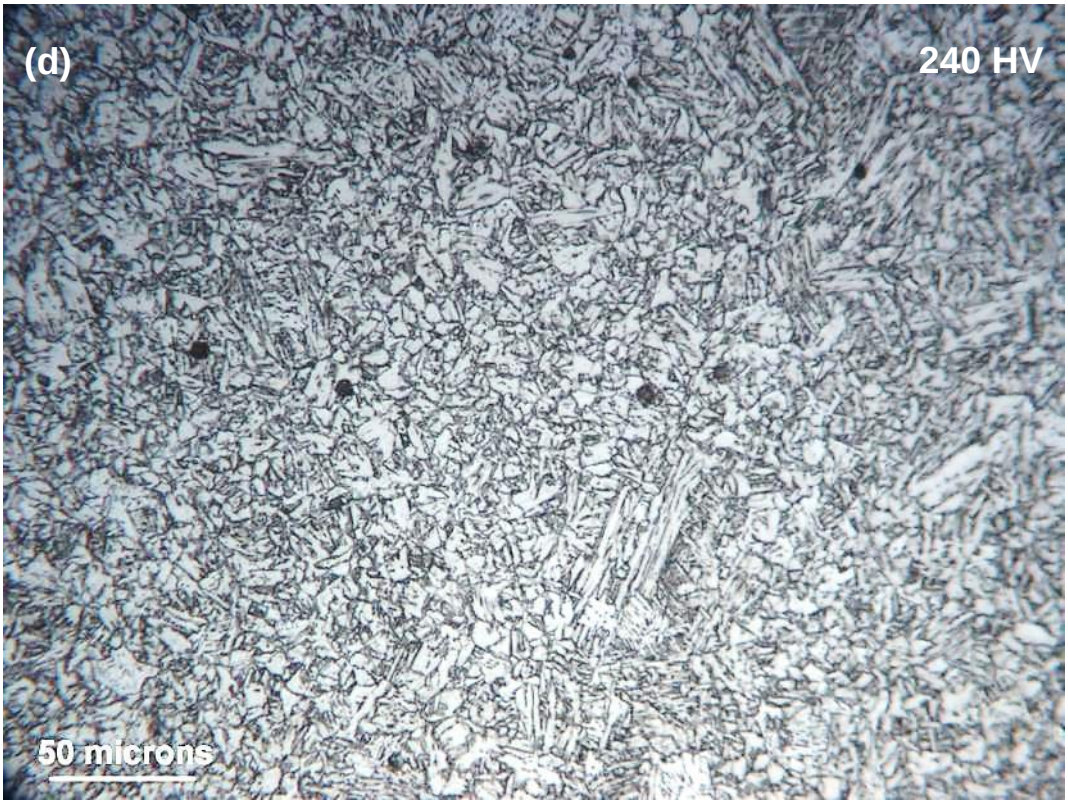
(d)
240 HV
50 microns

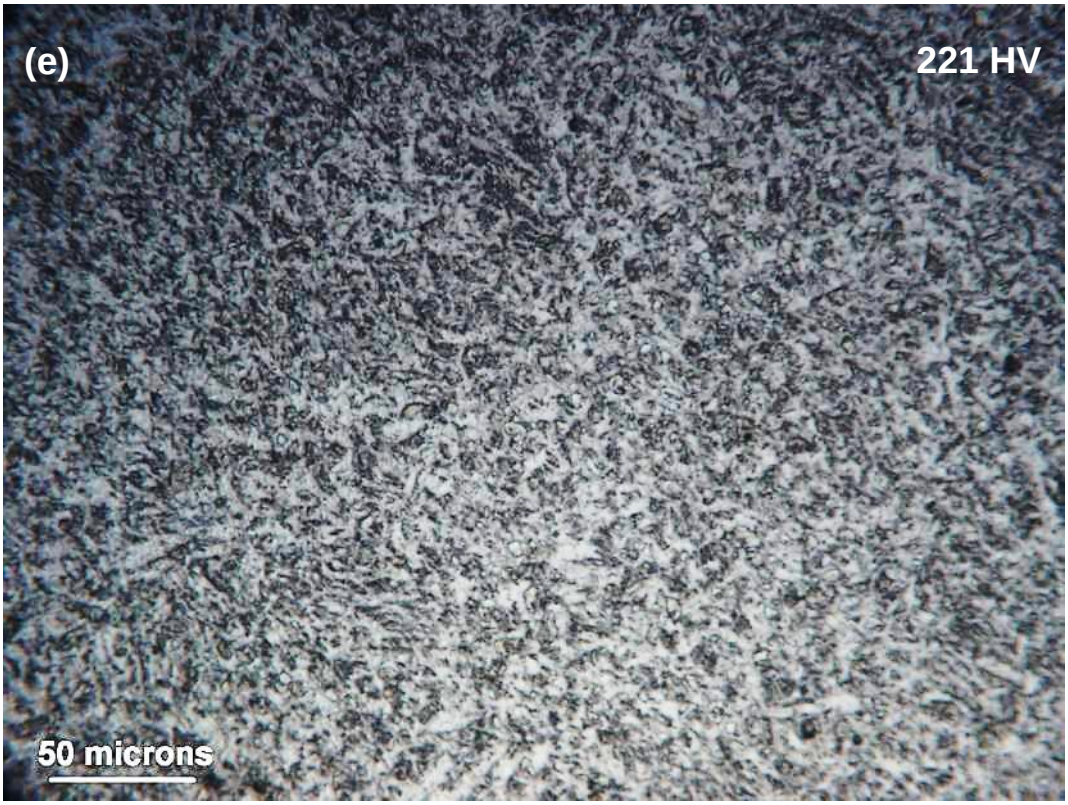
(e)
221 HV
50 microns

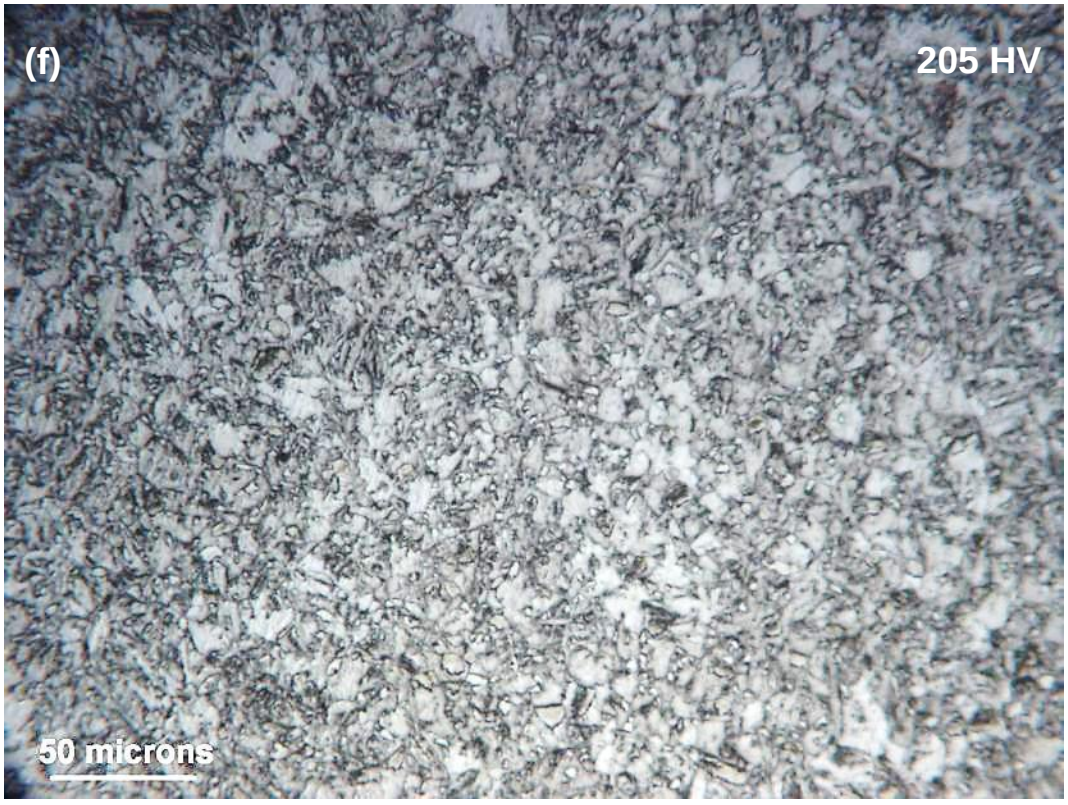
(f)
205 HV
50 microns

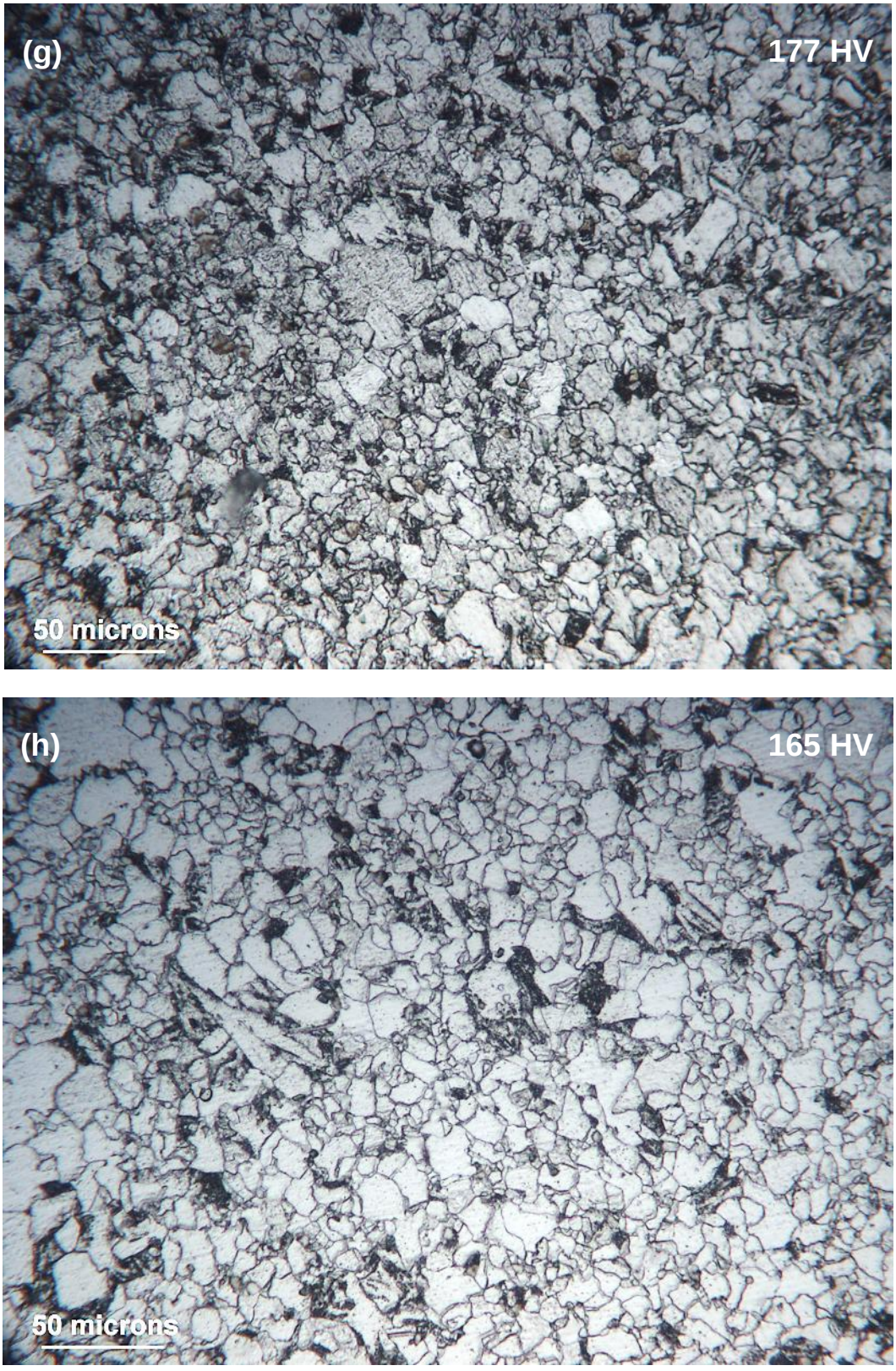

Figure 6-18 Optical micrographs of X70 steel after dilatometric cycles, cooled at $t_{8/5}$ of (a) 7 s, (b) 7.8 s, (c) 10 s, (d) 15 s, (e) 25 s, (f) 90 s, (g) 400 s, (h) 1000 s and their respective hardness HV0.5


(a)
293 HV
50 microns

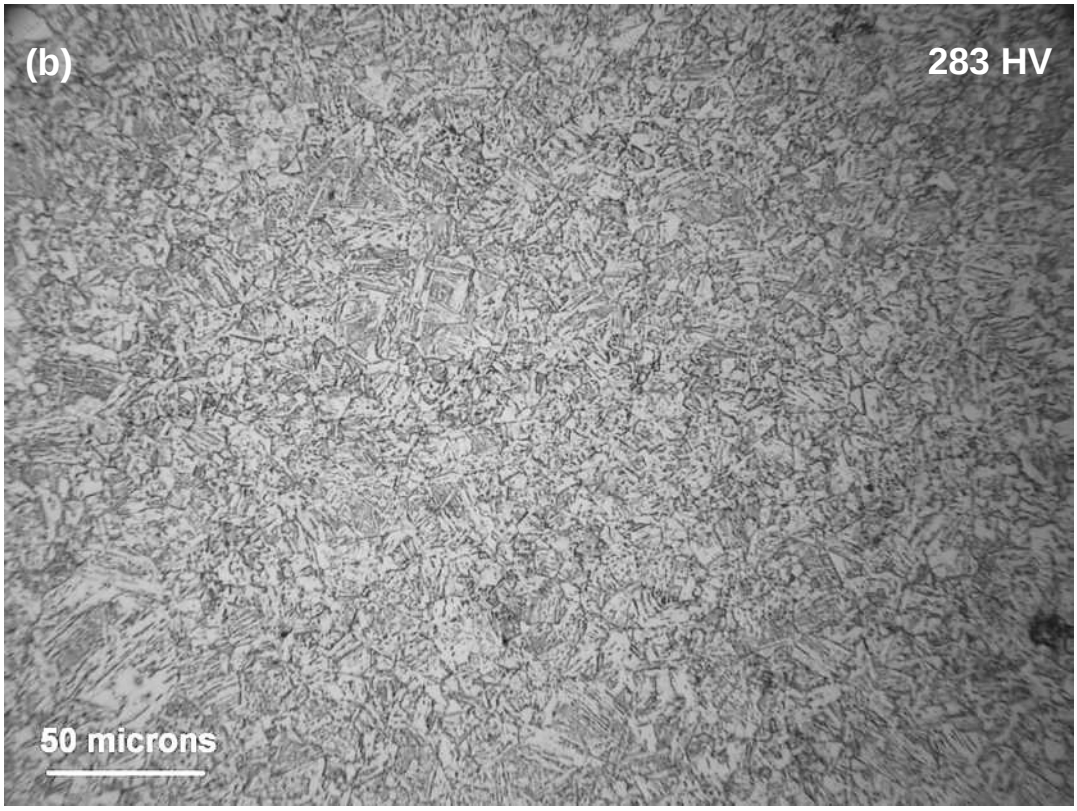
(b)
283 HV
50 microns

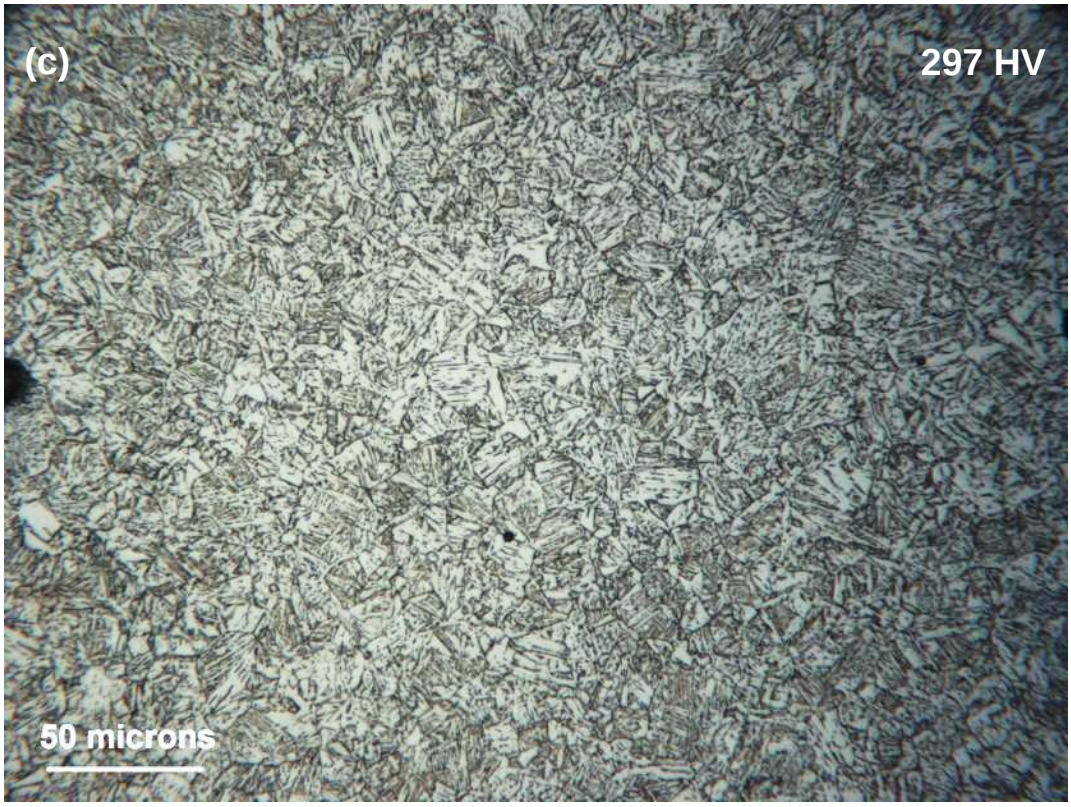
(c)
297 HV
50 microns

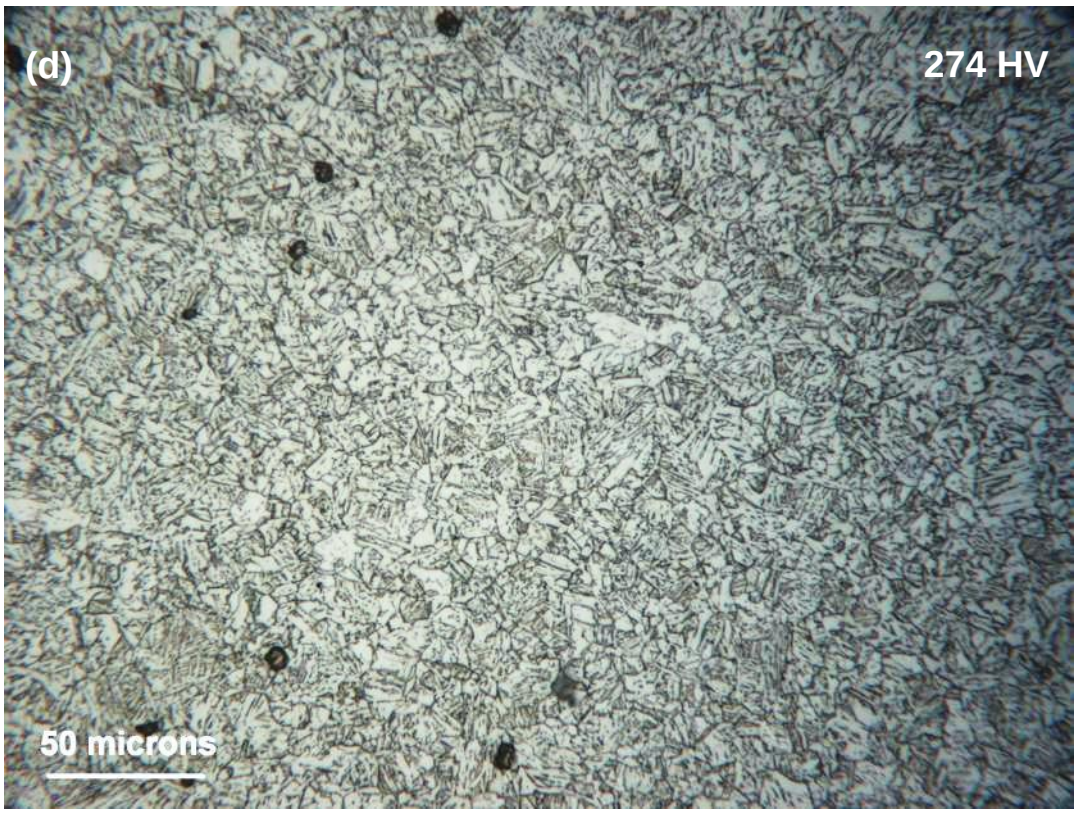
(d)
274 HV
50 microns

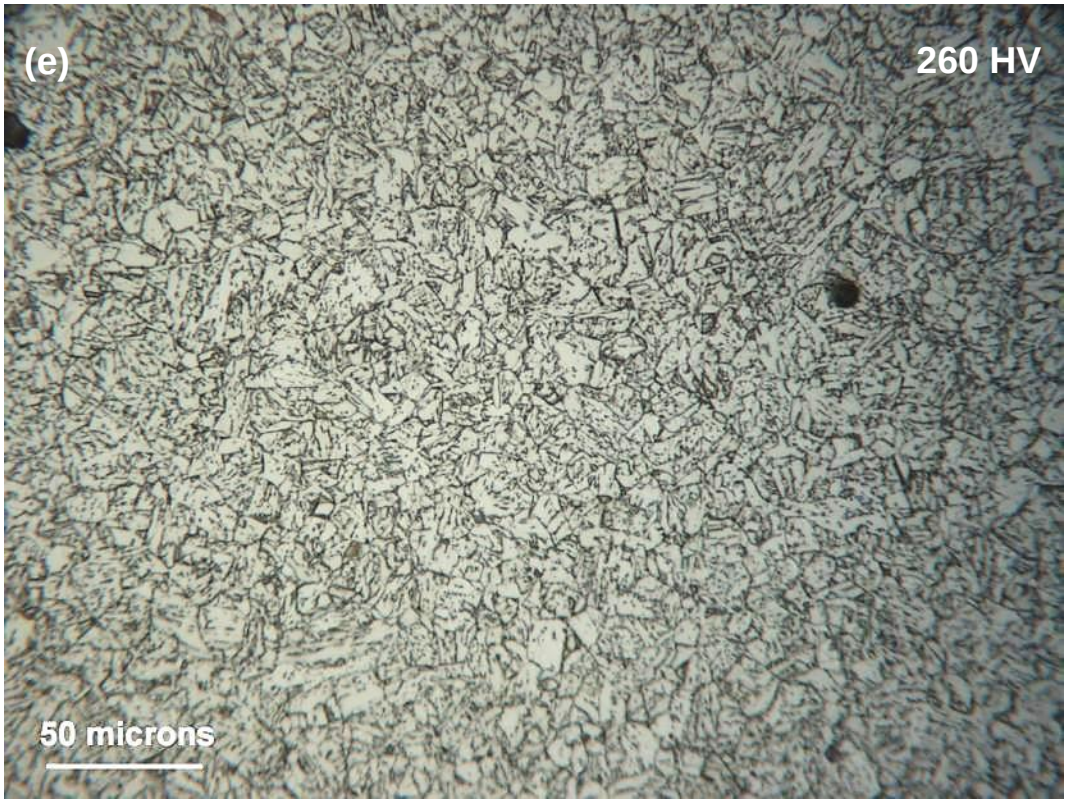
(e)
260 HV
50 microns

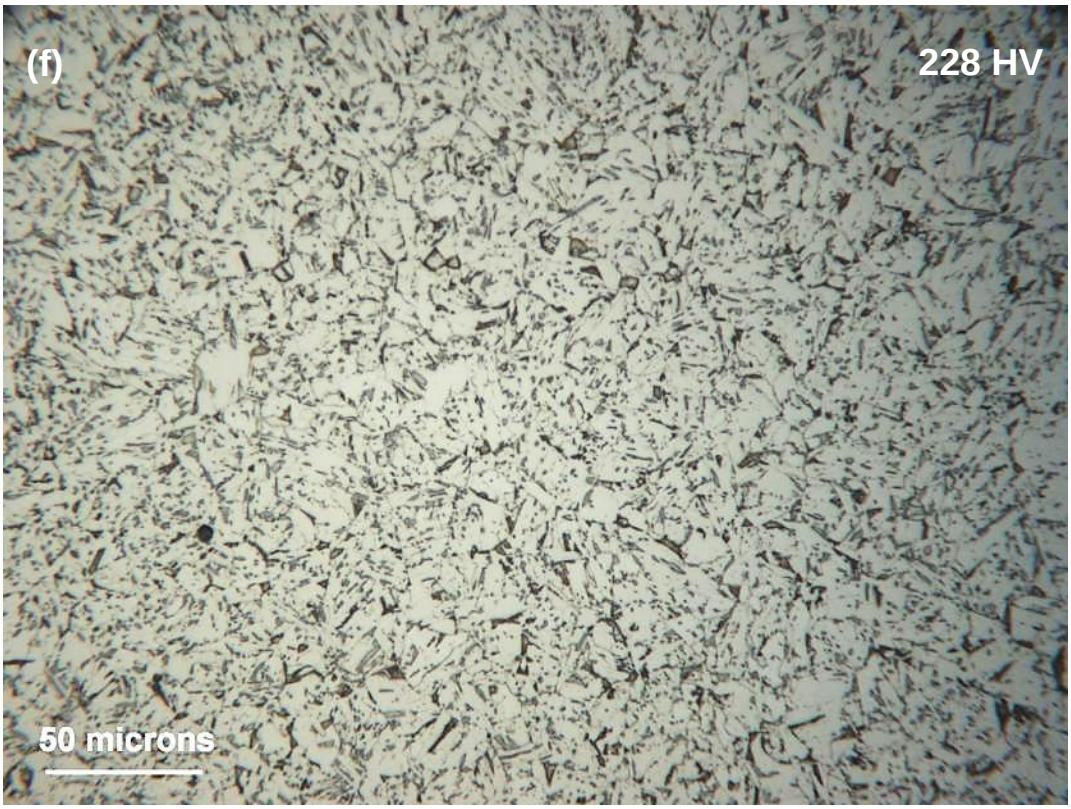
(f)
228 HV
50 microns

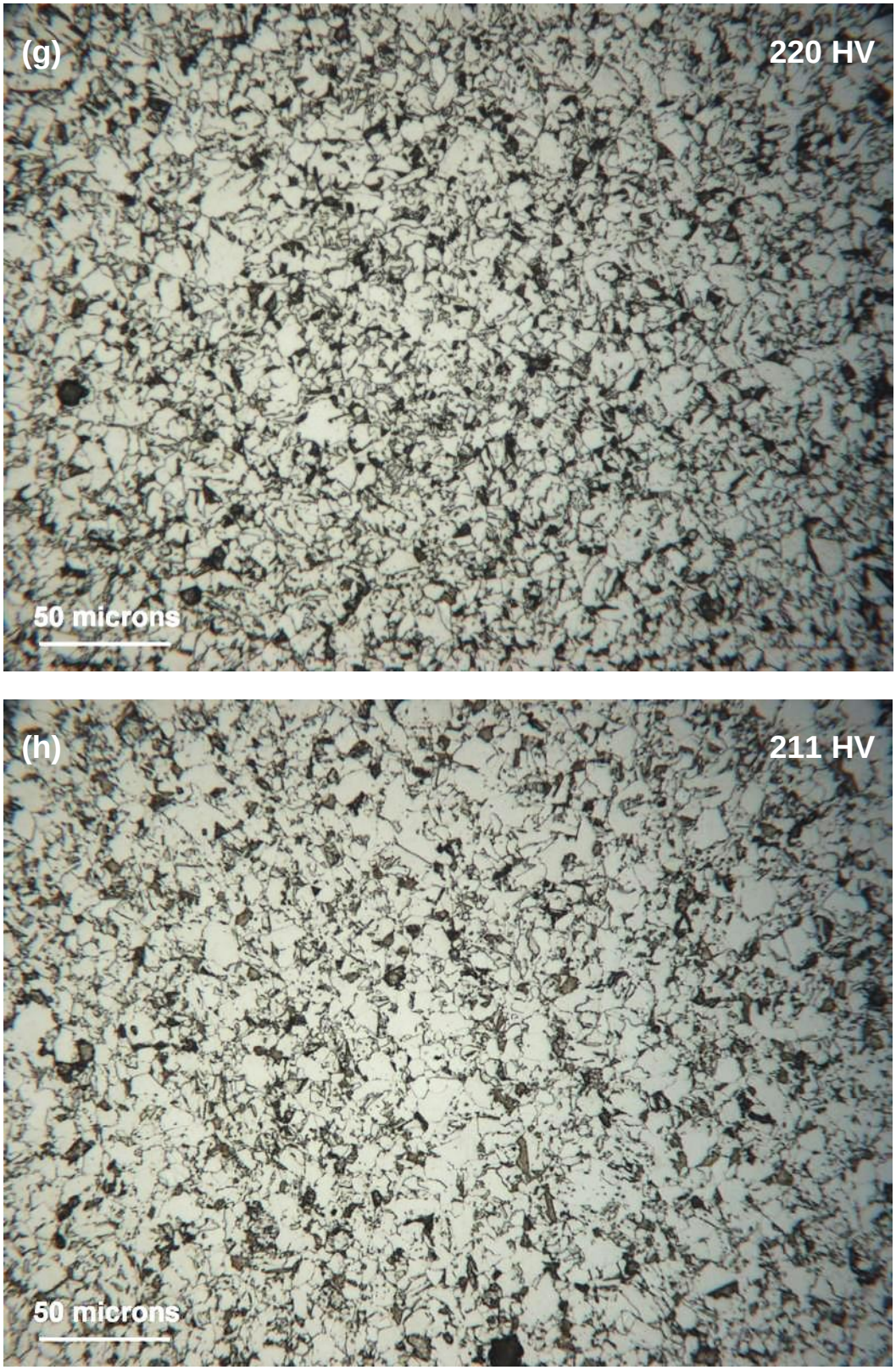

Figure 6-19 Optical micrographs of X100 steel after dilatometric cycles, cooled at $t_{8/5}$ of (a) 5.34 s, (b) 6.29 s, (c) 15 s, (d) 25 s, (e) 50 s, (f) 250 s, (g) 600 s, (h) 1000 s, and their respective hardness HV0.5

6.2.4.1 Comparison between cooling microstructures of different materials

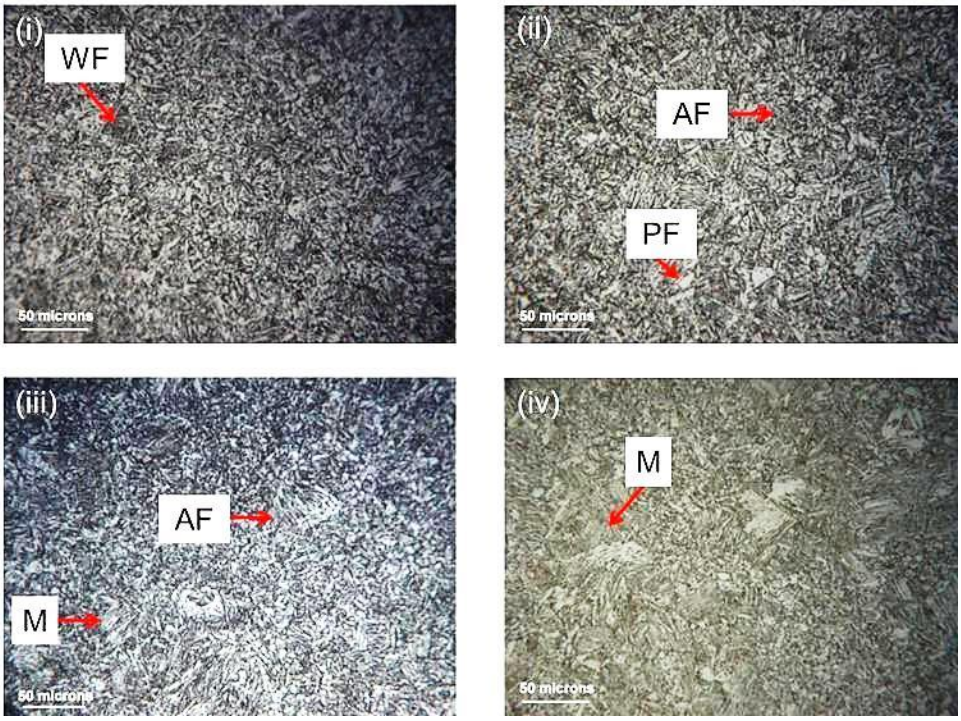

Figure 6-20 Optical micrographs of fast cooling rates (i) X65 (A) at $t_{8/5}$ 6s, (ii) X65 (B) at $t_{8/5}$ 5.34s, (iii) X70 at $t_{8/5}$ 7s and (iv) X100 at $t_{8/5}$ 5.34s

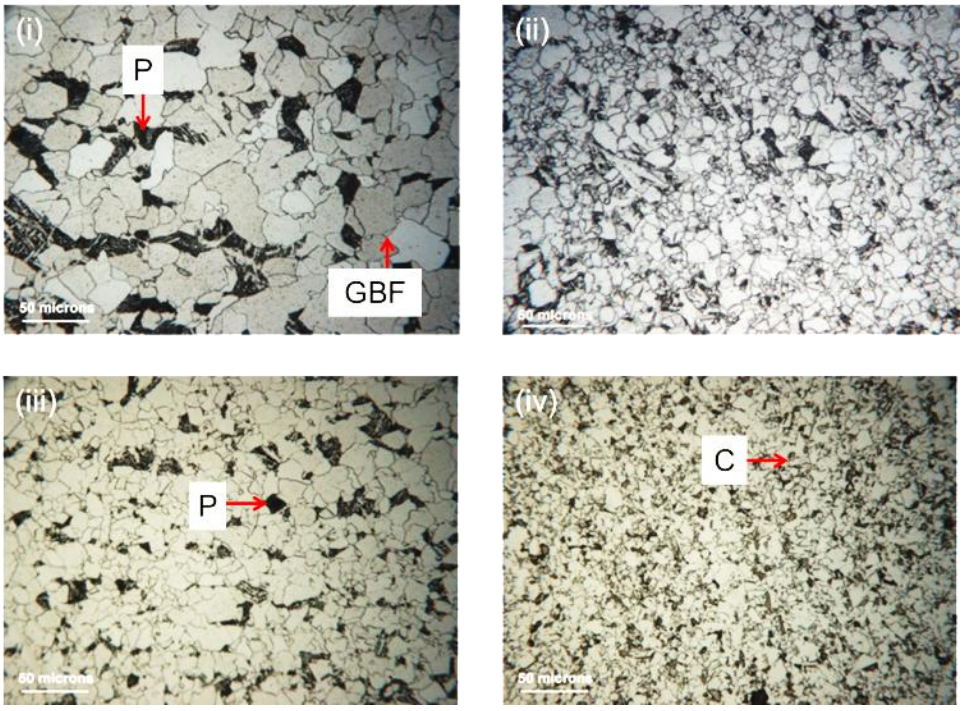

Figure 6-21 Optical micrographs of slow cooling rates (i) X65 (A), (ii) X65 (B), (iii) X70 and (iv) X100 all at $t_{8/5}$ of 1000s

6.2.4.2 Heat treated microstructures

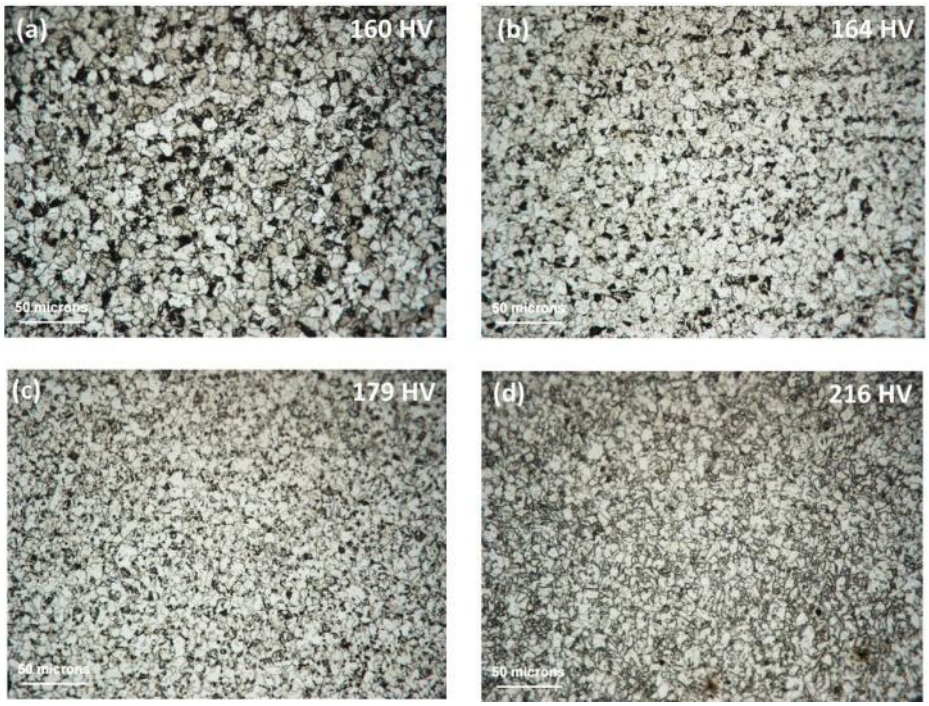

Figure 6-22 Optical micrographs of air quenched samples (a) X65 (A), (b) X65 (B), (c) X70 and (d) X100

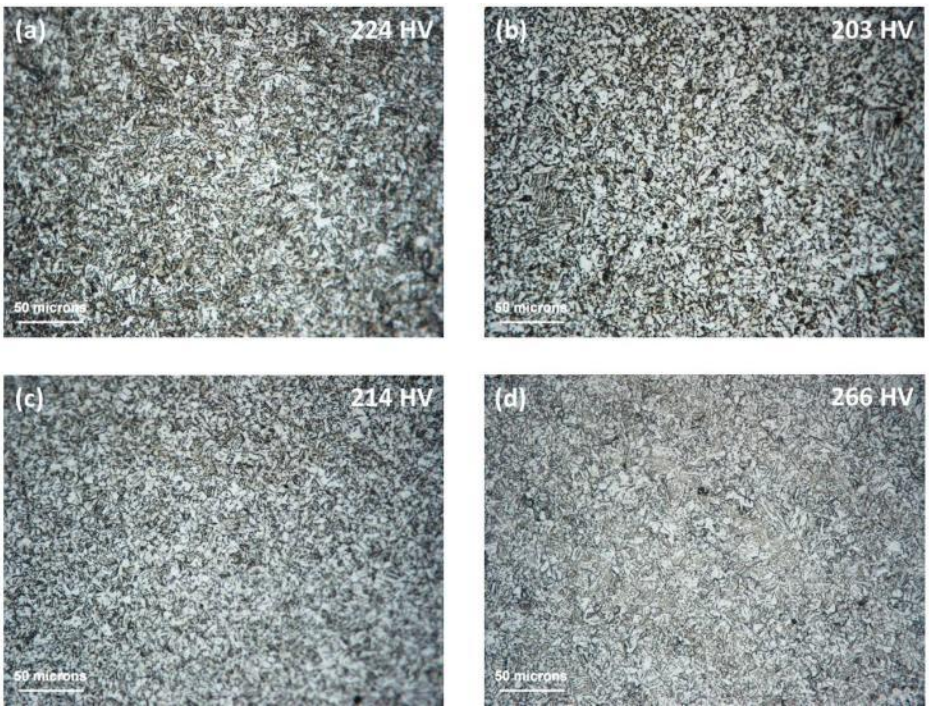

Figure 6-23 Optical micrographs of oil quenched samples (a) X65 (A), (b) X65 (B), (c) X70 and (d) X100

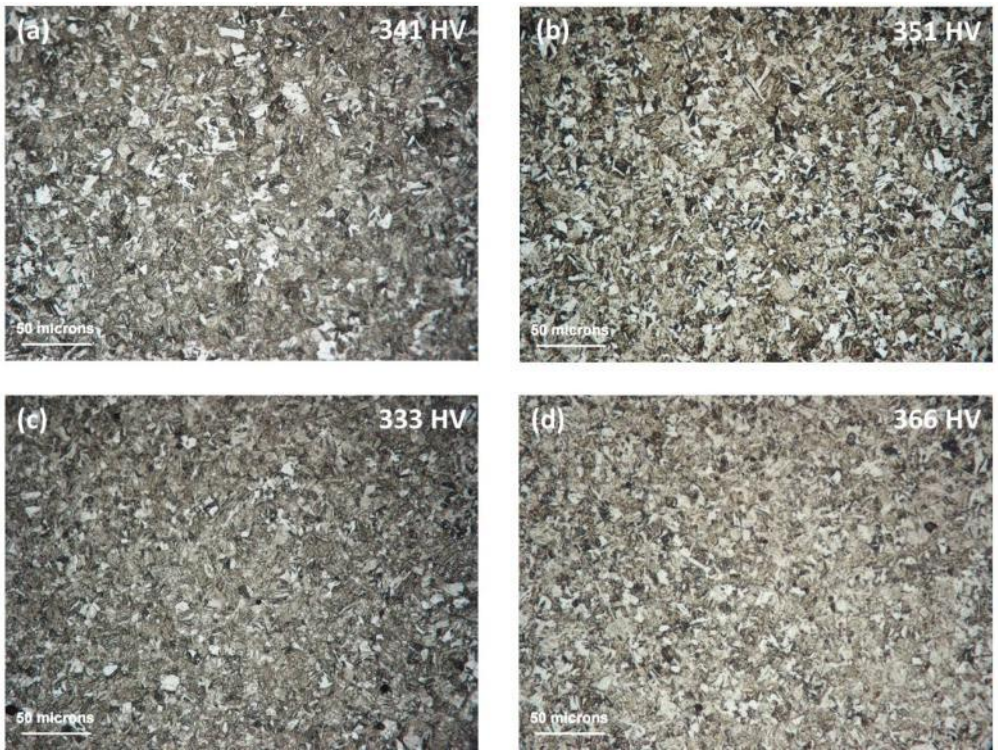

Figure 6-24 Optical micrographs of Water quenched samples (a) X65 (A), (b) X65 (B), (c) X70 and (d) X100

6.2.5 Hardness versus $t_{8/5}$

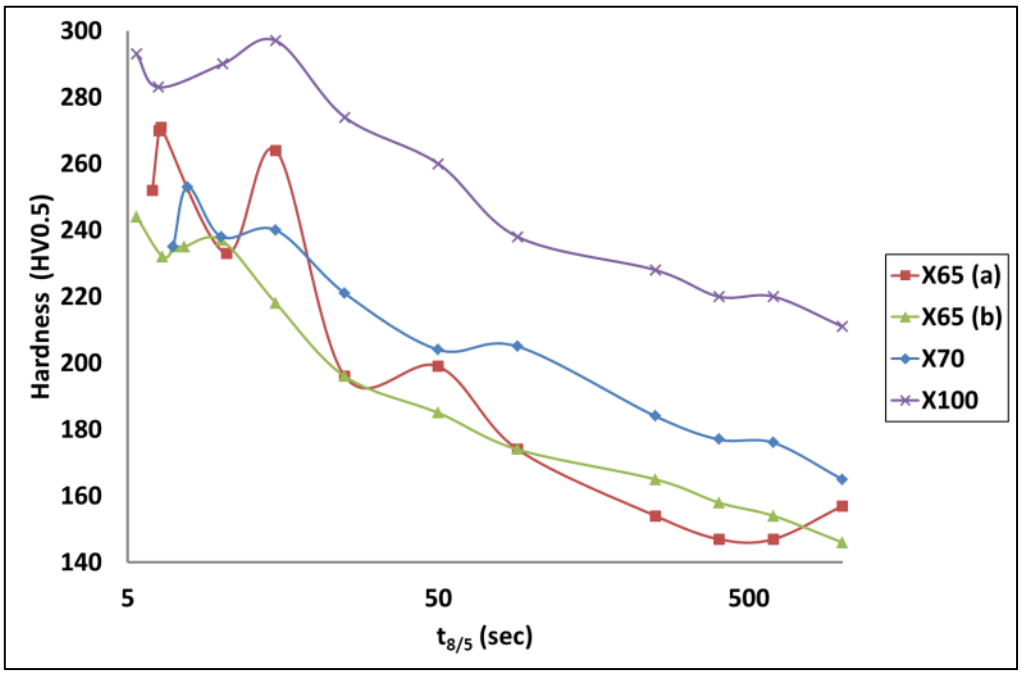

Figure 6-25 Hardness values against log of $t_{8/5}$

6.3 **Submerged arc welding**

These experiments were designed to capture the true welding thermal cycles of the HAZ. The first were the beads on plate (BOP) welds given in section 6.3.1. After acquiring the knowledge of thermocouple placements and other data related processes, full welds were made, using narrow groove submerged arc welding as given in sections 6.3.2.

6.3.1 Bead on plate (BOP) welds

The bead on plate welds were made as trials, so as to get used to the equipment's and to generate the initial thermal cycles. Four welds were made with thermocouples attached as explained earlier. Representation of the macros and micrographs, hardness traverses and thermal cycles are presented below.

6.3.1.1 Macrographs

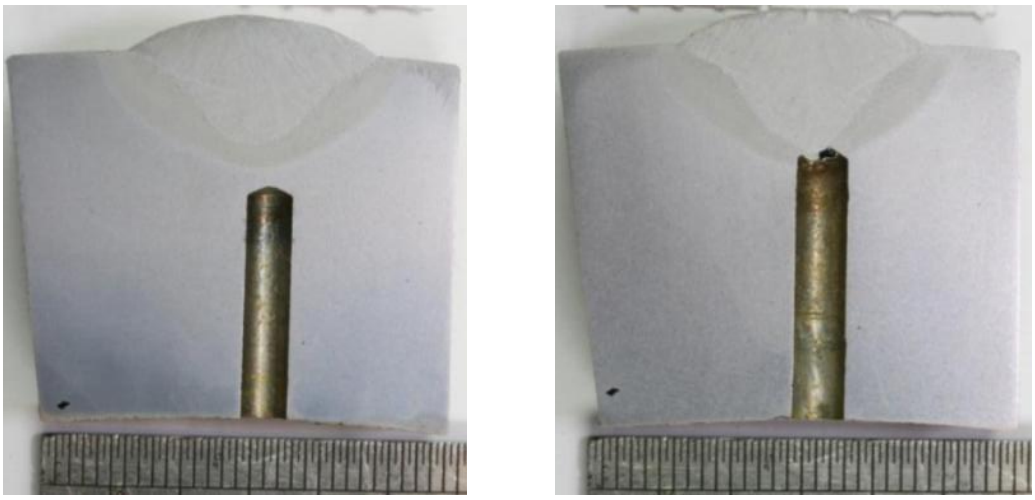

Figure 6-26 Weld 1 BOP macrographs

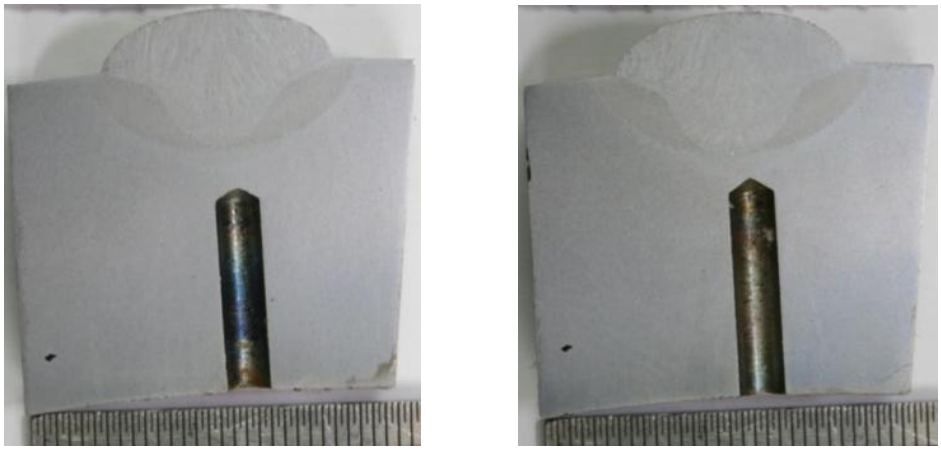

Figure 6-27 Weld 2 BOP macrographs

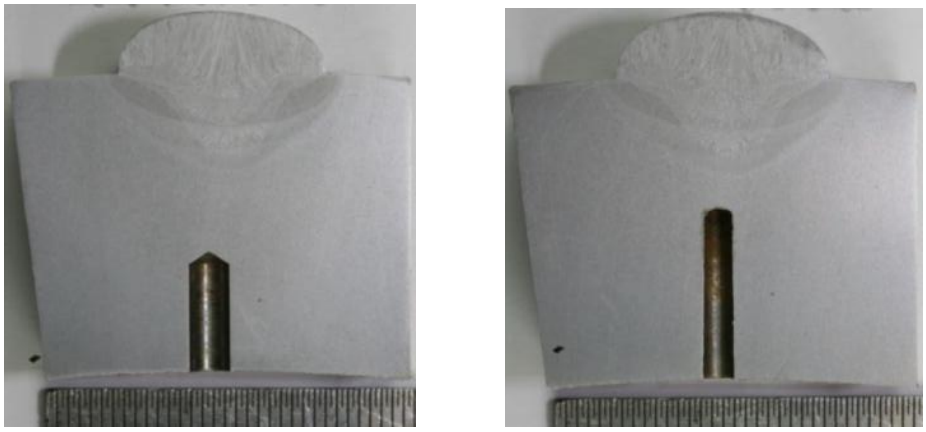

Figure 6-28 Weld 3 BOP macrographs

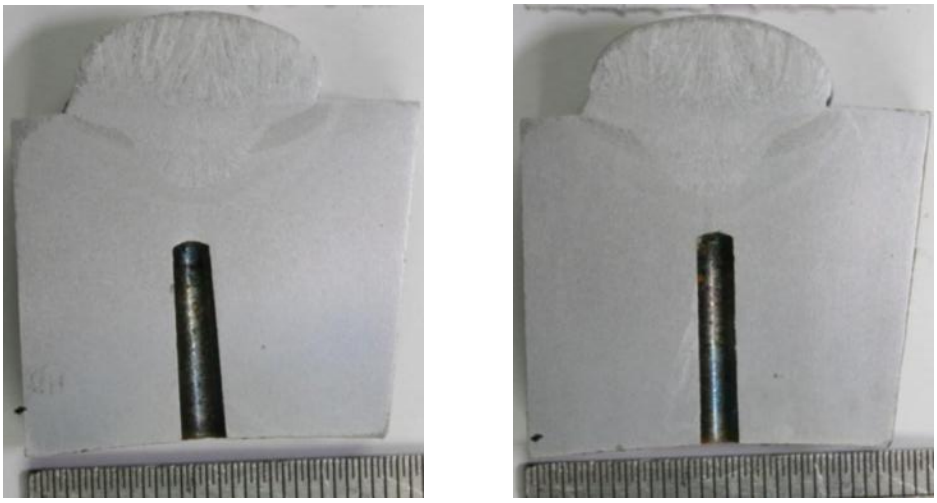

Figure 6-29 Weld 4 BOP macrographs

Table 6-3 Heat input for the BOP welds on X65 (A)

WELDS	PASSES	HEAT INPUT (kJ/mm)
Weld 1	1	1.66
Weld 2	1	1.82
	2	1.76
Weld 3	1	1.68
	2	1.73
	3	1.58
Weld 4	1	1.83
	2	1.76
	3	1.67
	4	1.65

6.3.1.2 Micrographs

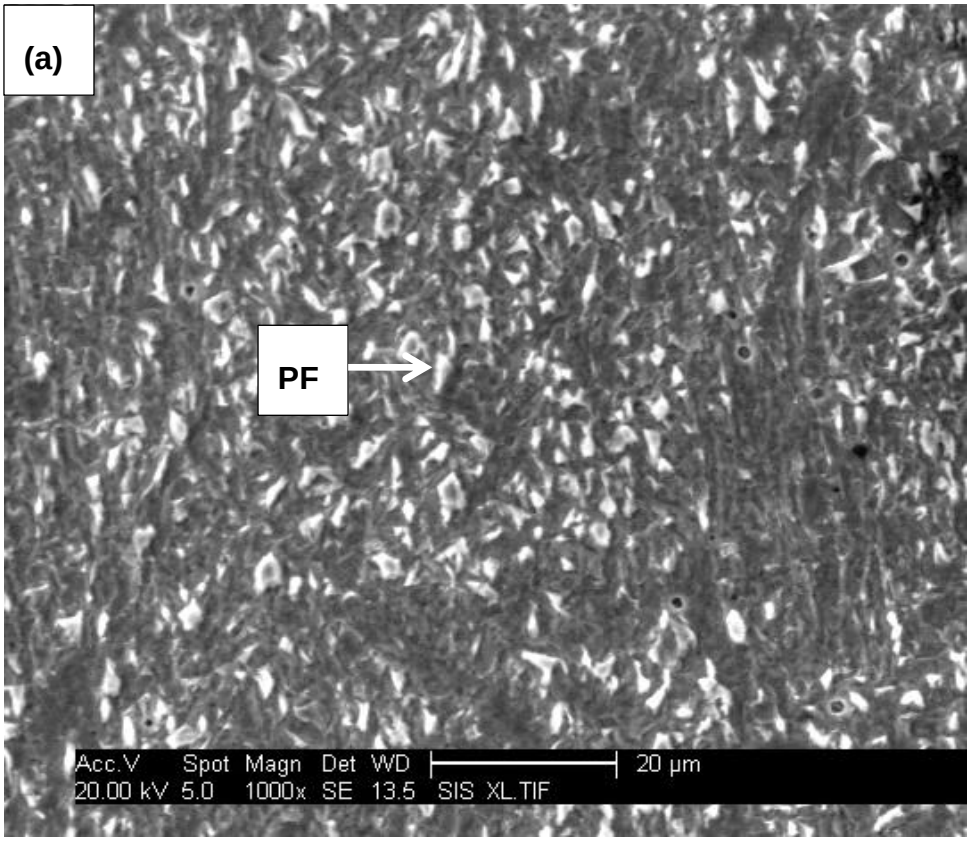

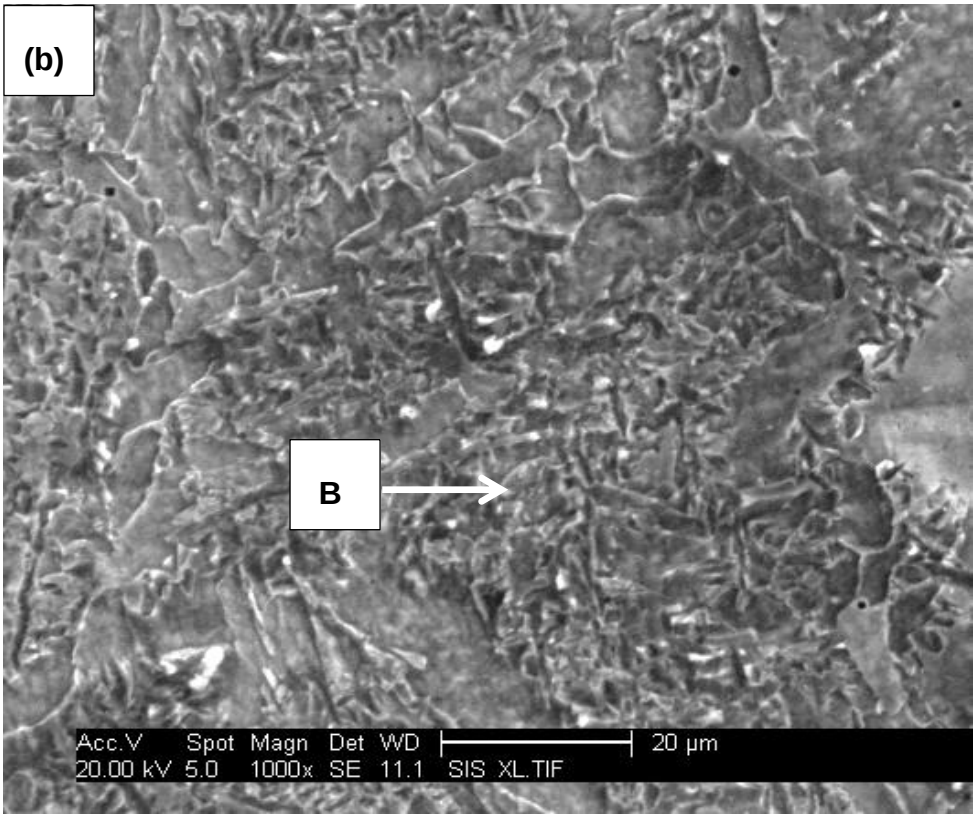

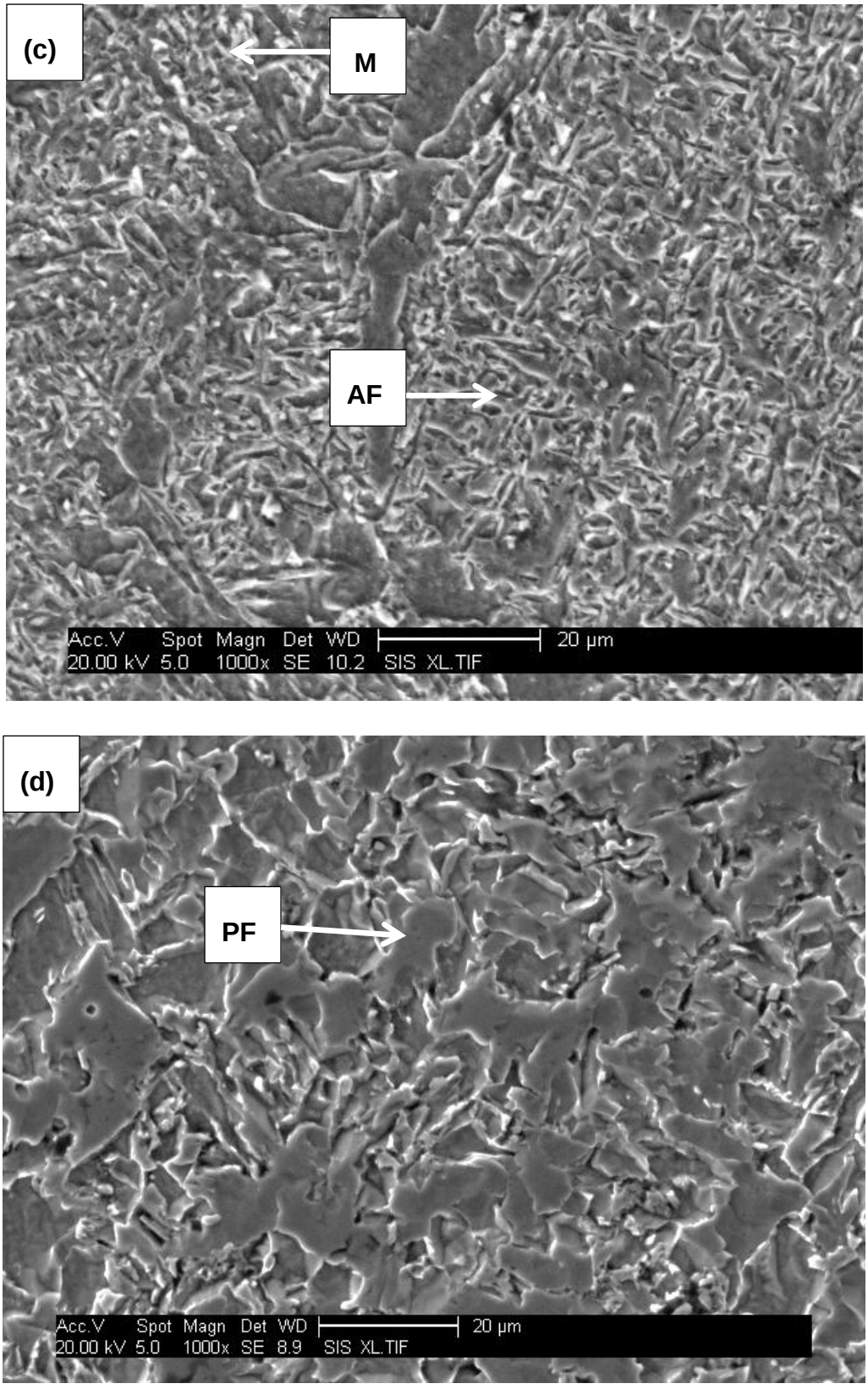

Figure 6-30 SEM micrographs of the weld metal for (a) Weld 1, (b) Weld 2, (c) Weld 3 and (d) Weld 4

6.3.1.3 Hardness

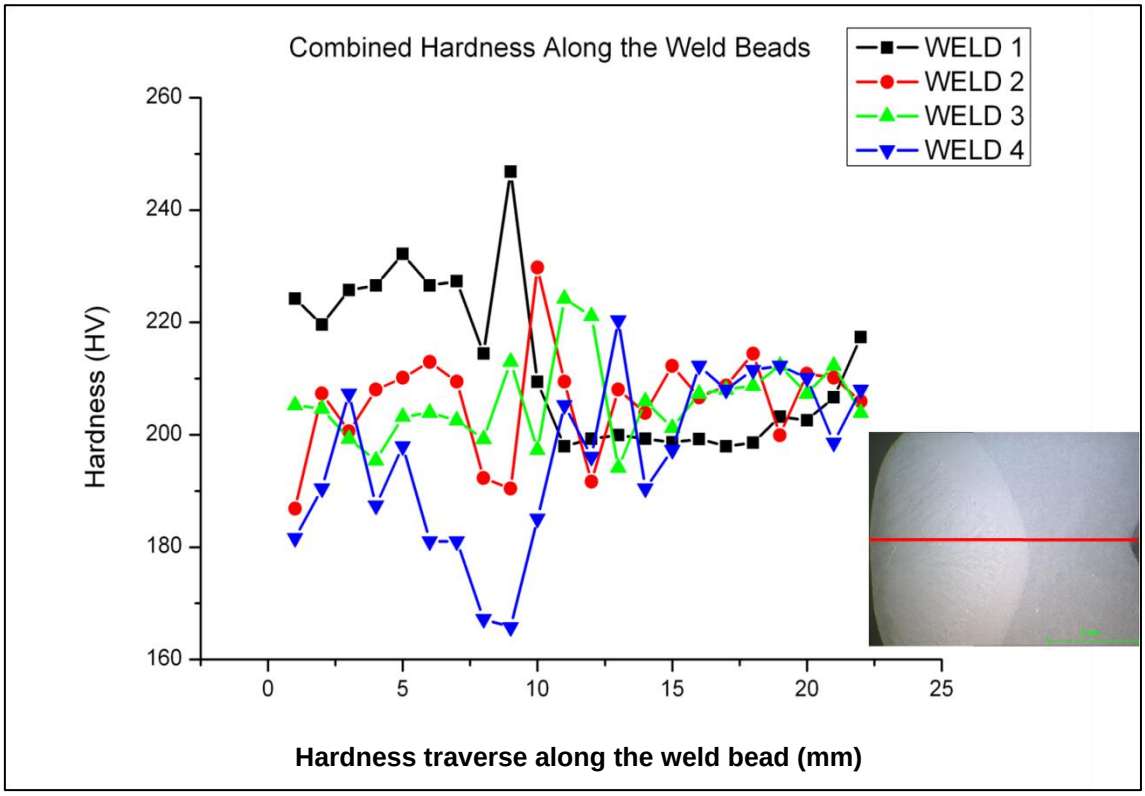

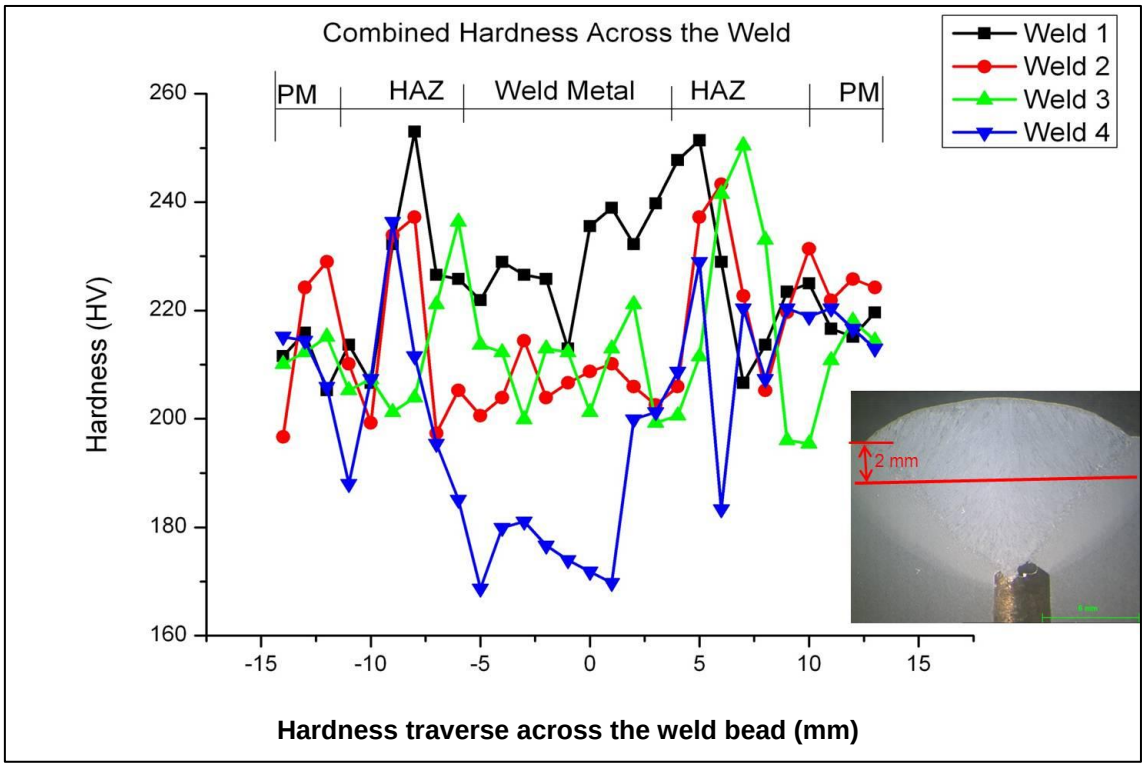

Figure 6-31 Hardness traverses along and across the weld beads

6.3.1.4 Thermal cycles

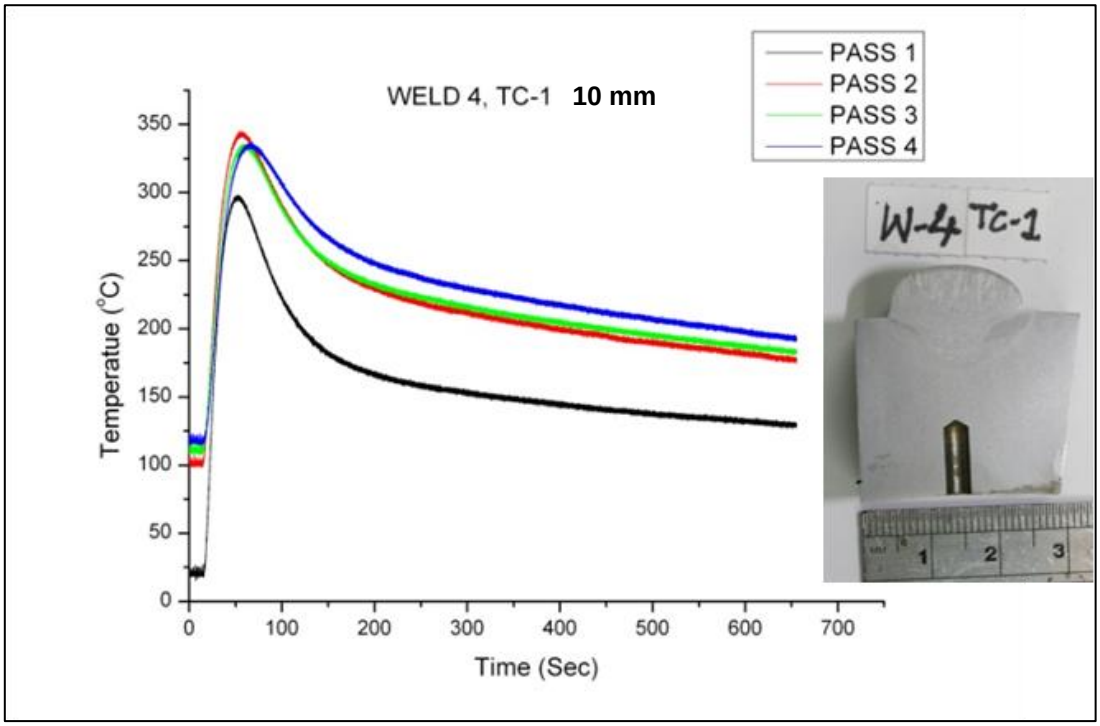

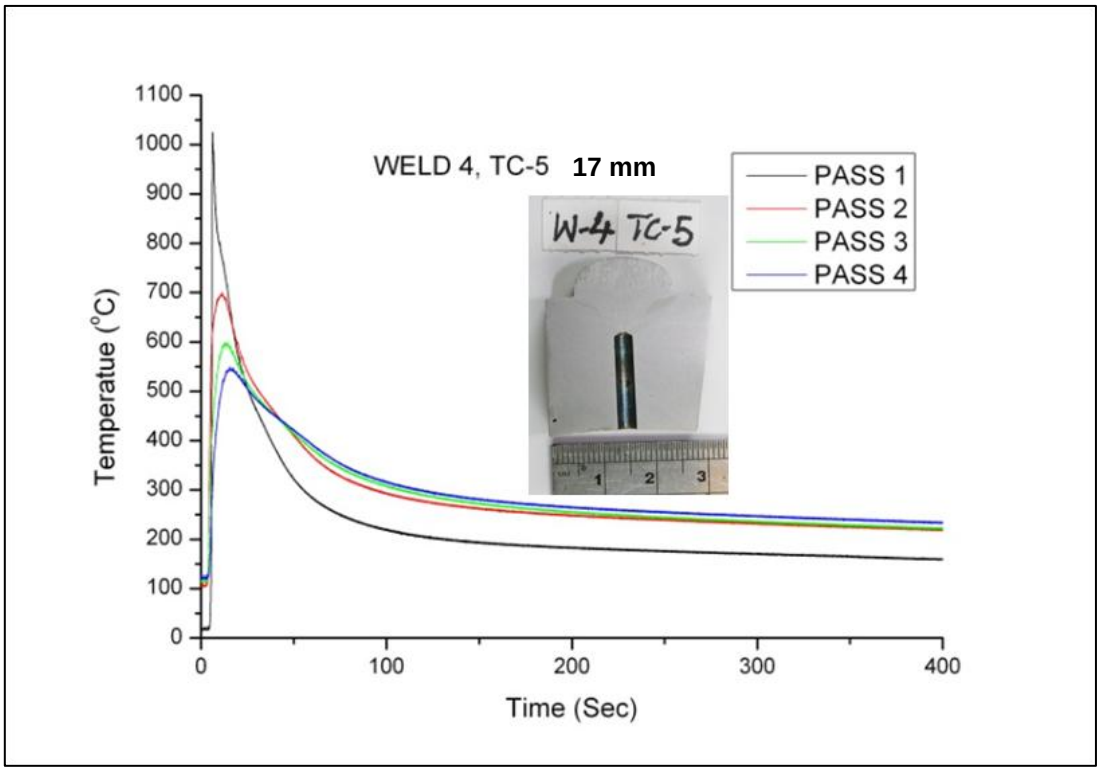

Figure 6-32 Thermal cycles of the BOP welds for TC-1 at 10 mm and TC-5 at 17 mm from the bottom

6.3.2 Full welds (Submerged arc welds)

The full welds (submerged arc welds) were made on X65 (A), X65 (B) and X70 pipeline steels. Three instrumented welds were made on each material, and named weld 1, weld 2 and weld 3 respectively. As explained in chapter five, thermocouples were attached in all the welds to record the thermal cycles, and the welding parameters were also recorded.

These welds were made so as to capture the true thermal cycles of the HAZ. Also to have a very good understanding of multi pass welds thermal cycles. CTOD tests were carried out to check for local brittle zones. Finally information obtained from these thermal cycles was simulated on charpy impact samples for further analysis.

Selected data from the welds will be presented here. This will include; macrographs and micrographs, hardness traverses, thermal cycles. CTOD results and their representative macrographs will be presented, hardness maps of the notch area will also be presented.

6.3.2.1 Macrographs

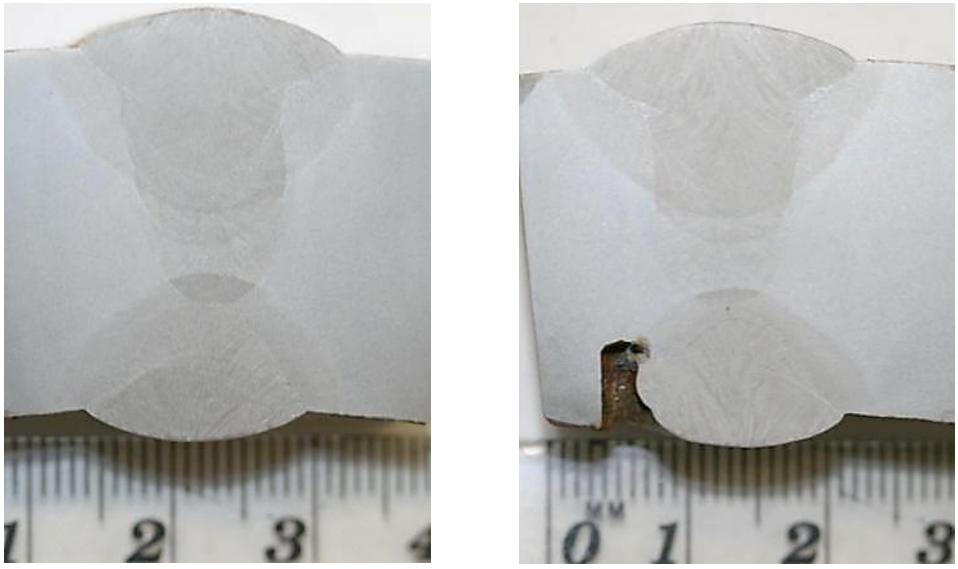

Figure 6-33 Macrographs of X65 (A) weld 1

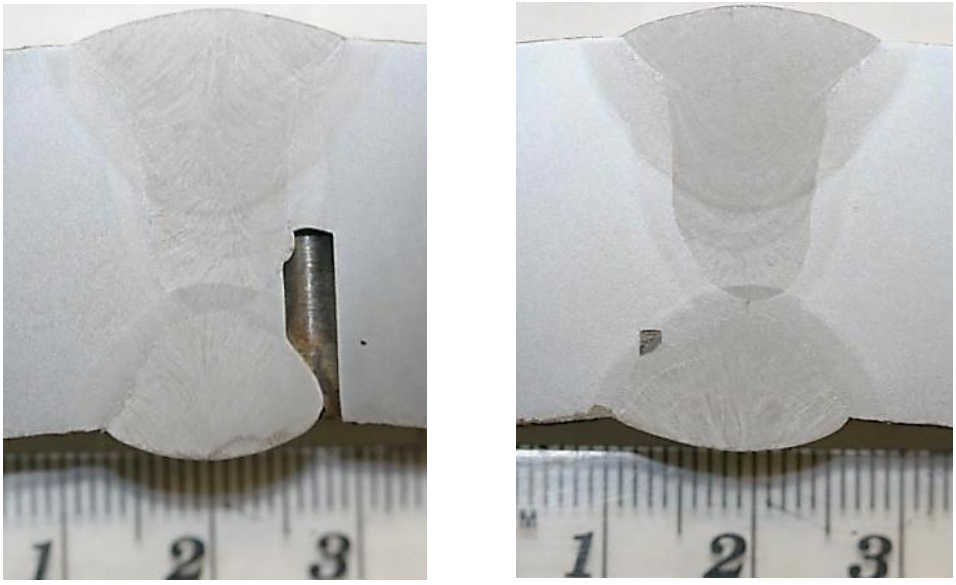

Figure 6-34 Macrographs of X65 (A) weld 3

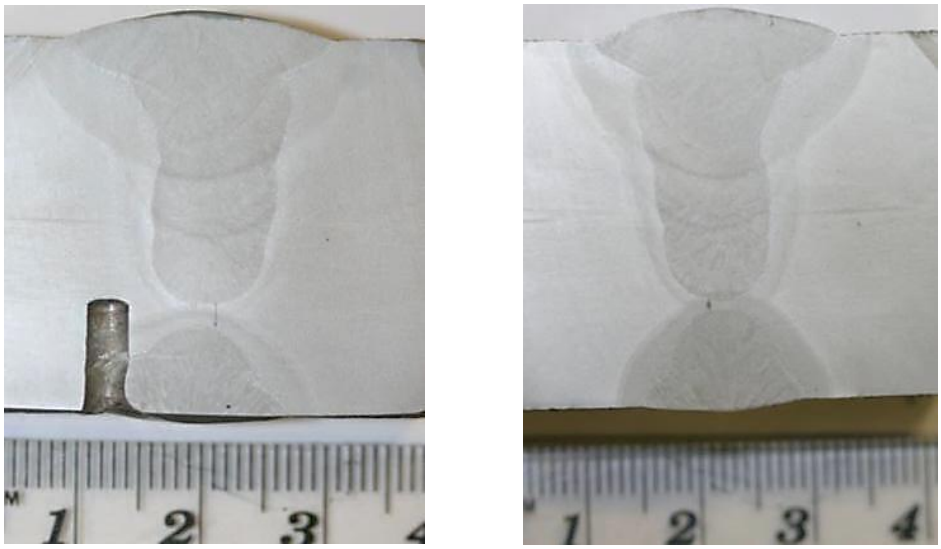

Figure 6-35 Macrographs of X65 (B) weld 1

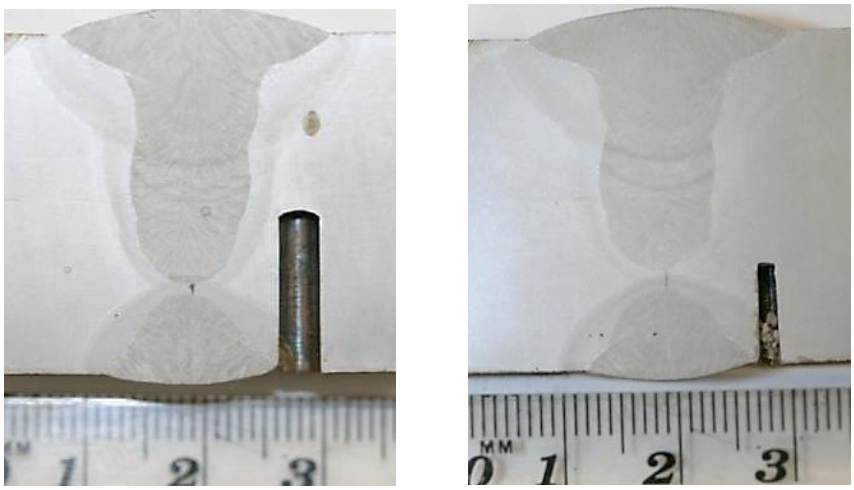

Figure 6-36 Macrographs of X65 (B) weld 3

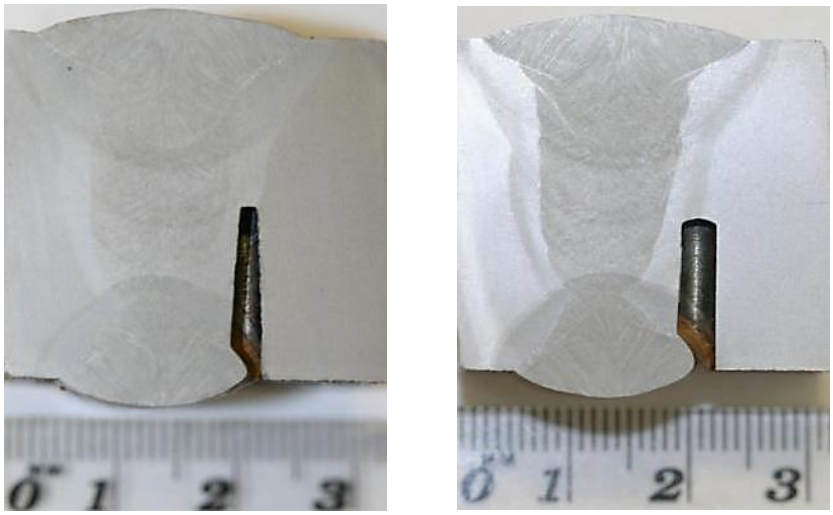

Figure 6-37 Macrograph of X70 weld 2

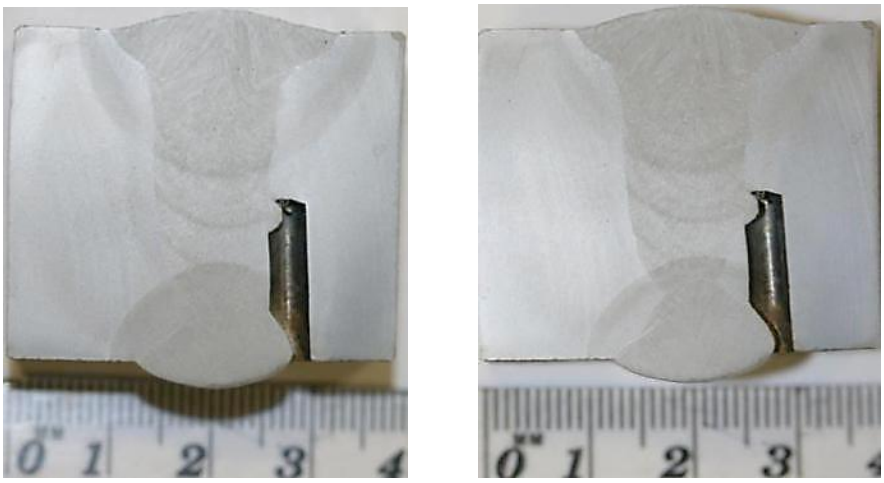

Figure 6-38 Macrograph of X70 weld 3

6.3.2.2 Microstructures of the full welds

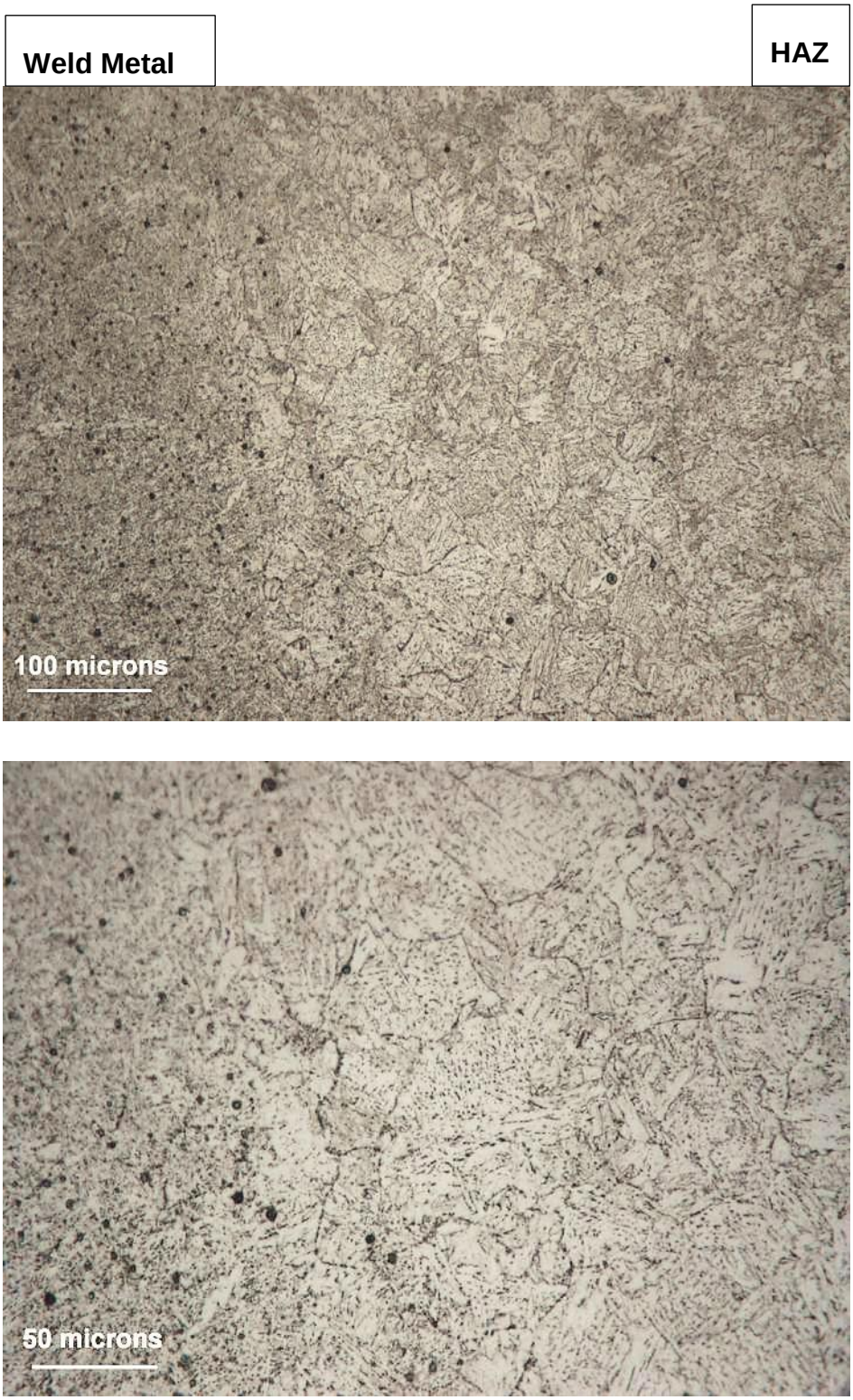

Figure 6-39 Optical micrographs of submerged arc welded X65 (A) showing from left to right; weld metal, fusion line and HAZ (15 mm from the bottom) at different magnifications

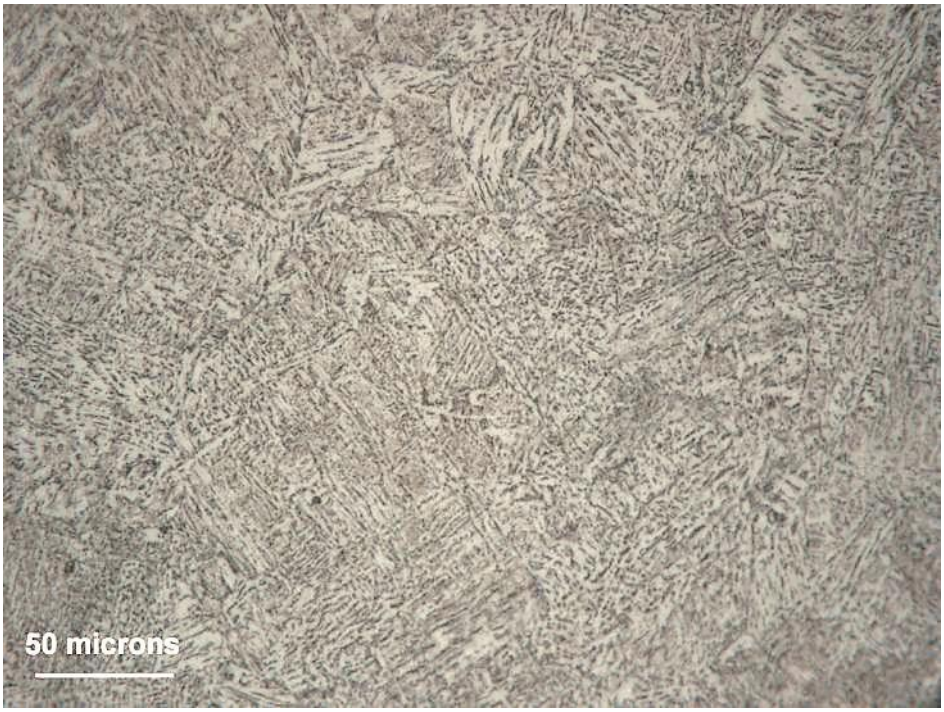

Figure 6-40 Optical micrograph of SAW X65 (A) HAZ at 10 mm from the bottom

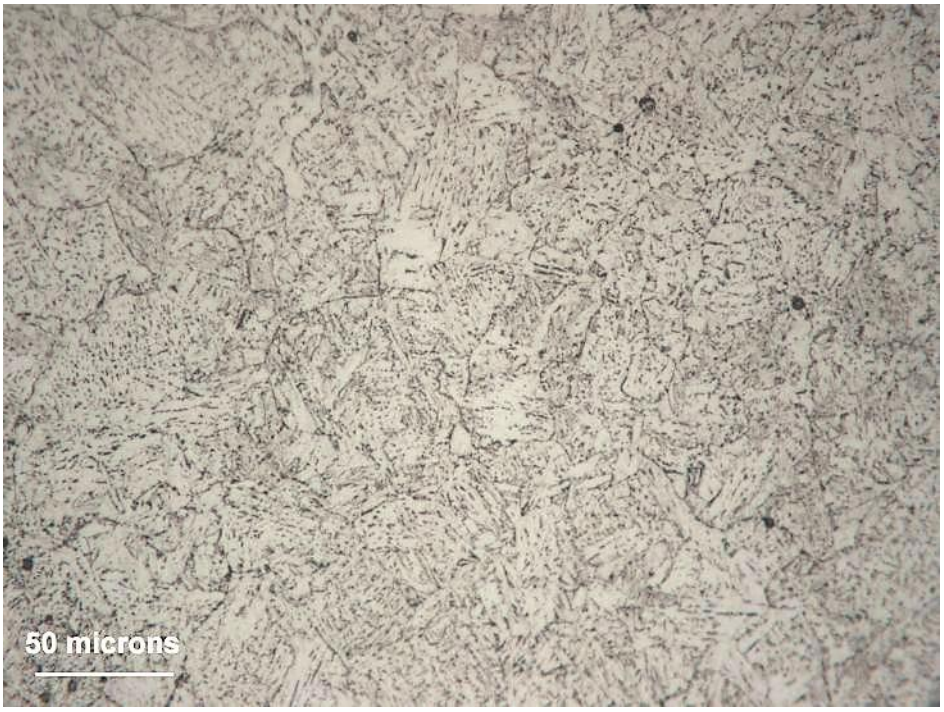

Figure 6-41 Optical micrograph of SAW X65 (A) HAZ at 15 mm from the bottom

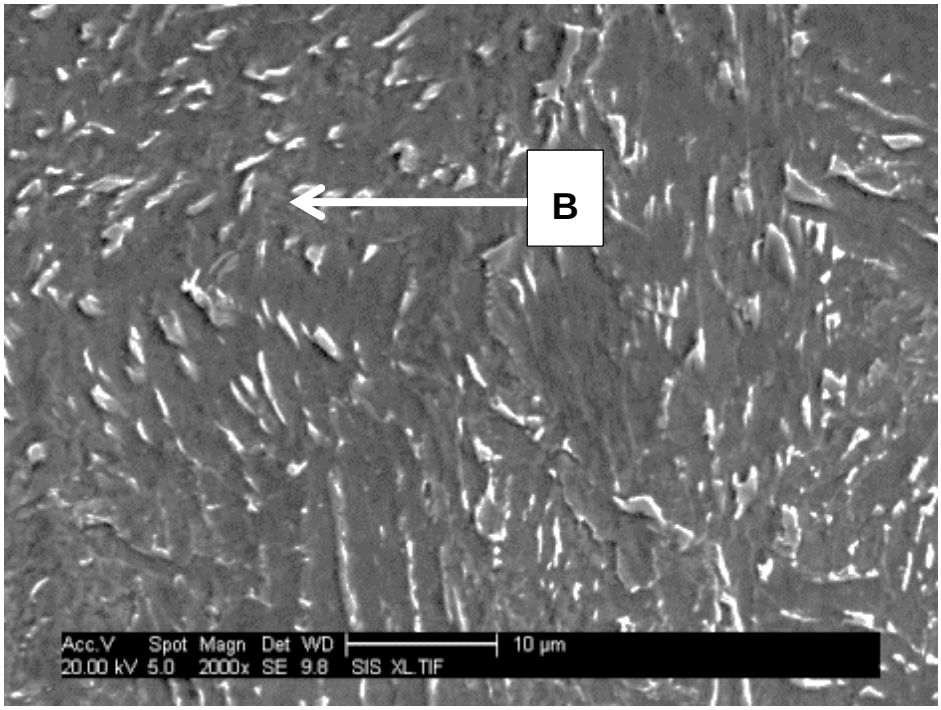

Figure 6-42 SEM micrograph of SAW X65 (A) HAZ at 10 mm from the bottom

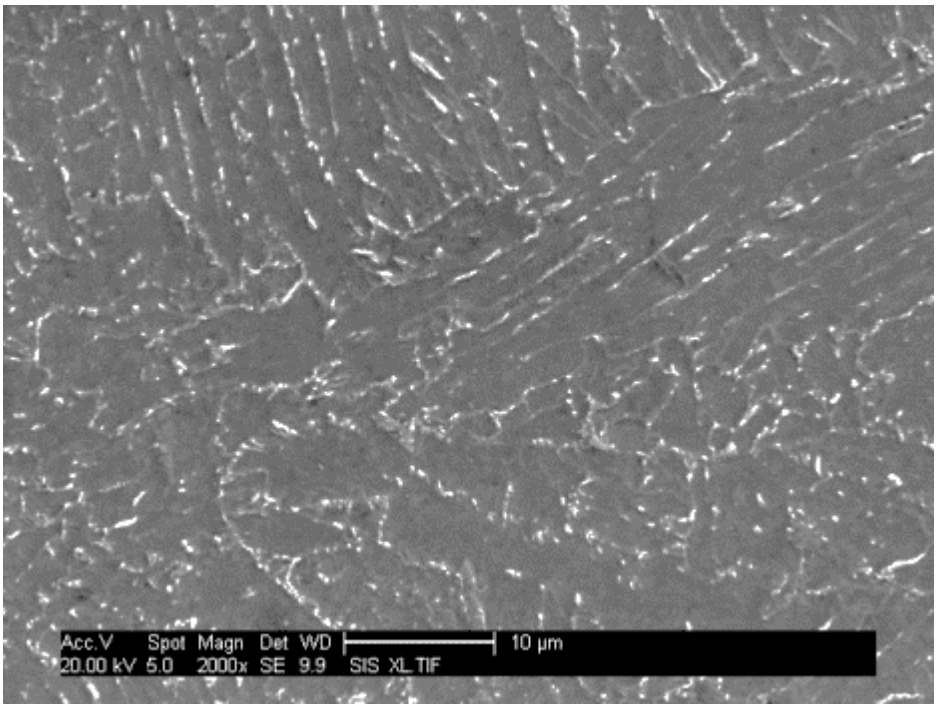

Figure 6-43 SEM micrograph of SAW X65 (A) HAZ at 15 mm from the bottom

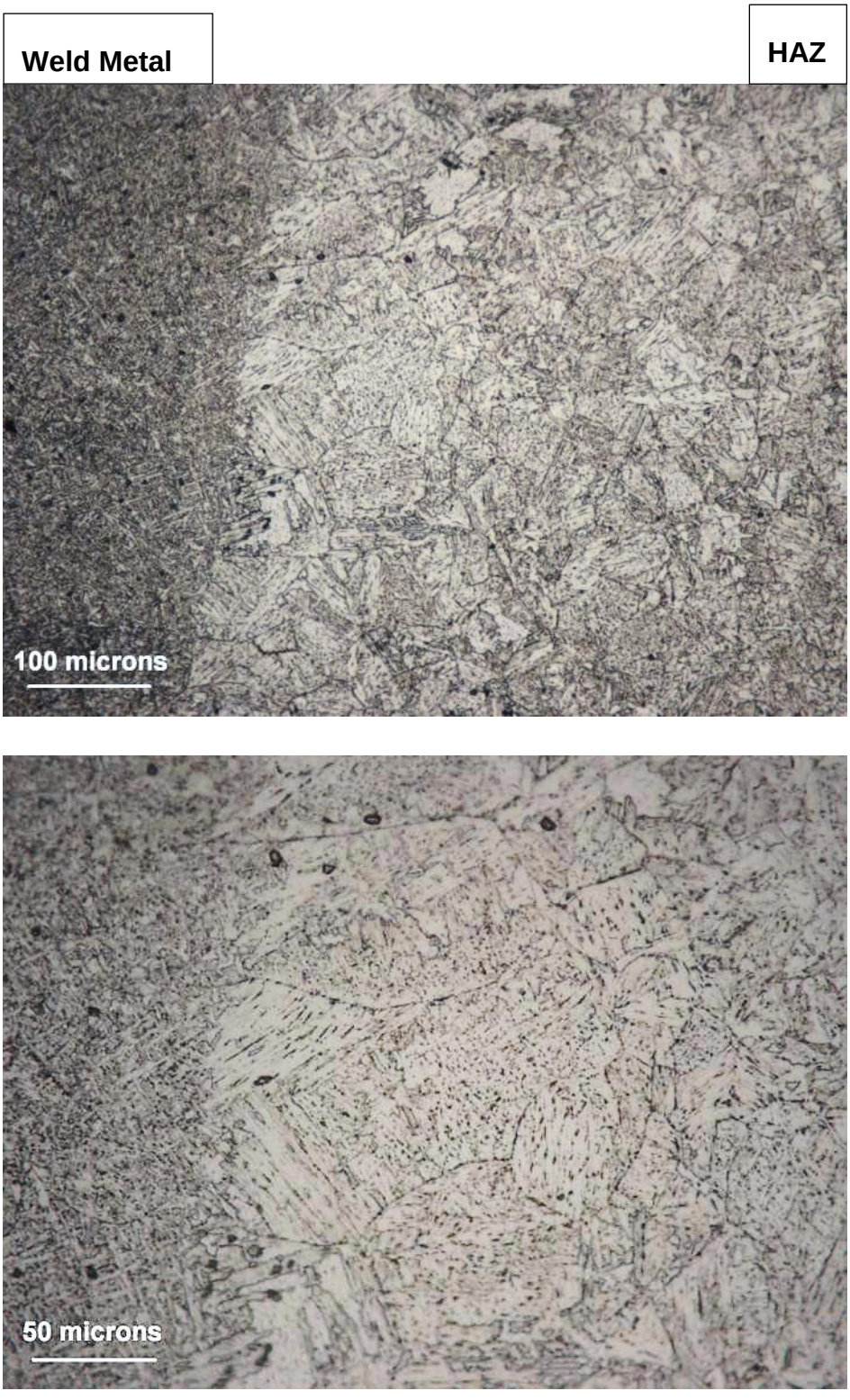

Figure 6-44 Optical micrographs of SAW X65 (B) showing from left to right; weld metal, fusion line and HAZ (15 mm from the bottom) at different magnifications

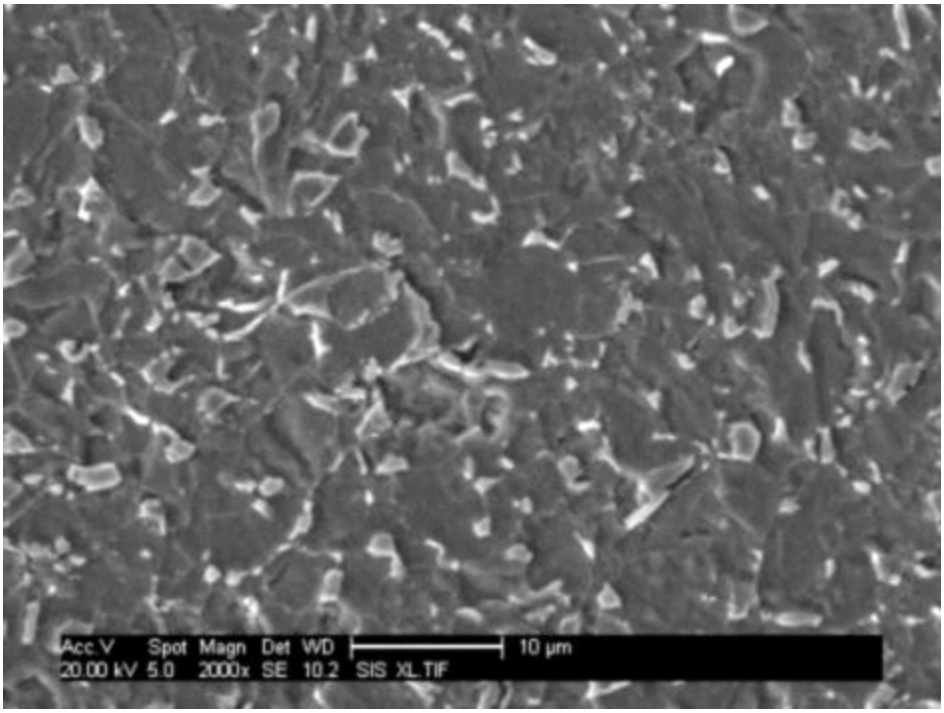

Figure 6-45 SEM micrograph of SAW X65 (B) showing the HAZ

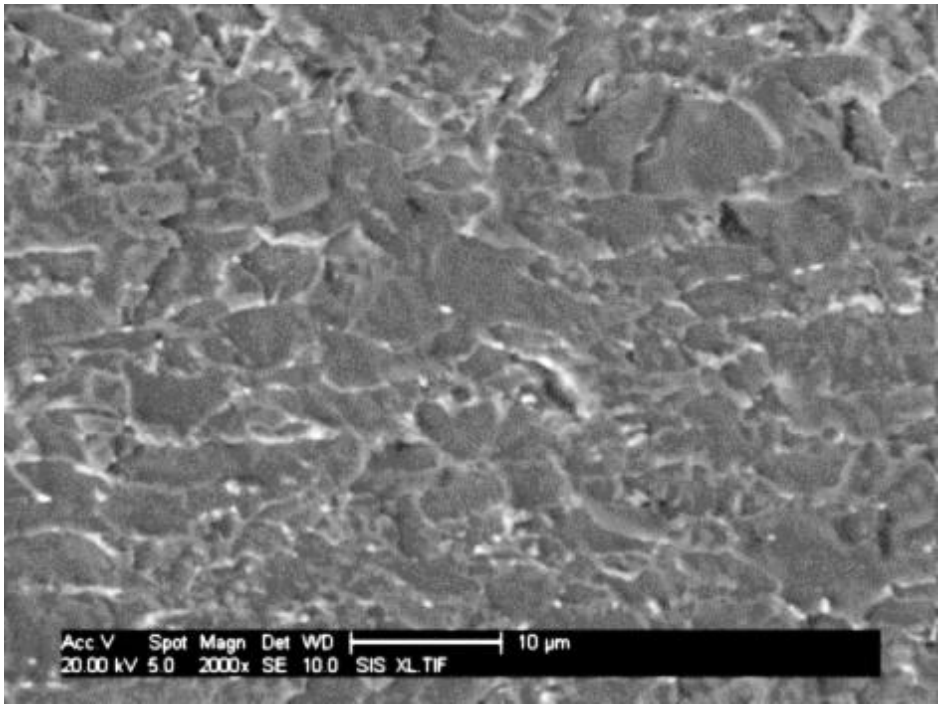

Figure 6-46 SEM micrograph of SAW X65 (B) showing the microstructure of the thermocouple position

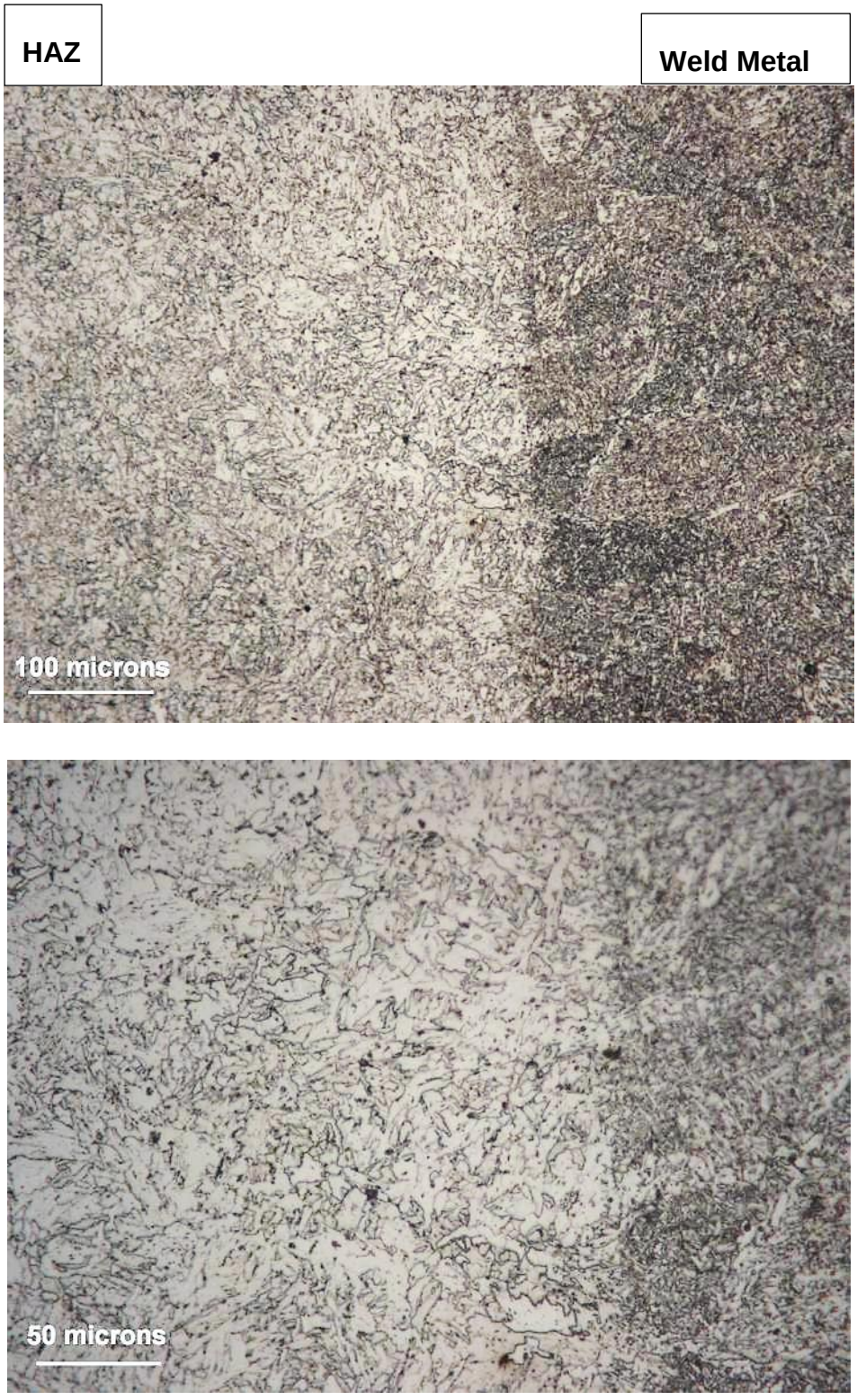

Figure 6-47 Optical micrographs of SAW X70 showing from right to left; weld metal, fusion line and HAZ (15 mm from the bottom) at different magnifications

Figure 6-48 Optical Micrograph of SAW X70 showing fusion line and HAZ at 15 mm from the bottom

Figure 6-49 Optical micrograph of SAW X70 showing the microstructure of the thermocouple position

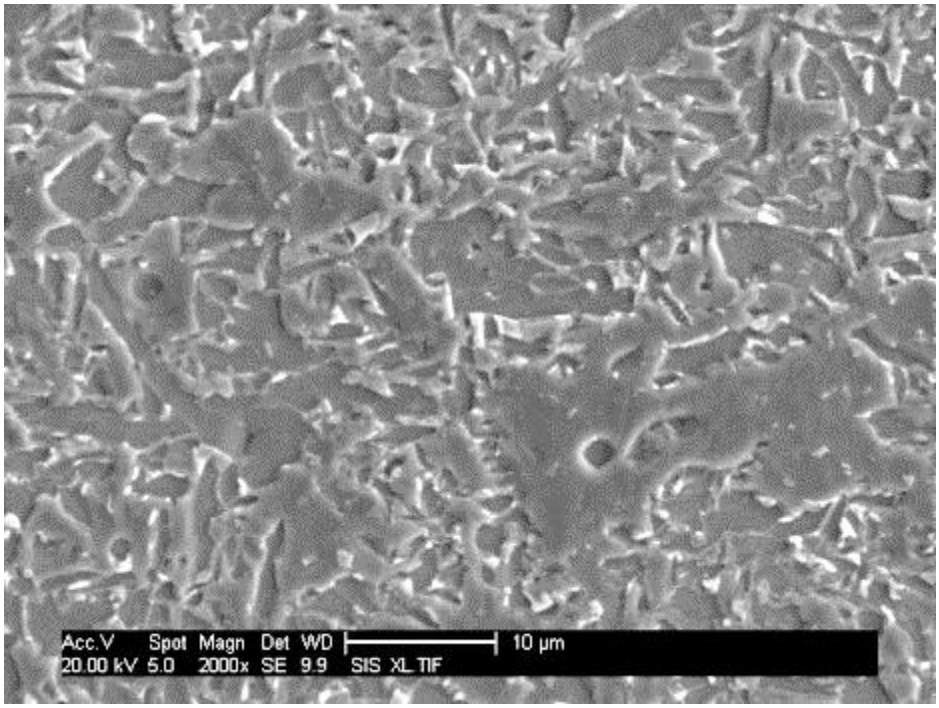

Figure 6-50 SEM micrograph of SAW X70 showing the HAZ at 15 mm from the bottom

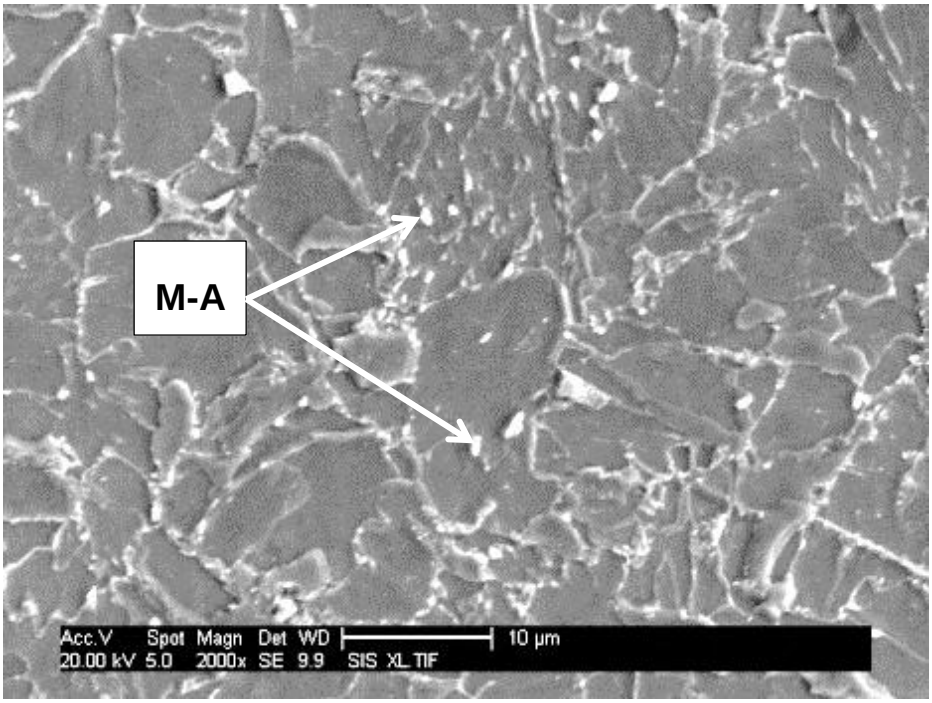

Figure 6-51 SEM micrograph of SAW X70 showing the microstructure of the thermocouple position

6.3.2.3 Comparison between nital and LePèra etchants

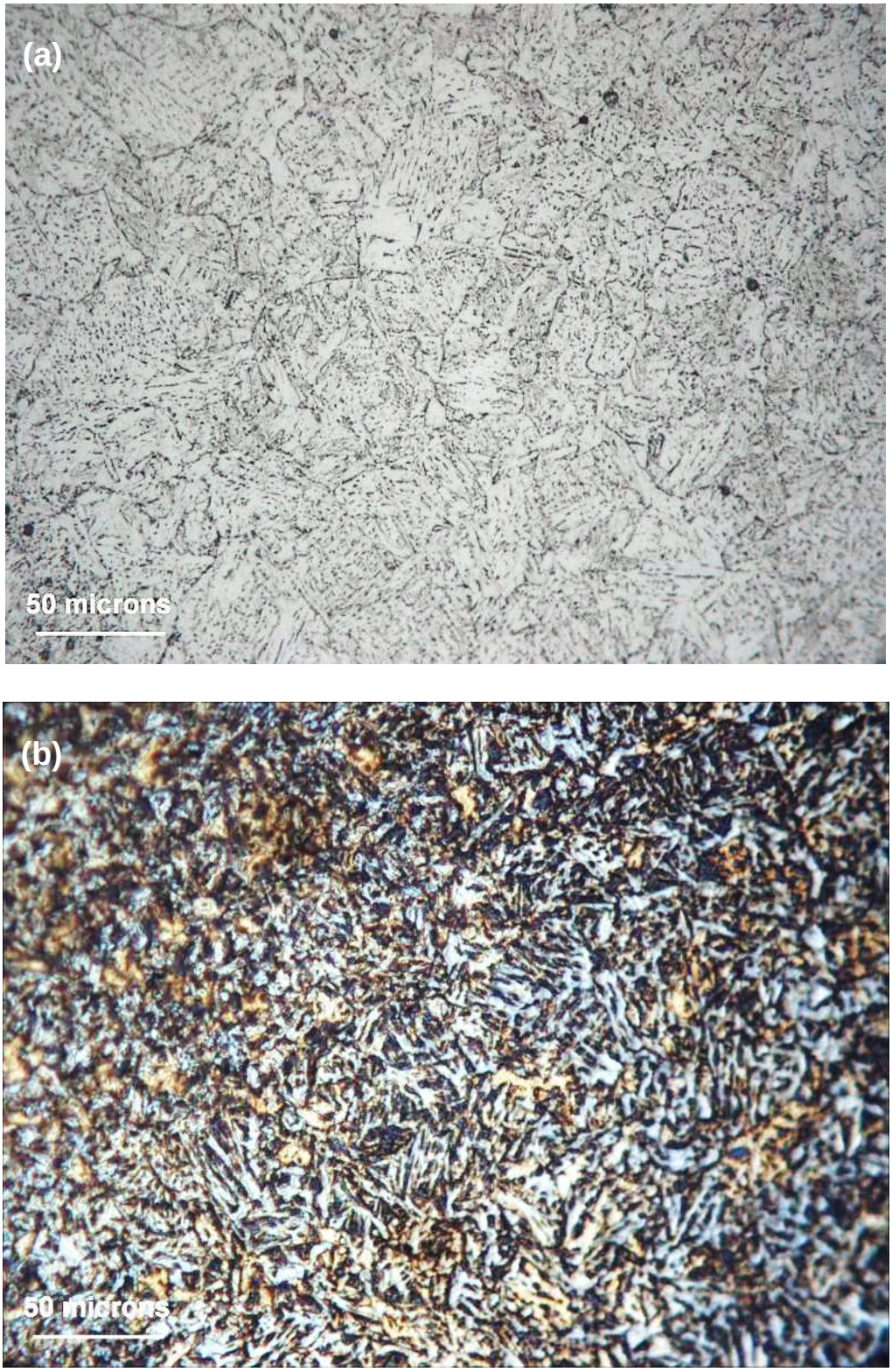

Figure 6-52 Optical micrographs of X65 (A) SAW HAZ at 15 mm from the bottom, showing (a) Nital etch and (b) LePèra etched

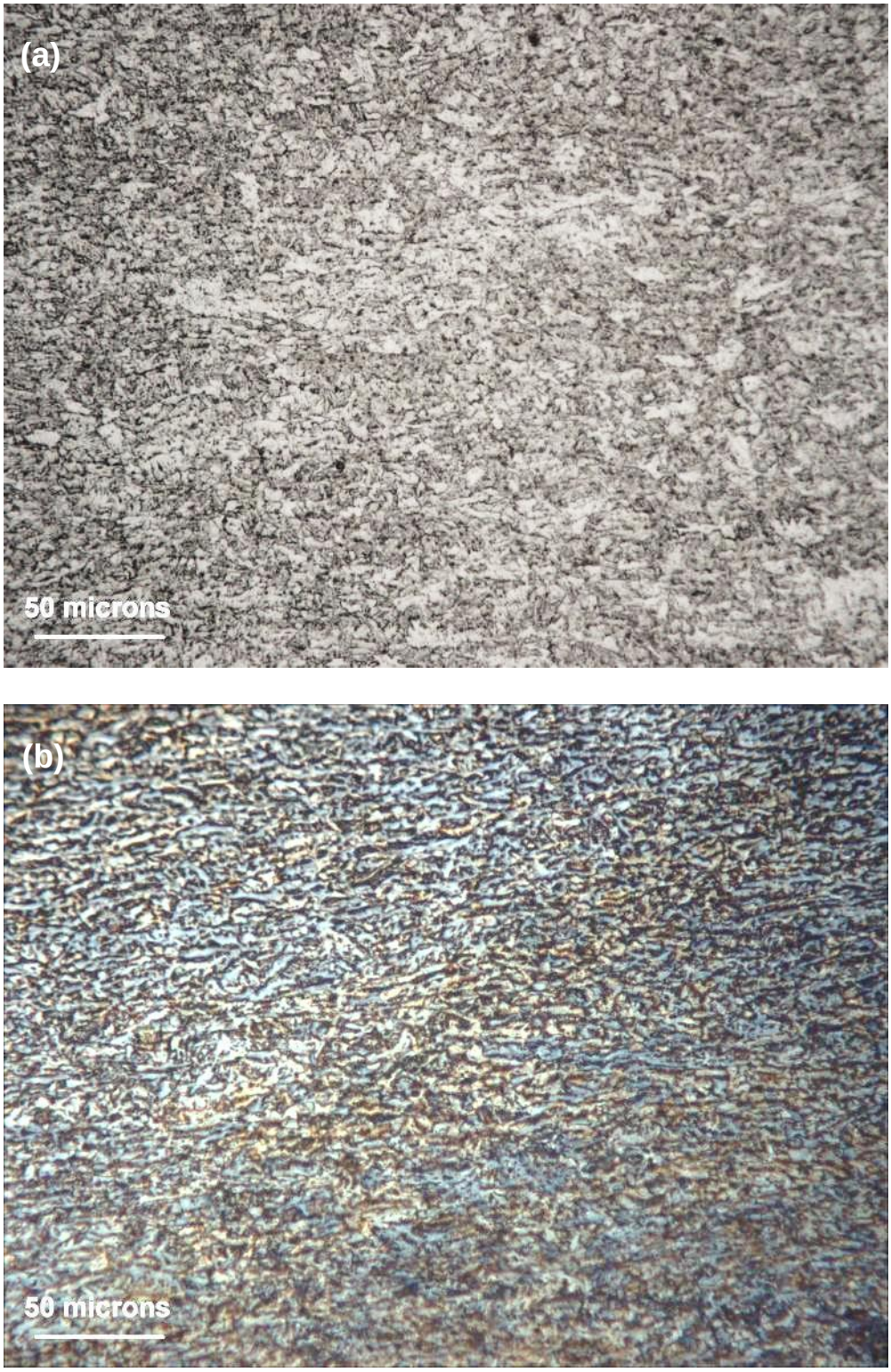

Figure 6-53 Optical micrographs of X65 (B) SAW TC area at 10 mm from the bottom, showing (a) Nital etch and (b) LePèra etched

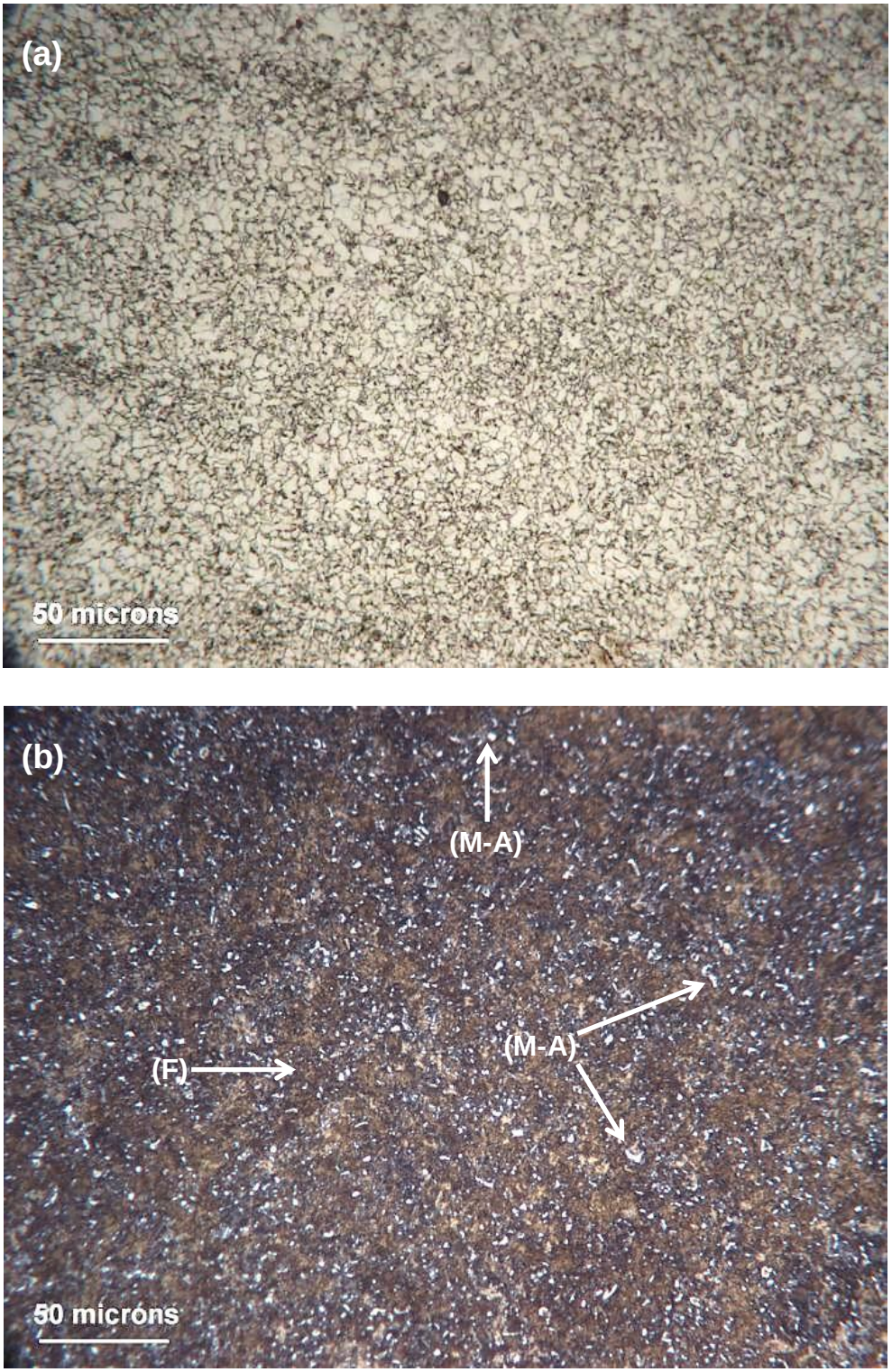

Figure 6-54 Optical micrographs of SAW X70 HAZ at 10 mm from the bottom, showing (a) Nital etch and (b) LePèra etched

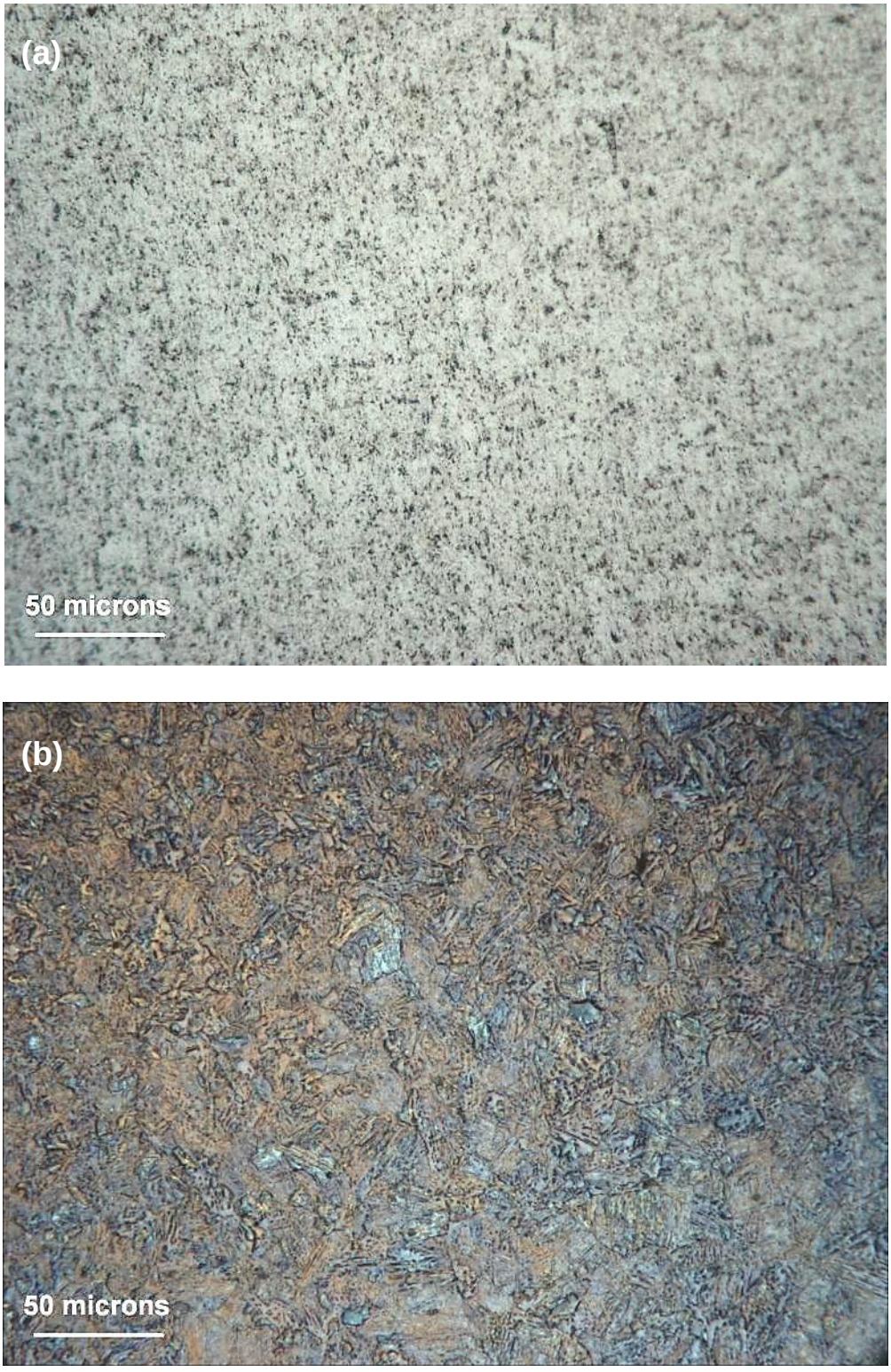

Figure 6-55 Optical micrographs of X70 tandem MIG HAZ at 10 mm from the bottom, showing (a) Nital etch and (b) LePèra etched

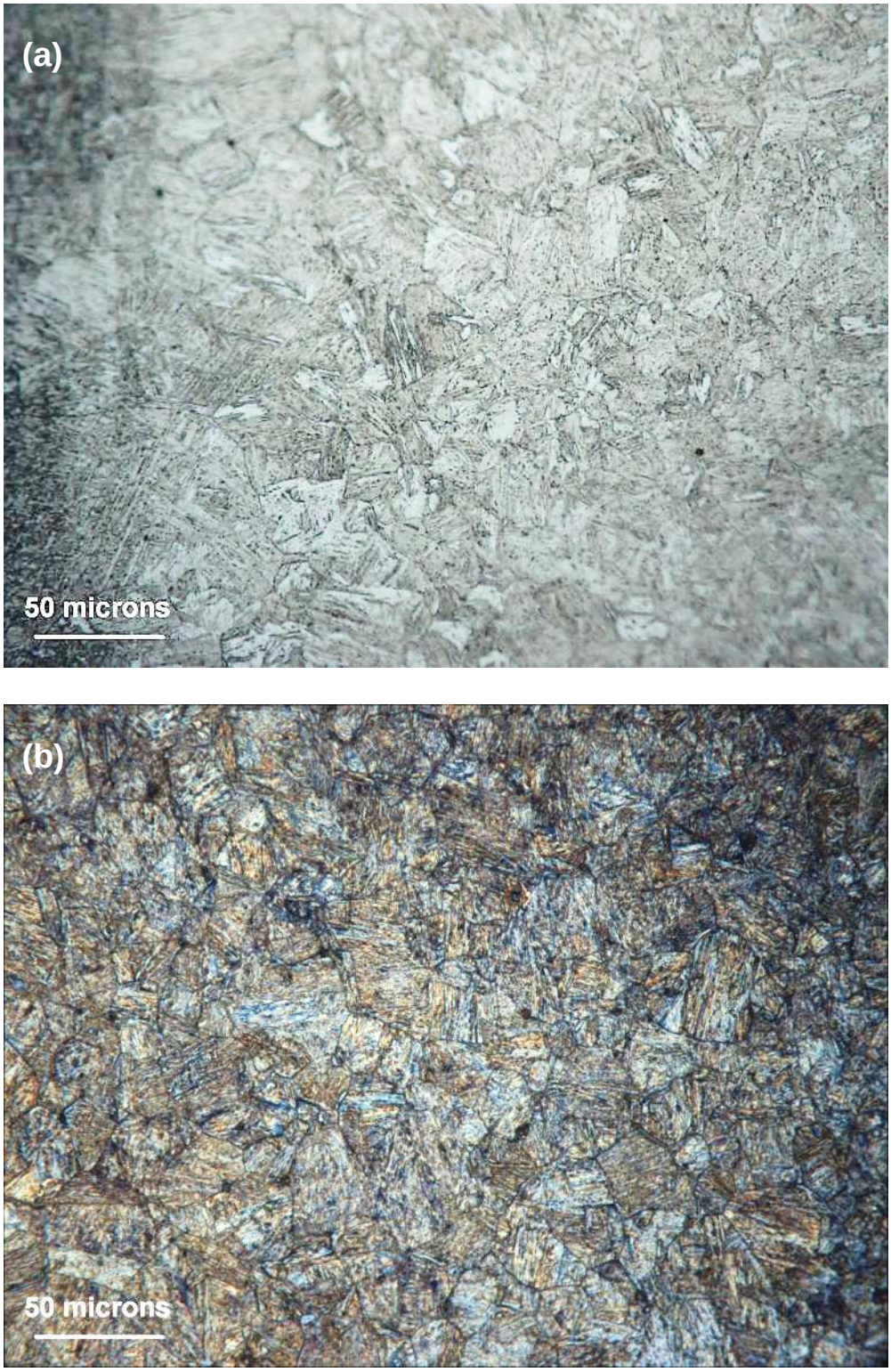

Figure 6-56 Optical micrographs of X100 tandem MIG HAZ at 10 mm from the bottom, showing (a) Nital etch and (b) LePèra etched

6.3.3 SAW hardness traverse across the welds

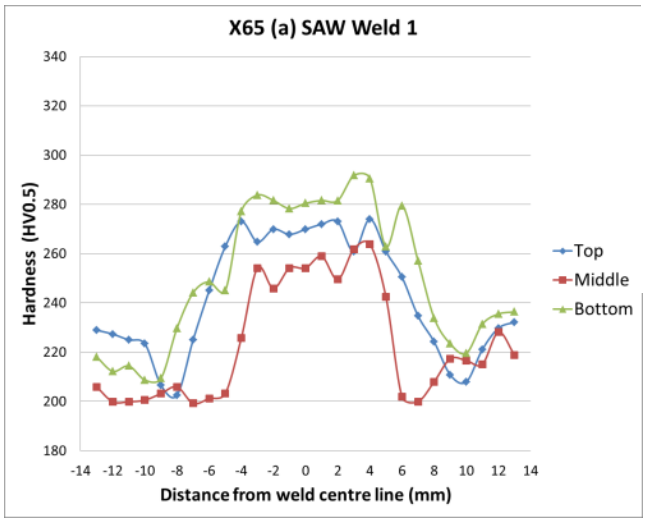

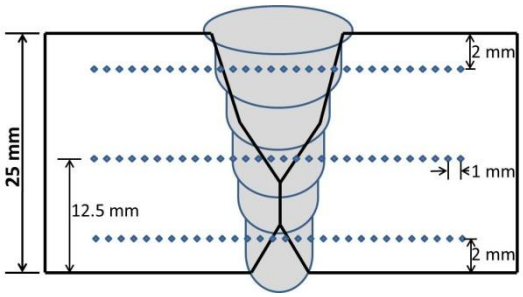

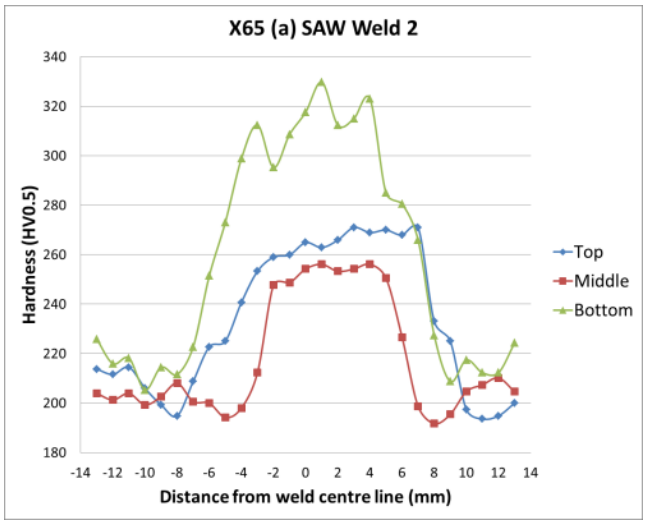

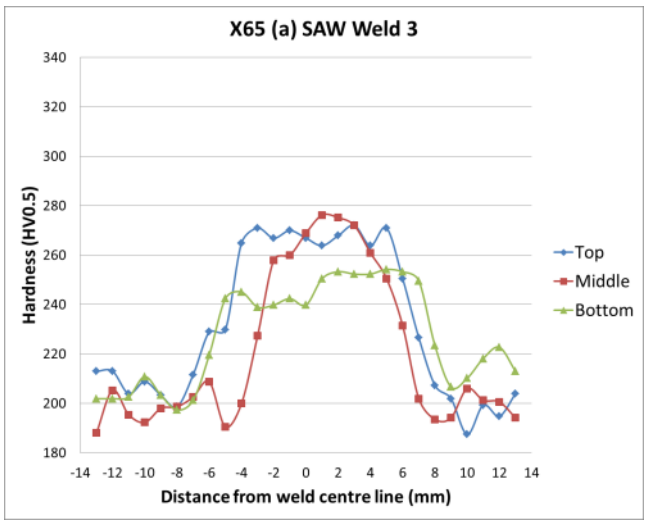

Figure 6-57 X65 (A) SAW hardness traverse across the welds

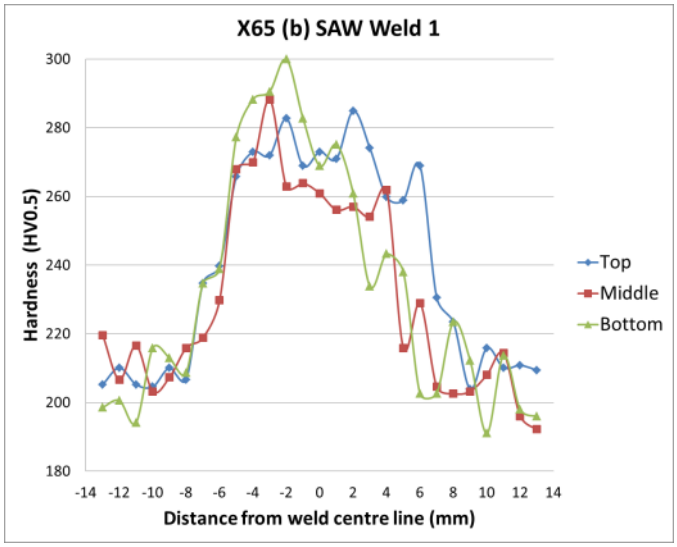

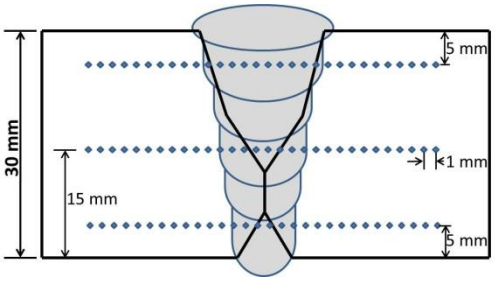

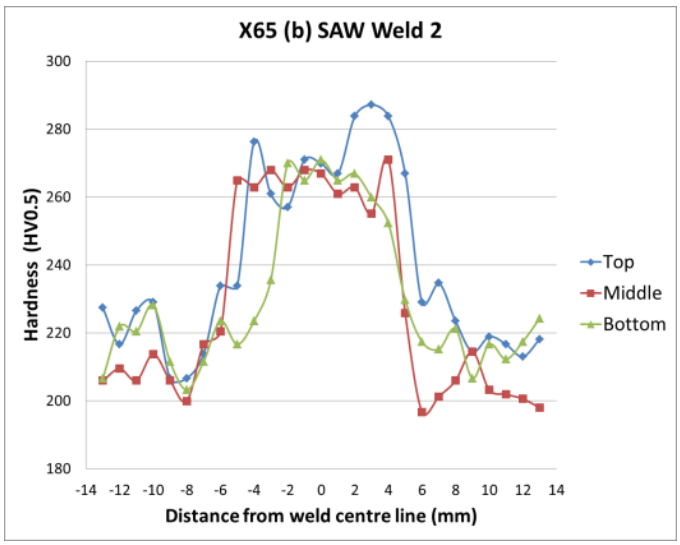

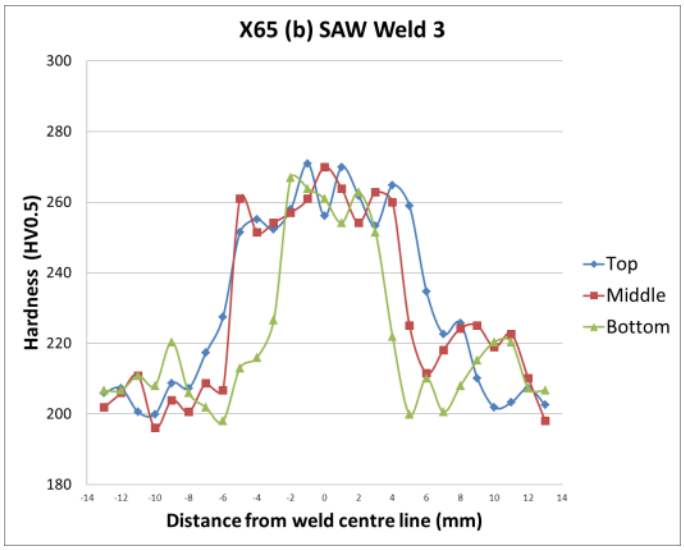

Figure 6-58 X65 (B) SAW hardness traverse across the welds

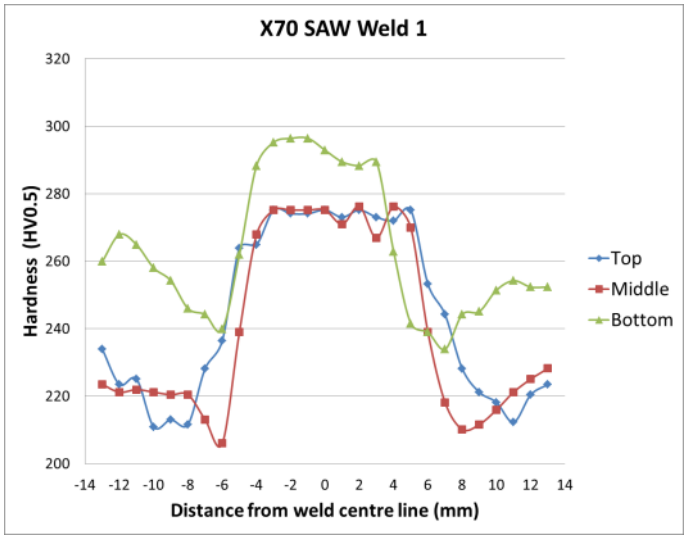

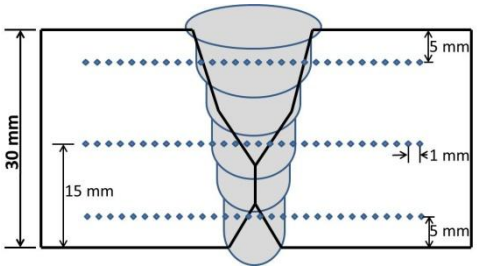

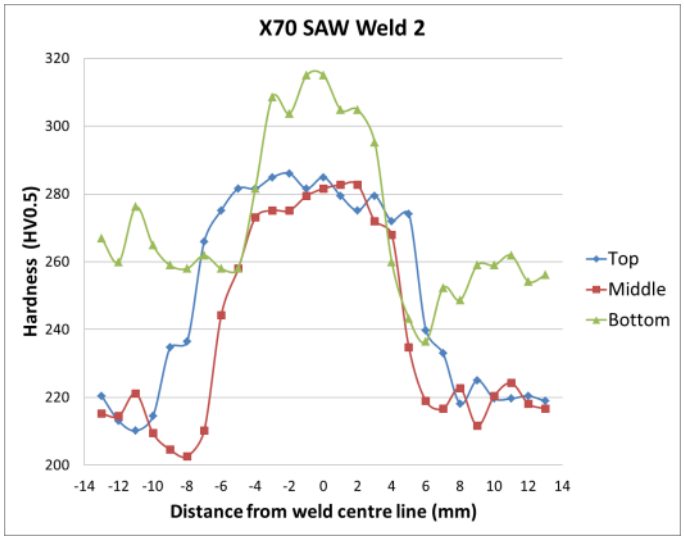

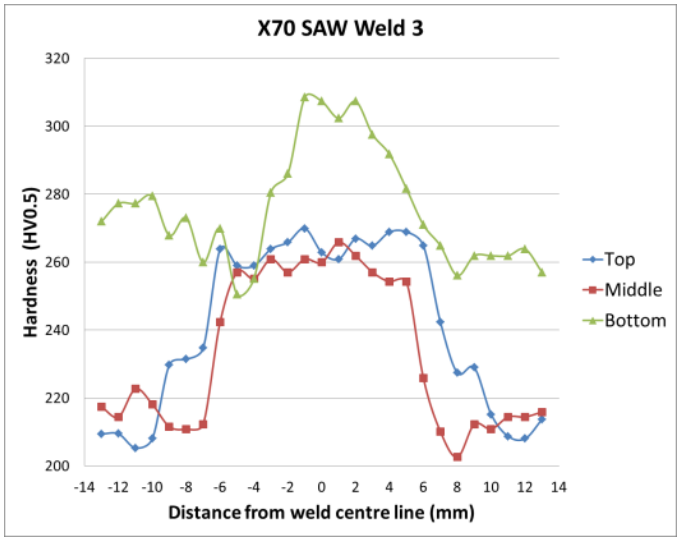

Figure 6-59 X70 SAW hardness traverse across the welds

6.3.4 Real thermal cycles of submerged arc welds HAZ

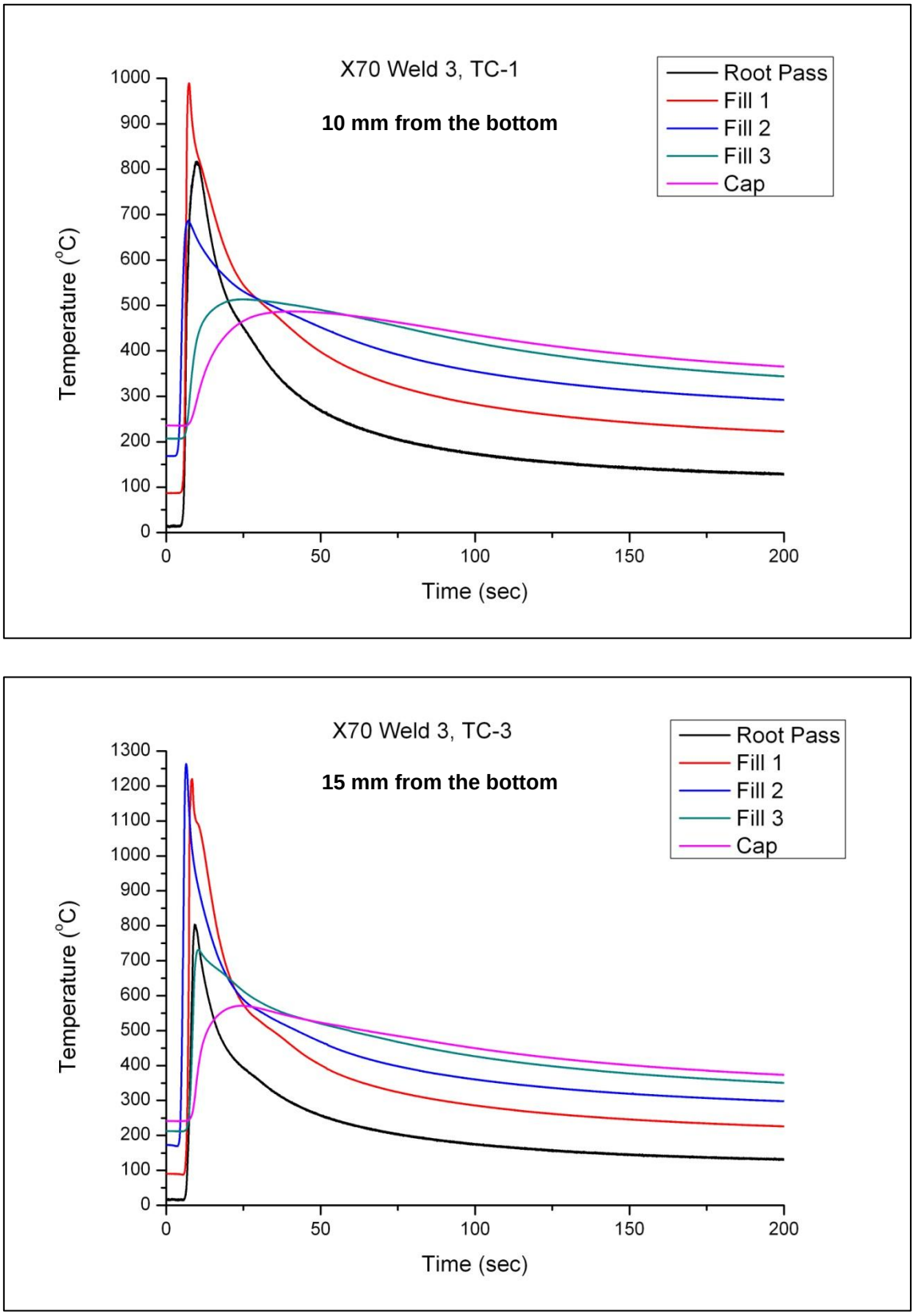

Figure 6-60 Representative thermal cycles of SAW full welds on X70 pipes

6.3.5 Crack tip opening displacement test (CTOD) results

Table 6-4 CTOD results of the HAZ from selected welds

Weld Name	HAZ CTOD (mm)	Fracture Mode
SAW X65 (A) Weld 1	δ = 0.83	M
SAW X65 (A) Weld 3	δ = 0.88	M
SAW X65 (B) Weld 1	δ = 1.03	M[(a)]
SAW X65 (B) Weld 3	δ = 0.26	U[(a)]
SAW X70 Weld 1	δ = 0.098	C
SAW X70 Weld 2	δ = 0.69	U

(a) The pre-crack shape failed to satisfy the requirements of BS 7448-2, i.e. greater than 20% variation in crack length and less than 1.3 mm minimum pre-crack length.

δ crack tip opening displacement (CTOD)

Δa Stable crack extension, including stretch zone width in mm

δc (C) critical δ at the onset of brittle crack extension when $\Delta a < 0.2$ mm

δm (M) δ at the first attainment of maximum F (force) plateau for fully plastic behaviour

δu (U) critical δ at the onset of brittle crack extension when $\Delta a \geq 0.2$ mm

6.3.5.1 CTOD samples macros showing crack tip placement

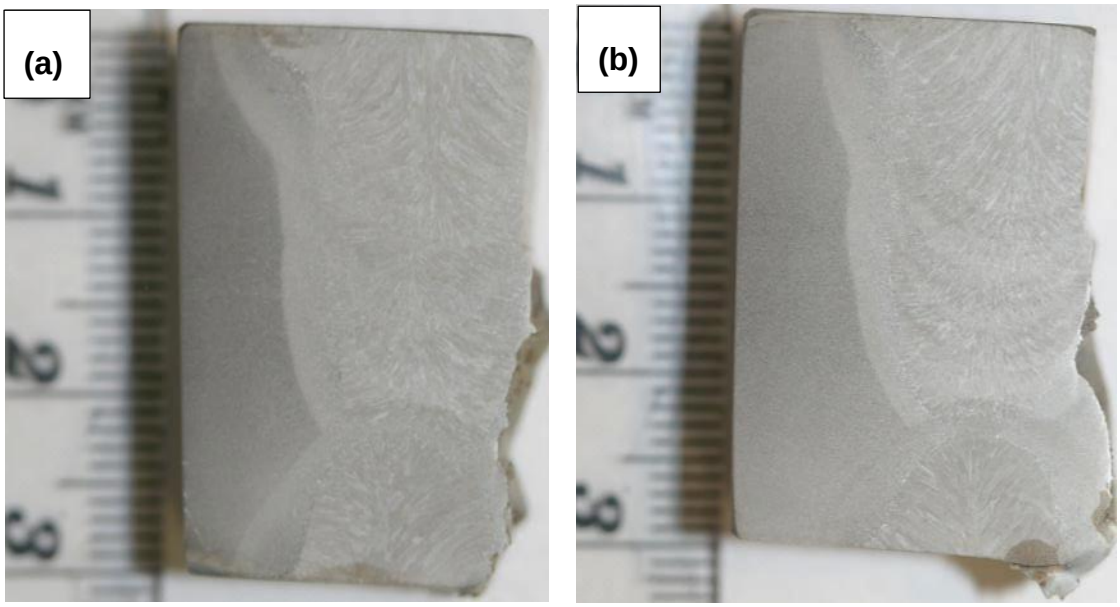

Figure 6-61 Macrographs of X70 SAW Welds CTOD (a) weld 1 and (b) weld 2

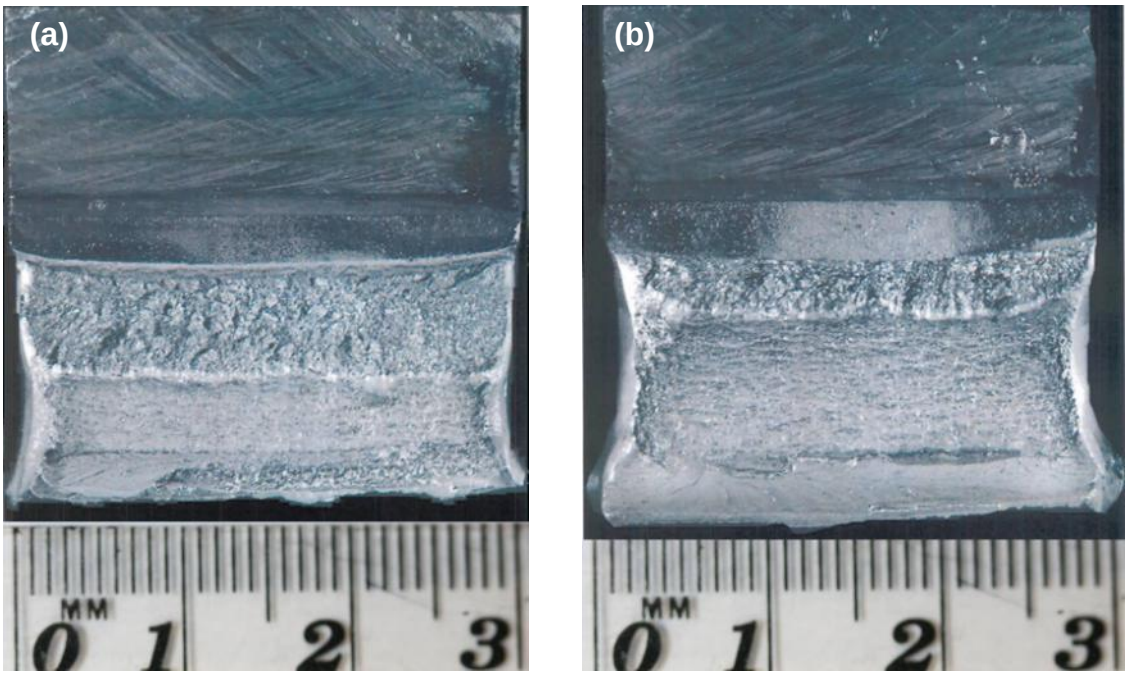

Figure 6-62 Pictures of the CTOD samples broken faces of X70 SAW (a) weld 1 and (b) weld 2

6.3.6 Hardness maps of the notch area

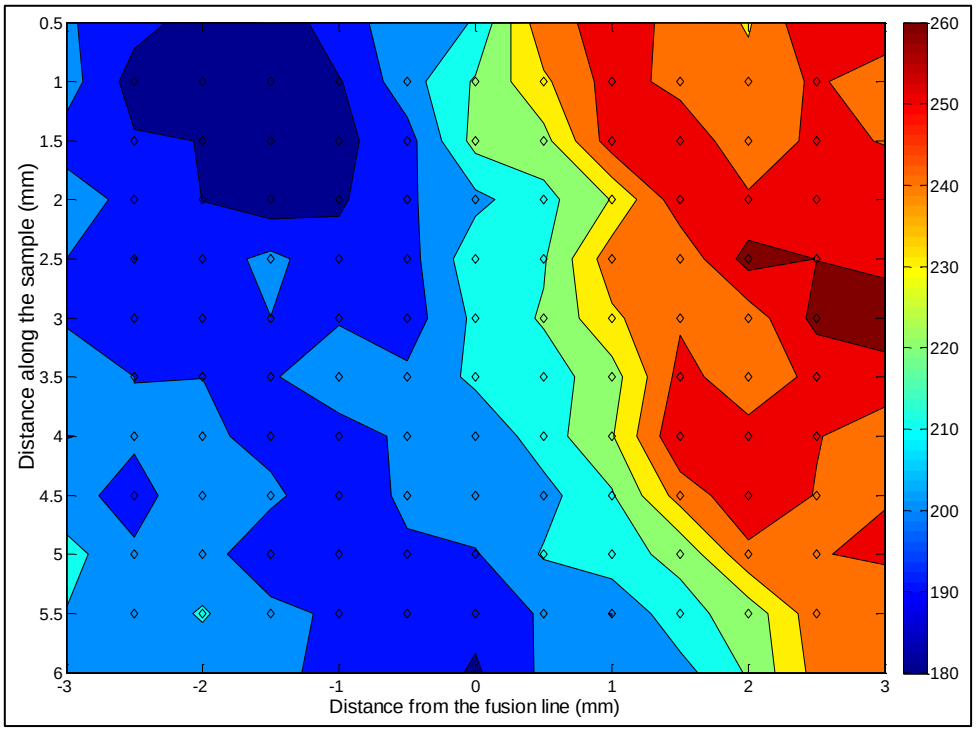

Figure 6-63 X65 (A) SAW weld 1 hardness map

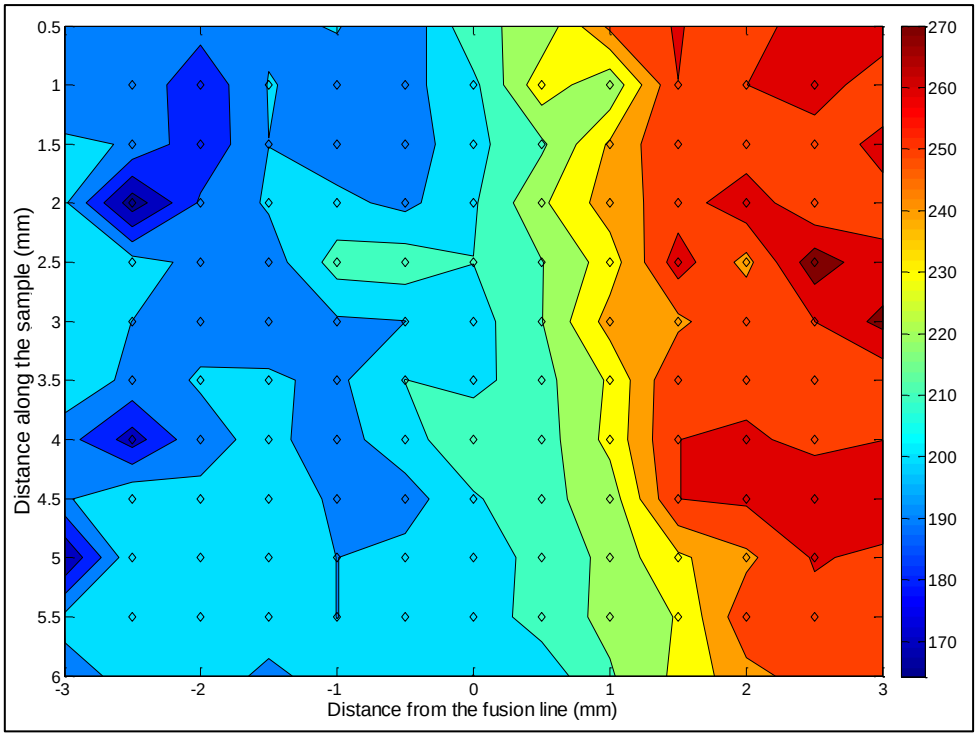

Figure 6-64 X65 (A) SAW weld 3 hardness map

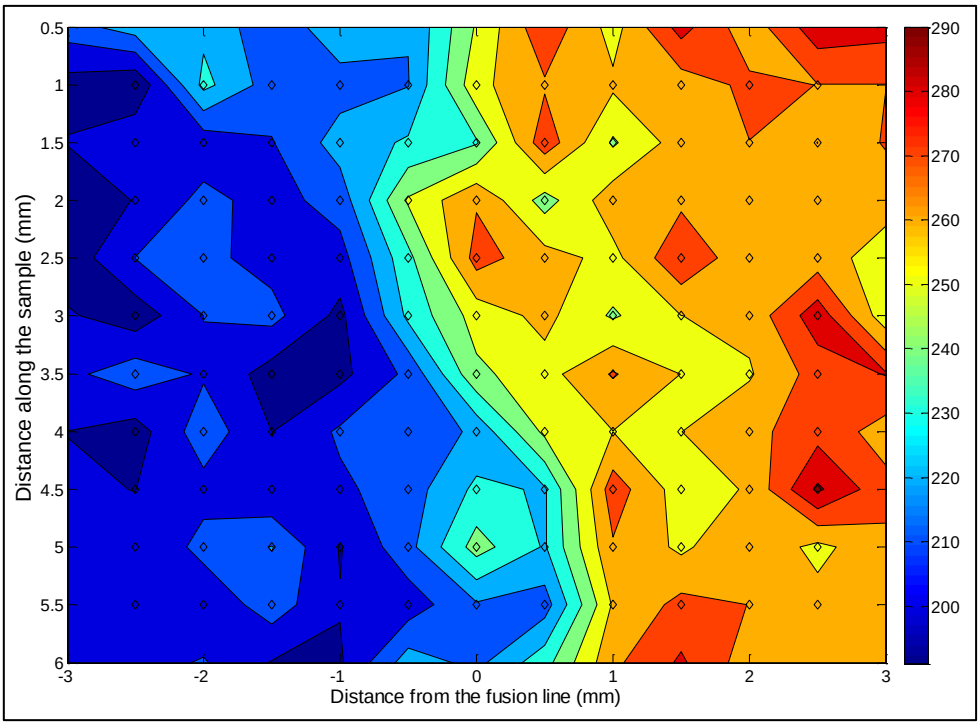

Figure 6-65 X65 (B) SAW weld 1 hardness map

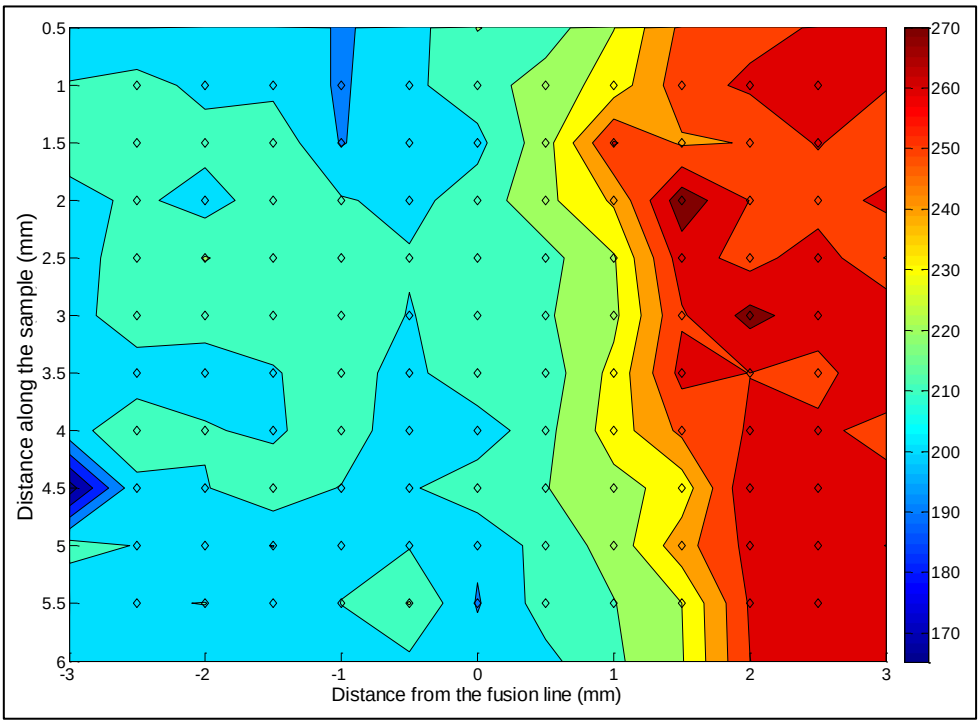

Figure 6-66 X65 (B) SAW weld 3 hardness map

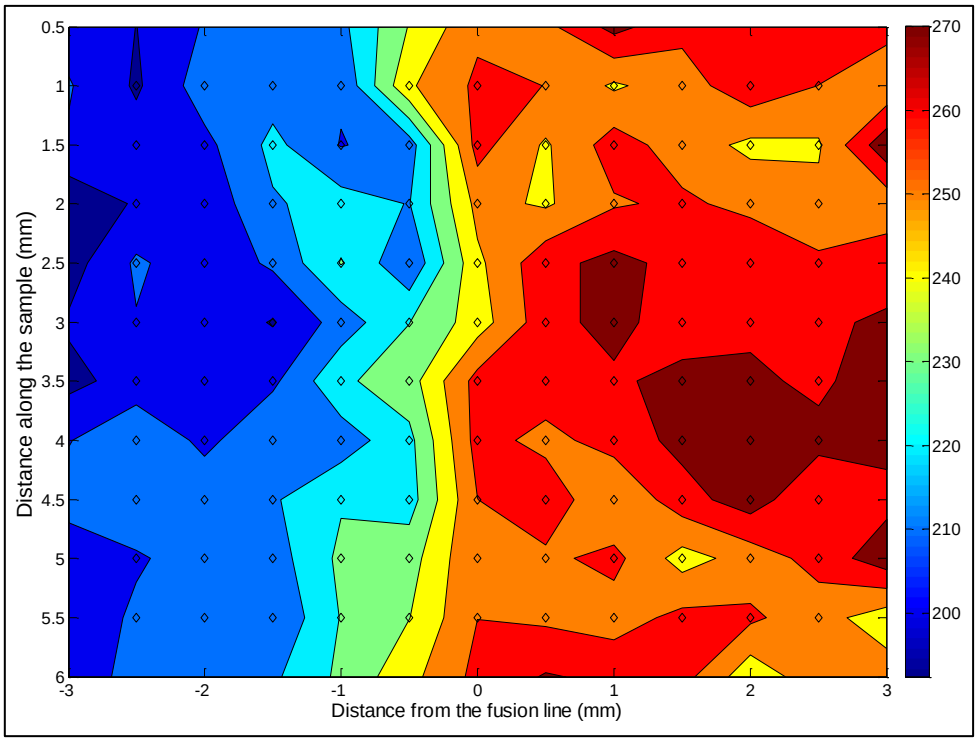

Figure 6-67 X70 SAW weld 1 hardness map

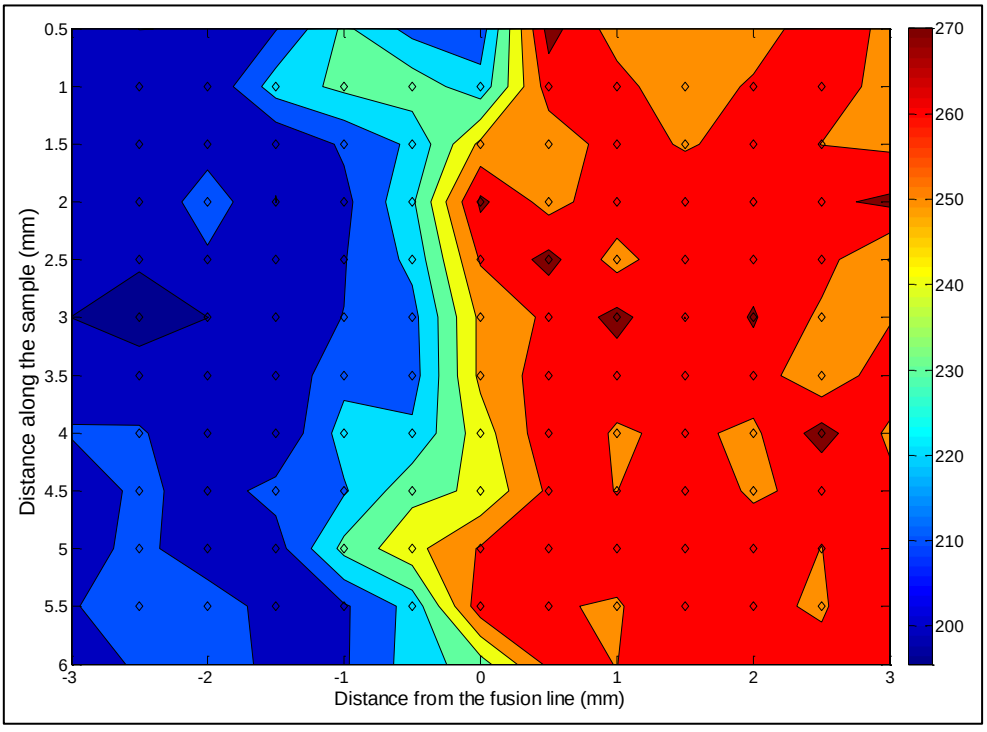

Figure 6-68 X70 SAW weld 2 hardness map

6.4 **Tandem MIG welds**

Narrow groove tandem MIG welds were made on X70 and X100 pipeline steels. These experiments were also conducted to acquire the thermal cycles of the welds. Two instrumented welds were made on each material, and named welds 1 and 2 respectively. Selected results based on these welds are presented here. These will include macrographs, micrographs, thermal cycles, hardness traverses, CTOD results and hardness maps etc.

6.4.1 Macrographs of tandem MIG welds

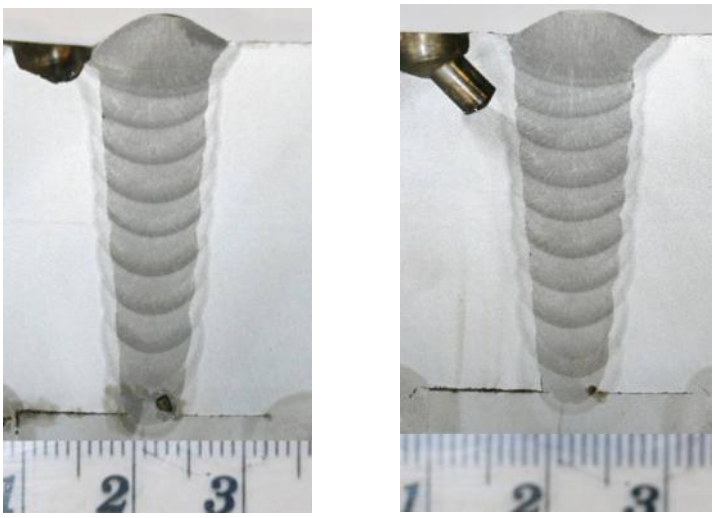

Figure 6-69 Macrographs of tandem MIG X70 weld 1

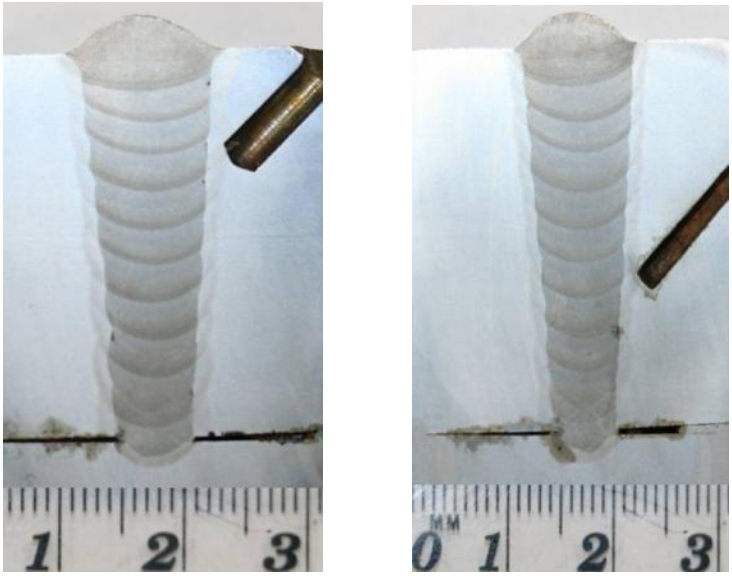

Figure 6-70 Macrographs of tandem MIG X70 weld 2

6.4.2 Micrographs of tandem MIG welds

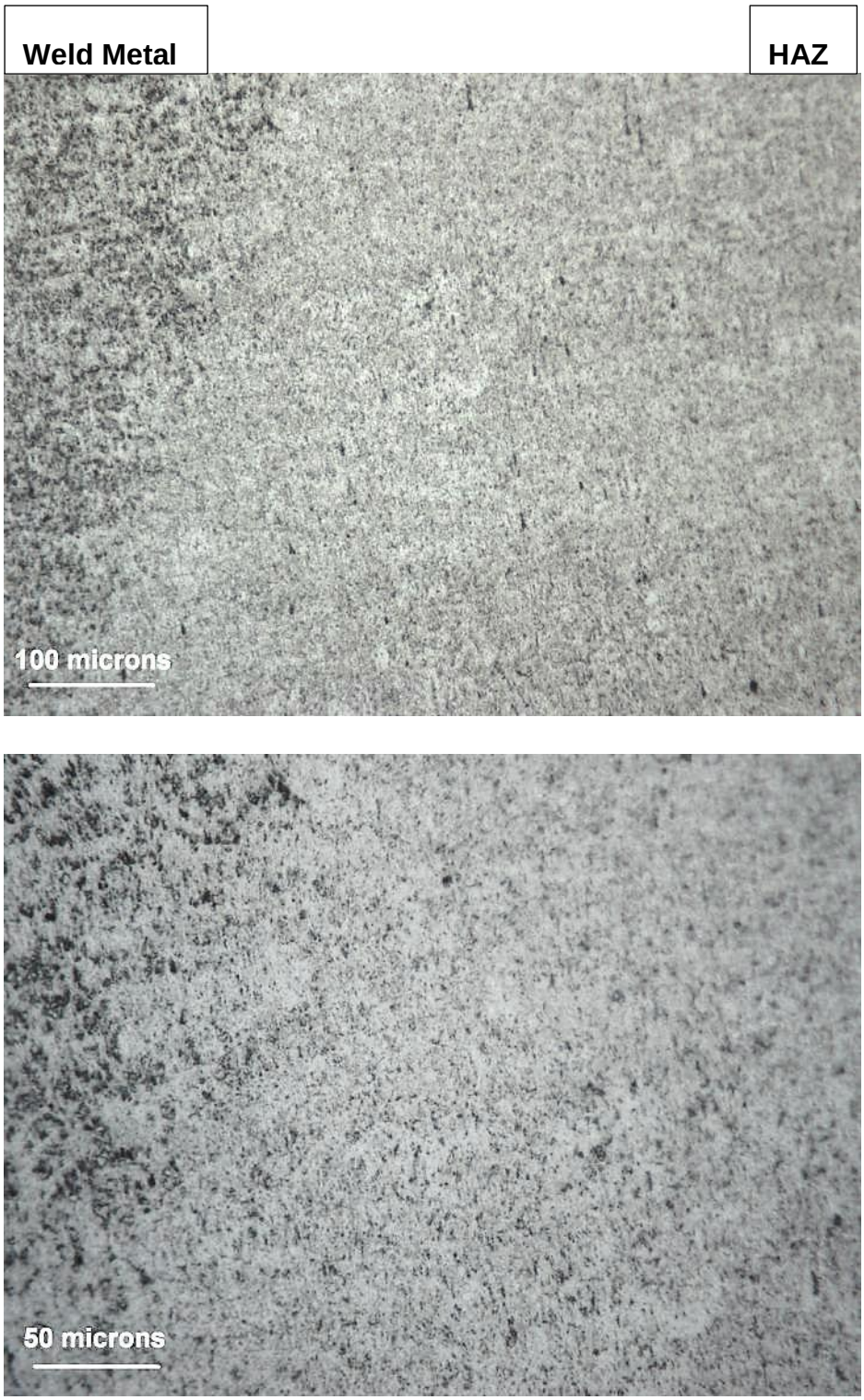

Figure 6-71 Optical micrographs of X70 tandem MIG welds, showing from left to right; weld metal, fusion line and HAZ (15 mm from the top) at different magnifications

Figure 6-72 Optical micrograph of X70 tandem MIG weld showing the microstructure of the thermocouple position

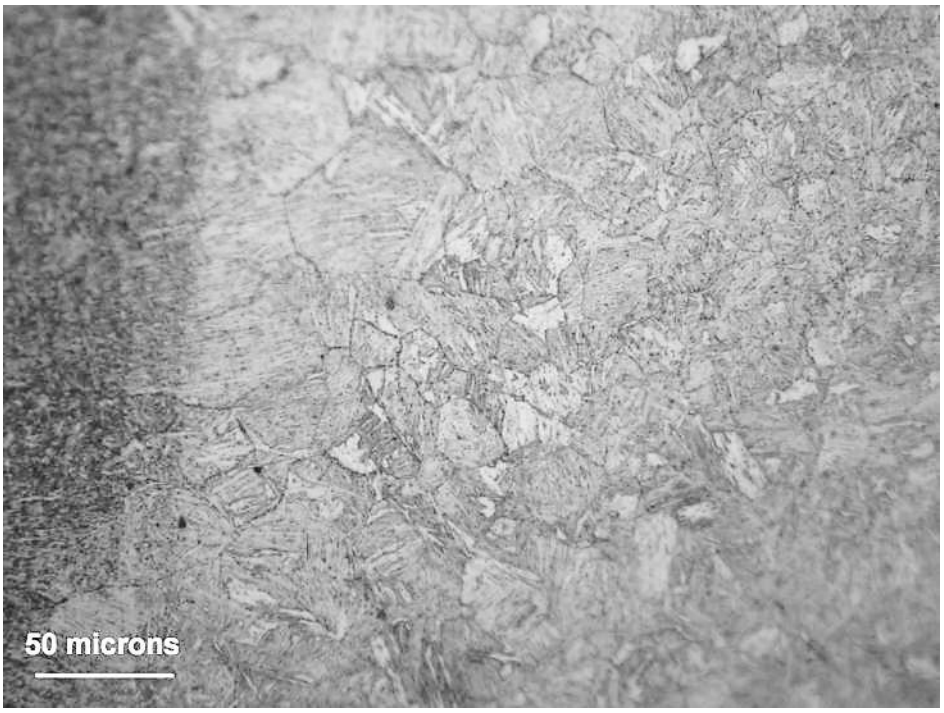

Figure 6-73 Optical micrograph of X100 tandem MIG weld, showing from left to right; weld metal, fusion line and HAZ at the middle of the weld

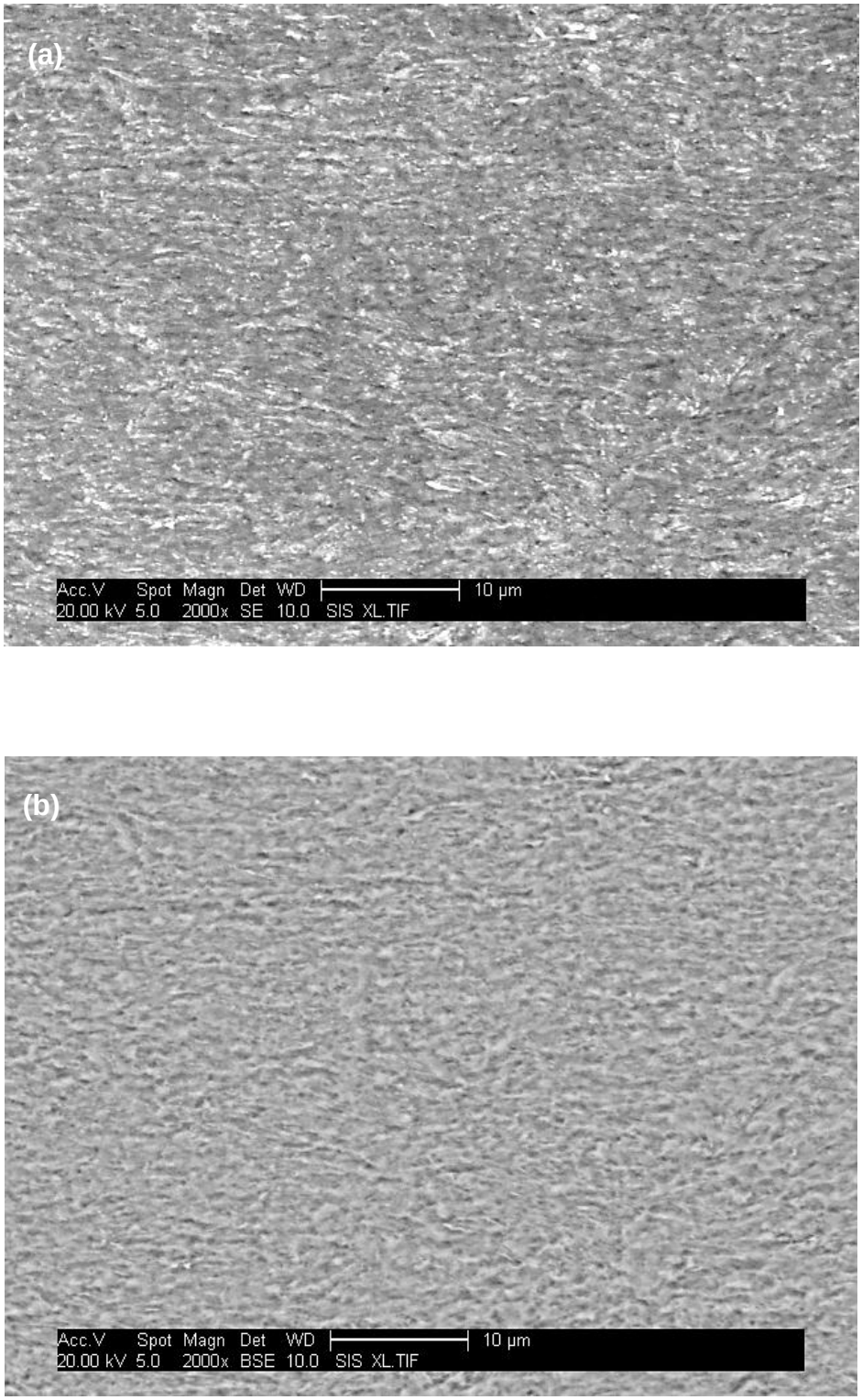

Figure 6-74 SEM micrograph of X70 tandem MIG weld 1 HAZ at 15 mm from the top, showing (a) secondary electrons and (b) backscattered electrons

6.4.3 Thermal cycles of the tandem MIG welds

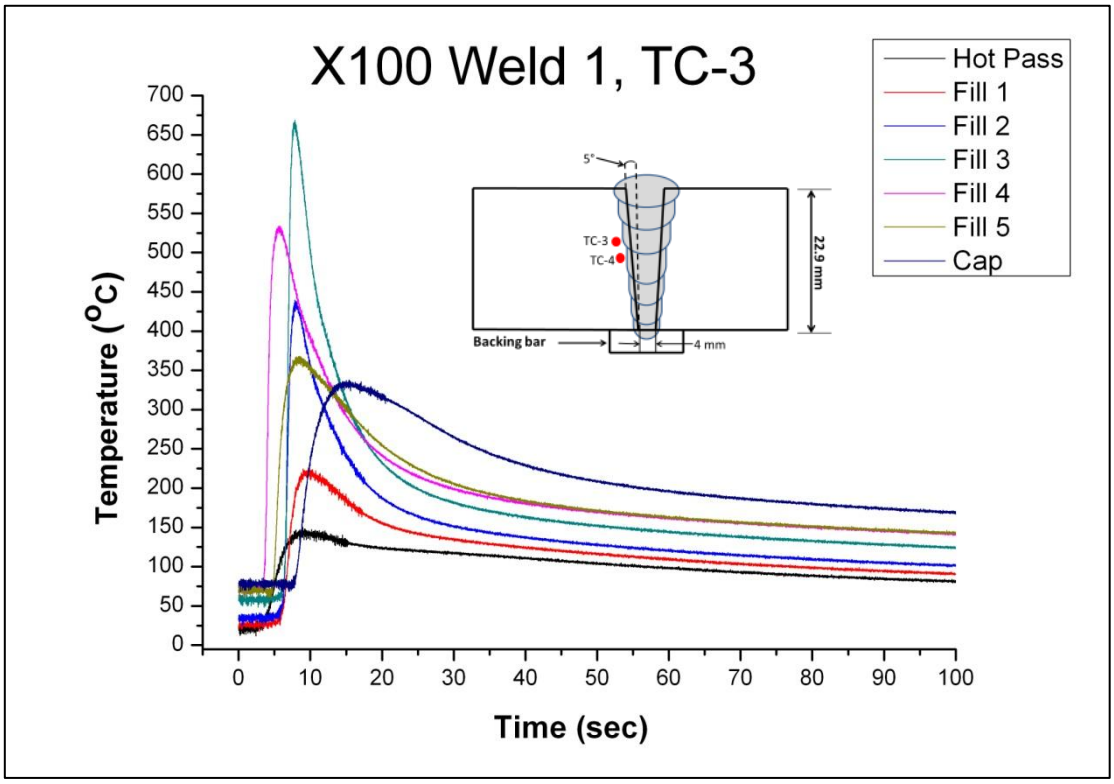

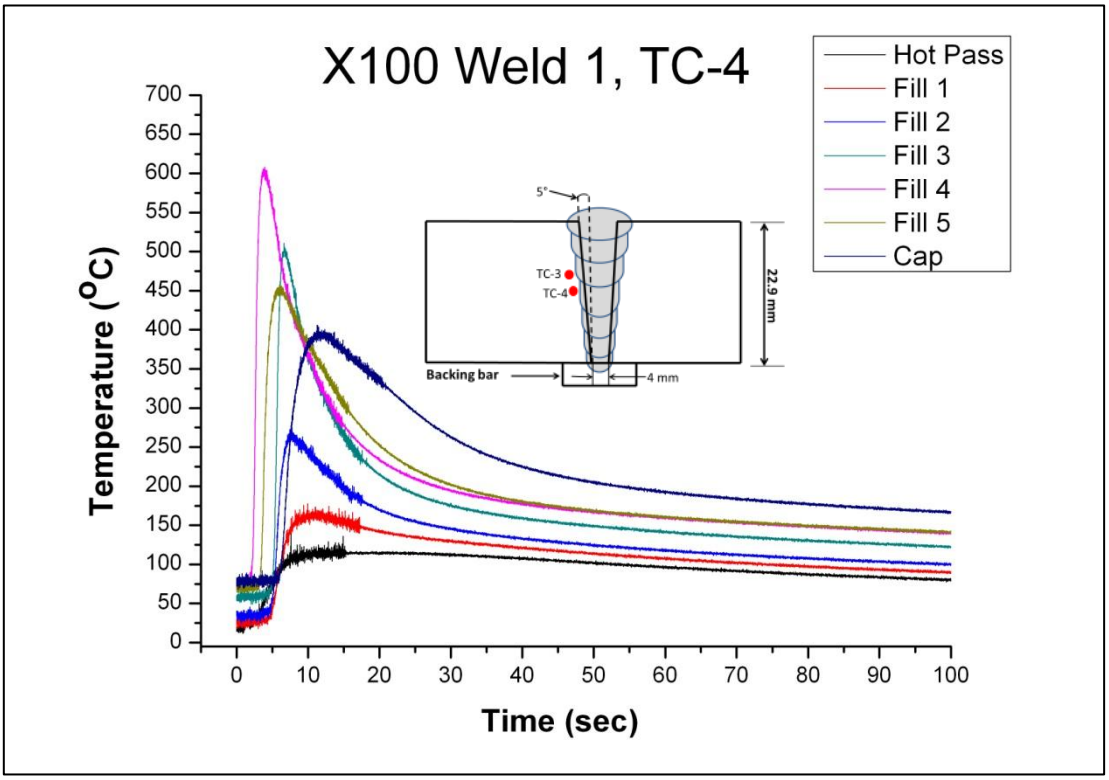

Figure 6-75 Representative thermal cycles of narrow groove tandem MIG welds, on X100 pipe

6.4.4 Tandem MIG welds hardness traverses

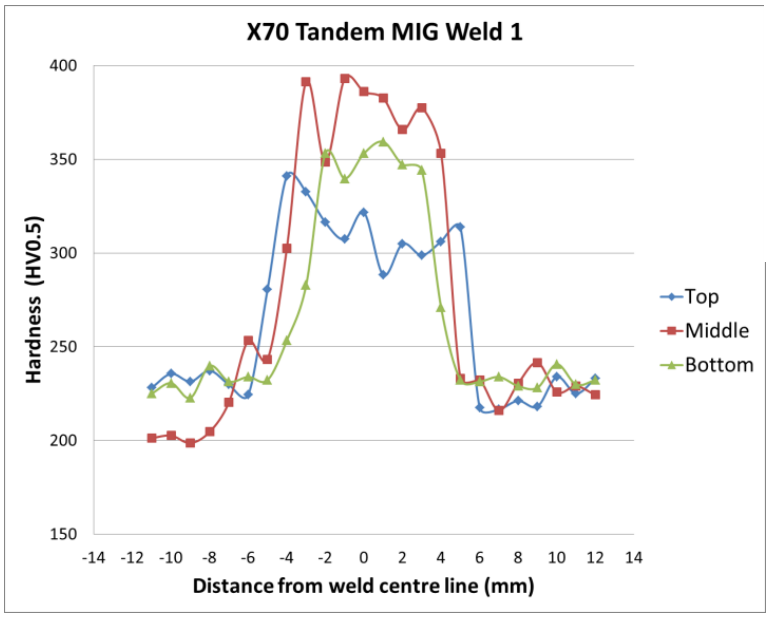

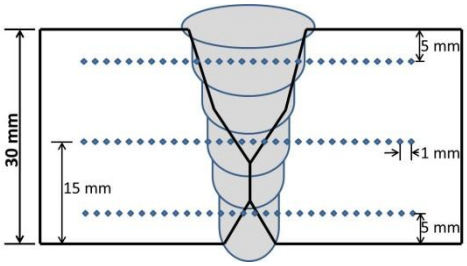

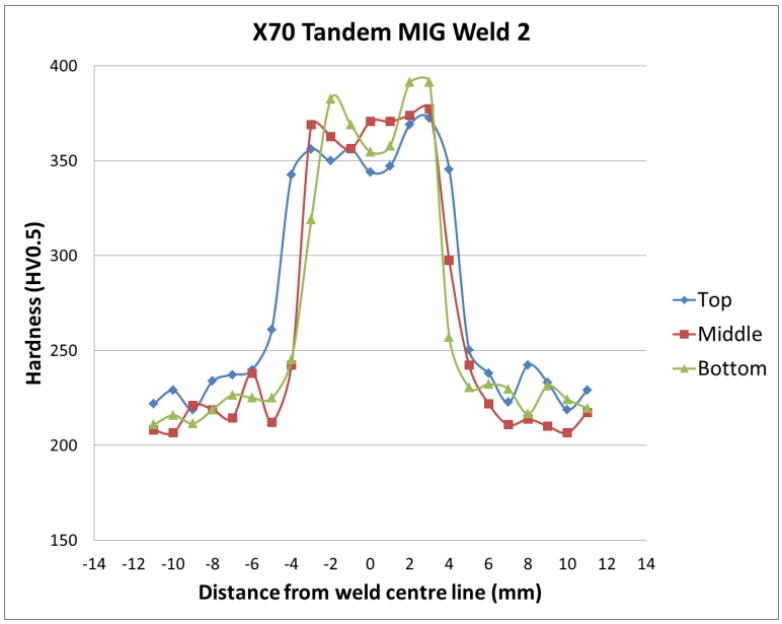

Figure 6-76 Hardness traverse across the narrow groove tandem MIG welds on X70

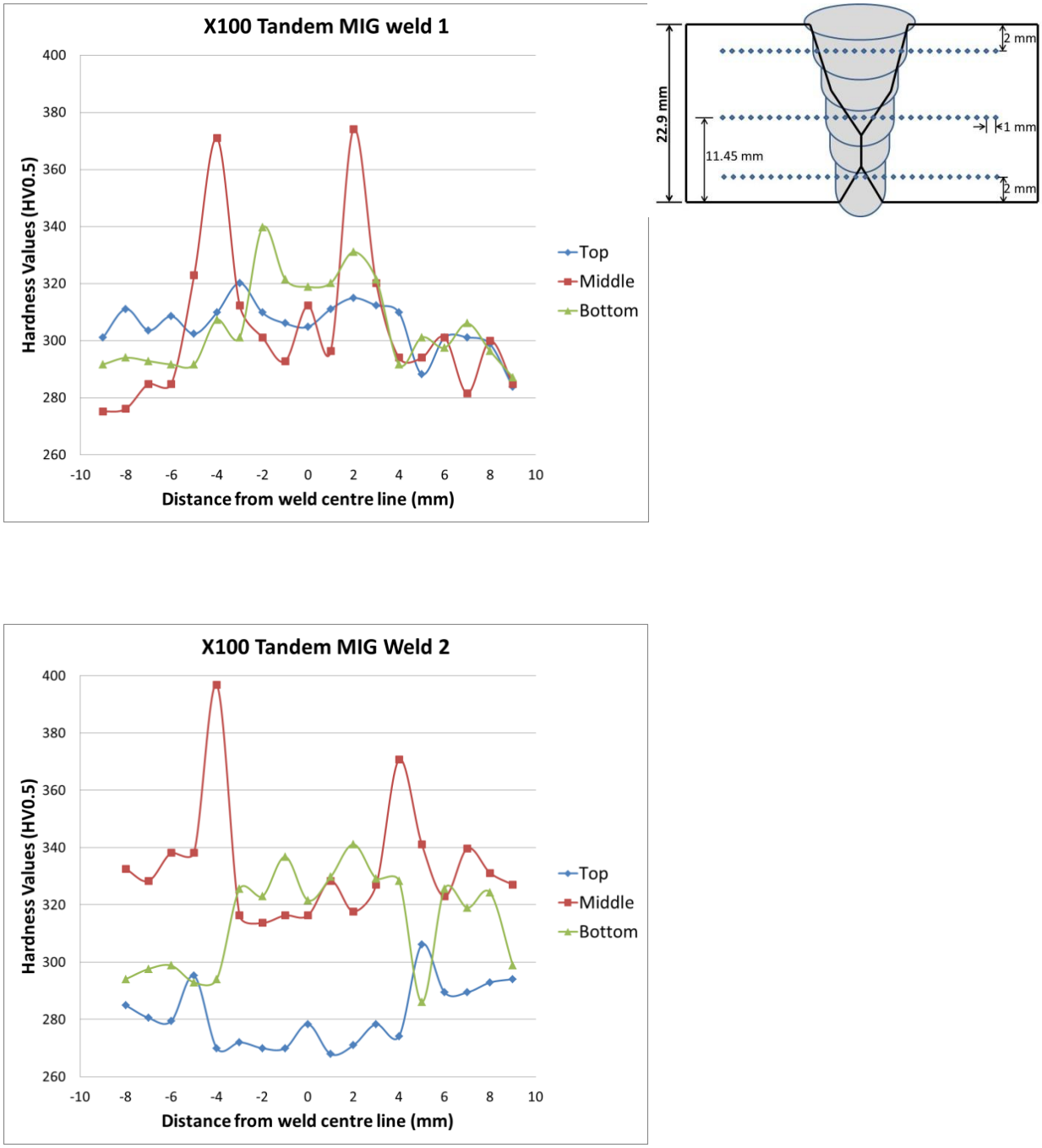

Figure 6-77 Hardness traverse across the narrow groove tandem MIG welds on X100

6.4.5 CTOD results of X70(a) tandem MIG welds

Table 6-5 CTOD results of the HAZ from the X70 tandem MIG welds

Weld Name	HAZ CTOD (mm)	Fracture Mode
Tandem MIG X70 Weld 1	δ = 0.36	M
Tandem MIG X70 Weld 2	δ = 0.06	C[(a)]

(a) The pre-crack shape failed to satisfy the requirements of BS 7448-2, i.e. greater than 20% variation in crack length and less than 1.3 mm minimum pre-crack length.

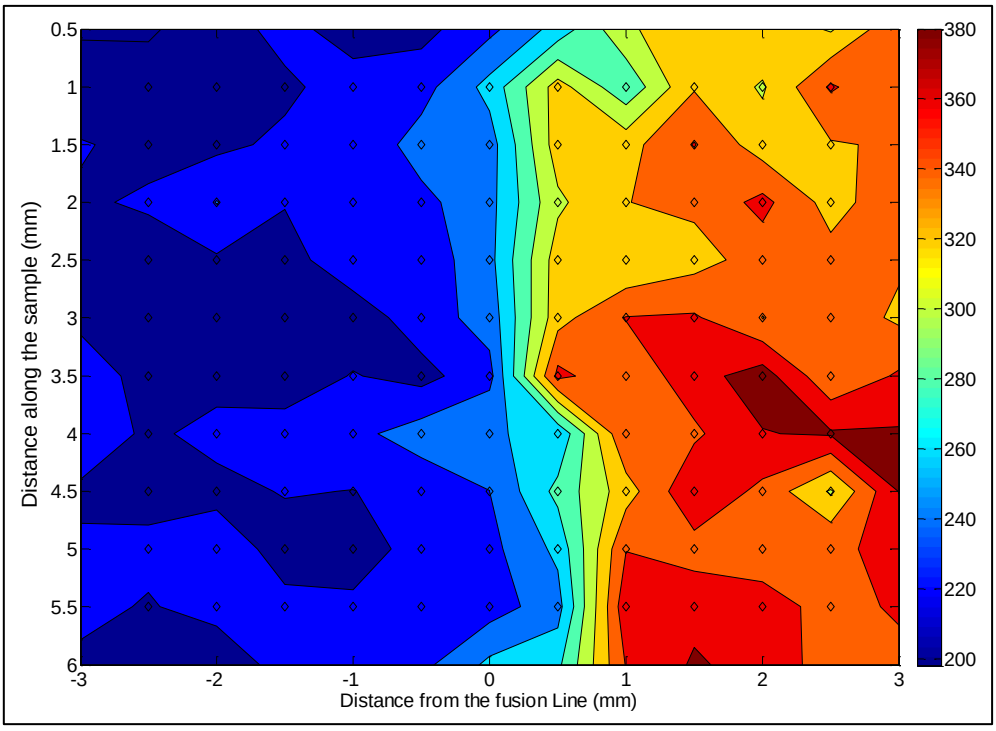

Figure 6-78 X70 tandem MIG weld 1 hardness map

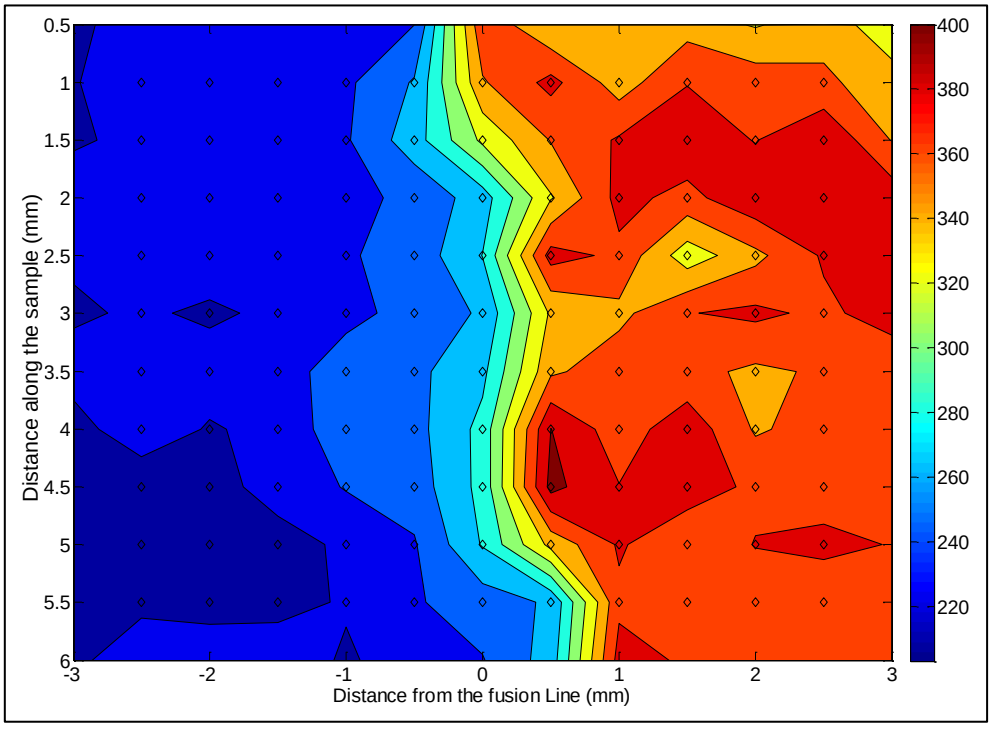

Figure 6-79 X70 tandem MIG weld 2 hardness map

6.5 **Thermal simulations**

Experimental thermal simulation was carried out in X65 (A), X65 (B) and X70 steel grades. A total of 35 different thermal cycles were simulated on X70 samples including trial test. 13 thermal cycles were selected and used on the two X65 grades.

Three charpy impact samples were given an identical simulation each time, so that the charpy impact tests could be carried out at different test temperatures (-40°C, -60°C and -80°C). Tables containing data about these thermal cycles and their respective charpy impact values are given in Appendix B.

Representative thermal cycle will be given below, and the charpy impact results will be displayed on plots. Fractographs and micrographs from selected samples will be presented below. Finally the hardness traverse of the samples will be presented.

6.5.1 Thermal cycles used for thermal simulation

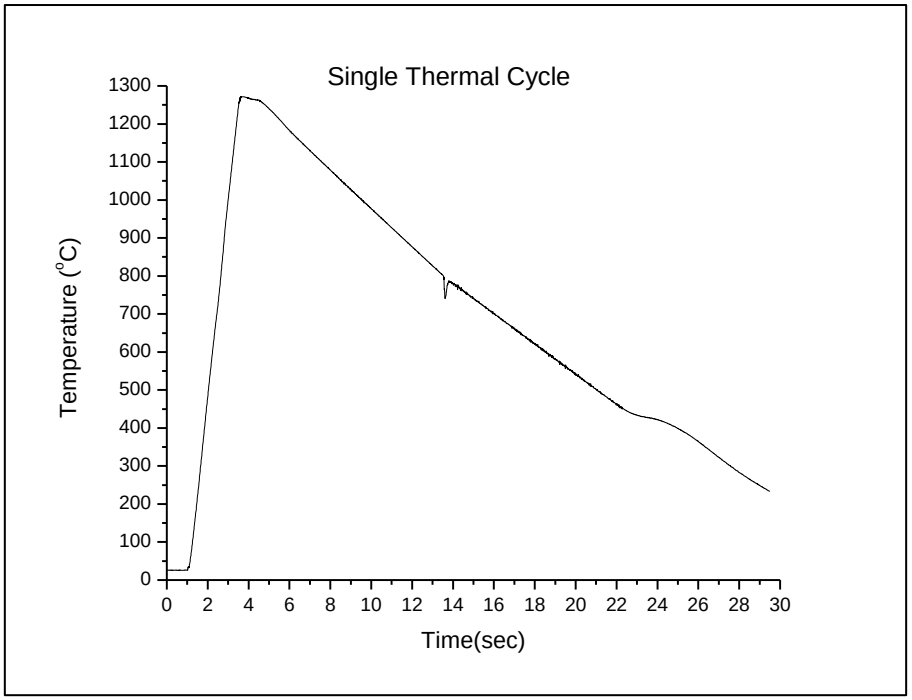

Figure 6-80 Single thermal cycle from the Gleeble machine data

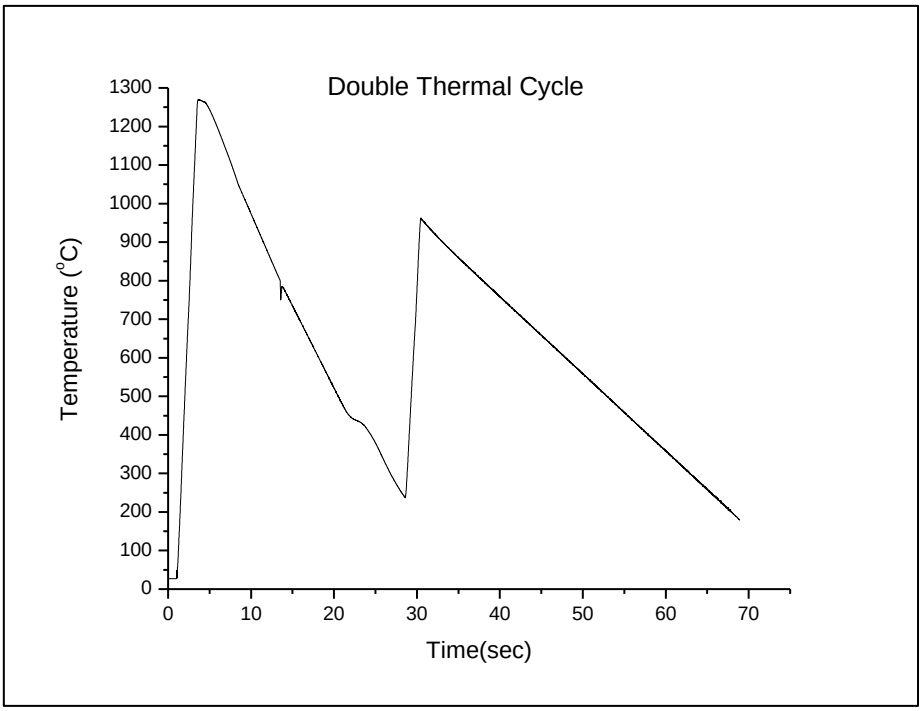

Figure 6-81 Double thermal cycle from the Gleeble machine data

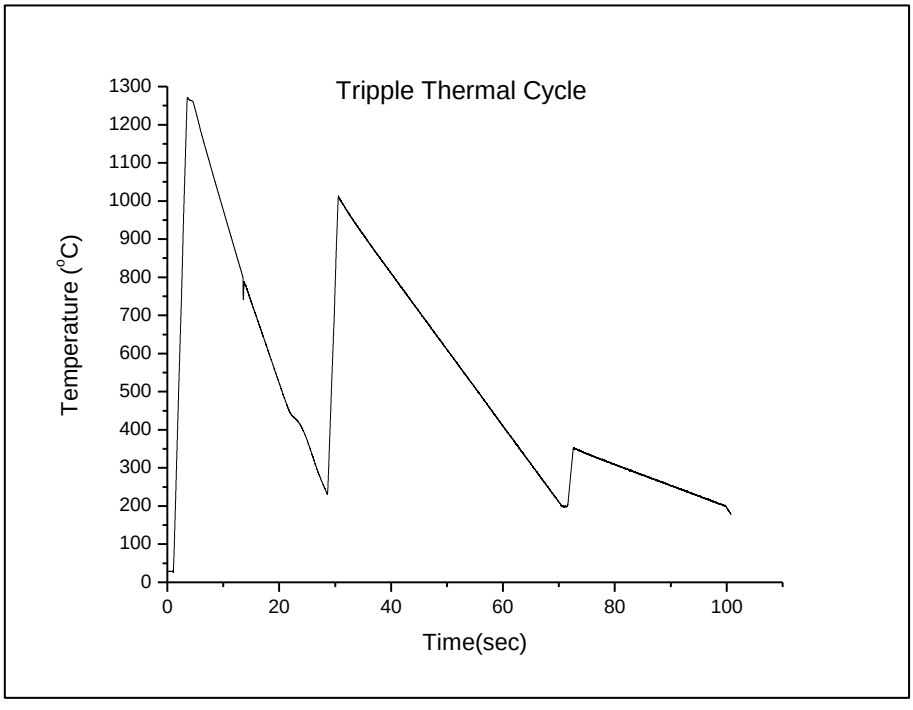

Figure 6-82 Triple thermal cycle from the Gleeble machine data

6.5.2 Charpy impact test results

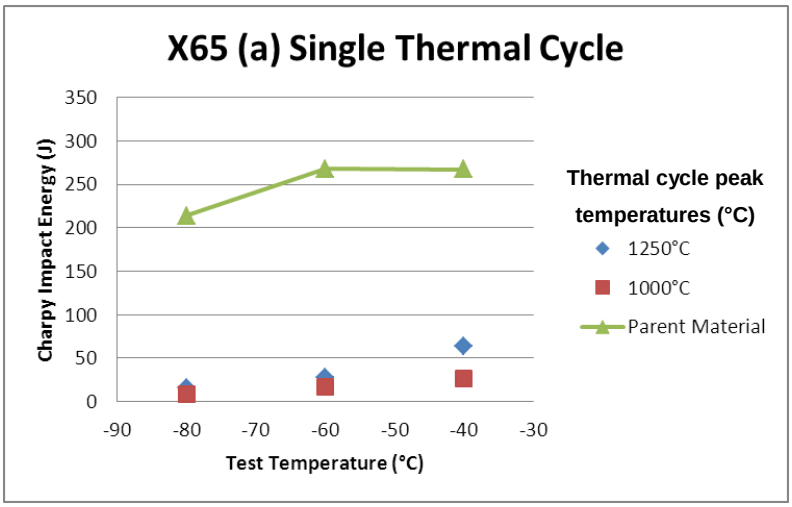

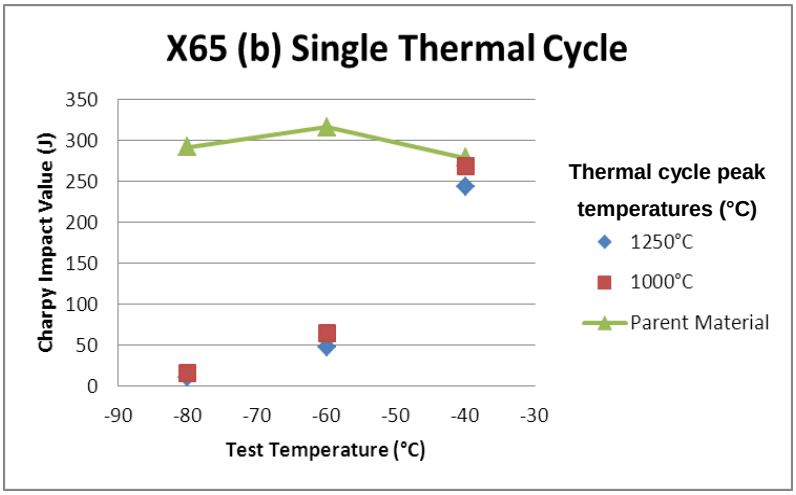

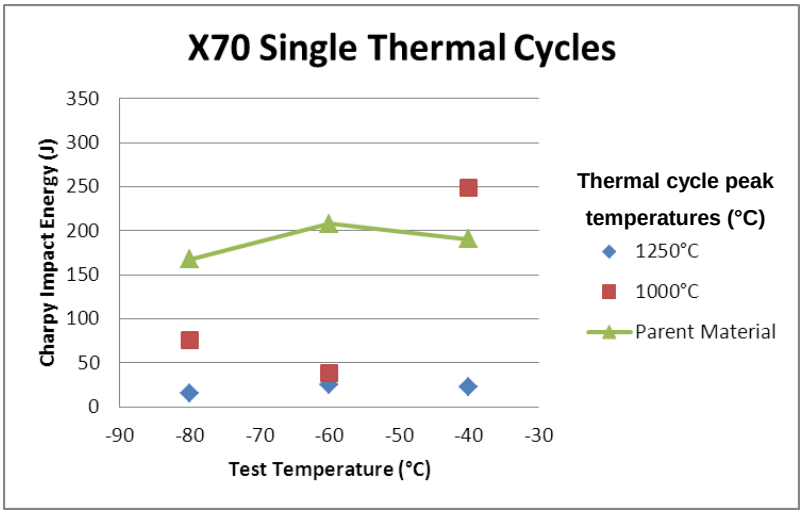

Figure 6-83 Charpy impact results of the single thermal cycles for X65 (A), X65 (B) and X70 at the same cooling rates

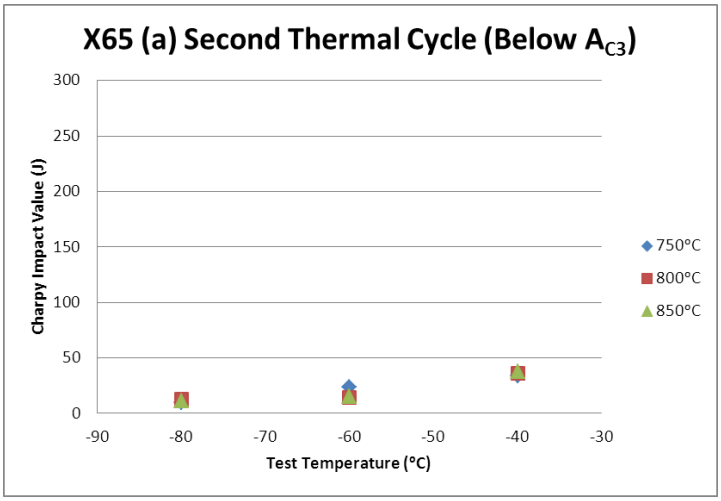

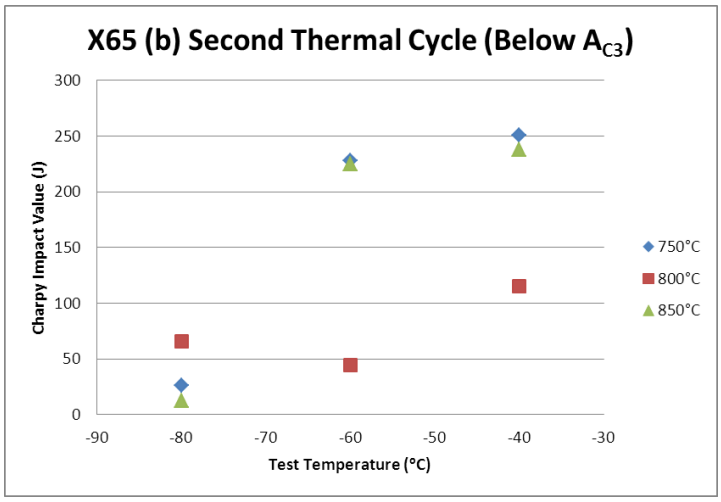

Figure 6-84 Charpy impact results of the double thermal cycles at intercritical temperatures (below A_{C3}) for X65 (A) and X65 (B) at the same cooling rate

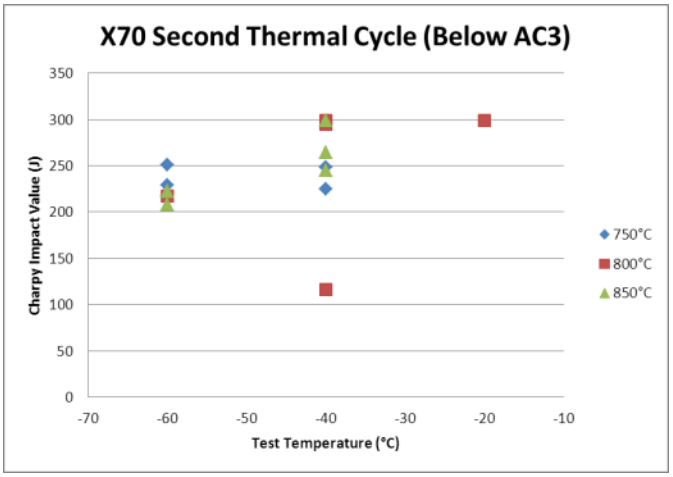

Figure 6-85 Charpy impact results of the double thermal cycles at intercritical temperatures (below A_{C3}) for X70 at a different cooling rate

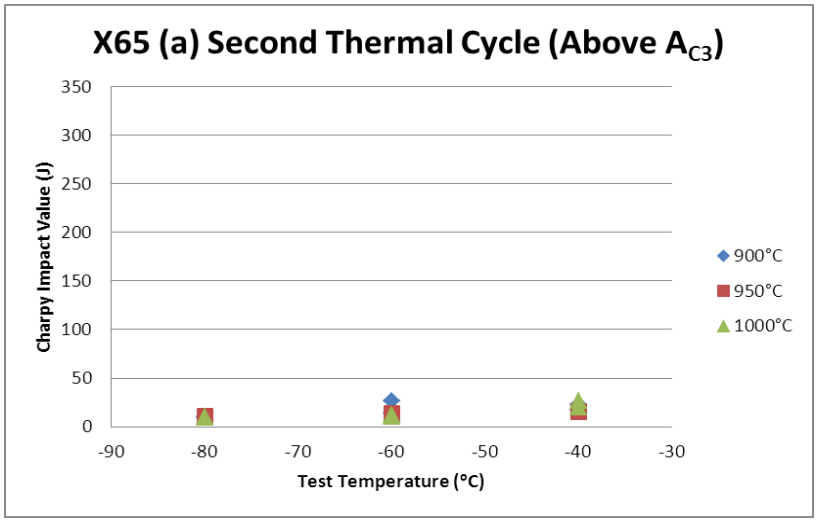

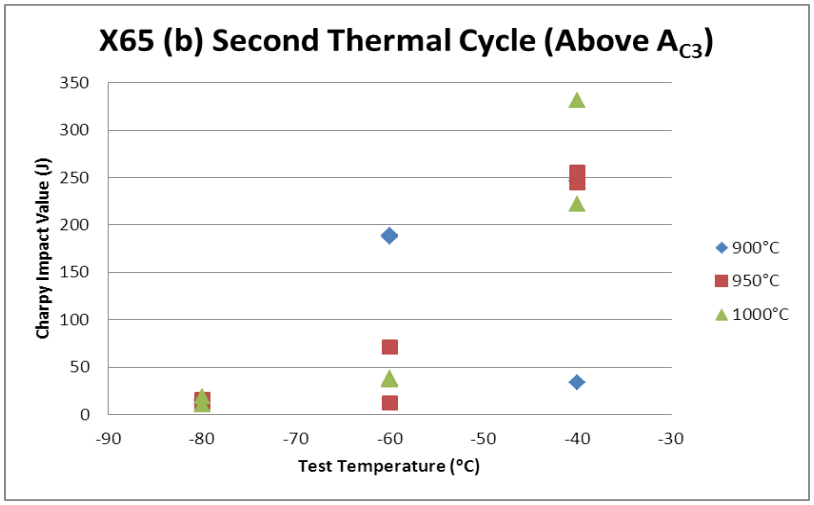

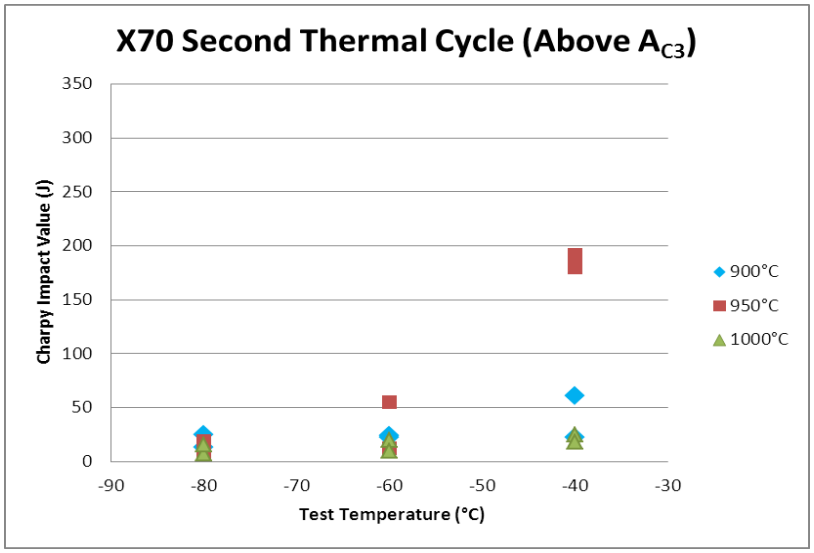

Figure 6-86 Charpy impact results of the double thermal cycles at supercritical temperatures (above A_{C3}) for X65 (A), X65 (B) and X70 at the same cooling rates

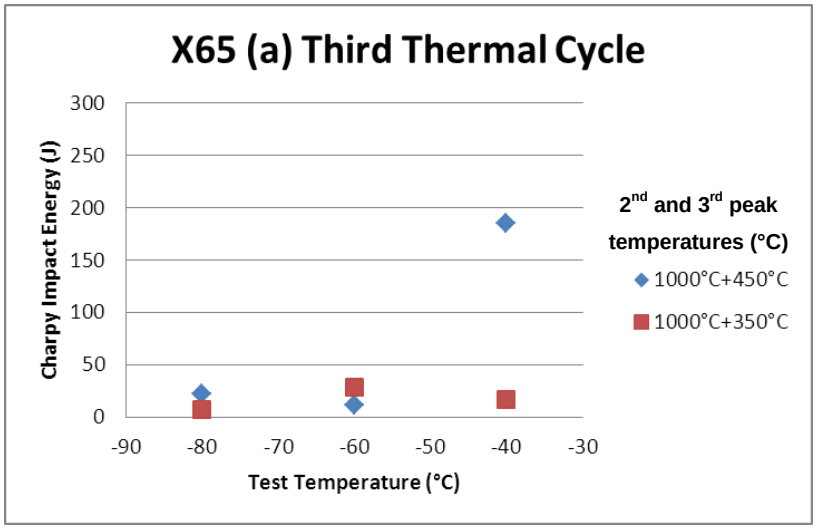

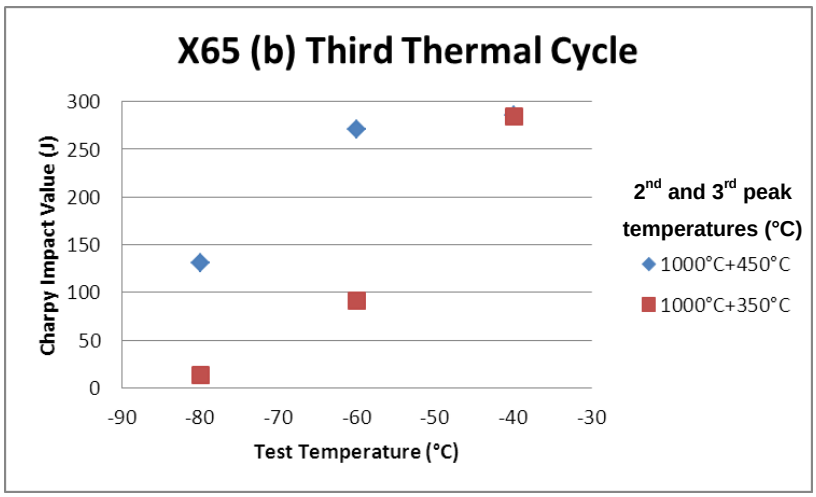

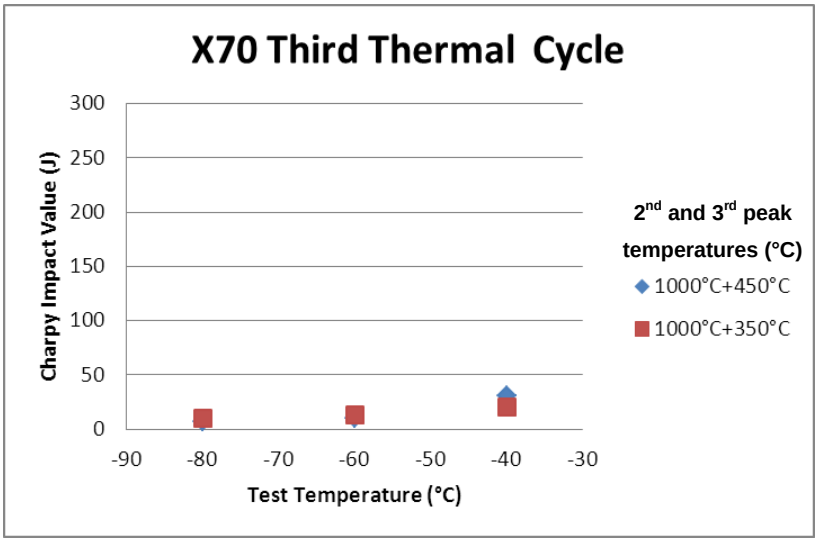

Figure 6-87 Charpy impact results of the triple thermal cycles for X65 (A), X65 (B) and X70 at the same cooling rates

6.5.2.1 Comparison between supercritical temperatures and cooling rates

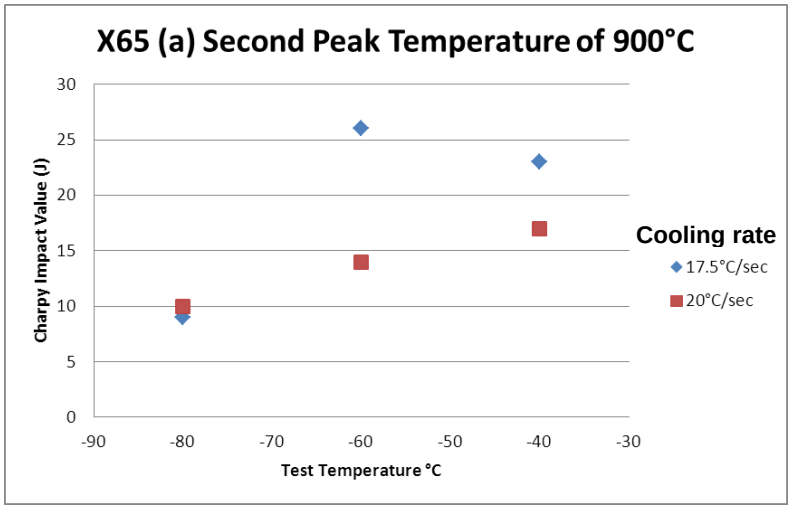

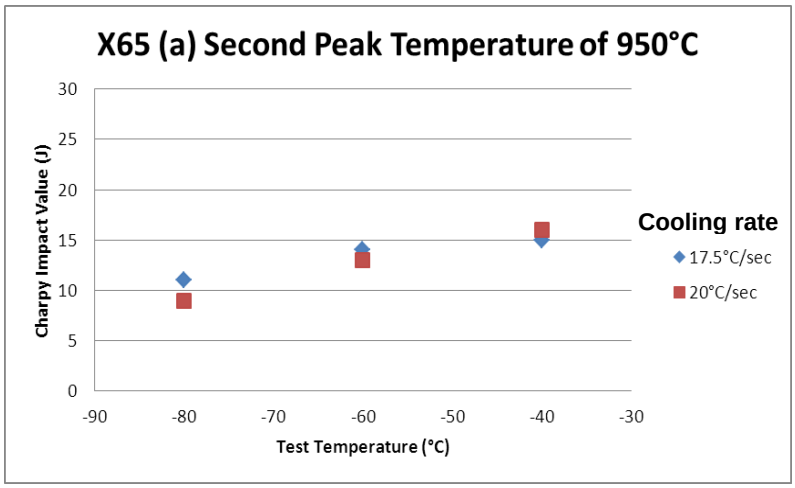

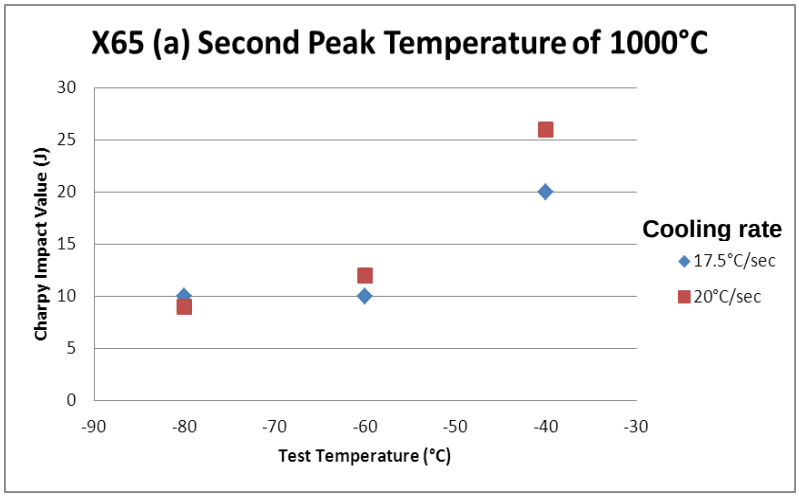

Figure 6-88 Comparison of the charpy impact results at different second peak temperatures with cooling rates for X65 (A)

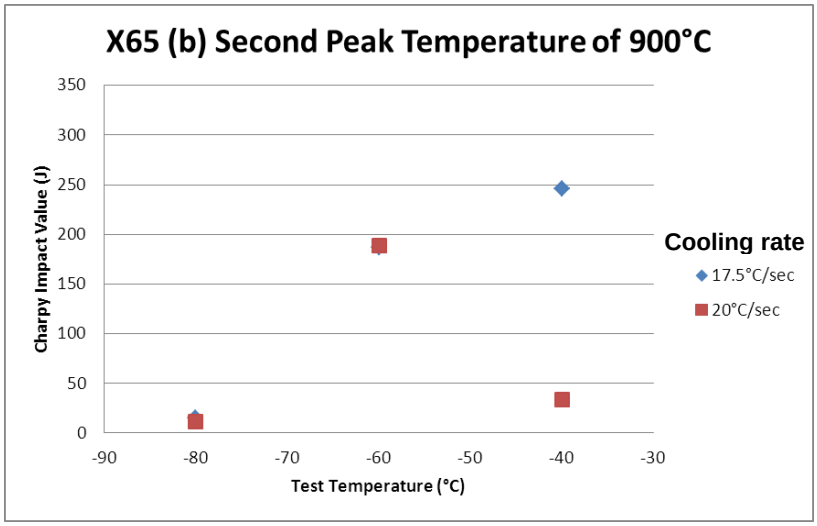

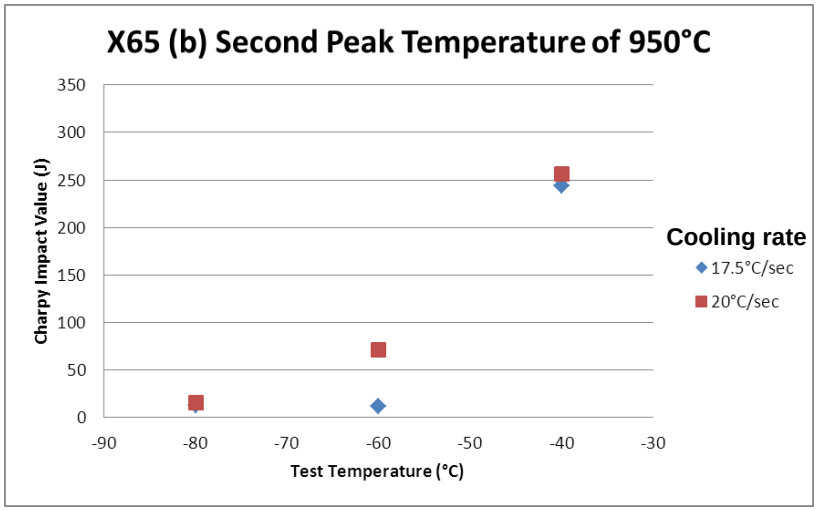

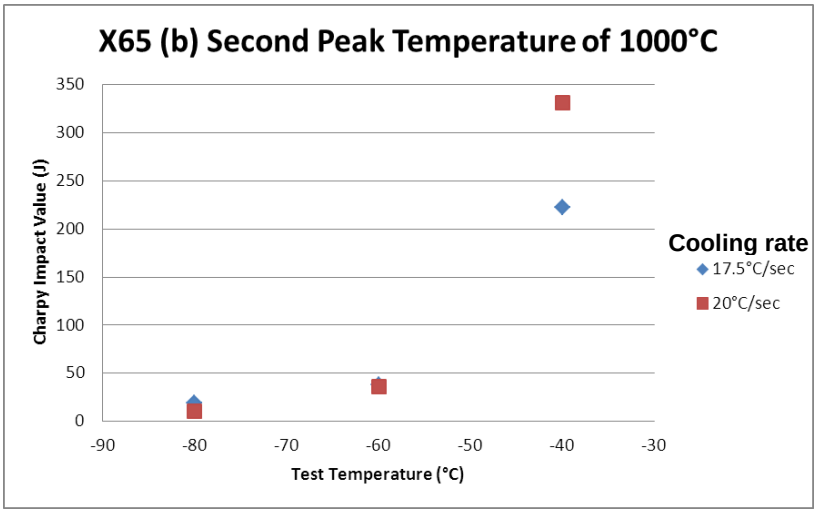

Figure 6-89 Comparison of the charpy impact results at different second peak temperatures with cooling rates for X65 (B)

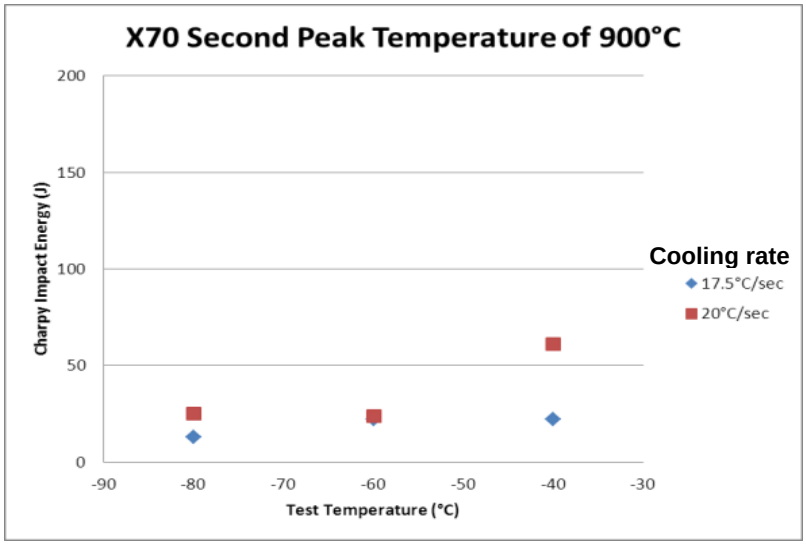

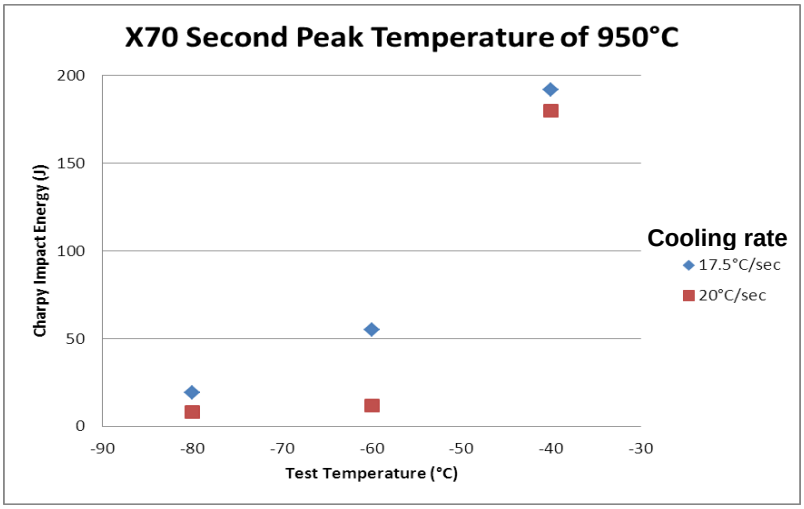

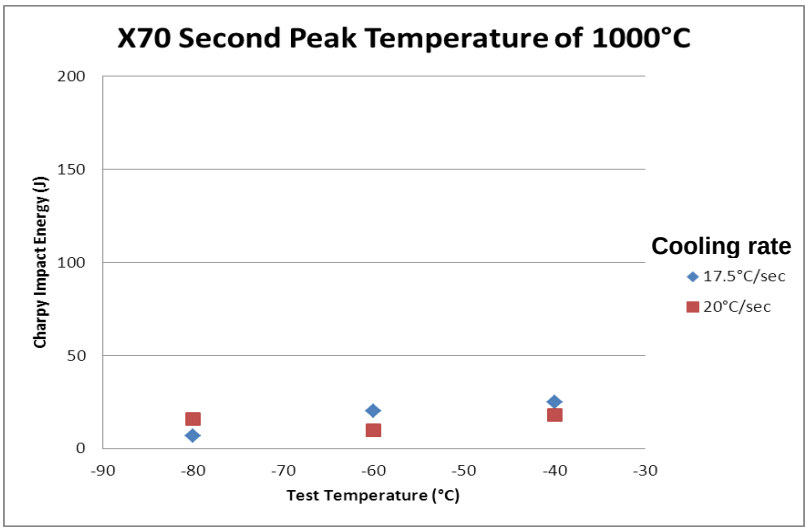

Figure 6-90 Comparison of the charpy impact results at different second peak temperatures with cooling rates for X70

6.5.2.2 Effect of cooling rate on the charpy impact results

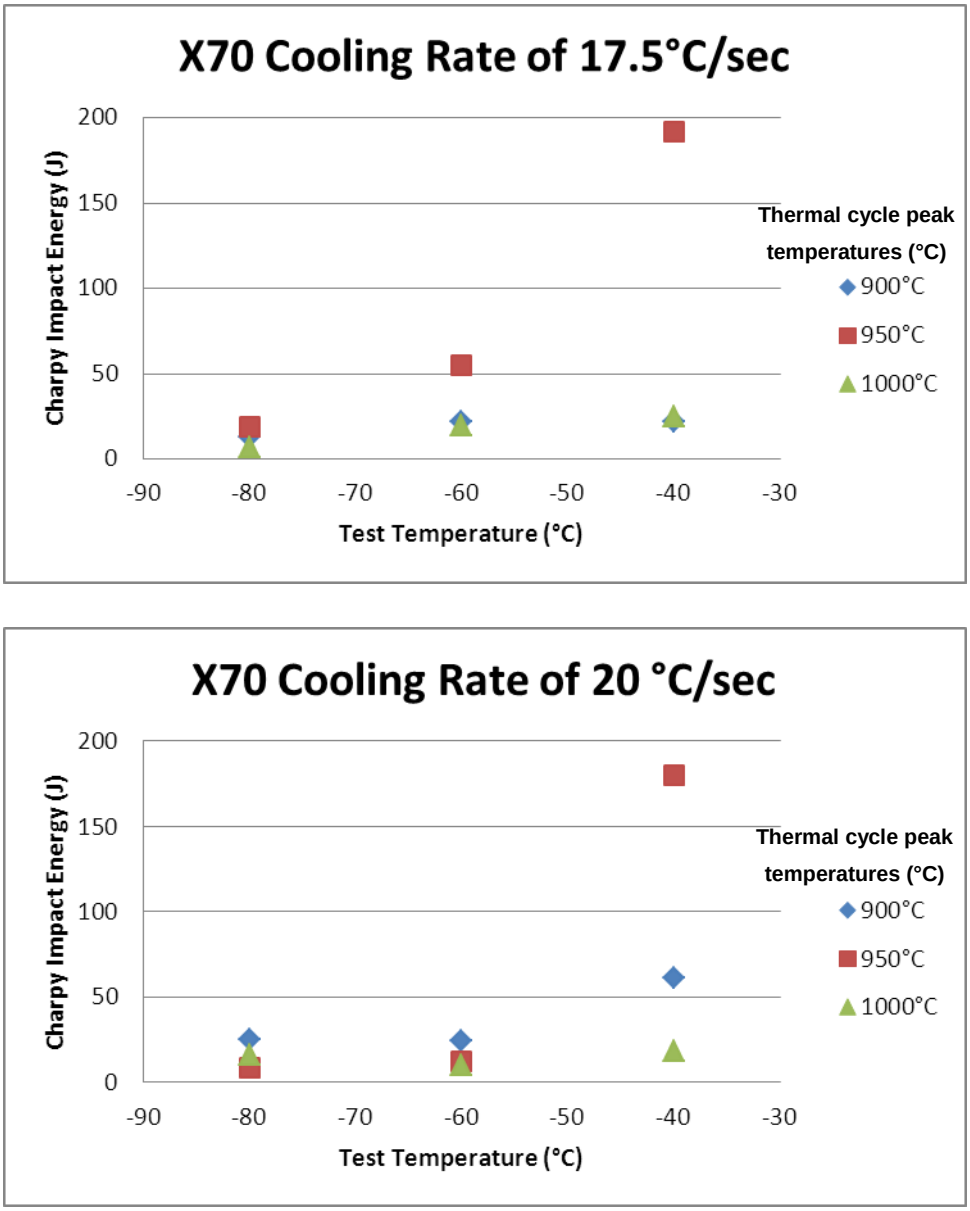

Figure 6-91 Effect of cooling rate on the charpy impact results for X70

6.5.3 Fractography of the broken charpy impact samples

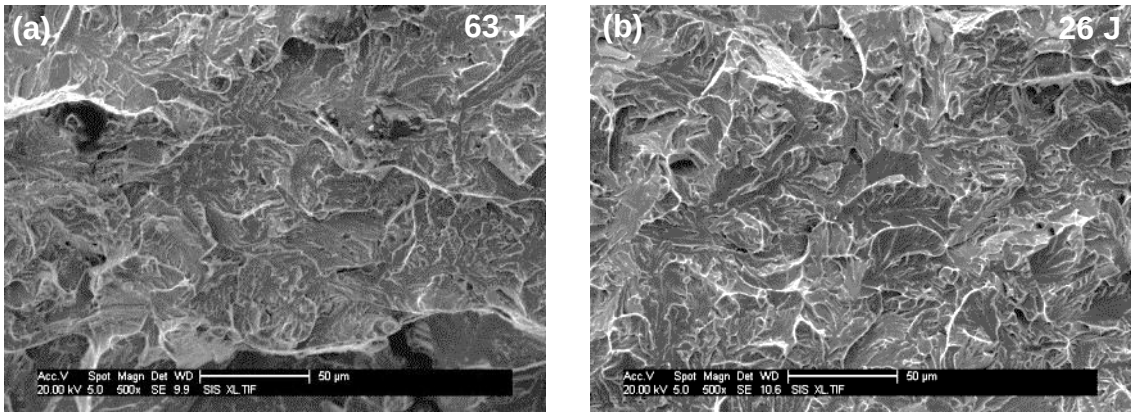

Figure 6-92 Fractographs of X65 (A) single thermal cycles at peak temperatures of (a) 1250°C and (b) 1000°C

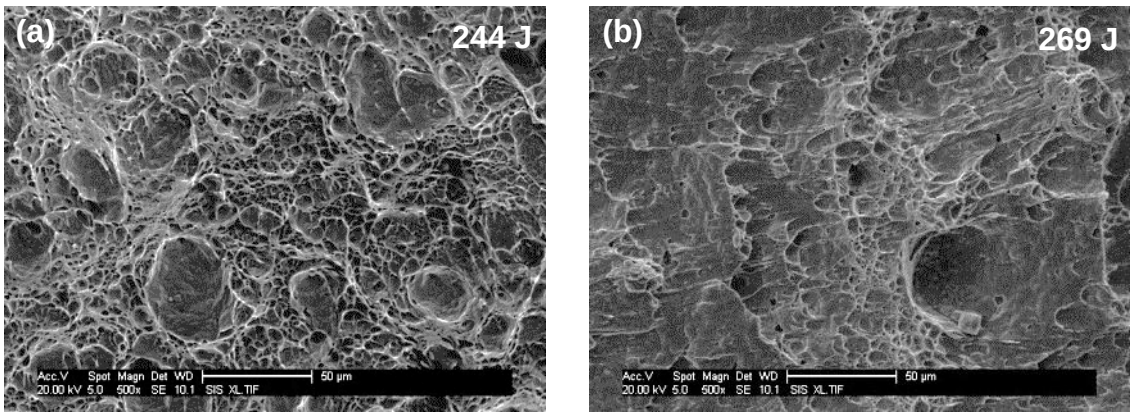

Figure 6-93 Fractographs of X65 (B) single thermal cycles at peak temperatures of (a) 1250°C and (b) 1000°C

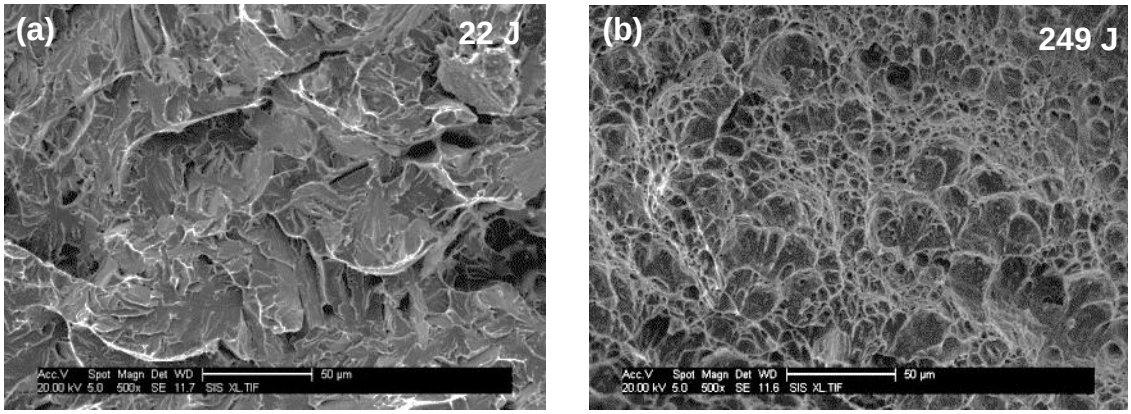

Figure 6-94 Fractographs of X70 single thermal cycles at peak temperatures of (a) 1250°C and (b) 1000°C

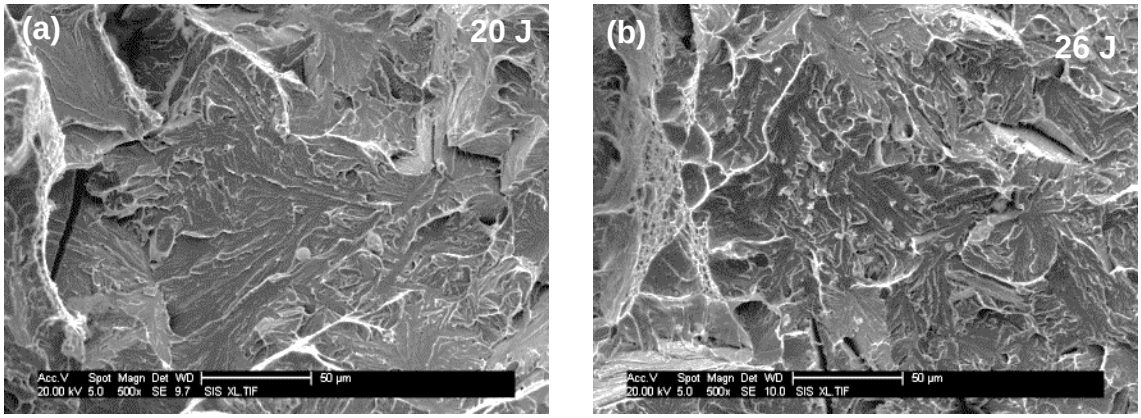

Figure 6-95 Fractographs of X65 (A) second thermal cycles of 1000° at cooling rates of (a) 17.5°C/s and (b) 20°C/s

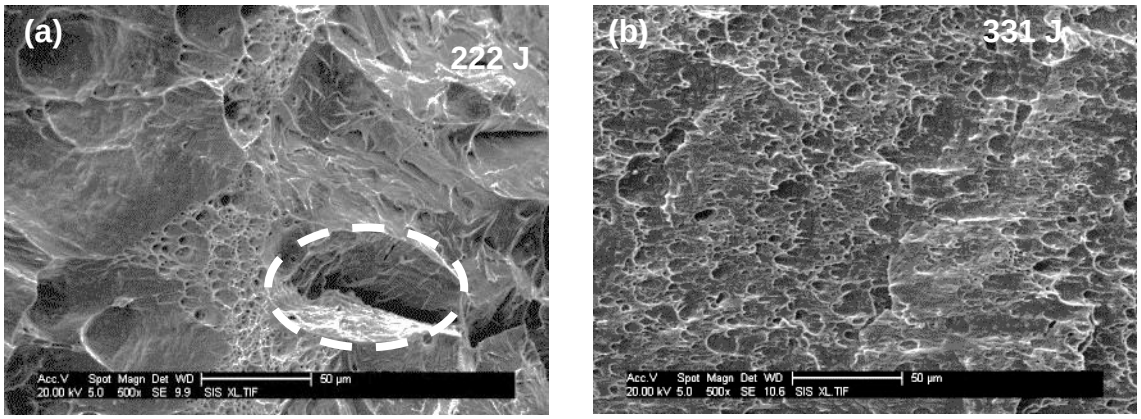

Figure 6-96 Fractographs of X65 (B) second thermal cycles of 1000° at cooling rates of (a) 17.5°C/s and (b) 20°C/s

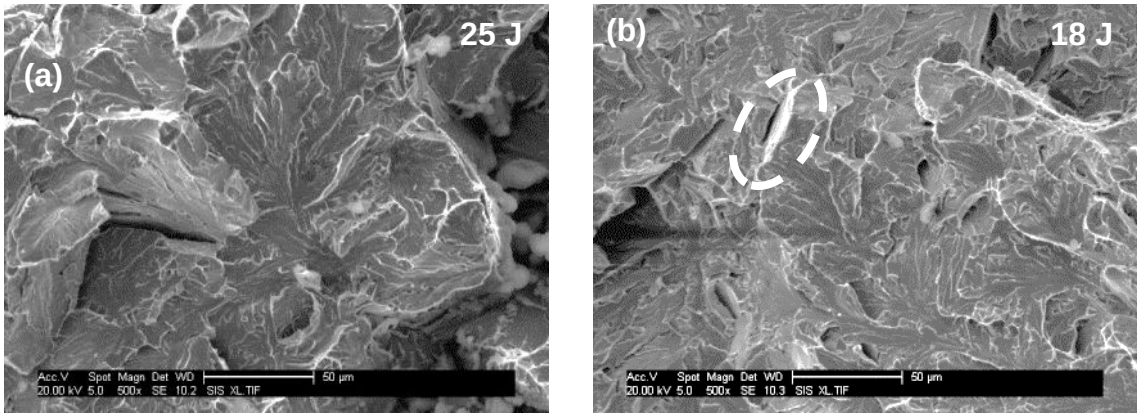

Figure 6-97 Fractographs of X70 second thermal cycles of 1000° at cooling rates of (a) 17.5°C/s and (b) 20°C/s

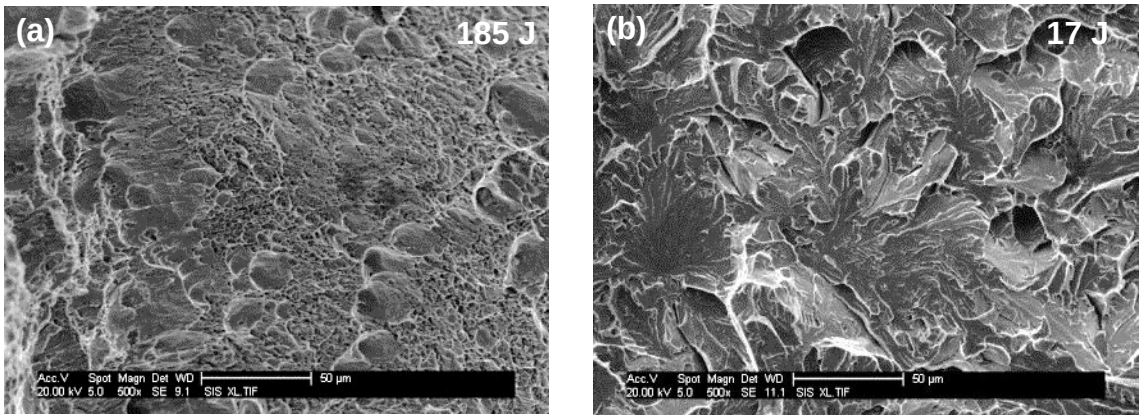

Figure 6-98 Fractographs of X65 (A) third thermal cycles with peak temperatures of (a) 450°C and (b) 350°C

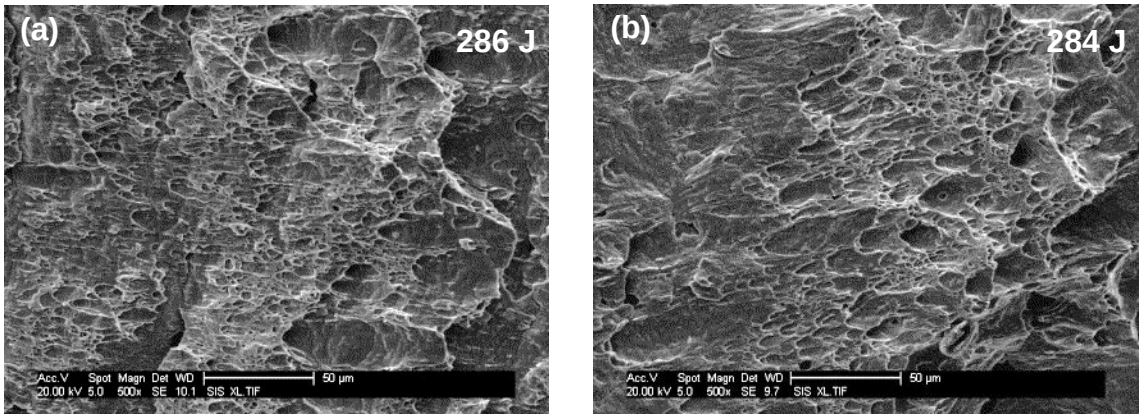

Figure 6-99 Fractographs of X65 (B) third thermal cycles with peak temperatures of (a) 450°C and (b) 350°C

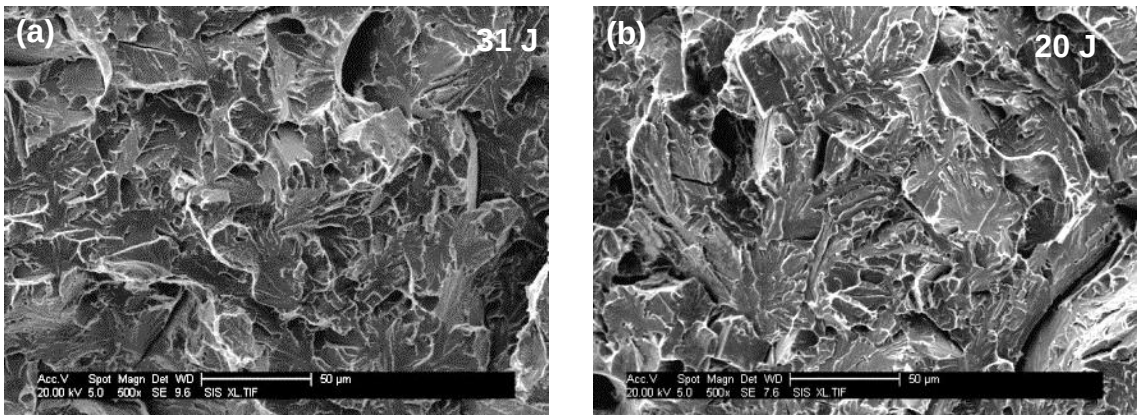

Figure 6-100 Fractographs of X70 third thermal cycles with peak temperatures of (a) 450°C and (b) 350°C

6.5.4 Microstructural characterisation of the charpy impact samples

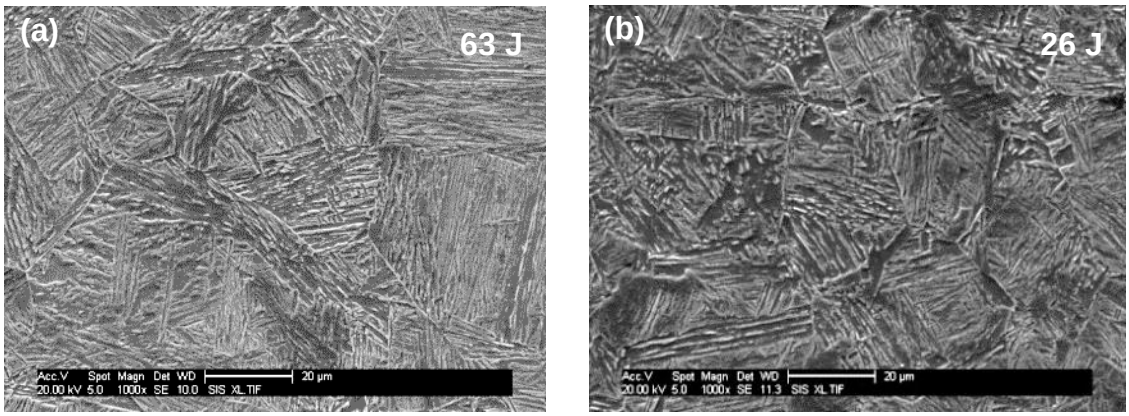

Figure 6-101 SEM micrographs of X65 (A) single thermal cycles at peak temperatures of (a) 1250°C and (b) 1000°C

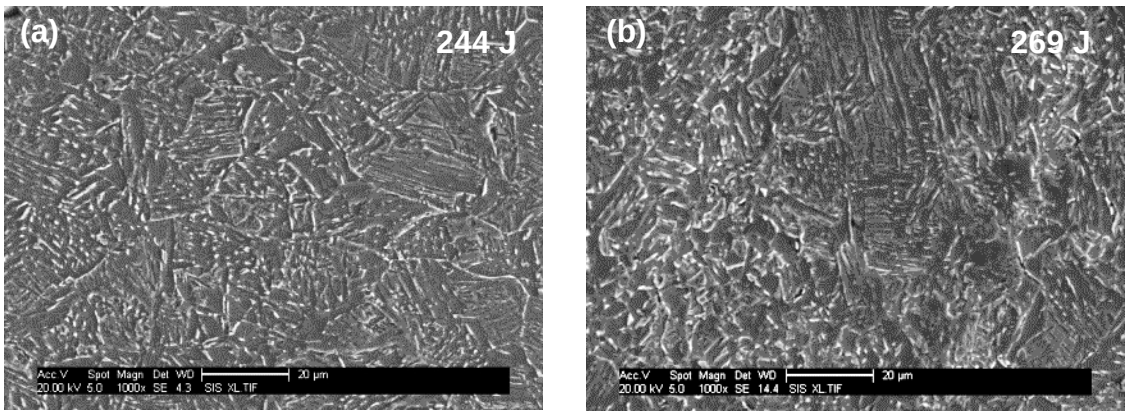

Figure 6-102 SEM micrographs of X65 (B) single thermal cycles at peak temperatures of (a) 1250°C and (b) 1000°C

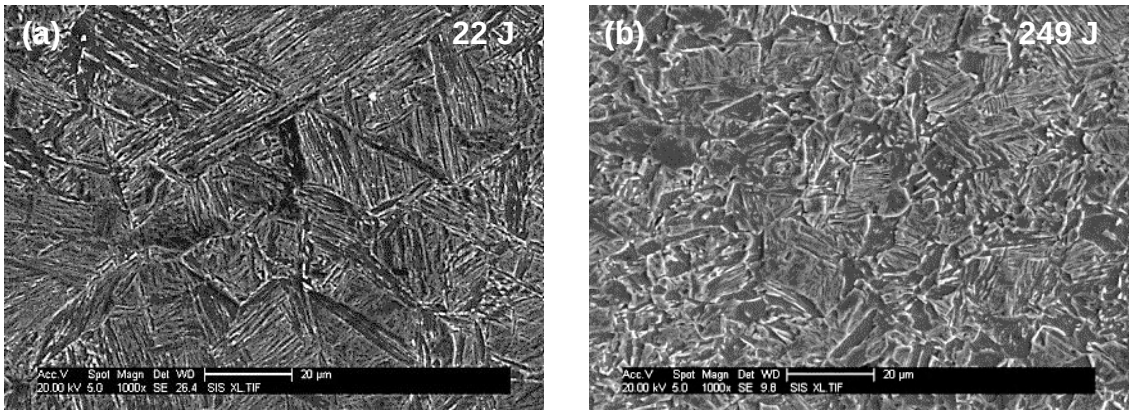

Figure 6-103 SEM micrographs of X70 single thermal cycles at peak temperatures of (a) 1250°C and (b) 1000°C

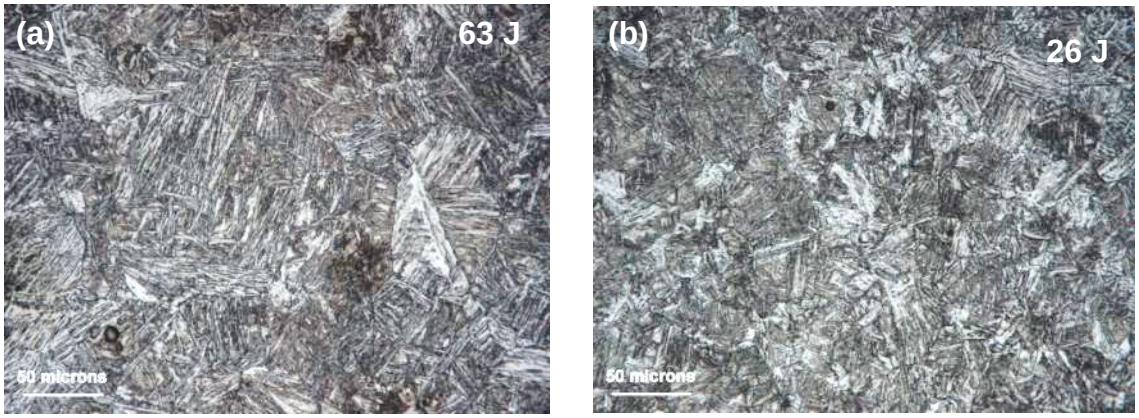

Figure 6-104 Optical micrographs of X65 (A) single thermal cycles at peak temperatures of (a) 1250°C and (b) 1000°C

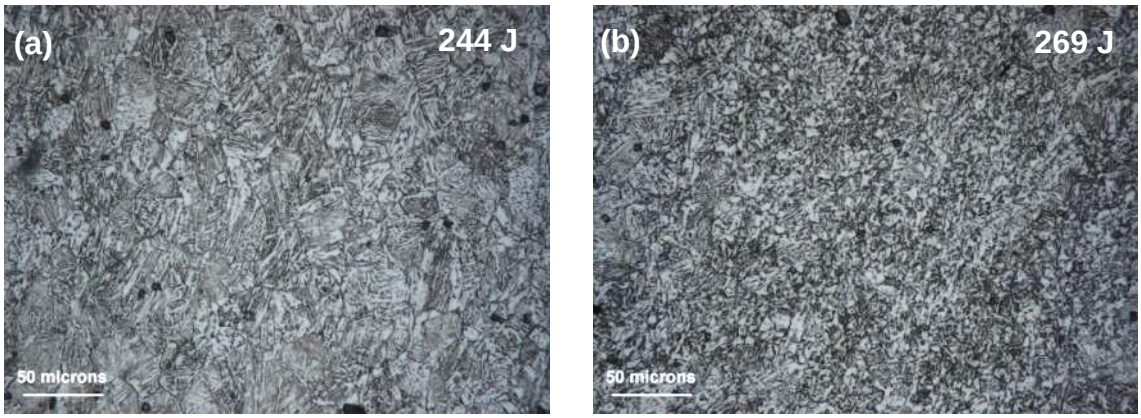

Figure 6-105 Optical micrographs of X65 (B) single thermal cycles at peak temperatures of (a) 1250°C and (b) 1000°C

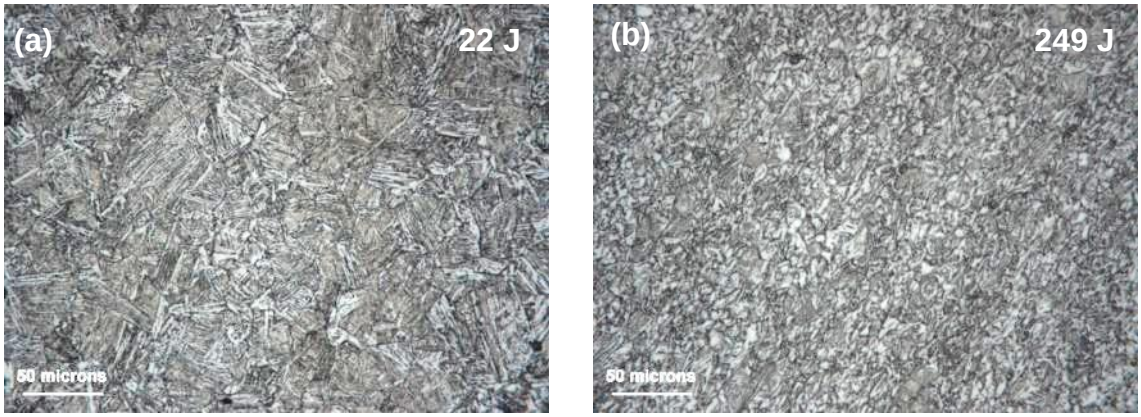

Figure 6-106 Optical micrographs of X70 single thermal cycles at peak temperatures of (a) 1250°C and (b) 1000°C

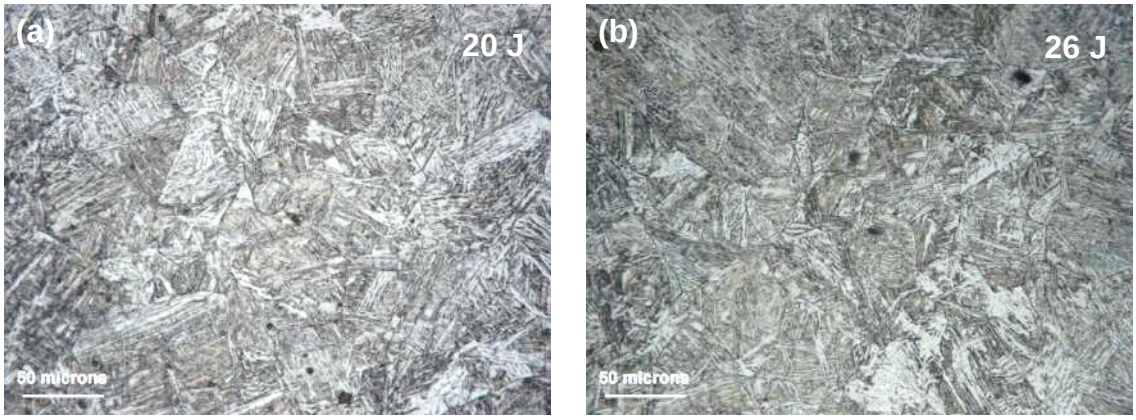

Figure 6-107 Optical micrographs of X65 (A) double thermal cycles with a second peak temperature of 1000°C, at cooling rates of (a) 17.5°C/s and (b) 20°C/s

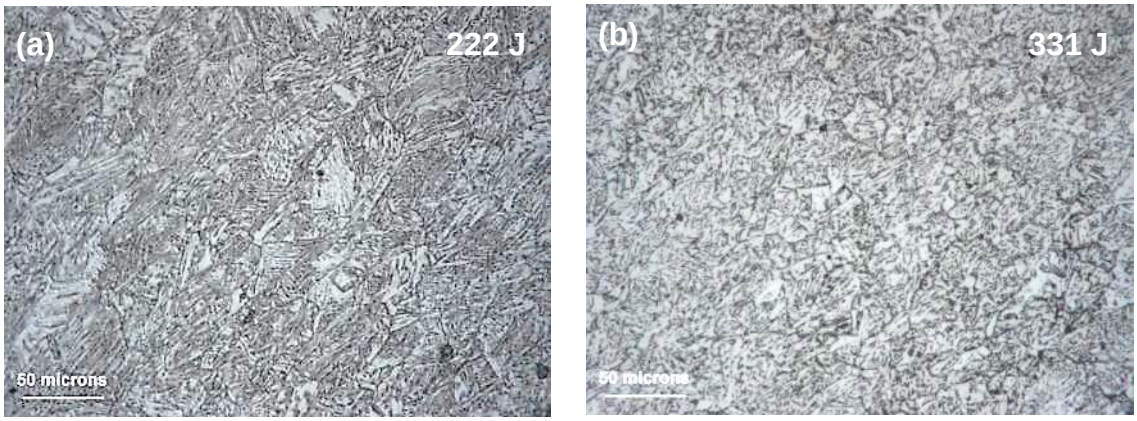

Figure 6-108 Optical micrographs of X65 (B) double thermal cycles with a second peak temperature of 1000°C, at cooling rates of (a) 17.5°C/s and (b) 20°C/s

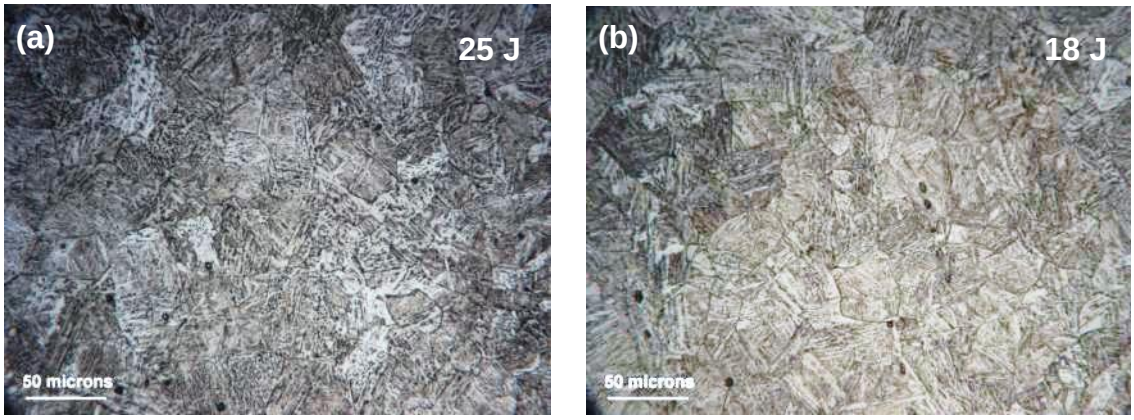

Figure 6-109 Optical micrographs of X70 double thermal cycles with a second peak temperature of 1000°C, at cooling rates of (a) 17.5°C/s and (b) 20°C/s

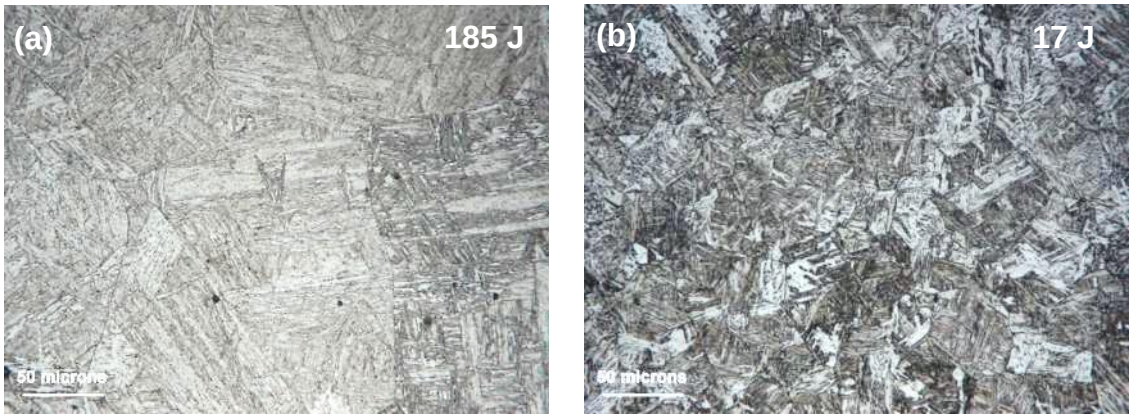

Figure 6-110 Optical micrographs of X65 (A) triple thermal cycles with third peak temperatures of (a) 450°C and (b) 350°C

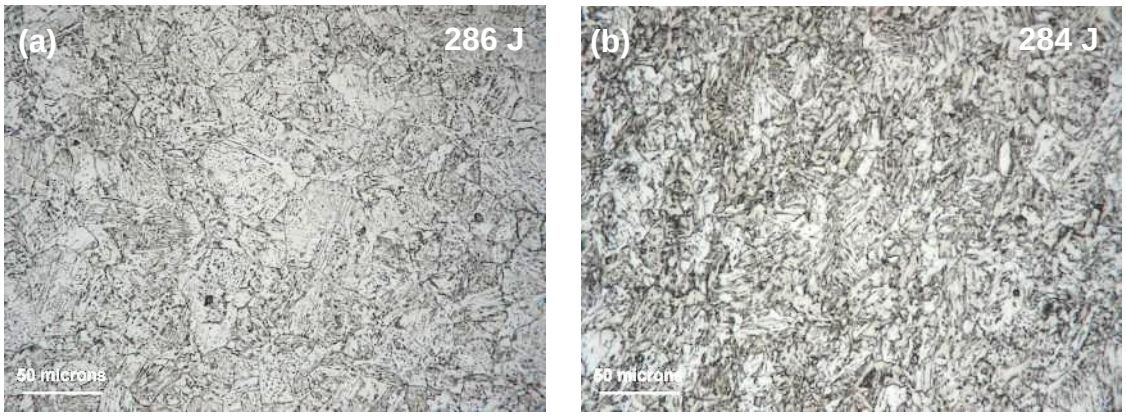

Figure 6-111 Optical micrographs of X65 (B) triple thermal cycles with third peak temperatures of (a) 450°C and (b) 350°C

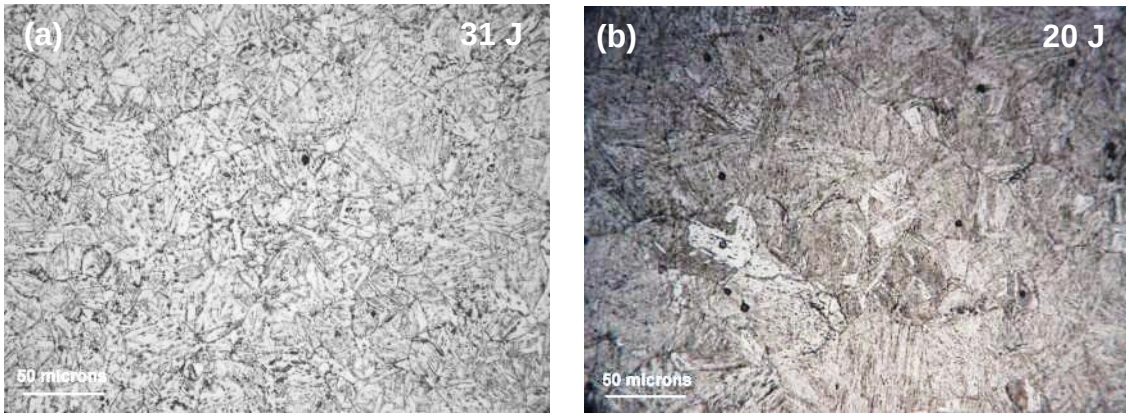

Figure 6-112 Optical micrographs of X70 triple thermal cycles with third peak temperatures of (a) 450°C and (b) 350°C

6.5.5 Hardness traverse of the charpy impact samples

Table 6-6 Hardness traverse HV0.5 (Average) for the X65 (A) charpy impact samples

		First Thermal Cycles		Second Thermal Cycles		Third Thermal Cycles		Hardness (HV0.5)		
No.	Heated at 500°C/s to	Cooled to (800°C) at	Cooled to (200°C) at	Heated at 500°C/s to	Cooled to (200°C) at	Heated at 500°C/s to	Cooled to (200°C) at	-40°C	-60°C	-80°C
1	1250	50 (9s)	35 (17.14s)	-	-	-	-	321 HV	305 HV	318 HV
2	1000	50 (9s)	35 (17.14s)	-	-	-	-	301 HV	278.4 HV	279.5 HV
3	1250	50 (9s)	35 (17.14s)	750	20 (27.5s)	-	-	245 HV	234 HV	230 HV
4	1250	50 (9s)	35 (17.14s)	800	20 (30.0 s)	-	-	239 HV	235 HV	235.6 HV
5	1250	50 (9s)	35 (17.14s)	850	20 (32.5s)	-	-	247.8 HV	245 HV	231 HV
6	1250	50 (9s)	35 (17.14s)	900	17.5 (40s)	-	-	254 HV	314 HV	253 HV
7	1250	50 (9s)	35 (17.14s)	900	20 (35.0s)	-	-	271.8 HV	276 HV	271.5 HV
8	1250	50 (9s)	35 (17.14s)	950	17.5 (42.85s)	-	-	269 HV	255 HV	262 HV
9	1250	50 (9s)	35 (17.14s)	950	20 (37.5s)	-	-	281 HV	262 HV	263 HV
10	1250	50 (9s)	35 (17.14s)	1000	17.5 (45.71s)	-	-	287 HV	276 HV	245 HV
11	1250	50 (9s)	35 (17.14s)	1000	20 (40)	-	-	303 HV	292 HV	277.6 HV
12	1250	50 (9s)	35 (17.14s)	1000	20 (40s)	450	5.5 (45.45s)	289 HV	258 HV	253 HV
13	1250	50 (9s)	35 (17.14s)	1000	20 (40s)	350	5.5 (27.27s)	271 HV	268.6 HV	270.7 HV

Table 6-7 Hardness traverse HV0.5 (Average) for the X65 (B) charpy impact samples

		First Thermal Cycles		Second Thermal Cycles		Third Thermal Cycles		Hardness (HV0.5)		
No.	Heated at 500°C/s to	Cooled to (800°C) at °C/s	Cooled to (200°C) at °C/s	Heated at 500°C/s to	Cooled to (200°C) at °C/s	Heated at 500°C/s to	Cooled to (200°C) at °C/s	-40°C	-60°C	-80°C
1	1250	50 (9s)	35 (17.14s)	-	-	-	-	292 HV	273 HV	262.6 HV
2	1000	50 (9s)	35 (17.14s)	-	-	-	-	262 HV	273 HV	261 HV
3	1250	50 (9s)	35 (17.14s)	750	20 (27.5s)	-	-	274 HV	270 HV	236 HV
4	1250	50 (9s)	35 (17.14s)	800	20 (30.0 s)	-	-	266 HV	248 HV	250 HV
5	1250	50 (9s)	35 (17.14s)	850	20 (32.5s)	-	-	261.7 HV	260 HV	228 HV
6	1250	50 (9s)	35 (17.14s)	900	17.5 (40s)	-	-	267.5 HV	265 HV	231 HV
7	1250	50 (9s)	35 (17.14s)	900	20 (35.0s)	-	-	245.5 HV	265.8 HV	229 HV
8	1250	50 (9s)	35 (17.14s)	950	17.5 (42.85s)	-	-	266.7 HV	245.8 HV	232.7 HV
9	1250	50 (9s)	35 (17.14s)	950	20 (37.5s)	-	-	267 HV	256 HV	235.5 HV
10	1250	50 (9s)	35 (17.14s)	1000	17.5 (45.71s)	-	-	286 HV	245 HV	246 HV
11	1250	50 (9s)	35 (17.14s)	1000	20 (40)	-	-	271 HV	250.8	243 HV
12	1250	50 (9s)	35 (17.14s)	1000	20 (40s)	450	5.5 (45.45s)	263 HV	266 HV	240.5 HV
13	1250	50 (9s)	35 (17.14s)	1000	20 (40s)	350	5.5 (27.27s)	260.6 HV	262 HV	227 HV

Table 6-8 Hardness traverse HV0.5 (Average) for the X70 charpy impact samples

		First Thermal Cycles		Second Thermal Cycles		Third Thermal Cycles		Hardness (HV0.5)		
No.	Heated at 500°C/s to	Cooled to 800°C at °C/s	Cooled to 200°C at °C/s	Heated at 500°C/s to	Cooled to 200°C at °C/s	Heated at 500°C/s to	Cooled to (200°C) at °C/s	-40°C	-60°C	-80°C
1	1250	50 (9s)	35 (17.14s)	-	-	-	-	288 HV	285 HV	268 HV
2	1000	50 (9s)	35 (17.14s)	-	-	-	-	286 HV	278.7 HV	277 HV
3	1250	50 (9s)	35 (17.14s)	950	17.5 (42.85s)	-	-	278.5 HV	254 HV	249 HV
4	1250	50 (9s)	35 (17.14s)	950	20 (37.5s)	-	-	279 HV	286 HV	283 HV
5	1250	50 (9s)	35 (17.14s)	900	17.5 (40s)	-	-	287 HV	288 HV	249 HV
6	1250	50 (9s)	35 (17.14s)	900	20 (35s)	-	-	257 HV	261 HV	238 HV
7	1250	50 (9s)	35 (17.14s)	1000	17.5 (45.71s)	-	-	271 HV	247 HV	292 HV
8	1250	50 (9s)	35 (17.14s)	1000	20 (40)	-	-	286 HV	280 HV	259 HV
9	1250	50 (9s)	35 (17.14s)	1000	20 (40s)	450	5.5 (45.45s)	246 HV	261 HV	260 HV
10	1250	50 (9s)	35 (17.14s)	1000	20 (40s)	350	5.5 (27.27s)	288 HV	275 HV	277 HV
11	1250	50 (9s)	35 (17.14s)	950	17.5 (42.85s)	450	5.5 (45.45s)	253 HV	251 HV	259 HV
12	1250	50 (9s)	35 (17.14s)	950	17.5 (42.85s)	350	5.5 (27.27s)	285 HV	266.7 HV	274 HV
13	1250	50 (9s)	35 (17.14s)	900	17.5 (40s)	450	5.5 (45.45s)	253 HV	252 HV	248 HV
14	1250	50 (9s)	35 (17.14s)	900	17.5 (40s)	350	5.5 (27.27s)	260.5 HV	270 HV	270.8 HV
15	1250	50 (9s)	35 (17.14s)	950	20 (37.5s)	450	5.5 (45.45s)	249 HV	278 HV	233 HV
16	1250	50 (9s)	35 (17.14s)	950	20 (37.5s)	350	5.5 (27.27s)	288 HV	285 HV	266 HV
17	1250	50 (9s)	35 (17.14s)	900	20 (35s)	450	5.5 (45.45s)	248.6 HV	237.8 HV	255.4 HV

6.5.6 Comparison of hardness (HV0.5) between the inner and the outer surfaces

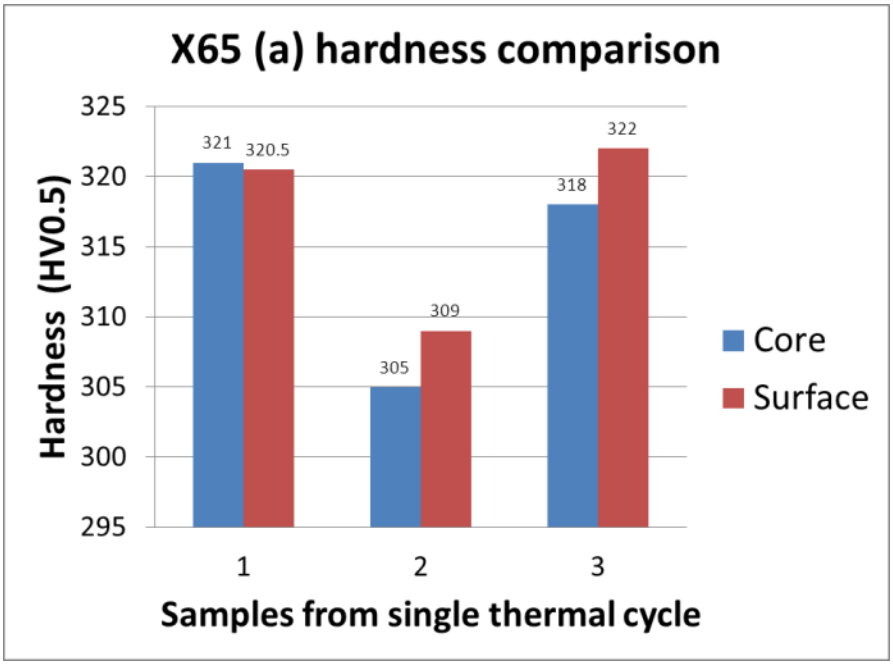

Figure 6-113 Hardness comparison on X65 (A) single thermal cycles, between inner and outer surfaces

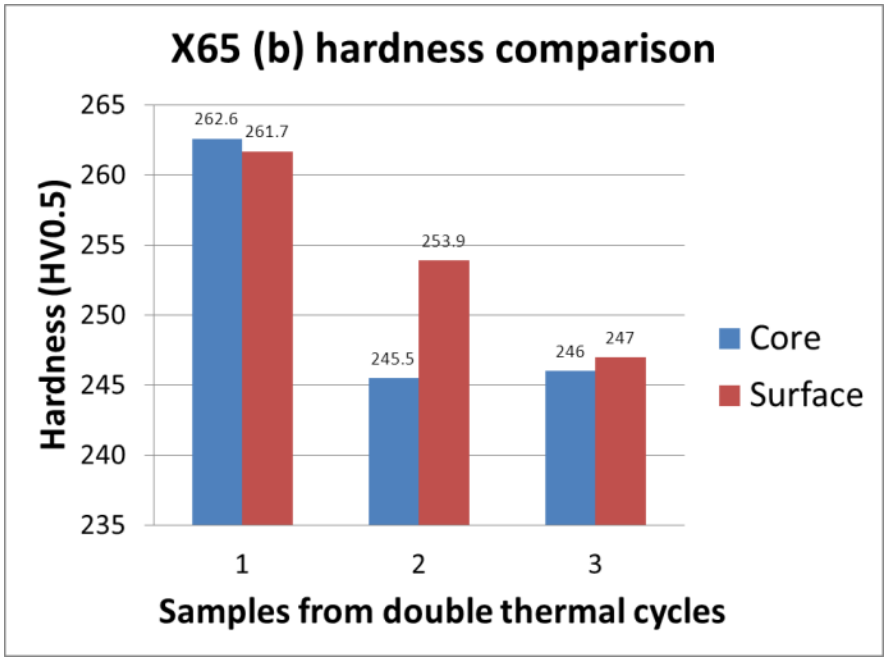

Figure 6-114 Hardness comparison on X65 (B) double thermal cycles, between inner and outer surfaces

7 DISCUSSION

This chapter will present a critical analysis and interpretation of the results. Direct and indirect comparisons with previous research will be made, based on the findings.

7.1 **Parent materials**

Under this heading, the parent materials will be discussed based on their mechanical and microstructural differences.

7.1.1 Parent materials mechanical and metallurgical analyses

The four pipeline steels used in this research have been analysed both mechanically and metallurgically. They all happen to be different from one another in one way or the other.

The X65 (a) seamless pipes with a wall thickness of 25.4 mm in the as rolled condition, is predominantly having polygonal ferrite (PF) and acicular ferrite (AF) phases, with a very little pearlite.[155; 156] While the thermo mechanically processed X65 (b), with a wall thickness of 31 mm, is showing an accelerated cooled structure, with very fine grains. Predominant phases are polygonal ferrite (PF), acicular ferrite (AF) and some bainite (B).[157]

X70 pipeline steel is a TMCP material, the parent structures mainly constitute of polygonal ferrite (PF) and bainite (B), with few acicular ferrite (AF) phases.[158; 159] And the X100 grade is also a TMCP material, its main constituents are acicular ferrite (AF) and bainite (B).[159; 160]

All the parent materials have satisfy the API 5L[98] and DNV-OS-F101[144] in terms of microstructures, hardness, impact toughness and tensile properties as shown in figure 6-1 to figure 6-6 on pages 79 - 85.

Hardness values (HV0.5) of the parent materials are given in figure 6-1 on page 79. X65 (a) has the lowest hardness of 191 HV0.5 and X65 (b) has 203 HV0.5. This reflects the parent materials structures because the latter is produced through TMCP route with a sub-micron grains structure, while the former is

having a rolled condition structure with larger grains. The X70 has a hardness of 209 HV0.5 and the X100 has 270 HV0.5. All the materials are within the maximum hardness values recommended by DNV as given in table 7-1.

The yield strength ($R_{t0.5}$) and tensile strength (Rm) specified for pipeline steels[98; 144] is given in table 7-1. The average values from the samples tested have been presented in figure 6-3 on page 80 for all the parent materials. The maximum YS/UTS ratio has been given as 0.93 in table 7-1 for all grades. Published data have shown that micro alloyed steels produced by accelerated cooling generally have a lower YS/UTS ratio ranging from 0.80 to 0.90.[13; 161] The X65 (a) and (b) have YS/UTS ratio of 0.81 and 0.83 respectively, while the X70 has 0.88 and the X100 YS/UTS ratio was 0.85, as shown in figure 6-4.

Impact toughness is very important in these pipeline steels. Charpy impact toughness (CVN) was used to characterise all the parent materials. The average and minimum CVN for these materials at their operating temperatures have been given in table 7-1.[98; 144] The Charpy impact results for the parent materials are shown in figure 6-2 on page 80.[3; 162]

As stated by the standards, the test temperatures for CVN should be the operating temperatures, and varies from one application to another. In this research, lower test temperatures were used throughout as worst case scenarios, they were -40°C, -60°C and -80°C.

Table 7-1 Mechanical properties requirements for the parent materials[144]

Materials	*Min. Yield strength $R_{t0.5}$ (MPa)*	*Min. Tensile Strength Rm (MPa)*	*Max $R_{t0.5}$ / Rm Ratio*	*Max. BM Hardness (HV10)*	*Average Charpy V-notch (J)*	*Min. Charpy V-notch (J)*
X65	450	535	0.93	270	45	38
X70	485	570	0.93	300	50	40
X100	555	625	0.93	300	56	45

All the four parent materials were showing an optimum CVN at -60°C, which means that the ductile to brittle transition temperatures (DBTT) have not been exceeded due to their excellent toughness.

7.2 **Dilatometric experiments (CCT Diagrams)**

Under this heading, the dilatation experiments will be explained, with respect to dilatation curves and their interpretations. CCT diagrams will be discussed together with the corresponding microstructures.

7.2.1 Thermal cycles and dilatation for CCTs

Total of forty seven samples from the investigated materials [12 of X65 (a), 13 of X65 (b), 11 of X70, and 11 of X100] were heated and cooled at different cooling rates in a Gleeble 3500™ machine and a dilatometer with a resolution of ± 2.5 mm. The samples were heated to 950°C at a distinctive heating rate of 400°C/s, this reflect the rate of heating from a real weld, as seen on the real thermal cycles of a submerged arc weld in figure 6-60. The heating rate used in these experiments differs from what has been reported in other papers.[113; 163] Even those researchers that tried to simulate welding thermal cycles, only heated their samples as fast as 150°C/s[109] and 200°C/s[164] heating rates.

The instantaneous heating normally observed in a weld is completely different from conventional heat treatment process or slow heating. The heating rate and the peak temperature, have a significant effect on the ferrite to austenite transformation (α-γ), and influence the initial austenite grain size. This initial austenite grain size condition is important in determining the final microstructural and mechanical properties of the material.[121]

By using high heating rate, the material was not allowed to undergo an equilibrium transformation. Therefore, in these experiments the samples were taken to the austenitic region in less than 3 seconds. Depending on the initial microstructure, there is no time for the dissolution of second phases before crossing the A_{C1} and A_{C3} temperatures. Thereby instant transformation of areas with higher carbon into austenite begins. Samples were then held for 300 seconds at 950°C for homogenization (austenitization).

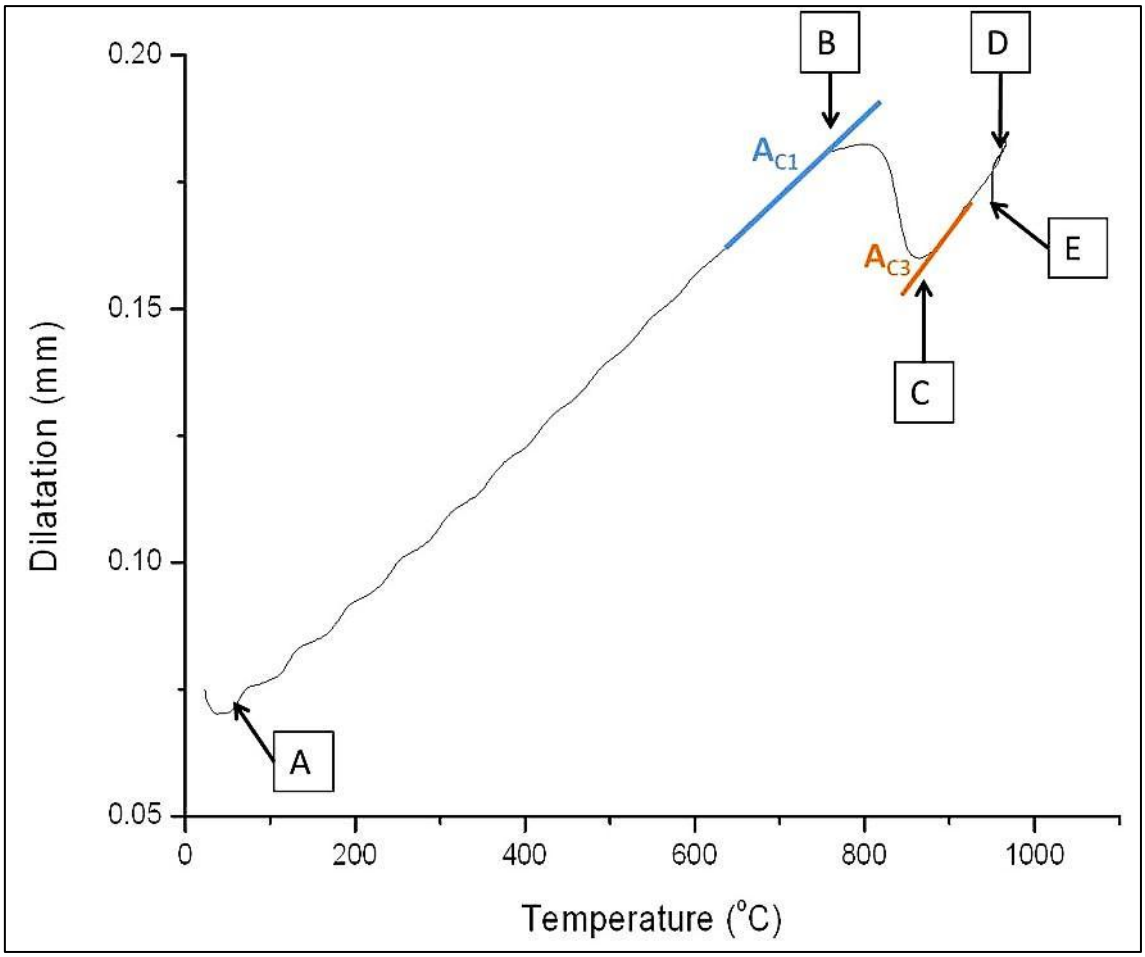

Figure 7-1 Continuous heating part of a dilatation curve

From the continuous heating part of the dilatation curve, the critical transformation temperatures i.e. A_{C1} and A_{C3} were determined.[107] After subjecting the samples to a series of heating and cooling sequence, the corresponding cooling rates, $t_{8/5}$ and hardness values were recorded as given in table 6-1.

The analysis of the dilatation curves,[107] leads to the determination of the experimental transformation temperatures of A_{C1} and A_{C3} for the pipeline materials, the theoretically calculated temperatures[165] were also obtained, so are the calculated martensite start temperatures M_S,[136] they are all given in table 6-2. The theoretical temperatures happen to be more conservative than the practical once, because the chemical composition was used to estimate the

transformation temperatures using the empirical formulas. Therefore, the available chemical analysis will influence the results, so also the present and absent of some elements might have significant influence.[136; 165]

Figure 7-1 describes the continuous heating and holding part of the dilatation curve. Points A-B represents the first part of the heating curve, at point B the volumetric contraction due to austenite formation begins. This point is termed as austenite transformation start (A_{C1}). Due to increase in temperature, this contraction compensates and reverses at point C, which is called the austenite transformation finish (A_{C3}). Point D represents the end of the instantaneous heating, and corresponds to the maximum temperature. Finally, points D-E represents the holding time of 300 seconds for austenitization.

Generally in steels, the cooling from austenitic region (γ-transformation) to room temperature determines its final microstructure and properties. In this research, CCT diagrams were constructed using a variety of cooling rates that covers most of the thermal cycles in multi-pass welds. The cooling rates were selected based on the information from the available published data.[91; 109; 163; 164] The various transformation start and finish temperatures from the austenitic transformation were also identified.

The non-isothermal decomposition of austenite into ferrite and pearlite is shown in figure 7-2. Points A and B were identified by extrapolating the linear portion of the cooling part from the dilatation curve. They are considered as start and finish points respectively. The tangential method was used to identify the transformation points. This method makes use of tangent lines dropped on the dilatation curve, and the point where deviation from linearity is observed, is taken as the transformation points.[107]

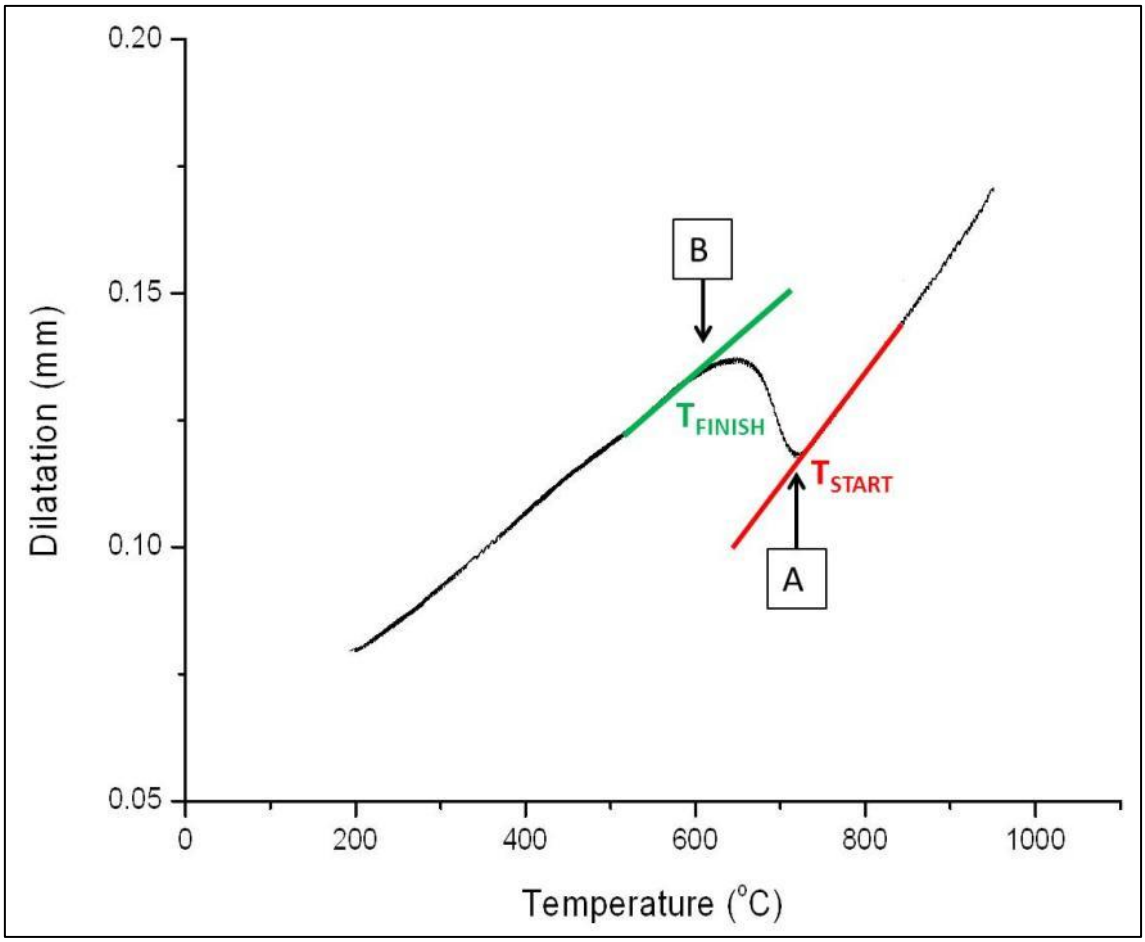

Figure 7-2 Cooling dilatation curve

7.2.2 CCT Diagrams

Continuous cooling transformation diagrams of the four pipeline steels used in this research were constructed. This is to see the influence of multi-pass welding thermal cycles on the parent materials, especially the metallurgical phase evolution in the heat affected zones. Figure 6-12 to figure 6-15 presented the non-equilibrium/continuous cooling curves, and the black dots are the transformation start and finish temperatures as observed from the dilatational curves, superimposed on the cooling curves.

In this chapter, new CCT diagrams are presented, with the transformation points joined together, marking out clearly the start and finish lines of the different phase domain within the CCT diagram of each material. The various phases were characterised from the metallographic examination of the samples,

and hardness traverses were made. Similar diagrams from available published research and electronic resources were all considered in the interpretations.

7.2.2.1 X65 (a) CCT diagram and microstructures

The CCT diagram of X65 (a) seamless pipe is shown in figure 7-3. Cooling range of 0.3°C/s to 50°C/s corresponding to $t_{8/5}$ of 1000 s to 6 s respectively were used, they are given in table 7-2. The ferrite start transformation mostly falls above the A_{C1} line, meaning that ferrite starts forming within the intercritical region upon cooling. This suggest that the alloy contains little amount of elements (Mo, Ni, Cu and Cr) that supresses the austenite to ferrite transformation.[13]

From the CCT diagram and available data, the highest cooling rate obtained for this material was 50°C/s ($t_{8/5}$ = 6 s), the corresponding micrograph is shown in figure 6-16 (a). The main microstructural constituents are widmanstätten ferrite (WF), polygonal ferrite (PF), some bainite (B) and/or acicular ferrite (AF) as explained in some papers.[155] This is due to the nature of the material in terms of composition and hardenability, coupled with a cooling rate that wasn't fast enough to produce a fully martensitic structure. There was almost a complete transformation of austenite before the martensite start temperature was reached, therefore, little or no martensite was formed. This reflects on the hardness value of (252 HV) obtained from the fastest cooled CCT sample, as compared to that of the water quenched sample with hardness value of (341 HV) and a fully martensitic structure as shown in micrograph (a) of figure 7-4.

But there was a noticeable presence of martensite in some samples, such as the sample cooled at the rate of 46.8°C/s ($t_{8/5}$ = 6.4 s), as shown in micrograph (b) in figure 6-16, it has a corresponding hardness value of 271 HV. Similar transformation was sustained up to a cooling rate of 20°C/s ($t_{8/5}$ = 15 s) shown in figure 6-16 (c), with a hardness of 264 HV. At this point, the bainitic reaction retards or almost ceased, even though there was a very little amount of bainite seen on the micrograph of the sample cooled at 12°C/s ($t_{8/5}$ = 25 s), also at this cooling rate the pearlitic islands starts to emerge as shown in figure 6-16 (d).

This means that the diffusion-less controlled transformation (martensite and bainite) have ceased and diffusion controlled phases such as pearlite start to emerge.

Pearlite becomes clearly visible at the rate of 3.33°C/s ($t_{8/5}$ = 90 s) shown in figure 6-16 (f) with a hardness of 174 HV, and keeps growing as the cooling rate is decreased further. At the slowest cooling rate used in this experiment i.e. 0.3°C/s ($t_{8/5}$ = 1000 s), the sample had fully transformed in to a ferritic matrix and pearlitic islands as shown in figure 6-16 (h), with a hardness of 157 HV.

Table 7-2 X65 (a) thermal cycles and the corresponding hardness values

Base Metal	Time ($t_{8/5}$) sec	6	6.3	6.4	10.4	15	25	50	90	250	400	600	1000
	CR (°C/s)	50	47.6	46.8	28.8	20	12	6	3.33	1.2	0.75	0.5	0.3
X65 (a)	Hardness (HV0.5)	252	270	271	233	264	196	199	174	154	147	147	157

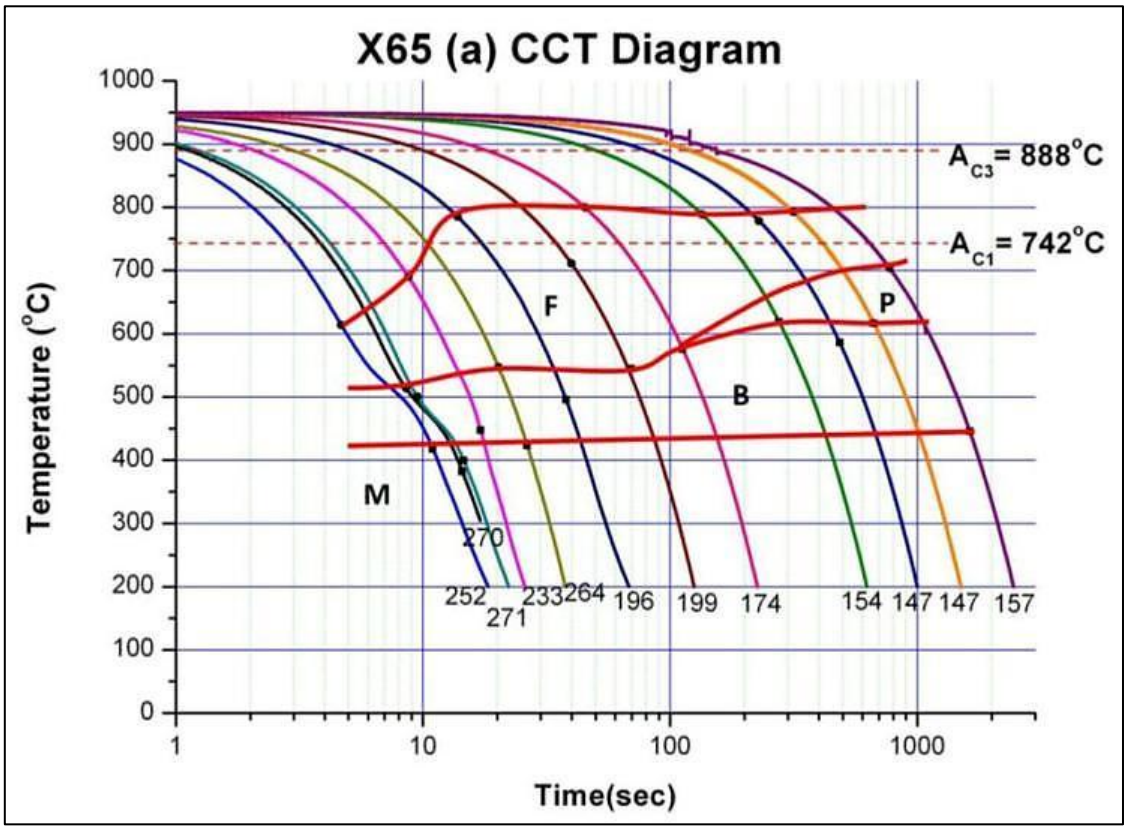

Figure 7-3 X65 (a) CCT diagram with various transformation lines identified

There was enough time for the grains to grow in to a mixture of very large (75 µ) and small grains (5 µ), with an average size of about 25 µ. The banded structure becomes obvious at a rate of 1.2°C/s ($t_{8/5}$ = 250 s) as shown in figure 6-16 (g), while the higher cooling rate samples had more of a mixed structure.

Figure 6-16 (d) is equivalent to that of the parent metal and thereafter, figure 6-16 (e) onwards it is a much softer matrix. Both the oil and water quenched samples as shown in figure 6-23 (a) and figure 6-24 (a) respectively, had higher hardness than that of the parent metal, while the air cooled or normalized sample shown in figure 6-22 (a) had a lower hardness of 160 HV than the parent metal.

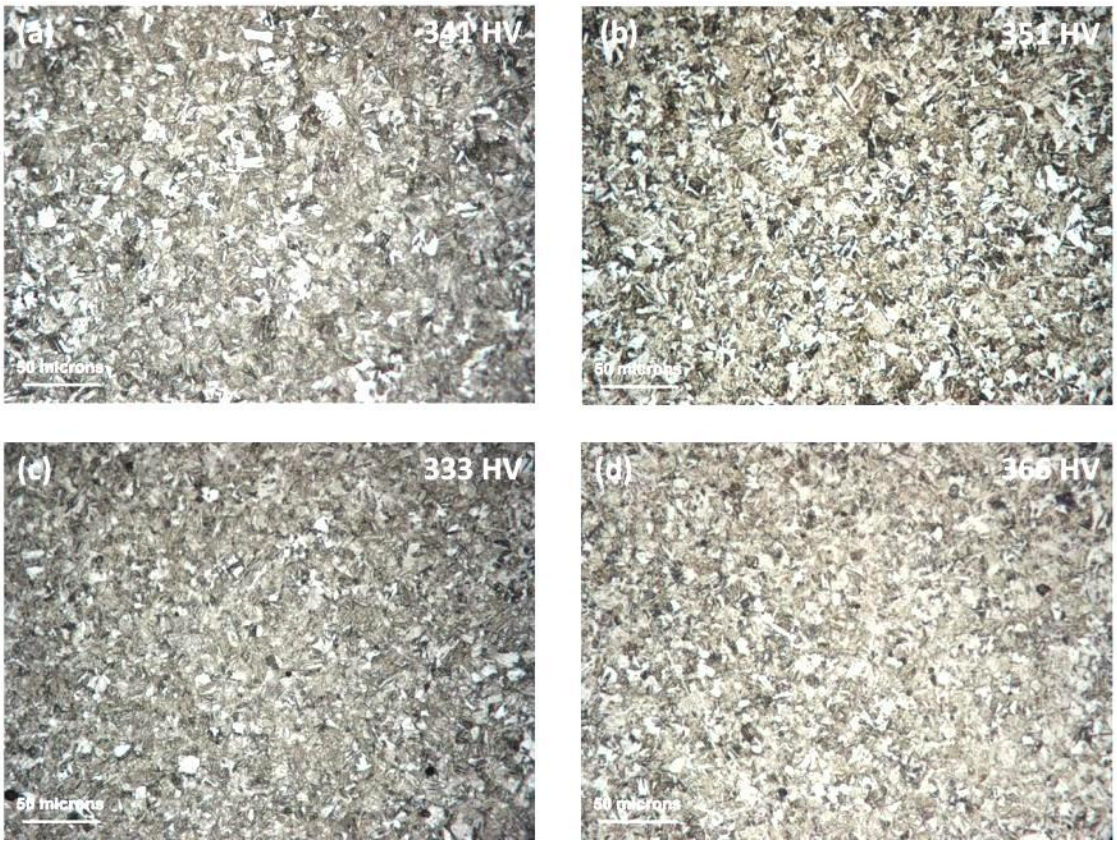

Figure 7-4 Optical micrograph of water quenched samples (a) X65 (A), (b) X65 (B), (c) X70 and (d) X100

7.2.2.2 X65 (b) CCT diagram and microstructural analysis

The X65 (b) is a TMCP material with a ferritic background and well dispersed bainitic islands,[155] as shown in figure 6-5 (b). The microstructure looks very similar to that of a thermo mechanically treated material plus accelerated cooling.[159] In CCT determination this material was subjected to thermal circles (cooling rates) ranging from 0.3°C/s to 56.2°C/s, corresponding to $t_{8/5}$ of 1000 s to 5.34 s respectively, as given in table 7-3.

Table 7-3 X65 (b) thermal cycles and the corresponding hardness values

Base Metal	**Time ($t_{8/5}$) sec**	5.34	7.1	7.59	10	15	25	50	90	250	400	600	1000
	CR (°C/s)	56.2	42.2	39.5	30	20	12	6	3.33	1.2	0.75	0.5	0.3
X65 (b)	**Hardness (HV)**	244	235	235	237	218	195	185	174	165	158	154	146

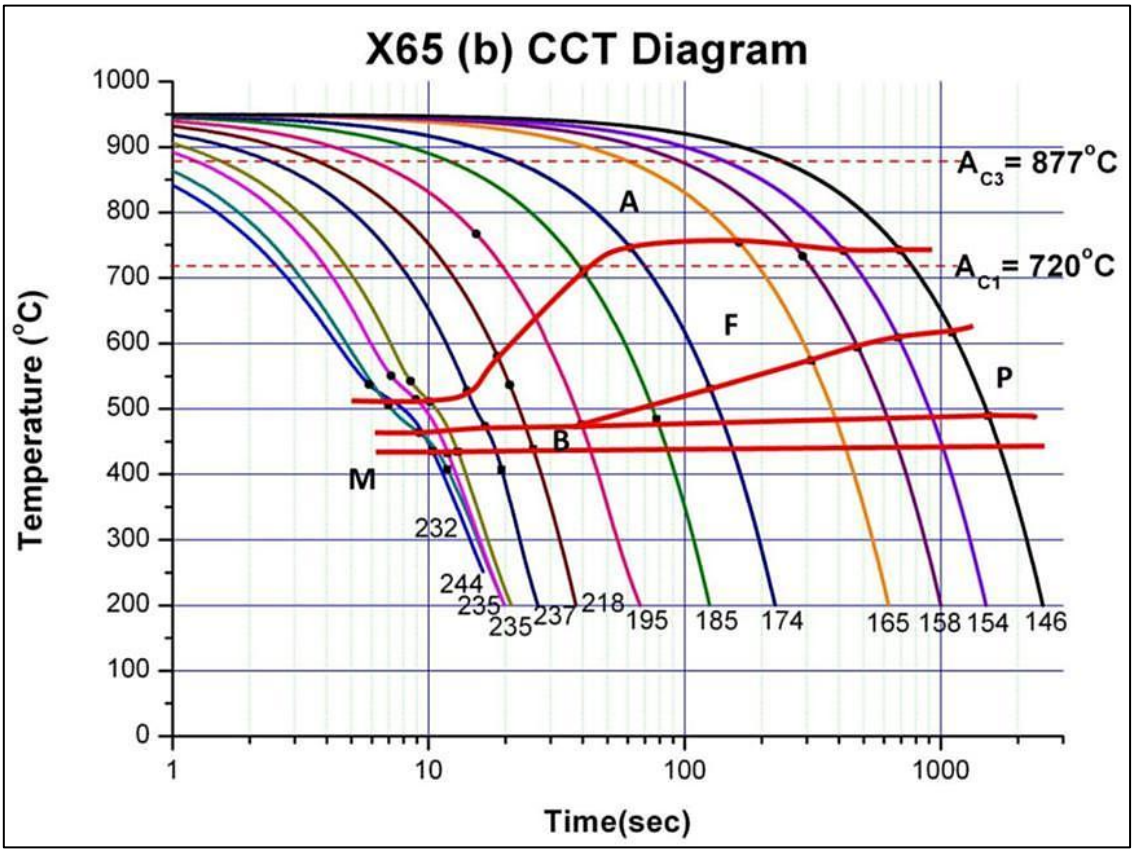

Figure 7-5 X65 (b) CCT diagram with transformation lines identified

The fastest cooling rate obtained for this material was 56.2°C/s ($t_{8/5}$ = 5.34 s). Micrograph (a) in figure 6-17 is showing some polygonal ferrite (PF) and some widmanstätten ferrite (WF). There was a little presence of bainite and martensite. This can be explained from micrograph (b) of the water quenched sample in figure 7-4, showing large amount of plate like martensite, with a hardness of 351 HV as compared to that of the fastest cooling rate of X65 (b) which showed a hardness of 244 HV. Similar transformation products were obtained with variations in the amount (%) of phases up to a cooling rate of 20°C/s ($t_{8/5}$ = 15 s) as shown in figure 6-17 (c).

Significant change in isothermal transformation products was observed at a rate of 12°C/s ($t_{8/5}$ = 25 s) as shown in figure 6-17 (d). At his point the pearlite start line was crossed and pearlite begins to nucleate. The pearlite islands were very small at the beginning, and becomes clearly visible at a rate of 1.2°C/s ($t_{8/5}$ = 250 s) as shown in figure 6-17 (f).

Grain growth continues as the cooling rate decrease, with the size of the PF and P becoming even larger, but with fewer islands of P. this is obvious at the slowest cooling rate of 0.3°C/s ($t_{8/5}$ = 1000 s) used on this material as shown in figure 6-17 (h).

7.2.2.3 X70 CCT diagram and the microstructural analysis

The X70 parent metal is also processed though the TMCP route, with the microstructure closely similar to that of a Cu-Ni type as reported by Graf et al.[158] Heat treatment cycles with a range of cooling rates from 42.8°C/s ($t_{8/5}$ = 7 s) to 0.3°C/s ($t_{8/5}$ = 1000 s) were used for this particular material as given in table 7-4. The CCT diagram of the X70 grade, as shown in figure 7-6 is similar to what has been constructed in previous researches.[102; 109; 166]

Fastest cooling rate of 42.8°C/s ($t_{8/5}$ = 7 s) was achieved, and the resulting phases were bainite (B) and some martensite (M) as shown in figure 6-18 (a). The hardness value is 235 HV as compared to the water quenched sample in figure 7-4 (c), which is showing a fully martensitic structure with an average hardness of 333 HV. This is similar to what Onsoien et al.[109] observed.

Table 7-4 X70 thermal cycles and the corresponding hardness values

Base Metal	Time ($t_{8/5}$) sec	7	7.8	10	15	25	50	90	250	400	600	1000
	CR (°C/s)	42.8	38.6	30	20	12	6	3.33	1.2	0.75	0.5	0.3
X70	Hardness (HV)	235	253	238	240	221	204	205	184	177	176	165

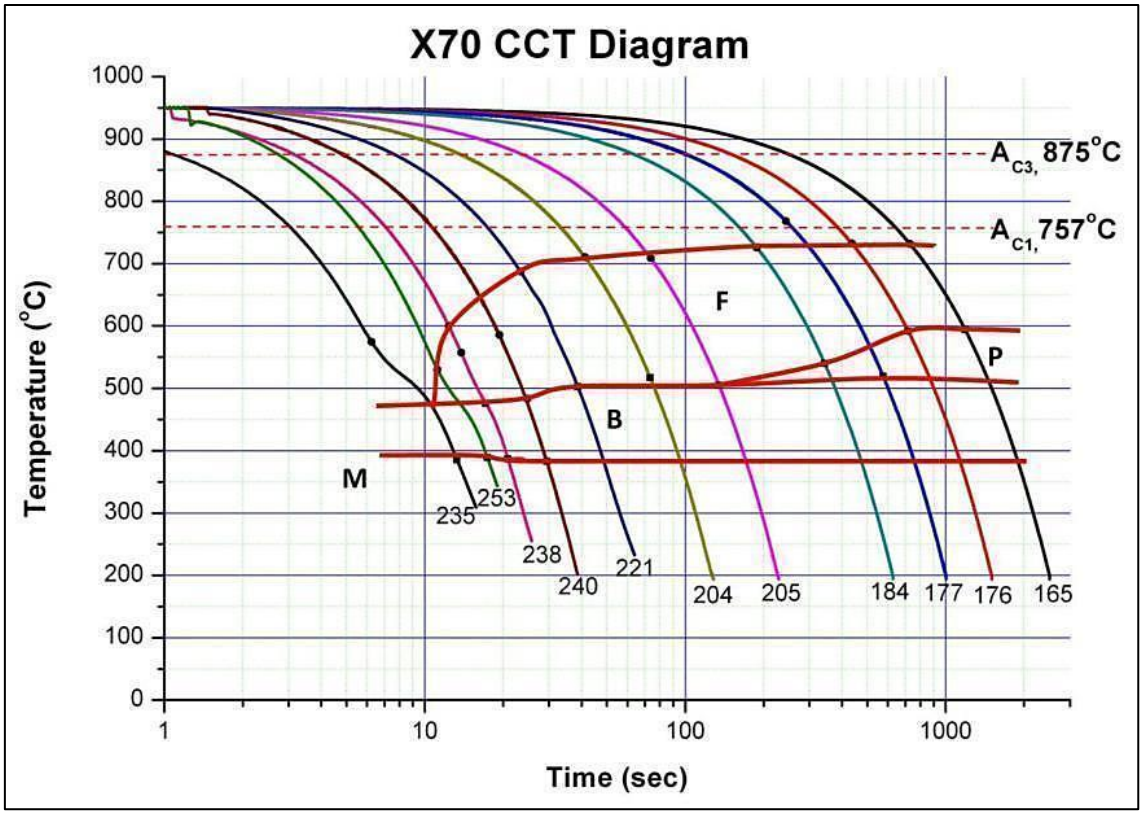

Figure 7-6 X70 CCT diagram showing the transformation lines identified

At the rate of 30°C/s ($t_{8/5}$ = 10 s) as shown in figure 6-18 (c), polygonal ferrite starts to emerge and becomes more pronounced at 20°C/s ($t_{8/5}$ = 15 s), the main constituents at this point are PF and B as shown in figure 6-18 (d).

At a cooling rate 12°C/s ($t_{8/5}$ = 25 s) with the corresponding micrograph shown in figure 6-18 (e), The diffusion based products were promoted as compared to the shear induced transformation products. The morphology of the PF was changing and the presence of carbide and some retained austenite was noticed.

Similar transformation products were observed with different morphologies up to a rate of 3.33°C/s ($t_{8/5}$ = 90 s) was reached, tiny islands of pearlite begin to evolve as shown in figure 6-18 (f). These islands continue to grow with decrease in cooling rate. The ferrite also changes in to large grains and keeps growing, some grain boundary ferrite was also observed.

At the slowest cooling rate of 0.3°C/s ($t_{8/5}$ = 1000 s), the sample had fully transformed in to a well-defined structure of non-equiaxed ferrite grains of various sizes, and pearlite colonies. This is shown in micrograph (iii) of figure 7-8, similar structures were observed by Thompson et al.[167]

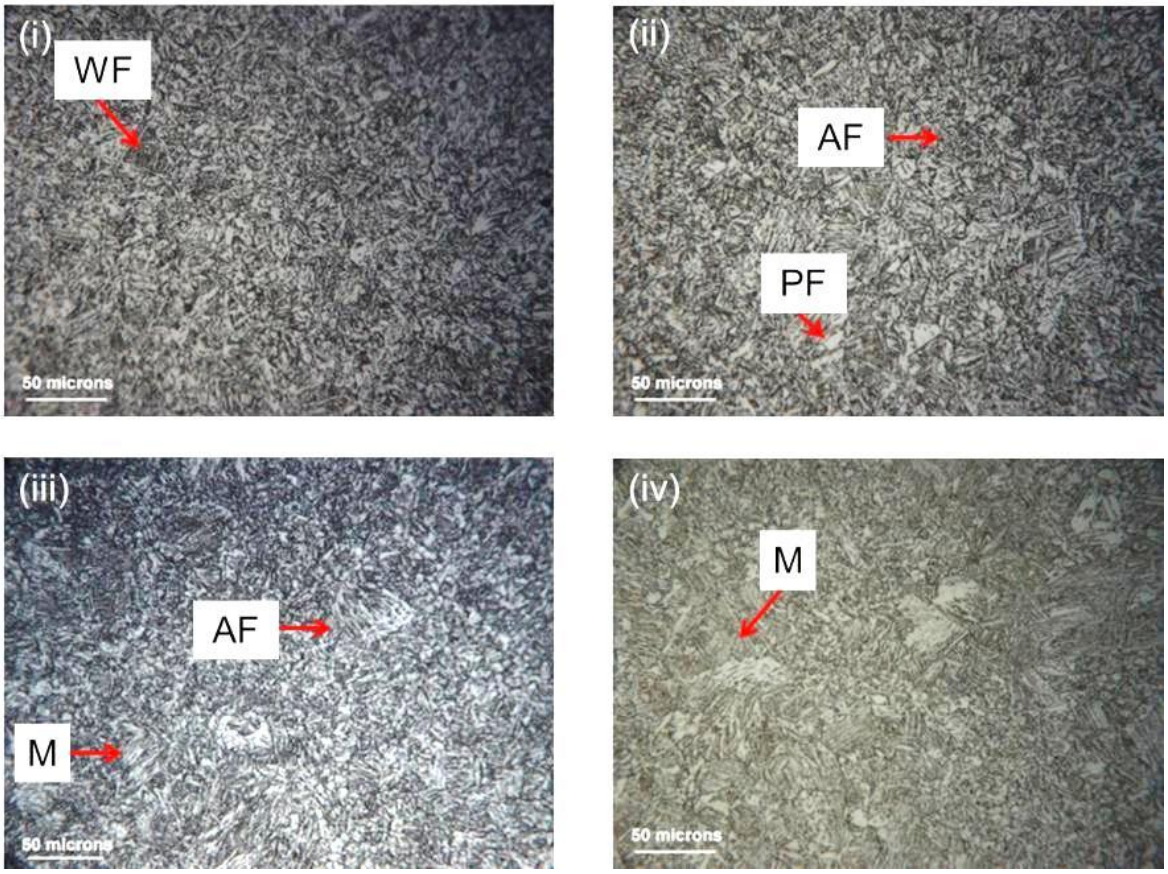

Figure 7-7 Micrographs of the fastest cooling rates for (i) X65 (a) at $t_{8/5}$ = 6 s, (ii) X65 (b) at $t_{8/5}$ = 5.34 s, (iii) X70 at $t_{8/5}$ = 7 s, (iv) X100 at $t_{8/5}$ = 5.34 s

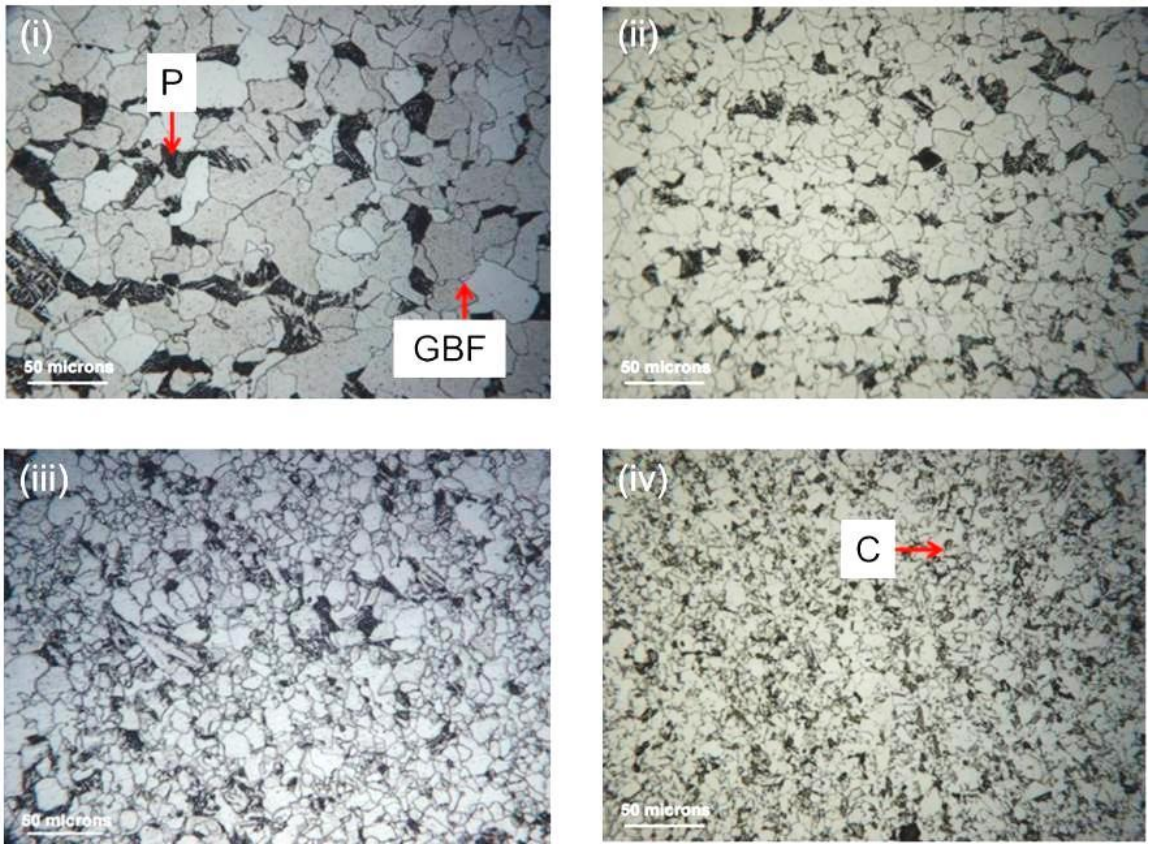

Figure 7-8 Micrographs of the slowest cooling rate (0.3°C/s) for (i) X65 (a), (ii) X65 (b), (iii) X70 and (iv) X100 all at $t_{8/5}$ of 1000 s

7.2.2.4 X100 CCT diagram and microstructural characterization

Maximum cooling rate of 56.2°C/s ($t_{8/5}$ = 5.34 s) was recorded for this material, with a hardness of 293 HV as shown in micrograph (iv) of figure 7-7. The microstructures constitute of polygonal ferrite (PF), widmanstätten ferrite (WF), acicular ferrite (AF) and some martensite. It is obvious that the fastest cooling rate did not result in to a fully martensitic structure such as that of the water quenched samples, as shown in figure 7-4 with a Vickers of 366 HV.

Bainite (B) starts to emerge at the rate of 47.7°C/s ($t_{8/5}$ = 6.29 s) shown in figure 6-19 (b), and increases to its peak at around 12°C/s ($t_{8/5}$ = 25 s) as shown in figure 6-19 (d), bainite was present all through to the slowest cooling rate of 0.3°C/s ($t_{8/5}$ = 1000 s). Polygonal ferrite becomes distinct from 12°C/s to the end, the morphology and amount was changing with cooling rate.

Table 7-5 X100 thermal cycles and the corresponding hardness values

Base Metal	**Time ($t_{8/5}$) sec**	5.34	6.29	10.09	15	25	50	90	250	400	600	1000
	CR (°C/s)	56.2	47.7	29.7	20	12	6	3.33	1.2	0.75	0.5	0.3
X100	**Hardness (HV)**	293	283	290	297	274	260	238	228	220	220	211

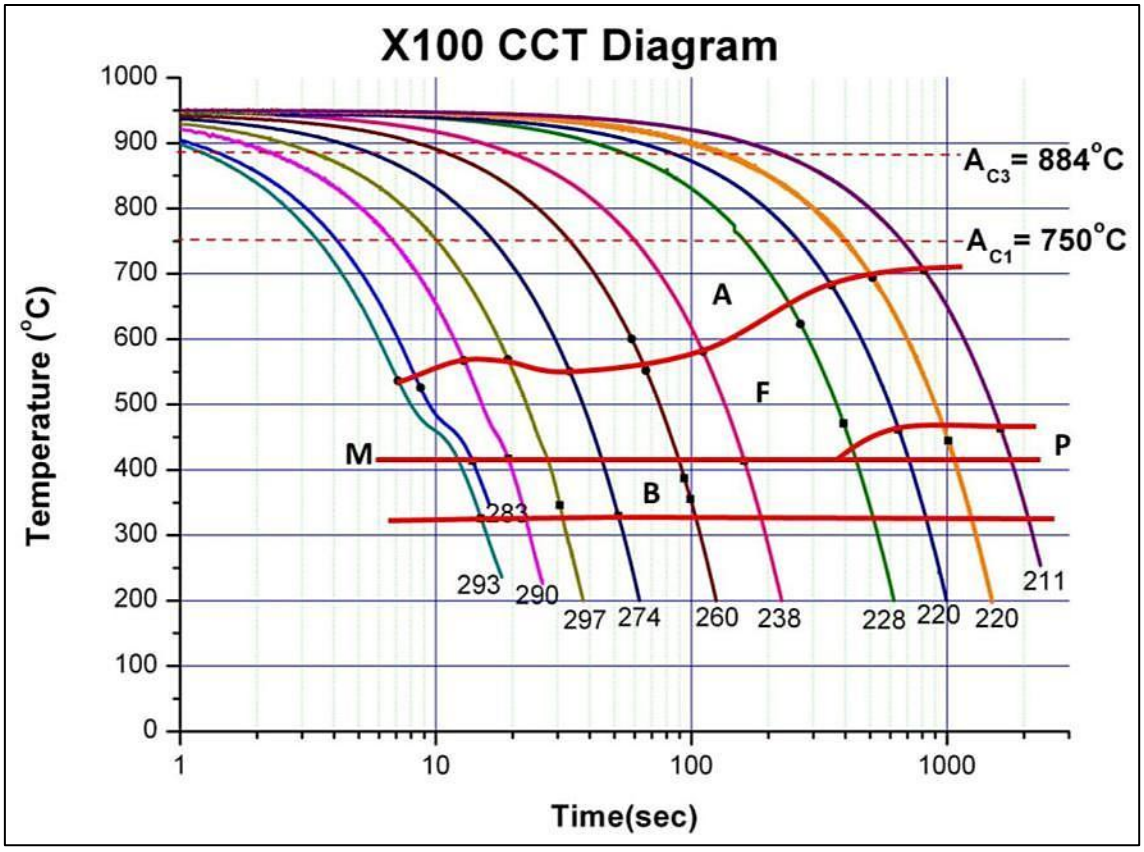

Figure 7-9 X100 CCT diagram indicating the transformation lines identified

At a cooling rate of 1.2°C/s ($t_{8/5}$ = 250 s), tiny dispersed colonies of pearlite starts to emerge, and becomes more pronounced with a decrease in cooling rate as shown in figure 6-19 (f). The pearlite islands in this case did not grow in size, but increase in amount. This can be seen on micrograph (iv) in figure 7-8, for a sample cooled at 0.3°C/s ($t_{8/5}$ = 1000 s).

In the X100 pipeline material, all the transformation points happen to be below the intercritical temperatures. Therefore it can be suggested that X100 has a

low temperature transformation all through.[164] At a comparatively slower cooling rate, the C-curve shifted to the right in the case of X100 grade, thereby more diffusion-less transformation products are produced.

7.2.3 Hardness versus log $t_{8/5}$ plots

Figure 6-25 presents the plot of the hardness against the cooling rate represented by $t_{8/5}$. As expected, the general trend was reduction in hardness with decrease of the cooling rate.[109; 168] The decrease was rapid from fast to intermediate cooling rates, and becomes more steady at slower cooling rates. This is as a result of the formation of larger amounts of ferrite, due to grain growth and recrystallization that is increasing with decreasing cooling rates (i.e. shift from diffusion-less to diffusion controlled transformation).[113; 167; 169].

An interesting feature of the plot is the reversal in hardness distribution trends observed at the higher cooling rates in all the steel grades used. This is similar to what Fonda and Spanos[163] and Yue et al.[164] have observed. The latter explained the hardness peaks to be where the martensitic transformation finished, and the drop in hardness was defined as the point where bainitic transformation replaces the martensitic transformation.

Another possible explanation is that at the higher cooling rates, where martensitic transformation is feasible, the hardness is at its peak. When the martensitic transformation is slow, then there will be more retained austenite formed, while if the transformation product is entirely bainitic, then retained austenite formation will decrease. This leads to the drop in hardness as retained austenite is softer than bainite. As the cooling rate decreases bainitic transformation will start, and more bainite is formed which is harder than retained austenite, leading to the increase in hardness.

7.2.4 Comparison between the four steels

A fully martensitic structure wasn't obtained in any of the four steel grades. This is due to the nature of the samples size[170] used, and the capability of the thermal simulator (absence of a suitable quenching medium).[109; 164] This make the maximum cooling rate (300°C/s) that was targeted to be impossible.

All the maximum hardness values recorded were not at the fastest cooling rates that were recorded, only the X65 (b) gave the maximum hardness of 244 HV at the fastest cooling rate used.

The two X65 materials have a similar trend in ferrite transformation start line, which happen to be above the A_{C1} line, while the X70 had the start line just below the A_{C1}. For the X100 pipeline material, the transformation start line was far away from the A_{C1} line. This is due to the difference in their chemical compositions and the various processing routes.[13; 158; 159; 171]

Figure 7-10 is showing the relationship between the transformation start temperatures and some cooling rates for all the pipeline steels used. The cooling rates between 50 - 12°C/s were selected because similar cooling rates were observed from the real thermal cycles of the welds.

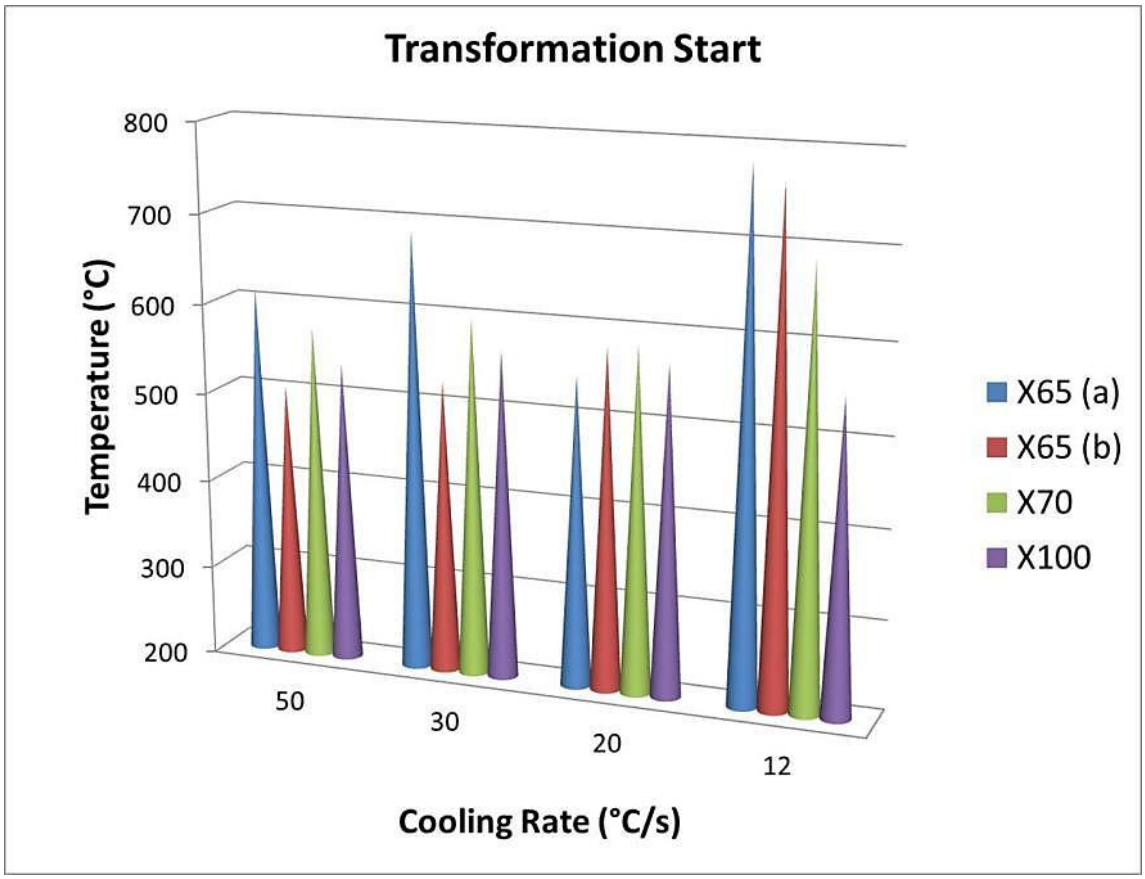

Figure 7-10 Relationship between the transformation start temperature of different materials and the cooling rates

The transformation finish temperatures were different for all the pipeline steels, as shown in figure 7-11. For the two X65 materials, the transformation finish temperatures were between 400°C to 500°C. For the X70 and X100 materials, the transformation finish temperatures were between 300°C to 400°C, especially in the higher cooling rates.

The diffusion controlled transformation products has shifted most to the right, on the X100 grade CCT diagram, and less on the X65 (b), while X65 (a) and X70 has similar pearlite transformation start. This is due to the hardenability issue, as the X100 has the highest carbon equivalent of 0.53, while X65 (b) has the lowest carbon equivalent of 0.39. X65 (a) and X70 have very similar trend, and their respective carbon equivalents are 0.40 and 0.41. Therefore, the presence of more diffusion-less product becomes more in the X100 CCT than in the other materials.

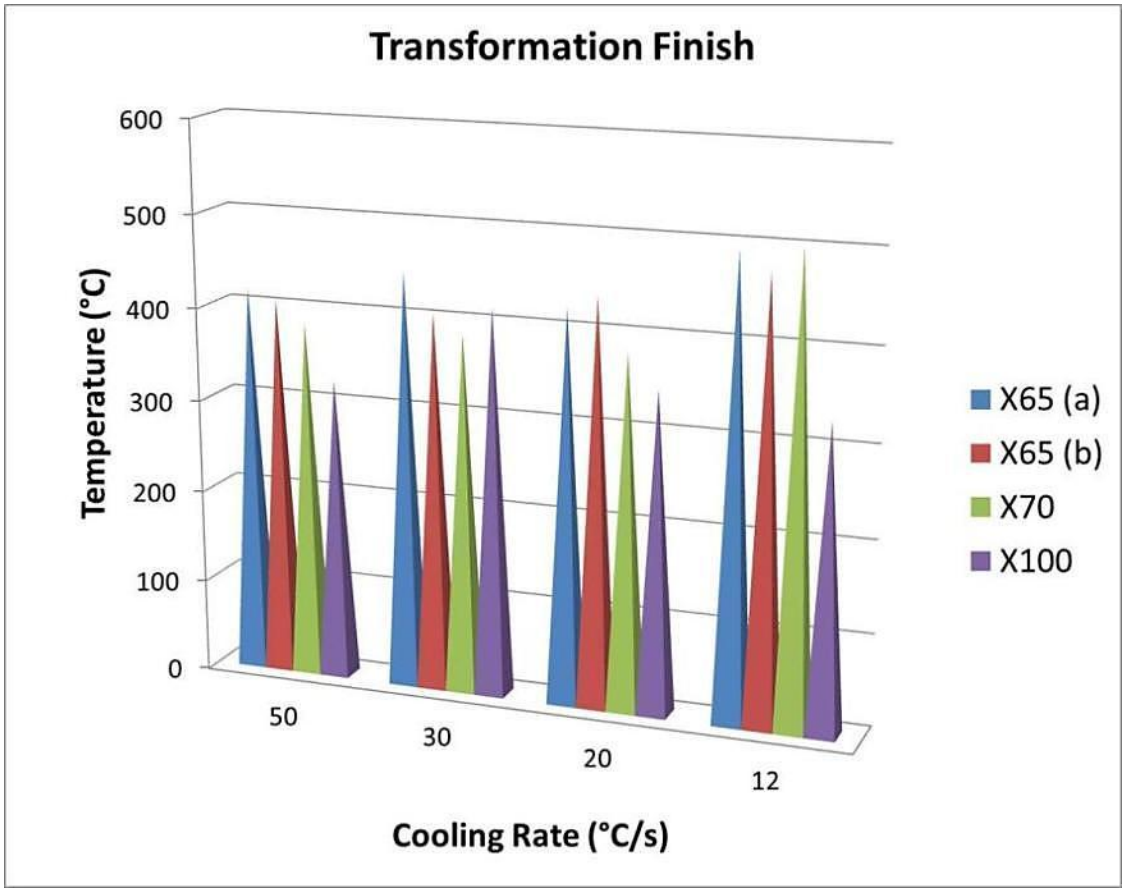

Figure 7-11 Relationship between the transformation finish temperature of different materials and the cooling rates

7.3 **Submerged arc welding**

Submerged arc welding has been known for its high productivity, high deposition rate in excess of 27 – 45 kg/hour and high reliability.[172] The submerged arc welding experiments were carried out in two stages, i.e. the bead on plate (BOP) welding and the full welds as was presented in chapter 6. The discussion will be based on the welding processes and the results obtained.

7.3.1 Bead on plate (BOP) welds

The bead on plate welds were made as trials towards the final welds, but a significant amount of information was gathered from the data. The trials were necessary, to see the possibility of using thermocouples to capture the true thermal cycles of the welds. Figure 6-26 to figure 6-29 on pages 112 - 113 are showing the macrographs of the BOP welds. It can be seen how the welds beads interact with each other, and how the increase in penetration was caused by the subsequent beads. Thermocouples positions are also visible on the macrographs.

Figure 6-30 on page 116 is showing the SEM micrographs of the BOP weld metal, at the hardness traverse positions. The micrographs were showing an evidence of grain growth from figures (a) with a single pass toward (d) with four passes, similar trend was observed by Keehan et al.[91] The main constituents of the weld metal are acicular ferrite (AF), polygonal ferrite (PF), bainite (B) and some martensite (M).[173] This is obvious from the hardness traverses both along and across the welds as shown in figure 6-31 on page 117.

The hardness reduces with increase in number of passes and grain size. Lowest hardness values were displayed by weld four as shown in figure 6-31, which is a direct consequence of the reheating or tempering effect from the subsequent weld beads.

The thermal cycles shown in figure 6-32 on page 118 were showing the thermal cycle histories recorded from the same position after all the four passes have been deposited.

Table 7-6 Thermal cycles data from the BOP welds

Weld and TC Numbers	Max Temp (°C)	t_{800} (sec)	t_{500} (sec)	$t_{8/5}$ (sec)
Weld 1, Pass 1, TC-5	1396	16.79	30.99	14.50
Weld 2, Pass 1, TC-5	1414	22.57	37.62	15.05
Weld 3, Pass 1, TC-5	1089	8.083	22.36	14.28
Weld 4, Pass 1, TC-5	1025	9.7	25.62	15.92

The thermocouples relative positions at 10 mm and 17 mm are shown in figure 5-5 on page 61. The cooling rates represented by $t_{8/5}$ are given in table 7-6. They are not far from the range of $t_{8/5}$ = 3 – 13 s suggested by Keehan et al.[91] where good strength and toughness are achieved. While the reheated beads especially in weld 4 were becoming coarser as the cooling rate decreases.

Rojko and Gliha[174] reported that weld metals are generally more stable and not affected very much by the thermal cycles of the subsequent passes, this is because the kinetics of austenite transformation is faster in the HAZ than in the weld metal.

7.3.2 Full submerged arc welds

The welding parameters used in these experiments were all developed and tested at Cranfield University. They are given in the welding procedure specifications in Appendix A.1 for all the SAW full welds made on X65 (a), X65 (b) and X70 pipeline steel grades.

There was a problem with slag removal at the beginning, which was attributed to the welding parameters used. A high voltage of 33 V was used at the beginning, which means reduced electrode melting rate and increased flux consumption.[175-177] Therefore, the more molten flux is in the groove, the more difficult to remove the solidified slag, due to the nature of the groove (Narrow groove).

The high voltage also leads to a concave deposited weld bead, which causes the flux to get trapped and difficult to remove.

This problem was corrected by reducing the voltage from 33 V to 26 - 28 V and reducing the amount of flux in the flux holder. Lower voltage results in a convex weld bead, leading to an easy removal of the flux.[26; 178]

The macrographs shown in figure 6-33 to figure 6-38 on pages 119 - 121 are the representative macrographs of the full submerged arc welds, showing the thermocouples positions in some cases. They are all showing the interaction and overlapping of the weld passes.

The optical micrographs of the different materials are presented in figure 6-39 to figure 6-54 on pages 122 - 132. They are showing the microstructures at different positions of the welds, including the heat affected zones, the fusion line and part of the weld metal. They are indicating how the various parent materials are responding to the welding thermal cycles, and the resulting phase formations.

7.3.2.1 X65 (a) SAW analysis

The HAZ of the X65 (a) SAW is showing large prior austenite grains as shown in figure 6-39 on page 122, this is the case for the HAZ at mid thickness (i.e. 15 mm from the bottom). The HAZ at 10 mm from the bottom differs from the above, because it has been completely transformed by the internal pass. And the structure becomes that of a bainitic phase with some widmanstätten ferrite. The SEM micrograph of the HAZ at 10 mm is also showing the presence of bainite as shown in figure 6-42.

Figure 6-57 on page 135, is showing the hardness traverses of the X65 (a), which is supporting the microstructures of the HAZ at the 10 mm from the bottom. This is because welds 1 and 2 were showing higher hardness at the bottom than at the middle and the top. But in weld 3, the hardness at the bottom drops, this can be related to the higher heat input recorded for the internal pass in weld 3 (H.I. = 1.69 kJ/mm) as given in Appendix A.1. This leads to the tempering of both the weld metal and the CGHAZ formed by the root pass, thereby dropping the hardness lower than in the other welds.

The CTOD results of welds 1 and 3 for X65 (a) were all showing a good toughness with a CTOD of δ_m as given in table 6-4 on page 139. The fractured face is also showing a ductile fracture. The hardness map around the crack tip area was also showing distinctively the different regions of the welds as seen in figure 6-63 and figure 6-64.

7.3.2.2 X65 (b) SAW analysis

The X65 (b) is a TMCP processed 48 inch outer diameter pipe normally used in long distant oil and gas transportation.[157] The macrographs as shown in figure 6-35 and figure 6-36 on pages 120 and 121 respectively are showing lack of penetration resulting from the internal pass. This is due to the lower heat input that was used for the internal passes on the X65 (b) as given in Appendix A.1.

The HAZ of the welds as shown in figure 6-44 on page 125 have very large prior austenite grains, even larger than those of X65 (a). The main constituents are acicular ferrite and bainite, with a few polygonal ferrites. The microstructure of the thermocouple position is shown in figure 6-46 on page 126, having a mixture of large and small grains. There wasn't a significant amount of martensite or M-A phase present in the micrograph.

In all welds, the weld metal is harder than the HAZ. The weld metal HAZ is ranging between 250 - 280 HV, while the HAZ ranges between 220 - 240 HV, as shown in figure 6-58 on page 136. In general, the hardness is fairly consistent, similar hardness pattern has been reported by Webster and Bateson.[179]

Both samples tested for CTOD, failed to satisfy the pre crack shape requirements of BS 7448-2, probably due to residual stresses in the welds.[180] Therefore, the pre-crack are classified as invalid in these samples. This could have been overcome by applying side compressions before the pre-cracking process.

Weld 1 with a CTOD of δ_m was showing a complete brittle fractured face, while weld 2 was showing a mixture of brittle and ductile fractures, with a CTOD of δ_u (mode of fracture).

7.3.2.3 X70 SAW analysis

The X70 macrographs in figure 6-37 and figure 6-38 on page 121 are showing an excellent weld with good penetration and side wall fusion. The thermocouples positions are also visible on the macrographs. The micrographs of the HAZ are showing a more refined grained structure. The main phases include polygonal ferrite, acicular ferrite and some bainite as seen in figure 6-47 and figure 6-48 on pages 127 and 128. The SEM micrograph of the HAZ in figure 6-50 on page 129 is showing a few islands of M-A phase, which are more distinct in the thermocouple position as shown in figure 6-51 on page 129.

Figure 6-59 on page 137, is showing the hardness traverses of the X70 welds. The top and middle hardness of the weld metal region are very close, mostly between 260 – 280 HV. While that of the bottom differs from one another as a result of the internal pass, which is the last pass. Weld 1 was showing the lowest hardness peak in the weld metal, which is below 300 HV. This can be related to the high heat input recorded for the internal pass in weld 1 as compared to both welds 2 and 3 with the lowest heat inputs, as given in Appendix A.1.

This shows that high heat input, leads to lower cooling rates, which in turn has resulted in to low hardness in weld 1 as compared to welds 2 and 3. Similar hardness profiles have been reported by Hashemi et al.[181] Also noticeable is the higher parent metal hardness at the bottom of all three welds. This could be due to the strain induced by the root passes, because they were laid when the samples were cold. Therefore, the surrounding material would have quenched the bottom material.

Another probable expiation could be the pipe was delivered in this condition, due to the compressive stresses and strains at the bottom from the rolling and forming processes during manufacturing. This can be seen from the hardness traverse along the samples (within the parent material) as shown in figure 7-12. The hardness at the bottom is going up in all the three welds as compared with the top and middle parts of the samples.

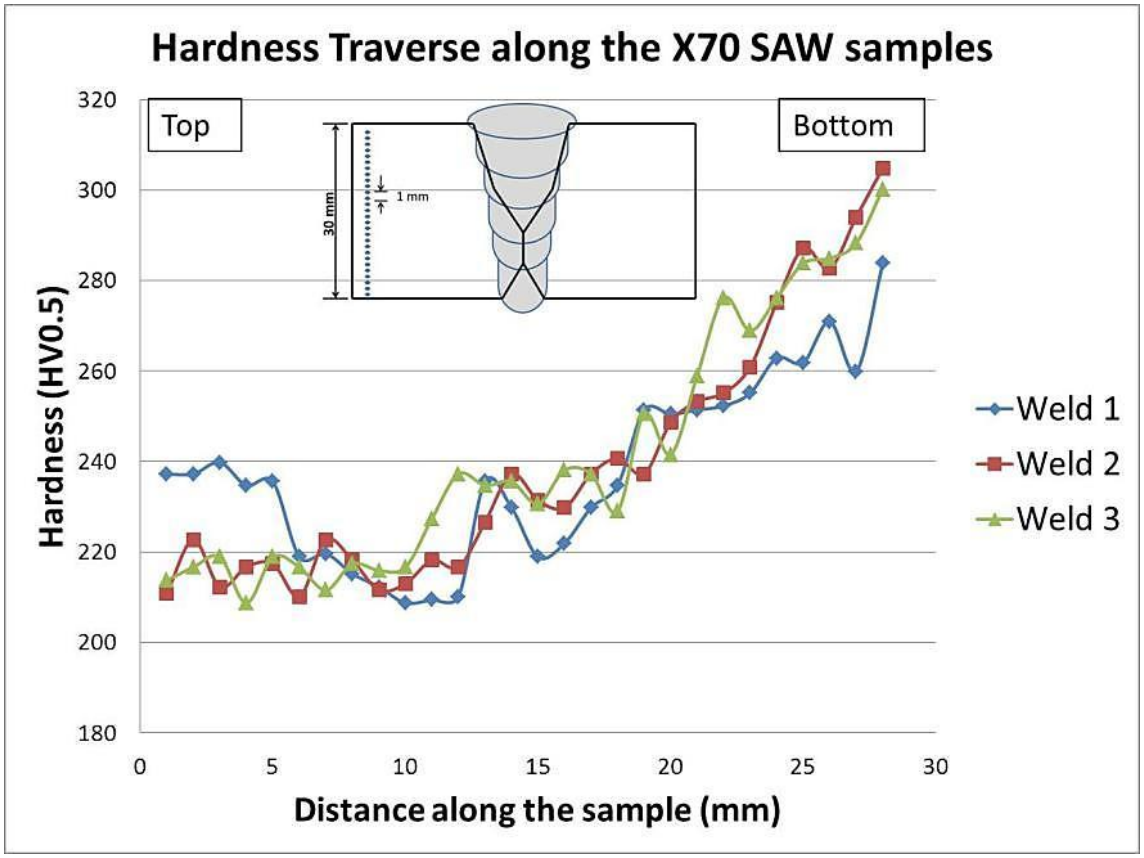

Figure 7-12 Hardness traverse along the X70 SAW samples from top to bottom

Welds 1 and 2 were tested for the presence of LBZ using CTOD test. The results as given in table 6-4 on page 139 are showing CTOD fracture modes of δ_c and δ_u respectively. The pre-crack positions are valid for all the welds, as shown on the macrographs of the CTOD samples in figure 6-61 on page 140, and the fractured faces in figure 6-62 on pages 140. The broken face in weld 1 is showing more of brittle region than in weld 2.

7.3.3 Effect of hardness on the CTOD

Haze and Aihara[182] made use of the Ritchie-Knott-Rice fracture model[183] to explain the influence of hardness on the CTOD values of a sample with LBZ. This has agreed with the hardness mappings of the notch areas shown earlier in figure 6-63 to figure 6-68. Base on the microstructural constituents, the CTOD values decreases with an increase in hardness.

The fracture model assumed that for a cleavage fracture to initiate, the crack tip tensile stress has to attain a critical fracture stress value.

The tensile stress increases with increase in the crack tip opening displacement, and becomes even higher with an increasing yield strength or hardness. Therefore, a brittle fracture initiates at low CTOD for steels with higher hardness, if critical fracture stress is assumed to be constant.[183]

They[182] showed that lowering the hardness of the HAZ, led to a significant increase in the CTOD of the LBZ containing areas. This could be achieved by lowering the carbon equivalent of the materials and using appropriate thermal cycles and/or pre-heat and post weld heat treatments.

7.3.4 SAW thermal cycles

As stated earlier, capturing of true welding thermal cycles was the main reason behind these experiments. This is to see whether the thermal cycles responsible for LBZ formation could be identified and correlated with the microstructures and the CTOD results, also to generate input for thermal simulations. Thermocouples were inserted in the HAZ of all the welds that have been discussed earlier as explained in chapters four and five, and the corresponding thermal cycles were recorded.

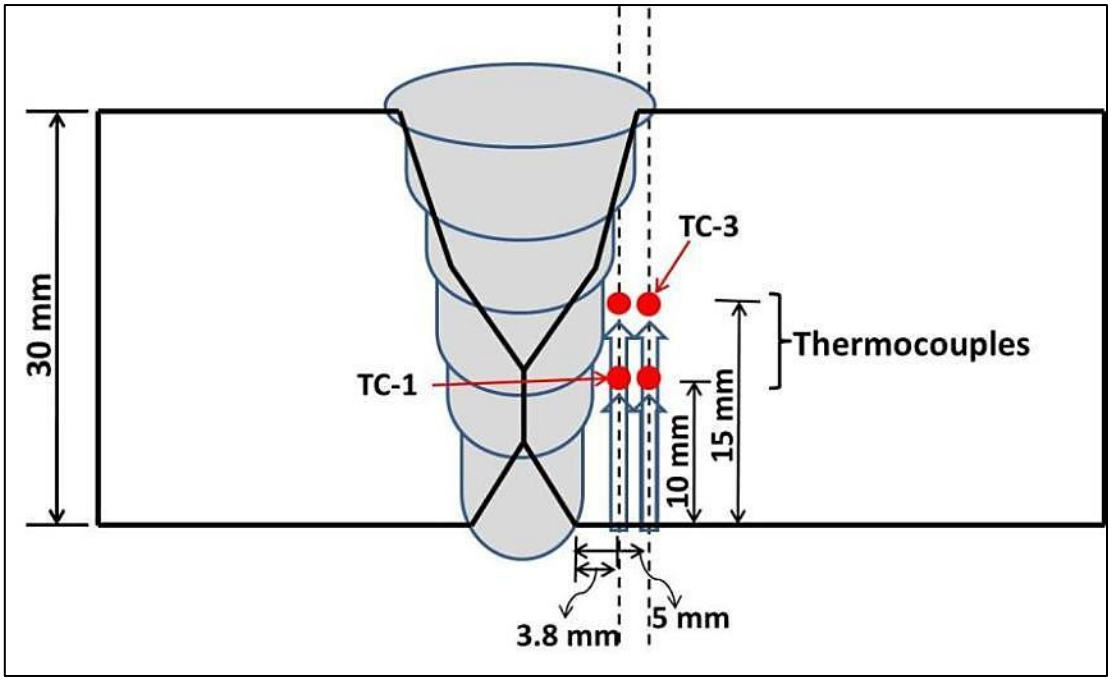

Figure 7-13 SAW TC arrangements showing thermocouples locations

Figure 6-60 on page 138 is showing representative thermal cycles of two thermocouples from X70 weld 3. They are showing the thermal cycles experienced by those particular thermocouples positions after depositing all the weld beads. Bleck et al.[184] have also made use of thermocouples to record the thermal cycles in a five wire SAW process.

Figure 7-13 is showing the relative position of the thermocouples related to the thermal cycles shown in figure 6-60. TC-1 was at 10 mm depth from the bottom, and 3.8 mm off set from the edge of the bottom weld prep. While TC-3 was at 15 mm depth from the bottom and 5 mm off set from the bottom of the weld prep.

Thermal cycles recorded by TC-1, were showing that during the root pass, that particular TC position has reached 814°C and cooled at a $t_{8/5}$ of 9.78 s. The fill 1 happen to be adjacent to the thermocouple, thereby recorded a higher temperature of 989° and a $t_{8/5}$ of 20.1 s.

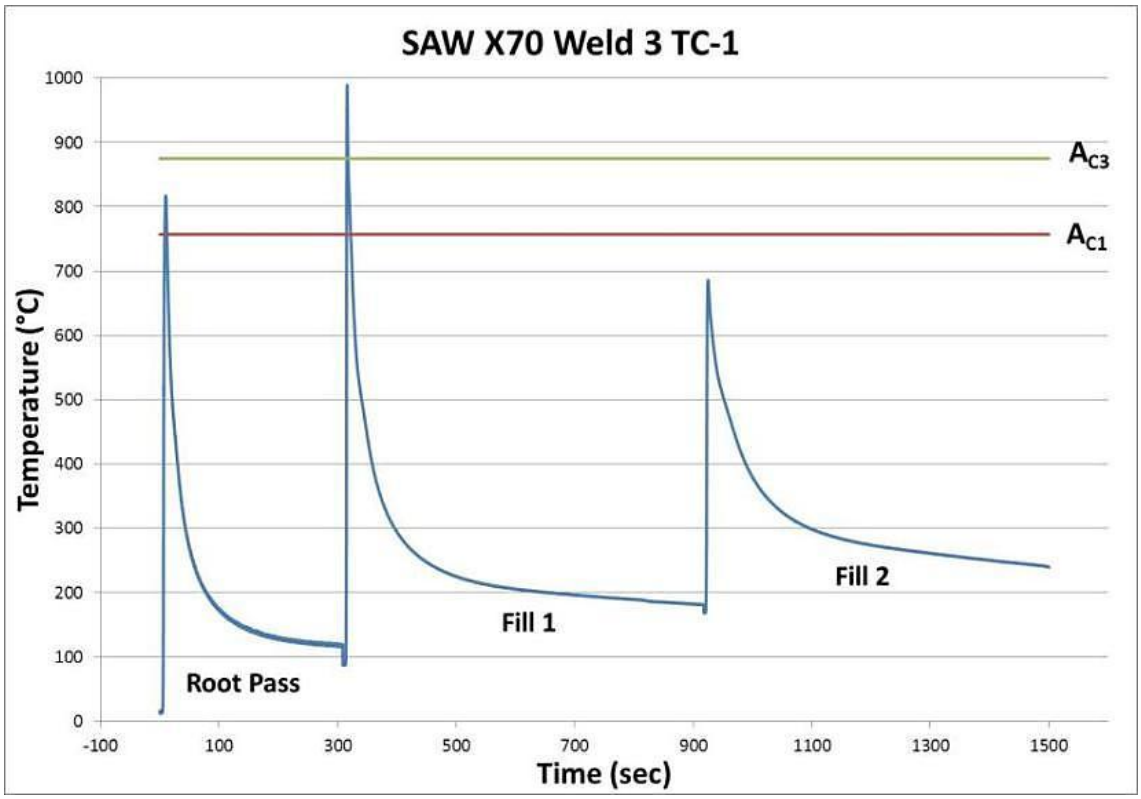

Figure 7-14 SAW X70 weld 3 TC-1 thermal cycles and the intercritical temperatures

This shows that the root pass has a faster cooling rate than fill 1, this is so because the plate was cold when the root pass was deposited, as no preheat was used.

Figure 7-14 is showing the relation of the thermal cycles from the various weld passes to the intercritical temperatures. The root pass is in the intercritical region, fill 1 is in the supercritical region and fill 2 was heated to subcritical temperatures. It is also evident how the cooling rate is decreasing with more weld passes.

TC-3 on the other hand, reached a peak temperature of 802.5°C during the root pass as shown in figure 7-15, and cooled much faster with a $t_{8/5}$ of 7.21 s, more than in TC-1. This is because TC-3 is 5 mm away as shown in figure 7-13, and heat transfer in SAW is mainly via conduction as the arc is buried in the flux.

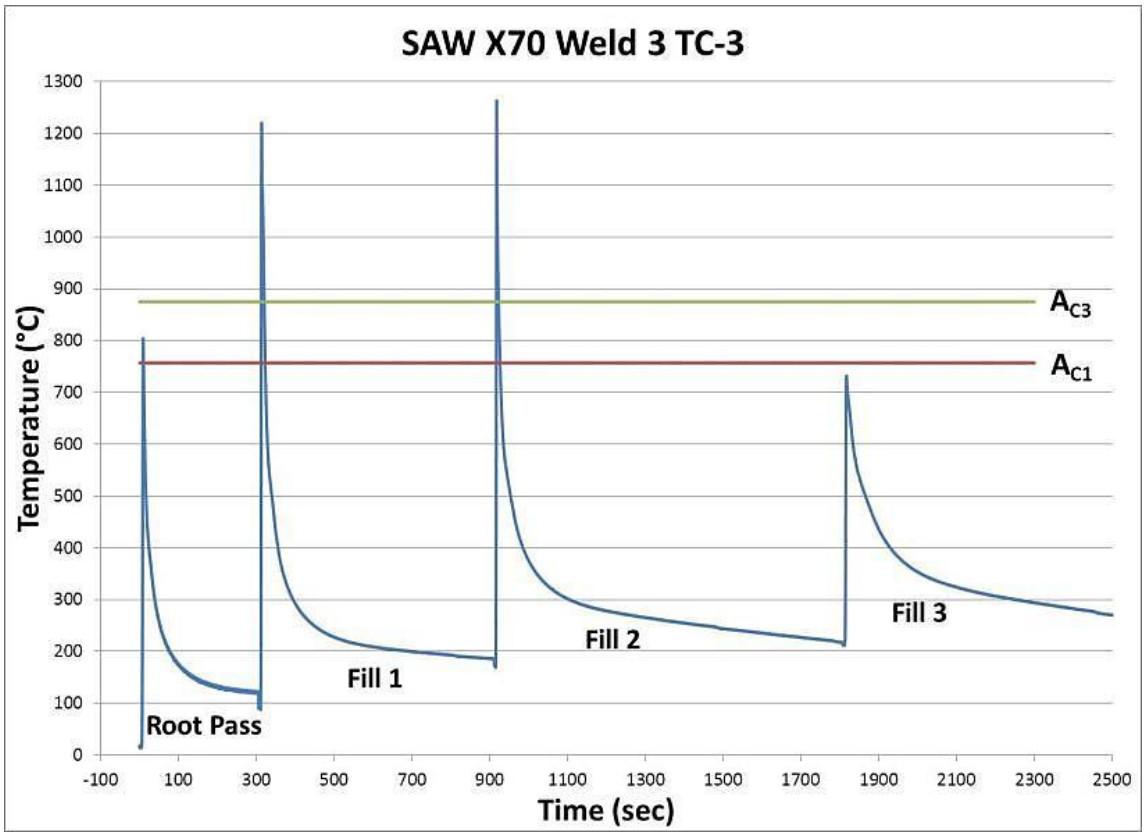

Figure 7-15 SAW X70 weld 3 TC-3 thermal cycles and the intercritical temperatures

Fill passes 1 and 2 has the highest peak temperatures of 1220°C and 1263°C, with a $t_{8/5}$ of 18.1 s and 28.64 s respectively. This means fill 1 cooled much faster than fill 2, due to the pre-heating effect from previous passes. The high peak temperatures from fill passes 1 and 2 are due to the higher heat inputs used when they were deposited and the positions of the thermocouples.

During fill 3, the thermocouple recorded a peak temperature of 730.8°C, which is a subcritical temperature. The cooling rate was also much slower than the previous passes. Therefore, both fill passes 1 and 2 have been heated to the supercritical region, while the root pass was heated to within the intercritical region as shown in figure 7-15.

7.3.5 Superimposition of thermal cycles on the CCT curves to understand phase evolution

Thermal cycles recorded by TC-1 and TC-3 were superimposed on the CCT diagram of the parent material (X70) as shown in figure 7-16 and figure 7-17 respectively. As explained in the literature review, figure 2-1 on page 6 was showing the effect of welding thermal cycles on the heat affected zones, the superimposed thermal cycles could be analysed in the same way.

The root pass in TC-1 is showing that the HAZ has not been heated high enough for transformation to take place. But the effect of the heat, which is just above the A_{C1} temperature, may have caused some local areas to transform in to austenite.[47] Due to the nature of the cooling as explained earlier, this may cause some martensite formation and some grain growth, leading to the formation of the CGHAZ, because it is the first pass.

Fill 1 been the second pass, has heated the HAZ to a temperature higher than the A_{C3}, which has been related to the formation of a reheated fine grained HAZ. The heating is high enough to produce more austenite, which may later transform in to M-A phase, depending on the kinetics of the process, and may also cause some grain refinement.[46] This is because the peak temperature is not high enough to enhance grain growth, as a result a refined microstructure is obtained.

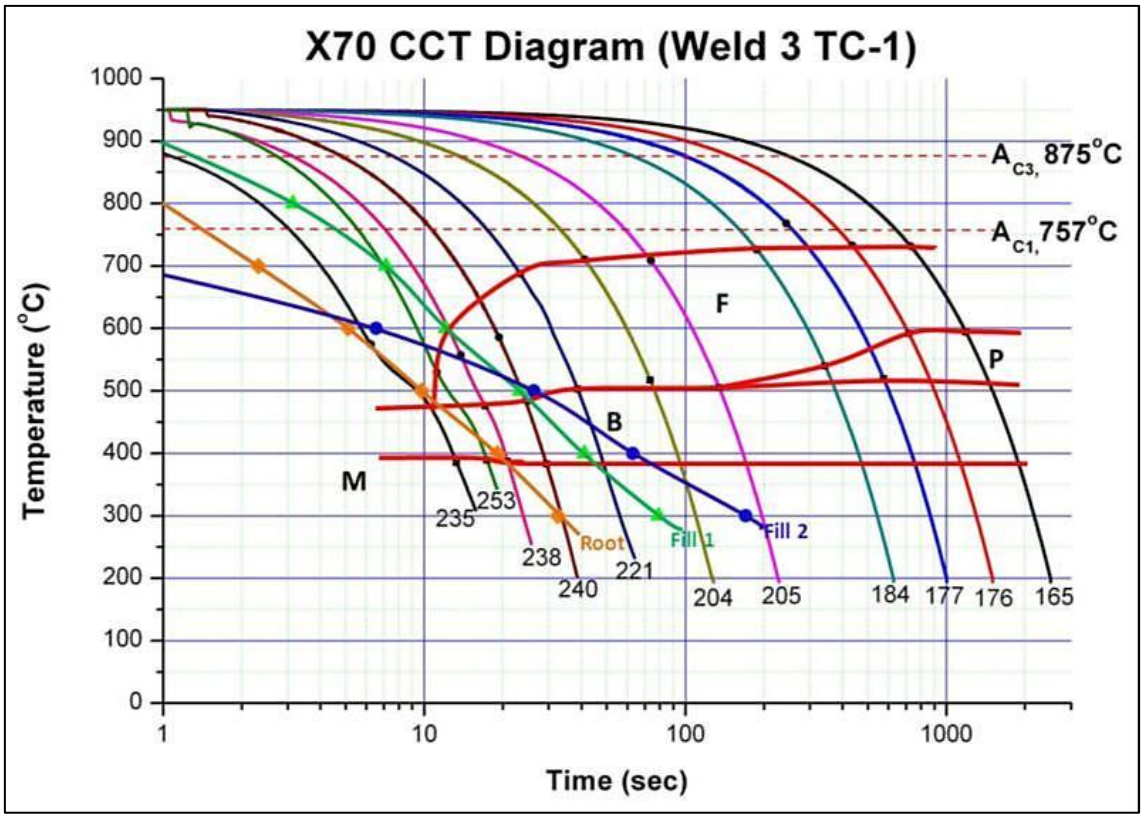

Figure 7-16 Superimposition of thermal cycles of weld 3 TC-1 on the CCT of the parent material

The effect of fill 2 from TC-1 as shown in figure 7-16 is that of a subcritically reheated temperature, which is just below the A_{C1} line. Therefore, the main structure remains, but the heating will have some annealing effect on the HAZ.[46] Consequently, fill 1 would have produce a bainitic microstructure with some polygonal ferrite as seen from the micrograph in figure 6-47 on page 127, and fill 2 has not changed the microstructure from what it was. Thus fill 1 determines the bulk of the final microstructure.

Looking at the superimposed thermal cycles of TC-3, as shown in figure 7-17, the root pass being the first, has similar effects to that of TC-1. But fill passes 1 and 2 have reheated the HAZ to a very high temperature far above the A_{C3}, which will lead to the formation of more austenite, which means potentially more M-A phase could be formed.

The relationship of the heat input with the peak temperatures for both TC-1 and TC-3 are shown in figure 7-18 and figure 7-19 respectively.

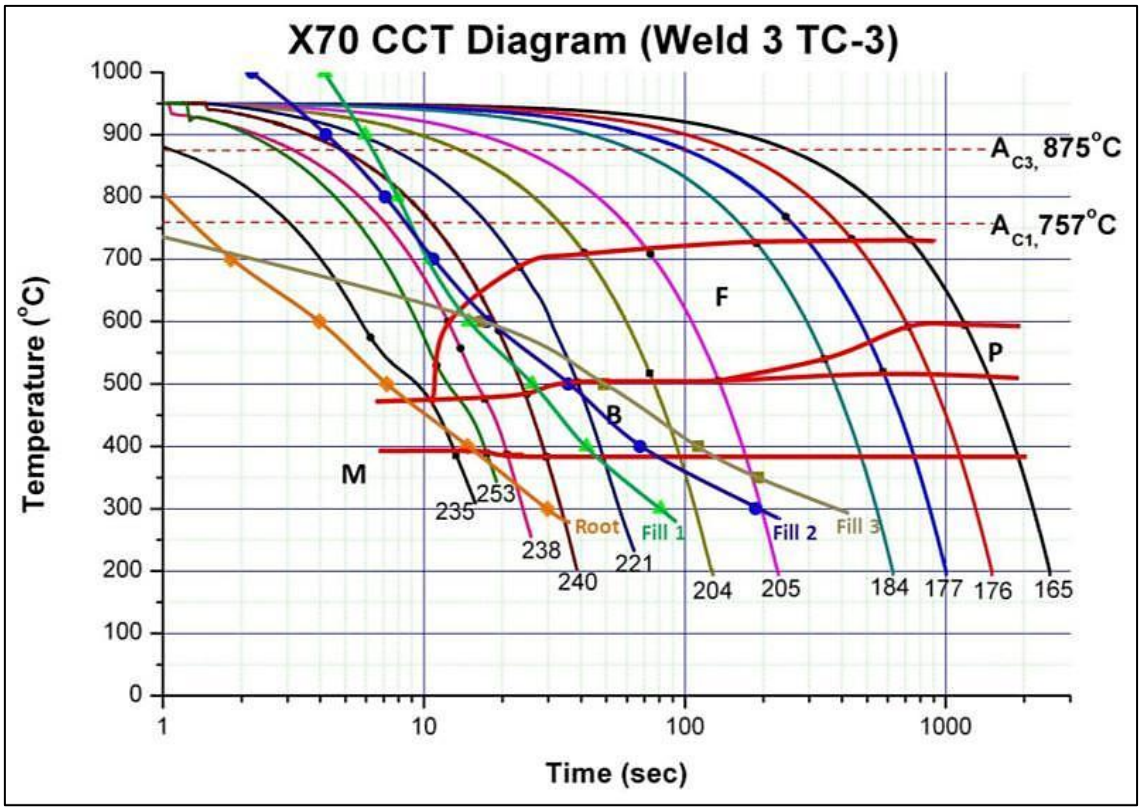

Figure 7-17 Superimposition of thermal cycles of weld 3 TC-3 on the CCT of the parent material

These cycles (i.e. fill passes 1 and 2) determines the HAZ microstructures, because fill 3 has the same effect to that of fill 2 from TC-1, which means the main structures has not changed, but only reheated to subcritical region.

The effect of these two peak thermal cycles, i.e. fill passes 1 and 2, shows that this particular region (HAZ) has been austenitized twice. But due to the nature of welding thermal cycles (rapid heating and cooling), there was no chance for homogenisation to take place, neither was carbon allowed to diffuse.

Therefore the chances of forming more M-A phase becomes higher in this case, because there are more areas with carbon enriched austenite. Moeinifar[141] suggest that an increase in the cooling rate and the heat input results to increase in the amount of M-A phase formed, and also determine the morphology of the grains.

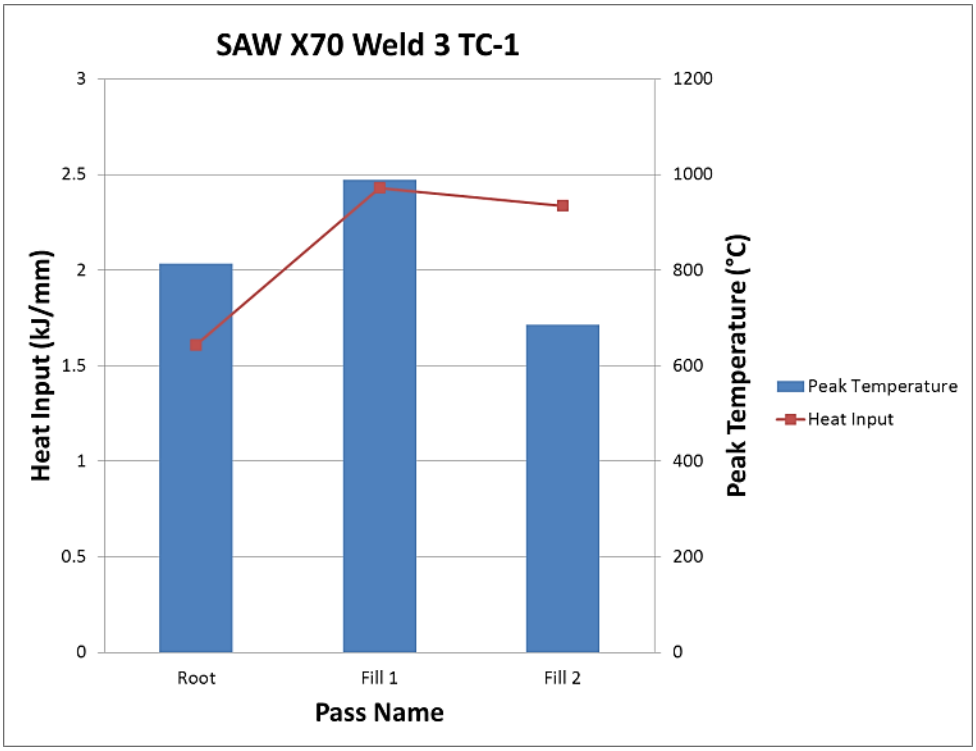

Figure 7-18 Relationship between heat input and peak temperature for X70 weld 3 TC-1

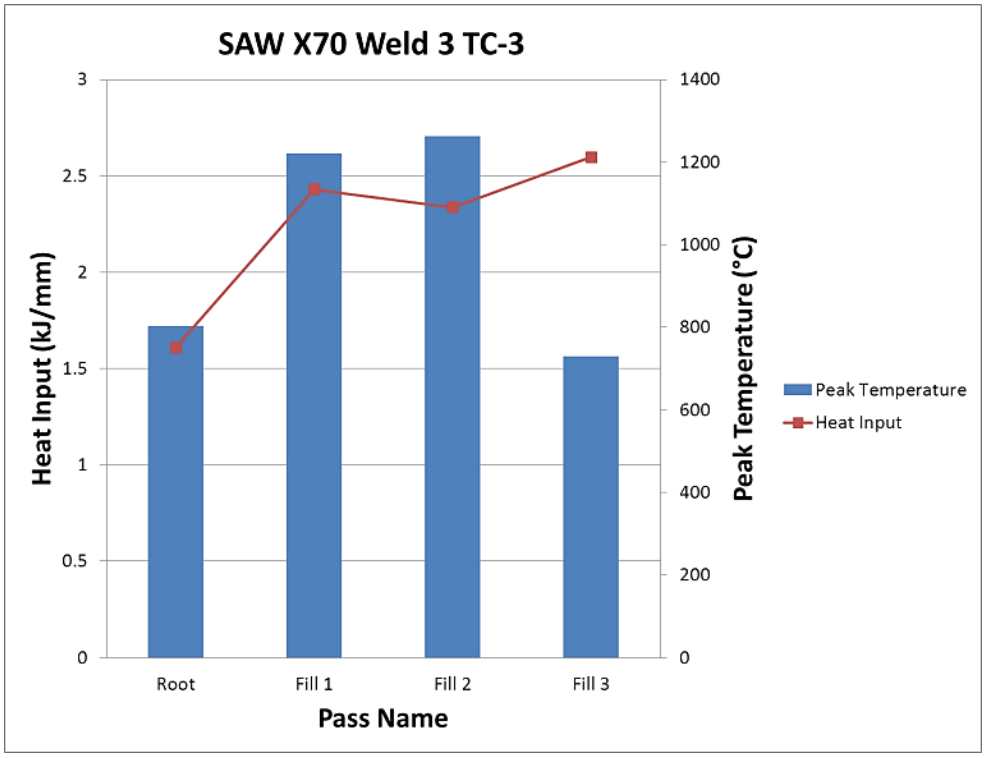

Figure 7-19 Relationship between heat input and peak temperature for X70 weld 3 TC-3

7.3.6 Identifying M-A phases

This has been discussed extensively in the literature review chapter. One of the methods explained earlier, which make use of LePèra etchant was employed in this research, as shown in figure 6-52 to figure 6-56 on pages 130 to 134.

The same positions were etched using both nital and LePèra etchants, as proposed by LePèra.[60] Martensitic phases appears white, bainitic appears black, while ferritic appears tan in most cases.[60]

Other researchers have recognised (residual) M-A as white coloured, ferrite as beige-brown coloured, and bainite/perlite as black or dark brown coloured.[185] SEM micrographs were also used in identifying the M-A phase as done by other researchers.[42; 139; 186; 187]

The above description, have led to the accurate interpretation of the phases in the X70 SAW, as shown in micrograph (b) of figure 6-54. It can be seen on the micrograph, there are a lot of tiny islands of M-A phase, well dispersed within the matrix.

It can be seen from micrographs (b) of figure 6-52 and figure 6-53 of the X65 grade submerged arc welded samples etched with LePèra reagent, that the volume fraction of M-A phase was less. X65 (a) has more M-A phase than X65 (b) as shown in the above mentioned micrographs respectively.

Tandem MIG welds, having low heat input, has produce an insignificant amount of M-A phase in both X70 and X100 samples, as shown in micrographs (b) in figure 6-55 and figure 6-56 respectively.

7.4 **Tandem MIG welds**

Narrow groove tandem MIG welding has been standardised at Cranfield University in recent years. Previous researches[145; 146; 188] have already design acceptable welding procedure specifications using this process. In this research, the procedure designed by Liratzis[145] for X100 pipes was adopted, and extended to the X70 pipes as modified by Girbo.[189] The welding procedure specifications given in Appendix A.2 were used for these welds.

7.4.1 Tandem MIG macrostructures

Figure 6-69 and figure 6-70 on page 144 are showing the macrographs of the X70 narrow groove tandem MIG welds 1 and 2 respectively. The macrographs of weld 1 are showing large porosity holes on both macrographs. While the macrographs of weld 2 are showing some lack of side wall fusion. These could be attributed to shielding gas and CTWD or arc length.[145; 172; 190; 191]

Inadequate shielding gas flow or misalignment of the gas shroud, are possible causes of porosity. Liratzis[145] proposed the use of 30 L/min gas flow rate to overcome this problem in his work. But that was for smaller wall thickness materials, contrary to this X70 grade which is a 31 mm thick pipe. This could be one of the possible reasons for porosity in the weld, even though a flow rate of 30 L/min was used. Another reason might be the reaction of the weld metal with the anti-spatter spray, which has been sprayed in the shroud and around the weld plate.

The lack of side wall fusion might be related to the arc length and the oscillation width. Due to the uneven nature of the jig, and the compensating characteristics of the welders, variations in arc length are inevitable.

7.4.2 Tandem MIG microstructures

Selected optical and SEM micrographs of the tandem MIG welds are presented in figure 6-71 to figure 6-74 from pages 145 to 147. The X70 micrograph shown in figure 6-71 is showing from left to right the weld metal, fusion line and the HAZ. Most of the structures are not easily resolvable at the magnifications used.

Some phases could be identified in the SEM macrographs shown in figure 6-74, there are some M-A phase fraction present, and some bainitic and acicular ferritic phases.

Figure 6-73 on page 146 is showing the X100 micrograph, also from left to right the weld metal, the fusion line and the HAZ. The phases are more distinct in this micrograph, as the coarse grains in the HAZ can be identified, and acicular ferrite and polygonal ferrite are also visible.

7.4.3 Tandem MIG thermal cycles

The thermal cycles of the tandem MIG welds have been recorded using thermocouples, as explained earlier. Capturing of the true welding thermal cycles is the main reason behind these experiments. This is to see the effect of the thermal cycles on the HAZ and to generate thermal cycles data to be used in the thermal simulation experiments, as carried out with the SAW welds. Representative thermal cycles are presented in figure 6-75 on page 148, they are showing the recorded thermal cycles from X100 weld 1, TC-3 and TC-4.

Thermal cycles from TC-3 and TC-4 are showing peak temperatures of about 670°C and 600°C, during fill passes 3 and 4 respectively. This is based on the thermocouples positioning used, which was shown in figure 5-14 on page 69. These thermal cycles happen to be amongst the highest recorded throughout the tandem MIG welds.

Therefore, it could be concluded that the thermal cycles are all within the subcritical region, where the heat from the subsequent weld, does not change the microstructure of the HAZ significantly, nor does it form brittle phases.

This could be related to the low heat input nature of the welding process, and the bevel design that was used.[190; 191] This led to a narrow HAZ, and a fast cooling rate even at low temperatures, ranging between 30 - 40°C/s. Hence, this is the reason why M-A phases are not significantly observed in these welds.

The hardness traverses also reflect the fast cooling nature of these welds, as a maximum of about 390 HV was recorded in all the welds.

The HAZ was showing a bit higher hardness than the weld metal. Figure 6-76 and figure 6-77 on pages 149 and 150 are showing the hardness traverses of the X70 and X100 pipeline steels respectively.

7.4.4 CTOD results of the X70 tandem MIG welds

The CTOD results of the X70 grade welds are given in table 6-5 on page 151. CTOD results of weld 1 were showing a fracture mode of δ_m (ductile fracture), while weld 2 have failed to satisfy the pre-crack shape requirements of BS 7448-2, which means there was a variation of more than 20% in crack length and less than 1.3 mm minimum pre-crack length.[192] This probably could have been resolved by compressing the sides of the samples before the pre-crack. This weld ends with a fracture mode of δ_c (brittle fracture).

Figure 6-78 and figure 6-79 on page 152, are showing the hardness maps of the pre-crack region for the X70 samples. Weld 2 was showing higher hardness values in the fusion line and HAZ, ranging between 260 – 360 HV. There are also a few Islands with high hardness, up to about 400 HV near the fusion line.

7.4.5 Probabilistic nature of the CTOD results

Depending on the chemical composition, and processing route among others,[193] M-A phases are always present in pipeline steels, even in some parent materials, but not in large amount enough to cause brittle failure. When the parent materials are subjected to different thermal cycles, especially in multi pass welds the tendency to form fairly large amount of M-A phase increases.

The chance of an M-A phase causing a brittle failure in a CTOD test, generally depends on the path taken by the crack. If the path taken happens to contain large amount of M-A phases, or a small amount, but the M-A is fairly large in size, then the chances of a brittle failure are very higher. But if the path taken has little or no M-A phase, or the sizes are too small, then the chances of brittle failure are limited.[47; 194-196]

7.5 **Thermal simulations**

The use of Gleeble thermo mechanical simulator to evaluate the heat affected zones fracture toughness using charpy impact samples has become more attractive in recent years. It offers an alternative way of generating the HAZ microstructure uniformly through the thickness of the specimen. Even though, thermally simulated charpy samples do not encounter problems such as microstructural inhomogeneity and crack tip placement as compared to a weld, they are still used as a fair representation of the HAZ.[16]

As presented earlier, in this research the true thermal cycles recorded from the weld HAZ were used for these simulations, this was one of the suggestions given by Pisarski[16] in a review he wrote. Single, double and triple thermal cycles were used to simulate the CGHAZ, ICRCGHAZ and SCRCGHAZ respectively.

Due to the nature of the thermal cycles of a weld, the heating is very fast, while cooling is non-linear, but is changing in a step wise mode. This can be seen from the real thermal cycles shown in figure 6-60, where cooling from the peak temperature up to about 800°C was very fast, and then the cooling tends to diminish from 800°C to about 200°C. Figure 5-18 on page 73 is showing the schematic representation of the triple thermal cycles used for the gleeble experiments.

7.5.1 Thermal cycles used for the simulation

The single thermal cycles used were divided into two groups based on peak temperatures which are 1000°C and 1250°C, while the cooling rates remains the same. Figure 6-80 on page 153 is a representative of the single thermal cycles which has been heated to 1250°C. In these experiments, a cooling rate of 50°C/s was used from the peak temperatures to 800°C, and then from 800°C to 200°C a cooling rate of 35°C/s was used. This is in agreement with some researchers,[140; 143] though their cooling rates were not derived from real welds, but from simulation results, such as welding software's and finite element analysis among others.

Cooling time in welding is normally defined as the time to cool from 800°C to 500°C, this is because most transformations are said to take place between this temperature regions known as $\Delta t_{8/5}$.[14; 49] Research conducted by Ikawa et al. [52] have shown that even at temperatures below 500°C transformation does exist, and can have a significant influence on toughness. Therefore, the need to carefully control the temperature up to 200°C is important.[52; 143]

A range of peak temperatures from 750°C to 1000°C were used for the second thermal cycles, cooling rates of 17.5°C/s and 20°C/s were also used. These second peak temperatures were carefully selected to cover different heating regimes within the HAZ, i.e. heating to subcritical, intercritical and supercritical regions. The second peak temperatures used are 750°C, 800°C, 850°C, 900°C, 950°C and 1000°C, similar peak temperatures were observed from the real welds as explained earlier. Figure 6-81 on page 154 is showing a representative of the second thermal cycles used.

Third peak temperatures of 350°C and 450°C were used, with a constant cooling rate of 5.5°C/s. This is because in a multi pass weld with more than two passes, the cooling rate decreases so much due to the effect of heat accumulation within the sample. Figure 6-82 on page 154 is a representation of a thermal cycle with all the three peak temperatures.

7.5.2 Charpy impact results

The charpy impact samples used in the thermal simulations were tested at different temperatures. The results were analysed based on the thermal cycles discussed above.

7.5.2.1 Single thermal cycle

Charpy impact toughness results of the simulated single thermal cycle's samples are presented in figure 6-83 on page 155. The figures are showing the results of the three materials used, i.e. X65 (a), X65 (b) and X70, as given in Appendix B.

The results are indicating the detrimental effect of the single thermal cycles on the impact toughness of the material grades as compared to the toughness of

the parent materials, as shown by the line plot in the figures mentioned. X65 (a) is showing a significant loss of toughness when subjected to both peak temperatures. The results are indicating decrease in toughness with decrease in test temperature.

The X65 (b) is indicating a completely different pattern from X65 (a), at a test temperature of -40°C, the toughness of the simulated samples was retained at both peak temperatures. While as the test temperatures decreases, the toughness also decreases, and it brings out the DBTT nature of the results.

On the other hand, the X70 results are not consistent like the two X65 grades. But the samples simulated at a peak temperature of 1250°C, were all showing a significant loss of toughness, i.e. at all test temperatures, the absorbed energy was below 50 J. At a peak temperature of 1000°C, the absorbed charpy impact energy at -40°C was 250 J, which happens to be more than that of the parent material at the same temperature. At -60°C the impact energy was below 50 J in all cases, while at -80°C the impact energy of the sample at 1000°C peak was above 50 J.

These results are confirming the harmful effect of simulated CGHAZ on the impact toughness of the parent materials. It can be said that both peak temperatures are above the A_{C3} line and have proven to be harmful by producing the coarse grained brittle structure. The 1250°C tend to be more harmful, and this is because the higher the peak temperature the more austenite that is produced. Due to the fast cooling rates associated with welding, there is no time for diffusion, therefore the carbon enriched austenite transforms in to a brittle phase (martensite).[143]

7.5.2.2 Double thermal cycles

Samples that were heated to second peak temperatures have been divided in to two, i.e. those heated within the intercritical temperatures (below A_{C3}), and those heated to the supercritical temperatures (above A_{C3}). These thermal cycles were in addition to the single thermal cycle of 1250°C the samples have already been subjected to.

The intercritically reheated samples for X65 (a) and X65 (b) have the same cooling rates of 17.5°C/s and 20°C/s, while that of the X70 is at different cooling rates of 10, 25 and 40°C/s. The same cooling rates were used on all the three grades of steels for the supercritical reheating (above A_{C3}).

Figure 6-84 on page 156, shows the charpy impact results of the intercritically reheated X65 (a) and (b), while figure 6-85 on page 156 is for the X70. The results are showing that the impact toughness of X65 (a) remains as bad as those from the single thermal cycles, if not worse, while X65 (b) is showing a different trend altogether.

The samples heated to 800°C are showing a drop in toughness at a test temperature of -40° and -60°C, as compared to the single thermal cycles, and they differ completely from the other intercritical temperatures. This drop of toughness at 800°C was observed in a research conducted by Moeinifar et al. which they related to the presence of M-A constituents.

X65 (b) samples heated to 750°C and 850°C are showing very similar trend in the charpy impact results. At a test temperature of -40°C, the toughness was retained in both samples, while at -60°C there was a massive gain in toughness as compared to the single thermal cycles, while at -80° there wasn't much change from the energy absorbed in the single thermal cycle.

Even though, the intercritically reheated X70 samples results given in figure 6-85, cannot be compared directly with the single or triple thermal cycles due to difference in cooling rates. The results are showing a ductile behaviour at all test temperatures, for virtually all the samples.

The supercritically reheated samples are shown in figure 6-86 on page 157. X65 (a) samples remain the same at all temperatures, while for the X65 (b) and X70 there was a different trend. For the X65 (b) samples, the 950°C and 1000°C are showing a similar pattern of absorbed energy, where at a test temperature of -40°C the samples retained their impact toughness when compared to those from the single thermal cycles.

At lower test temperatures, all the samples heated to supercritical region dropped in absorbed energy, in a similar way to the single thermal cycles. While for a second peak of 900°C, the absorbed energy wasn't stable like the others.

The X70 and X65 (b) samples heated to second peak temperatures of 900°C and 1000°C were showing an opposite trend to one another. Whereas the samples heated to a second peak of 950°C are showing a similar trend in both material grades. The X70 is showing a loss of toughness in most cases, with the impact toughness falling below 50 J, which is the average energy required for an X70 material as given in table 7-1. But the 950°C samples were showing a clearer trend, i.e. loss of toughness with decrease in test temperature.

This means that the X70 material is worse when heated to supercritical temperatures as compared to intercritical heating. X65 (b) maintain some degree of toughness at both intercritical and supercritical temperatures, while X65 (a) showed a significant loss of toughness at both heating temperatures.

The increase in the intercritical temperature (second peak temperature), generally leads to increase in the amount of transformed austenite,[197] which is rich in carbon content.[52] This enriched austenite transformed into M-A phase when subjected to favourable thermal cycles, such as those in high heat input multi pass welding.

7.5.2.3 Triple thermal cycles

After subjecting the samples to different second peak temperatures, third peak temperatures of 450°C and 350°C were added to samples that have been heated to first and second peak temperatures of 1250°C and 1000°C respectively. The results for all the material grades are given in figure 6-87 on page 158.

Results from X65 (a) grade are showing that the third peak temperature has no significant effect on the impact toughness. But the sample heated to a third peak temperature of 450°C, was showing a significant increase in toughness at a test temperature of -40°C. This could be due to the tempering effect and the dissociation of carbides[197] or an outcast.

The X65 (b) is showing an increase in impact toughness after been subjected to third peak temperatures, and shows a similar trend to the X65 (a) where the higher temperature of 450°C is showing a higher impact toughness, this is similar to what Haze and Aihara observed.[46]

On the other hand, the X70 is a complete opposite of the two materials, because the third peak temperatures did not show any improvement in the impact toughness. The results are showing that all the samples have remained below 50 J. This has proved the X70 to be a fully susceptible material to local brittle zones formation. Once the LBZ formed, subsequent thermal cycles do not recover the toughness at all, but rather only change the morphologies of the LBZ.[197]

7.5.3 Effect of cooling rates used on the charpy impact results

As mentioned earlier, the thermal cycles used are identical to the real welds thermal cycles. During the second peak thermal cycles, cooling rates of 17.5°C/s and 20°C/s were used, and figure 6-91 on page 162 is showing the charpy impact results of the X70 material cooled at those rates.

It can be seen that the samples cooled at the two cooling rates are hard to differentiate from each other in terms of absorbed impact energy. This is because the cooling rates are closed to each other and therefore falls within the same threshold, and produces quite similar results to one another. Figure 6-88 to figure 6-90 on pages 159 to 161 are agreeing to this explanation.

7.5.4 Fractography of the broken charpy impact samples

Fractographic examination of the broken charpy impact specimens for the three materials was carried out using a scanning electron microscope at higher magnifications. This was important in revealing the initiation sites, and to characterise the type of crack propagation (transgranular or intergranular).[21; 28; 198] and the mode of fracture, i.e. dimple, cleavage, fatigue or decohesive rupture.[199] Representative fractographs were chosen from samples fractured at -40°C for the different heating cycles, i.e. single, double and triple thermal cycles.

7.5.4.1 Single thermal cycles fractography

Fractographs of the single thermal cycles from both peak temperatures for the X65 (a) grade are presented in figure 6-92 on page 163. The fracture mode for both samples is of a primary cleavage, with a lot of small and uneven facets, both are classified as brittle failures.

The X65 (b) single thermal cycles fractographs in figure 6-93 on page 163, are showing fractograph (a) to have conical equiaxed dimples formed from micro void coalescence, and fractograph (b) to have more of elongated dimples, both fractures are ductile.

Contrary to the X65 grades, fractographs from the X70 single thermal cycles are having brittle and ductile fractures, as shown in figure 6-94 on page 163. Fractograph (a) is showing some small cleavage facets with some river lines, while fractograph (b) is showing a mixture of large and small elongated dimples, representing brittle and ductile fractures respectively.

7.5.4.2 Double thermal cycles fractography

From the double thermal cycles, fractographs of samples with second peak temperatures of 1000°C, fractured at -40°C are chosen to represent these cycles. Fractographs of X65 (a) are shown in figure 6-95 on page 164. Fractograph (a) is showing large quasi-cleavage facets, while (b) is showing a mixture of quasi-cleavage facets and some bands dimples, both samples are brittle.

Figure 6-96 on page 164 is presenting the fractographs of the X65 (b) samples, they both happen to be ductile. Fractograph (a) is showing some large facets with river lines of a ductile nature, and some islands of elongated dimples. An area where separation has occurred is also visible in the bottom right of the fractograph, while fractograph (b) is mainly shear elongated dimples.

Fractographs of the X70 double thermal cycle is showing a brittle fracture in both fractographs as shown in figure 6-97 on page 164. Fractograph (a) is exhibiting very large quasi-cleavage facets, with some river lines, while (b) is exhibiting more quasi-cleavage facets and some separations at the top.

7.5.4.3 Triple thermal cycles fractography

Triple thermal cycles were also represented by the samples fractured at -40°C, for both peak temperatures. The fractographs of the X65 (a) are showing a mixture of ductile and brittle fractures. Fractograph (a) is exhibiting a combination of large elongated and conical dimples, while fractograph (b) is more of large quasi-cleavage facets. The fractographs are shown in figure 6-98 on page 165.

X65 (b) fractographs are shown in figure 6-99 on page 165, and both happen to be ductile. Both fractographs are exhibiting shear dimpled fracture. On the other hand, all the fractographs of the X70 as shown in figure 6-100 on page 165 are having a brittle fracture. Both fractographs are showing complicated fractures, with some irregular facets.

7.5.5 Microstructural analysis of the broken charpy impact samples

The representative microstructures given in heading 6.5.4 are from the single, double and triple thermal cycles, fractured at -40°C. These cycles represents the various heat affected zones of a multi pass weld.

7.5.5.1 Single thermal cycles microstructures

Figure 6-101 to figure 6-103 on page 166 are the SEM micrographs of the single thermal cycles, corresponding to the coarse grain HAZ. All the micrographs are showing the presence of large prior austenite grains, depending on the initial grain size, which was said to have influence in the phases formed.[200]

The optical micrographs shown in figure 6-104 to figure 6-106 on page 167, have been compared with those of the various CGHAZ from the real welds, the similarities are obvious as seen in figure 7-20. This depends on the distance from the fusion line and the thermal cycles used, a wide range of CGHAZ microstructures could be characterized.[140]

For these experiments, all the single thermal cycles have a $t_{8/5}$ of 8.57 s, this is similar to what Li et al.[143] used (i.e. $t_{8/5}$ = 8 s).

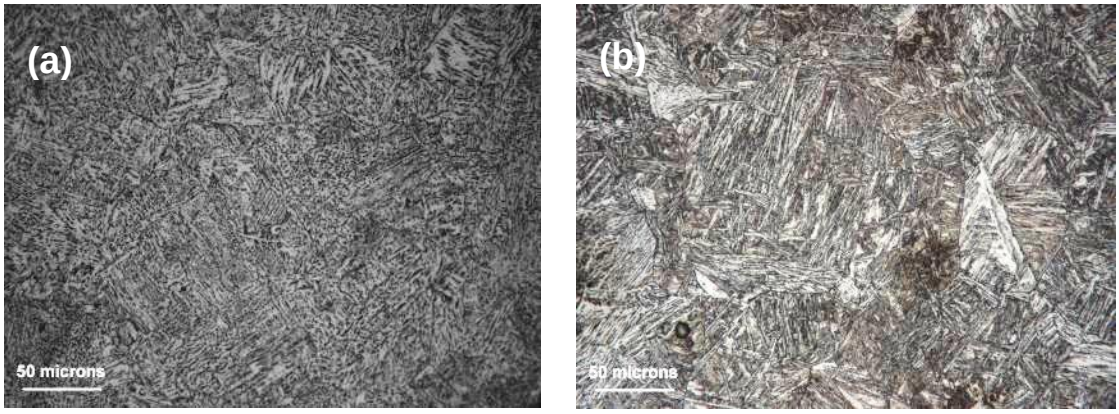

Figure 7-20 Optical micrographs of (a) real weld CGHAZ and (b) simulated CGHAZ for X65 (a) material

They[143] identified a sheaf-like form of bainitic microstructure, with a little presence of M-A phase. This is in agreement with the microstructures of the samples heated to 1250°C, while those heated to 1000°C have finer grains, especially in the TMCP materials as compared to the seamless material, which retains it coarse grained nature. Moeinifar et al.[140] worked on X80 material, but the structures and morphologies presented in their work are quite similar to what have been observed in this research.[140]

7.5.5.2 Double thermal cycles microstructures

The microstructures here are divided in to two, i.e. intercritically and supercritically reheated samples as presented in the earlier discussions. Samples heated to these regions have all been subjected to high temperatures, where partial austenitization is likely to take place, resulting in to localized austenitization with very high carbon contents ranging between 0.5 - 0.8%[52] or more than 1% in some cases.[20; 201] These carbon enriched zones, transforms in to martensite and retained austenite or M-A phases with different sizes and orientations, under the right conditions.[143]

M-A phase have been said to form at different favourable locations, such as prior-austenite grain boundaries as large bulky particles,[139] and some researchers identified the M-A phase at the bainitic boundaries with different sizes and morphologies.[202]

Figure 6-107 to figure 6-109 on page 168, are the representative optical micrographs of the double thermal cycles. They are showing the effect of reheating to 1000°C, after a single thermal cycle of 1250°C. The microstructures of the X65 (a), are both showing the presence of large grains even after the second thermal cycle. This confirms the low toughness values observed from both peak temperatures for the single thermal cycles.

Optical micrographs of the X65 (b) double thermal cycles are shown in figure 6-108 on page 168. The micrographs are exhibiting two distinct microstructures, with different grain sizes and orientation. Micrograph (a) with a CR of 17.5°C/s is showing a large grain size, with mainly bainitic and martensitic phases, there is a little presence of WF. On the other hand, micrograph (b) cooled at 20°C/s is showing smaller grain sized structure, predominantly bainitic with small presence of M and PF.

This agrees with both the difference in hardness and toughness between the two samples, micrograph (a) having higher hardness with a lower toughness, and micrograph (b) with a lower hardness, but a much higher toughness.

The X70 double thermal cycles optical micrographs as shown in figure 6-109 on page 168 are showing coarse grain microstructures with similar constituents, predominantly bainitic, with distinct prior-austenite grain boundaries.[143] They are showing the exact opposite of X65 (b) in terms of hardness and toughness behaviours, after been subjected to the same thermal cycles.

7.5.5.3 Triple thermal cycles microstructures

Figure 6-110 on page 169 is showing the optical micrographs of the X65 (a) samples subjected to triple thermal cycles. The microstructural constituents include bainitic and acicular ferritic phases, the large prior austenite grains obtained from the effect of the second thermal cycles were observed on these cycles as well.

The predominant microstructural constituents of the X65 (b) samples from the triple thermal cycles remain the same with those of the double thermal cycles.

There wasn't any significant change in terms of the grain size, but some tempered structures appeared in the micrographs as shown in figure 6-111 on page 169. This is confirming the tempering effect of the third thermal cycle.[197]

For the X70 pipeline steel, there was more evidence of grain refinement especially on the samples heated to a third peak temperature of 450°C. The microstructural constituents remain the same with those of the double cycles, mainly bainitic in nature. The optical micrographs are shown in figure 6-112 on page 169.

7.5.6 Characterization of M-A phase

The formation of M-A phases in steels has been related to several factors by different researches. Suzuki et al.[142] have identified heat input as one of the controllers in the formation of M-A phase, and more M-A phase is likely to form at 5 kJ/mm. In this research, heat input range of 1-3 kJ/mm was used throughout, which is less than what they have specified. They also suggest that at higher heat inputs (up to 60 kJ/mm) the M-A phase disintegrate, but this is out of range for a normal girth pipe welding. This might apply to pipe manufacturing, where multiple wire SAW is used, but the cumulative heat input might not get as high as 60 kJ/mm in most cases.

The maximum formation of M-A phase could also be related to the second peak temperature, which may be within a wide range of temperatures. In this research, temperatures within the intercritical and supercritical regions were used, and the supercritical temperatures tends to produce more M-A phases than the intercritical ones. This is contrary to what many researchers[139; 141; 203] have report and an addition to what others[46] have found.

Bonnevie et al.[197] relate the maximum formation of M-A phase to a temperature range of 20°C to 50°C above the A_{C1} temperature. They also report that the amount of M-A phase is not the only cause to loss of toughness, but the morphology is also critical, especially the large and bulky M-A's are particularly harmful to toughness.[204]

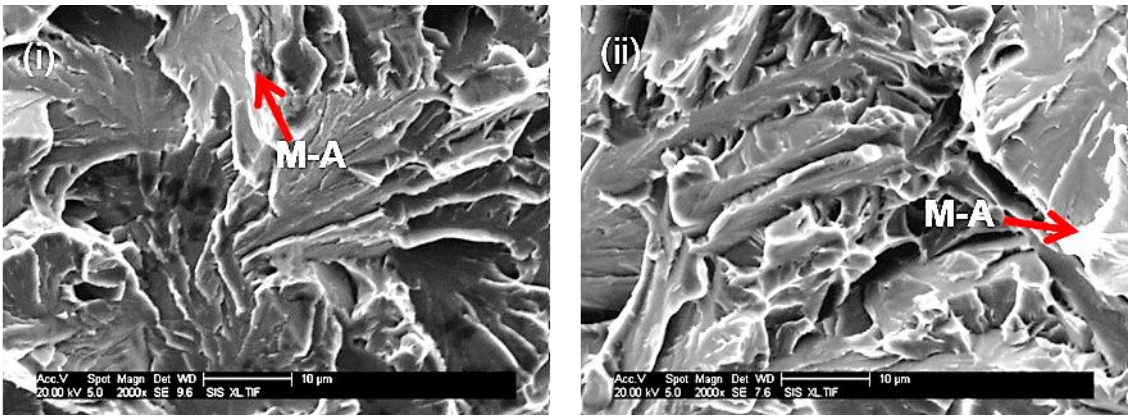

Figure 7-21 M-A phase on the fractographs of X70 triple thermal cycles (i) 450°C and (ii) 350°C

The area fraction and morphology of M-A have also been related to cooling rate, the higher the cooling rate the less the amount and the smaller the M-A size.[141]

Scanning electron microscope was used to characterise and identify the M-A phase in this research. Figure 7-21 is showing the presence of M-A phase on the fractographs of the X70 triple thermal cycles, at the third peak of 450°C and 350°C. A bulky and large M-A phase is presented in fractograph (ii) while fractograph (i) is showing a lath M-A along the grain boundary.

SEM micrographs of the supercritically reheated X70 samples, with a second peak temperature of 1000°C are shown in figure 7-22 and figure 7-23, in low and high magnifications respectively.

The presence of M-A phase was characterised on the supercritically reheated X70 samples, because they have the higher chances of producing M-A phase. It can be seen in figure 7-22 that there is high volume fraction of M-A phase in both samples. The M-A morphology in the samples cooled at 17.5°C/s are more of lath shape, while for those cooled at 20°C/s are bulky. This is more evident in the higher magnification micrographs as shown in figure 7-23, which has proved the reason behind the loss of toughness in these samples as explained earlier.[204]

This also disagrees with the findings of Moeinifar et al.[141] with regards to the effect of cooling rate. It can be seen from the micrographs, that the sample with the higher cooling rate produce more and bulkier M-A phase than the slower cooled sample, though the difference is not much. The presence of M-A at the prior austenite grain boundaries is also visible in figure 7-22, especially on the sample cooled at 20°C/s, this is very detrimental for the impact toughness.

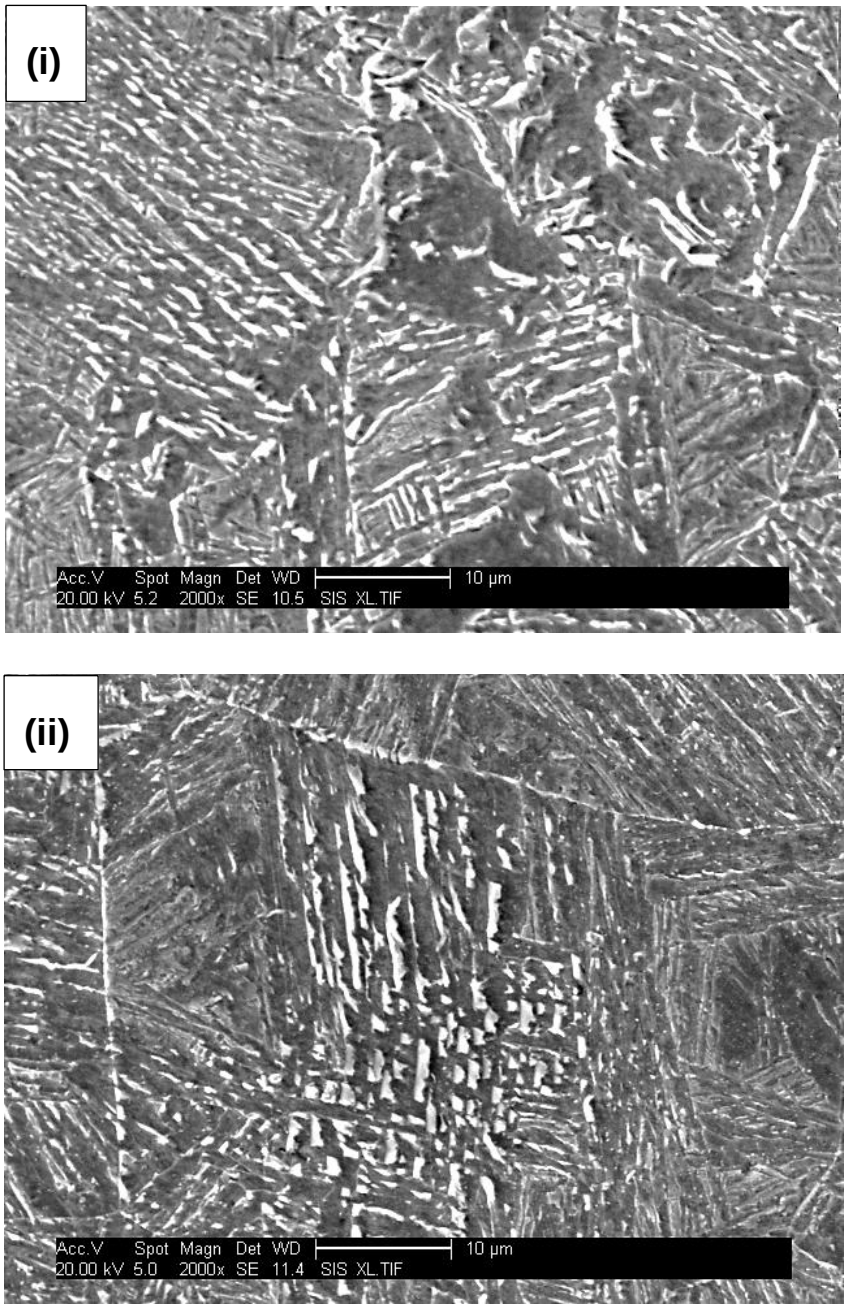

Figure 7-22 SEM micrographs of X70, double thermal cycle samples at a second peak temperature of 1000°C and cooling rates of (i) 17.5°C/s and (ii) 20°C/s

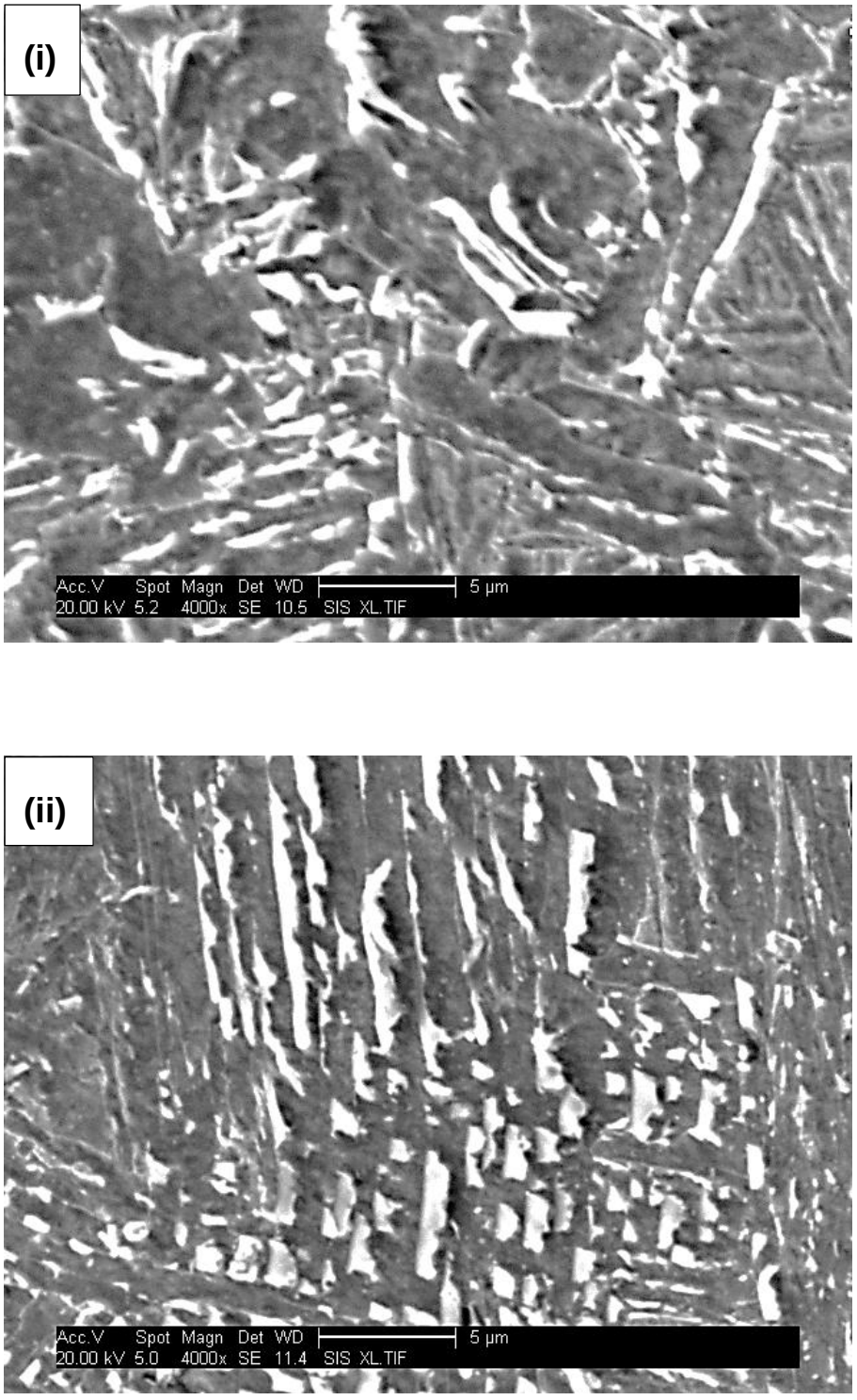

Figure 7-23 Higher magnification SEM micrographs of X70, double thermal cycle samples at a second peak temperature of 1000°C and cooling rates of (i) 17.5°C/s and (ii) 20°C/s showing the M-A phases

7.5.7 Hardness traverses

The microhardness traverse results of all the materials at different thermal cycles are given in table 6-6 to table 6-8 on pages 170 to 172. The results are not showing any distinct relation between the microhardness values and the charpy impact values at different test temperatures, though hardness can be related to microstructural constituent, which have a significant influence on the toughness of the material.[182]

The influence of the reheating temperatures on the microhardness of the double thermal cycles cooled at 20°C/s, and fractured at -40°C is shown in figure 7-24. It can be seen that there is a steady increase in hardness as the second peak temperature is increased in the supercritical region.

This is contrary to what Moeinifar et al.[139] have found that the supercritical region is showing the lowest hardness due to grain refinement and less blocky M-A constituents. This could be due to the difference in the cooling rates they used, which are far from those recorded from the real welds. The trend observed here could be due to the increase in the presence of M-A phase as the second peak temperatures are increased.

7.5.8 Comparison of hardness between inner and outer surfaces

A random comparison between the inner and the outer surfaces of the single thermal cycles of X65 (a) and double thermal cycles of X65 (b) was carried out. This is to see if there is any significant difference in hardness between the case and the core, so as to validate the uniformity of heating and cooling associated with the Gleeble thermo mechanical simulator, as claimed by the manufacturers.[147]

Figure 6-113 on page 173, is showing the hardness comparison between the surface and the core of the single thermal cycles of the X65 (a) grade. This is a validation process, therefore, the samples are selected randomly not in any particular order.

It can be seen from the figure that the maximum difference in hardness between the surface and the core is 4 HV, while the minimum is 0.5 HV. There isn't a particular trend, because in sample 1 the core is harder, while in samples 2 and 3 the surface is harder.

In the double thermal cycles, there is not much difference as well, the maximum difference of 8.4 HV was recorded in sample 2, as shown in figure 6-114 on page 173. The minimum difference recorded was on sample 1, with a difference of 0.9 HV. This has confirmed the assumption that there is a fairly uniform heating and cooling even with a 10 mm square and diameter samples.

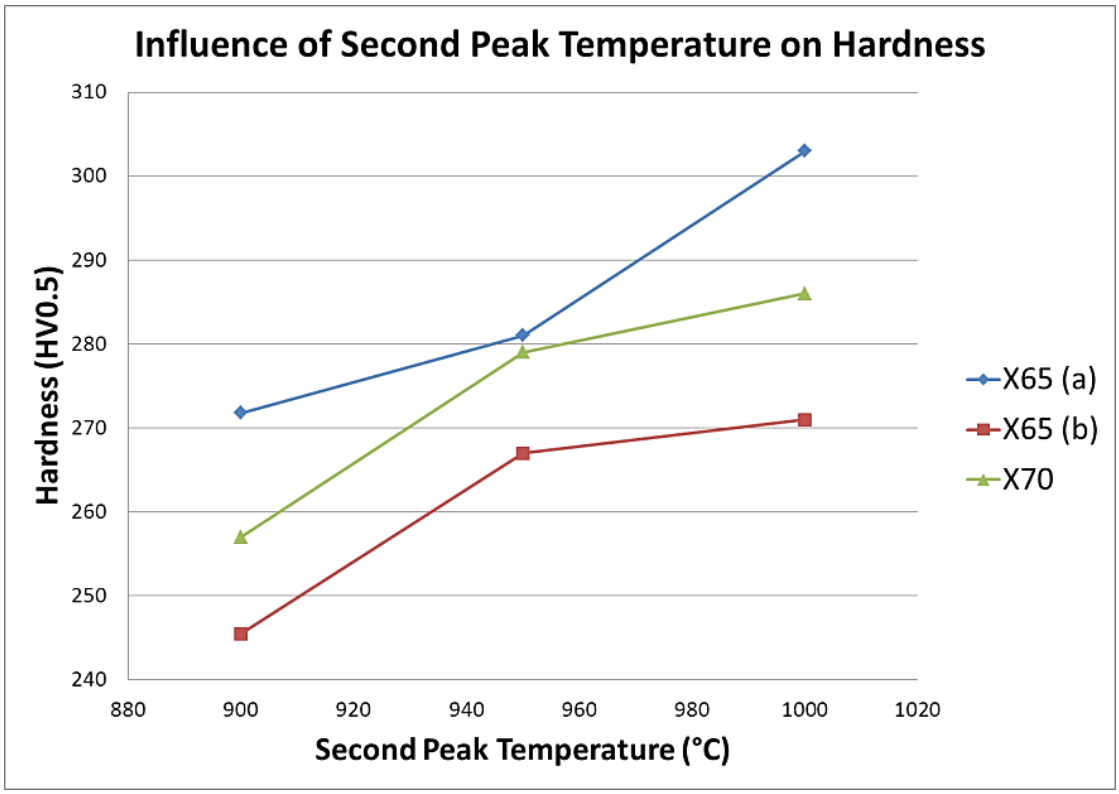

Figure 7-24 Influence of second peak temperature on the hardness values of X65 (a), X65 (b) and X70 grades

8 CONCLUSIONS

- From the CCT diagrams of the four API-5L steel grades, it could be interpreted that similar thermal cycles can produce different metallurgical phases depending on the composition, processing route and the starting microstructures of the material.
- The real welding thermal cycles recorded were showing that the HAZ, depending on the welding process and pass sequence, have been reheated through various temperature regions viz. subcritical, inter-critical and supercritical part of the phase diagram.
- The thermal cycles responsible for low toughness in some of the pipeline steels have been interpreted from the real welding thermal cycles and the results from the thermal simulation experiments. It was found that the first and second thermal cycles are responsible for the formation of low toughness phases in the welds. This corresponds to single and double thermal cycles in the thermal simulations experiments.
- In our given scope of investigation, the third thermal cycles have little or no effect in most cases, but have some tempering effect on the microstructures.
- The impact toughness values of the thermal simulated samples could be correlated to the peak temperature of the second thermal cycle for some grades. The initial microstructure of the steel is an important factor towards determining the influence of thermal cycles on the toughness of the thermally simulated specimens.
- The X65 (b) grade has shown significantly high toughness at both intercritical and supercritical temperatures as compared to the other grades. This could be due to its starting microstructure been very fine (sub-micron size) and many other factors including chemical composition and thermal cycles.
- There is no difference in hardness between the surface and the core of the samples when thermally simulated in the Gleeble thermo-mechanical

simulator. This indicates a relatively uniform heating and cooling cycles throughout the cross section of the samples.

- The formation of M-A phase is more pronounced at temperatures above the A_{C3} line, i.e. supercritical temperatures. However, some samples showed brittle behaviour even when heated to a temperature below A_{C1}. This can be due to several other factors which generate brittle behaviour e.g. presence of stress raiser in the microstructure. An inhomogeneity in composition could also be a reason for such unpredictable failures.
- The amount and morphology of the M-A phase is significantly influenced by heating in to the intercritical and supercritical regions. Other factors that affect it include the peak temperatures and the cooling rate.
- From the instrumented welds, it could be deduced that submerged arc welding is more susceptible to the formation of M-A phase as compared to tandem MIG welding with low heat input.
- From the materials used in this research, it could be concluded that X70 grade welded with SAW is more susceptible to M-A formation than all the other grades welded with SAW.
- The materials welded with tandem MIG welding both have less chances of M-A formation, thus better toughness properties.
- This research has shown that thermal simulation can be used to evaluate the thermal response of a material in a multiple thermal cycle situation, and the corresponding microstructures. This can be achieved via:
    - Construction a CCT diagram
    - Thermal simulation using Charpy impact samples and thermal cycles from a real weld
    - Metallurgically and mechanically analysing the samples in order to evaluate their response to the thermal cycles

9 RECOMMENDATIONS

This chapter is divided into two, recommendation to companies on how they can reduce the formation of brittle phases in multi-pass welds or to avoid them completely where necessary. And recommendation for future work on what should be done to continue with the research.

9.1 **Recommendation to companies**

- The use of CCT diagrams and thermal simulation using real welding thermal cycles to establish the susceptibility of a material to local brittle zones formation will prove vital to pipeline steel manufacturers and pipeline welding companies.
- Multiple thermal cycles simulation is necessary to evaluate their effect on a material, this could be achieved by using thermo mechanical simulators.
- The multiple thermal cycles for simulation should be based on the intended heat input that will be used for a particular project.
- A welding procedure specification should be designed based on the susceptibility of the materials to LBZ. Low heat input should be used for susceptible materials to avoid higher peak temperatures in the second thermal cycles, which might lead to LBZ formation. While for materials that are not susceptible, there is no harm in using the optimal heat input, even if it is high.
- Collaboration between the welding companies and the steel manufactures in evaluating the susceptibility of the pipe material to LBZ before embarking on a project will be very helpful.

9.2 **Recommendation for future work**

- More welds should be done to explore different weld preparation and their influence on HAZ thermal cycles.
- A standardised way of attaching thermocouples should be developed and modelled to prove it. This will ensure other researches and companies can use the method to record thermal cycles from the HAZ of their welds, especially in the high heat input processes.
- More CTOD tests need to be carried out to accurately validate the presence of LBZ in the welds and the simulated samples.
- Modelling of the various welding processes normally used in pipeline industries is necessary. In order to have a comprehensive understanding of the various isotherms from different welding processes and their consequential thermal cycles.
- Computer simulation and modelling of the thermal cycles, in relation to heat input and the resulting metallurgical phases should be carried out. This can be validated with the available data from this research, and will ease the processes of characterizing materials as susceptible or not based on the given parameters.
- A dilatometer should be used on the charpy impact samples used for the HAZ simulation. This will give the transformation temperatures as well as the respective thermal cycles. It will make it easier to locate the transformation points on a CCT diagram for further analysis.
- EBSD analysis needs to be carried out on the samples to characterize the grains, the boundary angles, and to map the phases correctly.
- Misorientation maps should be made using EBSD to accurately characterise the presence of some phases in both the welds and in the specimens used for simulations.

REFERENCES

1. Sandrea, R. and Sandrea, I. (2010), "Deep water crude oil output: How large will the uptick be?", *Oil and Gas journal,* vol. 108, no. 41, pp. 1-10.

2. Yapp, D. and Blackman, S. A. (2004), "Recent developments in high productivity pipeline welding", *Journal of the Brazilian Society of Mechanical Sciences and Engineering,* vol. 26, no. 1, pp. 89-97.

3. Liessem, A., Schröder, J., Pant, M., Erdelen-Peppler, M., Liedtke, M., Höhler, S. and Stallybrass, C. (2008), "Manufacturing challenges of high strength line pipes", *New Developments on Metallurgy and Applications of High Strength Steels, Buenos Aires 2008 - Proceedings of the International Conference on New Developments on Metallurgy and Applications of High Strength steel,* Vol. 1, Buenos Aires, pp. 543.

4. Demofonti, G. and Mannucci, G. (2008), "A critical review of the developed and available know how devoted to a safe use of X100 grade steel in large diameter pipelines", *New Developments on Metallurgy and Applications of High Strength Steels, Buenos Aires 2008 - Proceedings of the International Conference on New Developments on Metallurgy and Applications of High Strength steels,* Vol. 1, Buenos Aires, pp. 625.

5. Chunming, W., Xingfang, W., Jie, L. and Ning'an, X. (2006), "Transmission electron microscopy of martensite-austenite islands in pipeline steel X70", *Materials Science and Engineering A,* vol. 438, no. 440, pp. 267-271.

6. Bae, J. H., Yoo, J. Y., Kim, K., Kim, C. M. and Kang, K. B. (2006), "Development of high strength linepipe steels with excellent weldability", in Xi'an, Shaanxi 710065, China; Tubular Goods Research Centre of China National Petroleum Corp. (CNPC), .

7. Traizet, A. -., Galand, E., Chovet, C. and Leduey, B. (2008), "Welding consumables development for high strength steel joints for oil & gas applications", *New Developments on Metallurgy and Applications of High Strength Steels, Buenos Aires 2008 - Proceedings of the International Conference on New Developments on Metallurgy and Applications of High Strength steels,* Vol. 1, Buenos Aires, pp. 685.

8. Widgery, D. (2008), "Welding arctic pipelines", *Welding in the World,* vol. 52, no. SPEC. ISS., pp. 591-596.

9. U.S. Energy Information Administration (2010), *Annual energy outlook 2010,* DOE/EIA-0383(2010), www.eia.doe.gov/oiaf/aeo, USA.

10. Timokhina, I. B., Hodgson, P. D., Ringer, S. P., Zheng, R. K. and Pereloma, E. V. (2007), "Precipitate characterisation of an advanced high-

strength low-alloy (HSLA) steel using atom probe tomography", *Scripta Materialia,* vol. 56, no. 7, pp. 601-604.

11. Mishra, S. K., Das, S. and Ranganathan, S. (2002), "Precipitation in high strength low alloy (HSLA) steel: A TEM study", *Materials Science and Engineering A,* vol. 323, no. 1-2, pp. 285-292.

12. Bhadeshia, H. K. D. H. and Honeycombe, R. (2006), *Steels Microstructure and Properties,* 3rd ed, Elsevier, UK.

13. Sampath, K. (2006), "An understanding of HSLA-65 plate steels", *Journal of Materials Engineering and Performance,* vol. 15, no. 1, pp. 32-40.

14. Kou, S. (2003), *Welding Metallurgy,* 2nd ed, John Wiley and sons, USA.

15. Amano, K., Kudo, J., Itakura, N. and Nakano, Y. (1989), "Metallurgical and welding factors controlling local brittle zone in weld HAZ", *Proceedings of the International Offshore Mechanics and Arctic Engineering Symposium,* Vol. 3, pp. 683.

16. Pisarski. (TWI UK), (1996), *A Review of HAZ Toughness Evaluation* (unpublished Report), UK.

17. Ouro, C. R., de S. Bott, I. and Bastian, F. L. (1996), "Influence of local brittle zone size on the heat affected zone toughness of structural steel for offshore applications", *ASM International (USA), pp. 519-524, 1996; ASM International (USA), pp. 519-524, 1996,* 519-524, 1996;, pp. ASM International (USA), p.

18. Tian, Z. (1998), "Study on local brittle zone fracture toughness of TMCP steels", *Journal of Iron and Steel Research International,* vol. 10, no. 4, pp. 50-53.

19. Kenney, K. L., Reuter, W. G., Reemsnyder, H. S. and Matlock, D. K. (1997), "Fracture initiation by local brittle zones in weldments of quenched and tempered structural alloy steel plate", *ASTM Special Technical Publication,* vol. 1321, pp. 427-449.

20. Lambert, A., Drillet, J., Gourgues, A. F., Sturel, T. and Pineau, A. (2000), "Microstructure of martensite-austenite constituents in heat affected zones of high strength low alloy steel welds in relation to toughness properties", *Science and Technology of Welding and Joining,* vol. Vol.5, no. 3, pp. 168-173.

21. Siciliano, F., Stalheim, D. G. and Gray, J. M. (2009), "Modern high strength steels for oil and gas transmission pipelines", *Proceedings of the Biennial International Pipeline Conference, IPC,* Vol. 3, pp. 187.

22. Asahi, H. (2005), "Recent progress of line pipe for natural gas transportation", *Journal of the Japan Welding Society.,* vol. 74, no. 4, pp. 14-19.

23. Widgery, D. J. (2002), "Welding high strength pipelines: From laboratory to field", *Svetsaren, a Welding Review,* vol. 57, no. 2, pp. 22-25.

24. Jang, J., Lee, B., Ju, J., Kwon, D. and Kim, W. (2002), "Crack-initiation toughness and crack-arrest toughness in advanced 9 pct Ni steel welds containing local brittle zones", *Metallurgical and Materials Transactions A (USA),* vol. 33A, no. 8, pp. 2615-2622A.

25. Komizo, Y. -. (2008), "Overview of recent welding technology relating to pipeline construction", *Transactions of JWRI,* vol. 37, no. 1, pp. 1-5.

26. Renwick, B. G. and Patchett, B. M. (1976), "Operating characteristics of the submerged arc process", *Welding Journal (Miami, Fla),* vol. 55, no. 3, pp. 69s-76s.

27. Ito, R., Hiraoka, K. and Shiga, C. (2005), "Softening characteristics in ultra-narrow-gap GMAW joints of ultra-fine grained steel", *Science and Technology of Welding and Joining,* vol. 10, no. 4, pp. 468-474.

28. Zhou, J., Taylor, D. and hodgkinson, D. (2008), "Further-large scale implementation of advanced pipeline technologies", *7th International Pipeline Conference,* 2008, Calgary, Alberta Canada, ASME, USA, pp. 353.

29. Widgery, D. J. (2006), "Mechanised welding of pipelines", *Svetsaren,* vol. 60, no. 1, pp. 23-26.

30. Nakata, H., Kami, C. and Mathuo, N. (2008), "Development of API X80 grade electric resistance welding line pipe with excellent low temperature toughness", *JFE Technical Report,* , no. 12, pp. 27-31.

31. Shanmugam, S., Ramisetti, N. K., Misra, R. D. K., hartmana, J. and Jansto, S. G. (2008), "Microstructure and high strength-toughness combination of a new 700 MPa Nb-microalloyed pipeline steel", *Materials Science and Engineering A,* vol. 487, pp. 26-37.

32. Wang, W., Shan, Y. and YAng, K. (2009), "Study of high strength pipeline steels with different microstructures", *Materials Science and Engineering A,* vol. 502, pp. 38-44.

33. Keehan, E., Karlsson, L., Andren, H. -. and Bhadeshia, H. K. D. H. (2006), "New developments with C-Mn-Ni high-strength steel weld metals, Part A-Microstructure", *Welding Research,* vol. 1, pp. 200-s-210-s.

34. Reip, C. -., Kempken, J. and Schlüter, J. (2008), "Metallurgical aspects of high-strength steel grades and their processing through CSP® technology", *New Developments on Metallurgy and Applications of High Strength Steels, Buenos Aires 2008 - Proceedings of the International Conference on New Developments on Metallurgy and Applications of High Strength steels,* Vol. 1, Buenos Aires, pp. 557.

35. Grimpe, F., Meimeth, S., Meuser, H., Muthmann, E., Liessem, A. and Stallybrass, C. (2008), "The development of high strength heavy plate for the pipe industry using modern experimental and numerical methods", *New Developments on Metallurgy and Applications of High Strength Steels, Buenos Aires 2008 - Proceedings of the International Conference on New Developments on Metallurgy and Applications of High Strength steels,* Vol. 1, Buenos Aires, pp. 493.

36. Aristotile, R., Di vito, L. F. and Barsanti, L. (2004), "Welding of X100 steels for gas pipelines", *Welding International,* vol. 18, no. 11, pp. 877-882.

37. Andrews, R. M., Morgan, G. C. and Beattie, W. J. (2004), "The significance of low toughness areas in the seam weld of linepipe", *Proceedings of the Biennial International Pipeline Conference, IPC,* Vol. 2, pp. 1833.

38. Bruce, B., Ramirez, J., Johnson, M. and Gordon, R. (2004), "Welding of high strength pipelines", *Proc.of IPC 2004 International Pipeline Conference,* Vol. 1,2 and 3, Calgary-Alberta, pp. 1499.

39. Bai, D., Collins, L., Hamad, F., Chen, X. and Klein, R. (2007), "Microstructure and mechanical properties of high strength linepipe steels", *Materials Science and Technology Conference and Exhibition, MS and T'07 - "Exploring Structure, Processing, and Applications Across Multiple Materials Systems",* Vol. 6, pp. 3808.

40. Zhao, M. -., Yang, K. and Shan, Y. (2002), "The effects of thermo-mechanical control process on microstructures and mechanical properties of a commercial pipeline steel", *Materials Science and Engineering A,* vol. 335, pp. 14-20.

41. Widgery, D. (2010), "Double jointing of high strength pipelines", *Welding in the World,* vol. 54, no. 11-12, pp. R360-R365.

42. Rojko, D. and Gliha, V. (2005), "The Influence of simulated thermal cycle on the formation of microstructures of multi-pass weld metal", *Metalurgija,* vol. 44, no. 1, pp. 19-24.

43. Evans, G. M. (1995), "Microstructure and properties of ferritic steel welds containing Al and Ti", *Welding Journal (Miami, Fla),* vol. 74, no. 8, pp. 249s-261s.

44. Tweed, J. H. and Knott, J. F. (1983), "Effect of reheating on microstructure and toughness of C-Mn weld metal.", *Metal science,* vol. 17, no. 2, pp. 45-54.

45. Zalazar, M., Quesada, H. J. and Asta, E. P. (2000), "Microstructure produced in the welding of steels for wide diameter pipes", *Welding International (UK),* vol. 14, no. 1, pp. 48-52.

46. Haze, T. and Aihara, S. (1986), *Metallurgical factors controlling HAZ toughness in HT50 steels,* IIW Doc. IX-1423-86, IIW, UK.

47. Machida, S., Yoshinari, H. and Suzuki, Y. (1995), "Statistical study on the effect of local brittle zones (LBZs) on the fracture toughness (crack tip opening displacement) of multipass welded joints", *ASTM Special Technical Publication,* , no. 1207, pp. 264-290.

48. Adams, C. M. (1958), "Cooling rates and peak temperatures in fusion welding", *Welding Journal,* vol. 37, no. 5, pp. 210.

49. Easterling, K. (1992), *Introduction to the Physical Metallurgy of Welding,* 2nd ed, Butterworths, London.

50. Di Nunzio, P. E., Cesile, M. C., Anelli, E. and Richard, G. (2008), "Prediction of microstructure and hardness of multipass heat affected zone in high strength steel girth welds", *New Developments on Metallurgy and Applications of High Strength Steels, Buenos Aires 2008 - Proceedings of the International Conference on New Developments on Metallurgy and Applications of High Strength steels.* Vol. 1, pp. 597.

51. Smith, W. F. (2004), *Foundation of Materials science and Engineering,* Third ed, McGraw-Hill, U.S.A.

52. Ikawa, H., Oshige, H. and Tanoue, T. (1980), *Effect of martensite-austenite constituents on HAZ toughness of high strength steel,* IIW Doc. IX-1156-80, American Technical Society, USA.

53. Leslies, W. C. and Hornbogen, E. (1996), "Physical metallurgy of steels", in Robert, W. C. and Peter, H. (eds.) *Physical Metallurgy,* 4th ed, North Holland, , pp. 1555-1620.

54. Bhadeshia, H. K. D. H. (1997), "Martensite and Bainite in steels: Transformation mechanism and mechanical properties", *J. PHYS. IV FRANCE,* vol. 7, pp. 367-376.

55. Fiore, S. R., Vaze, S., Bowker, J. T., Gianetto, J. A., Hudson, M. G., Khurana, S. and Doriing, D. V. (2009), "Development of optimized weld metal chemistries for pipeline girth welding of high strength line pipe",

Proceedings of the Biennial International Pipeline Conference, IPC, Vol. 3, pp. 417.

56. Gianetto, J. A., Bowker, J. T. and Dorling, D. V. (2005), "Assessment of properties and microstructure of X100 pipeline girth welds", *Welding in the World,* vol. 49, no. 11-12, pp. 77-89.

57. Offerman, S. E., van Dijk, N. H., Sietsma, J., Grigull, S., Lauridsen, E. M., Margulies, L., Poulsen, H. F., Rekveldt, M. T. and van der Zwaag, S. (2010), "Grain nucleation and growth during phase transformations", *Science AAAS,* [Online], vol. 298, , pp. February 25, 2010-1005 available at: www.sciencemag.org.

58. McMahon, J. A. and Thomas, G. (1973), "Development of economical, tough, ultra-high-strength Fe-Cr-C steels.", *Inst Met (London) Monogr Rep Ser,* vol. 1, no. 3, pp. 180-184.

59. Ale, R. M., Rebello, J. M. A. and Charlier, J. (1996), "A metallographic technique for detecting martensite-austenite constituents in the weld heat-affected zone of a micro-alloyed steel", *Materials Characterization (USA),* vol. 37, no. 2-3, pp. 89-93.

60. Lepera, F. S. (1979), "Improved etching technique for determination of percent martensite in high-strength dual-phase steels", *Metallography,* vol. 12, pp. 263-268.

61. Yong, Z., Furen, X., Jingwu, Z., Yiyin, S., Wei, W. and Ke, Y. (2006), "In situ TEM study of the effect of M-A films at gain boundaries on crack propagation in an ultra-fine acicular ferrite pipeline steel", *Acta Materialia,* vol. 54, pp. 435-443.

62. Clark, M. D., Edwards, G. R. and Landau, A. (1998), "Metallographic techniques for microstructural characterization of SMAW filler metal for HSLA 100 steel", *Trends in Welding Research,* 1998, Pine Mount G.A., ASME, USA, pp. 173.

63. Randle, V. (2009), "Electron backscatter diffraction: Strategies for reliable data acquisition and processing", *Materials Characterization,* vol. 60, pp. 913-922.

64. Kim, Y. M., Lee, H. and Kim, N. J. (2008), "Transformation behaviour and microstructural characteristics of acicular ferrite in linepipe steels", *Materials Science and Engineering A,* vol. 478, pp. 361-370.

65. Li, X., Wiskel, J. B., Ivey, D. G. and Omotoso, O. (2008), "Characterization of microstructure in high strength microalloyed steels using quantitative X-ray diffraction", *Proceedings of the International*

Pipeline Conference, 2008, Calgary, Alberta, Canada, ASME, Canada, pp. 445.

66. Zhao, Y. T., Shang, C. J., Yang, S. W., Wang, X. M. and He, X. L. (2006), "The metastable austenite transformation in Mo-Nb-Cu-B low carbon steel", *Materials Science and Engineering A,* vol. 433, pp. 169-174.

67. Venegas, V., Caleyo, F., González, J. L., Baudin, T., Hallen, J. M. and Penelle, R. (2005), "EBSD study of hydrogen-induced cracking in API-5L-X46 pipeline steel", *Scripta Materialia,* vol. 52, no. 2, pp. 147-152.

68. Li, Y., Ji, L., Feng, Y., Han, X. and Huo, C. (2009), "Effect of micro-texture on fracture separation in X80 line pipe steel", *Proceedings of the Biennial International Pipeline Conference, IPC,* Vol. 3, pp. 139.

69. Komizo, Y. and Terasaki, H. (2009), "Controlling the phase evolutions during welding toward developments of high strength steel weld metal with martensite microstructure", *ASM Proceedings of the International Conference: Trends in Welding Research,* pp. 268.

70. Babu, S. S., Elmer, J. W., David, S. A. and Quintana, M. A. (2002), "In situ observations of non-equilibrium austenite formation during weld solidification of an Fe-C-Al-Mn low-alloy steel", *Proceedings of the Royal Society A,* vol. 458, pp. 811-821.

71. Babu, S. S., Elmer, J. W., Specht, E. D., Vitek, J. M. and David, S. A. (2005), "Application of in-situ diffraction experiments to understand nonequilibrium phase transformations in structural alloys", *Proceedings of an International Conference on Solid-Solid Phase Transformations in Inorganic Materials 2005,* Vol. 2, pp. 475.

72. Babu, S. S., Elmer, J. W., Vitek, J. M. and David, S. A. (2002), "Time-resolved X-ray diffraction investigation of primary weld solidification in Fe-C-Al-Mn steel welds", *Acta Materialia,* vol. 50, no. 19, pp. 4763-4781.

73. Zhao, M. -., Hanamura, T., Qiu, H. and Yang, K. (2005), "Lath boundary thin-film martensite in acicular ferrite ultralow carbon pipeline steels", *Materials Science and Engineering A,* vol. 395, no. 1-2, pp. 327-332.

74. Yoo, J. -., Seo, D. -., Ahn, S. -. and Kang, K. -. (2008), "Development of high strength linepipe steel", *New Developments on Metallurgy and Applications of High Strength Steels, Buenos Aires 2008 - Proceedings of the International Conference on New Developments on Metallurgy and Applications of High Strength,* Vol. 1, pp. 641.

75. Elmer, J. W., Wong, J. and Ressler, T. (2001), "Spatially resolved X-ray diffraction mapping of phase transformations in the heat-affected zone of carbon-manganese steel arc welds", *Metallurgical and Materials*

Transactions A: Physical Metallurgy and Materials Science, vol. 32, no. 5, pp. 1175-1187.

76. Oku, N., Asakura, K., Inoue, J. and Koseki, T. (2009), "In-situ observation of phase transformation in steels", *ASM Proceedings of the International Conference: Trends in Welding Research,* pp. 272.

77. Elmer, J. W., Palmer, T. A., Zhang, W., Wood, B. and DebRoy, T. (2003), "Kinetic modelling of phase transformations occurring in the HAZ of C-Mn steel welds based on direct observations", *Acta Materialia,* vol. 51, pp. 3333-3349.

78. Shome, M. and Mohanty, O. N. (2006), "Continuous cooling transformation diagrams applicable to the heat-affected zone of HSLA-80 and HSLA-100 steels", *Metallurgical and Materials Transactions A,* vol. 37A, no. 7, pp. 2159-2169A.

79. Gliha, V. (2005), "The microstructure and properties of materials at the fusion line", *Metalurgija,* vol. 44, no. 1, pp. 13-18.

80. David, S. A., Babu, S. S. and Vitek, J. M. (2003), "Welding: Solidification and microstructure", *JOM,* vol. 55, no. 6, pp. 14-20.

81. Callister, W. D. (2007), *Materials Science and Engineering An Introduction,* 7th ed, John Wiley and Sons, UK.

82. Alexandrov, B. T. and Lippold, J. C. (2004), *Methodology for in-situ investigation of phase transformations in welded joints,* IIW-IX-2114-04, IIW.

83. Nippes, E. F. and Savage, W. F. (1949), "Development of specimen simulating weld heat-affected zone", *Welding Journal,* vol. 28, pp. 534s-545s.

84. Farson, D., Richardson, R. and Li, X. (1998), "Infrared measurement of base metal temperature in gas tungsten arc welding", *Welding Journal (Miami, Fla),* vol. 77, no. 9, pp. 396-s.

85. Alexandrov, B. T. and Lippold, J. C. (2007), "Single sensor differential thermal analysis of phase transformations and structural changes during welding and postweld heat treatment", *Welding in the World,* vol. 51, no. 11-12, pp. 48-59.

86. Shanmugam, S., Ramisetti, N. K., Misra, R. D. K., Mannering, T., Panda, D. and Jansto, S. (2007), "Effect of cooling rate on the microstructure and mechanical properties of Nb-microalloyed steels", *Materials Science and Engineering A,* [Online], no. 460-461, pp. 335-343 available at: www.elsevier.com/locate/msea.

87. Guang, X., Lun, W., Shenfu, Y., Li, L. and Feng, L. (2008), "A new method for accurately plotting CCT curves", *Materials Letters,* vol. 62, pp. 3978-3980.

88. Zhao, M. -., Yang, K., Xiao, F. -. and Shan, Y. -. (2003), "Continuous cooling transformation of undeformed and deformed low carbon pipeline steels", *Materials Science and Engineering A,* vol. 355, no. 1-2, pp. 126-136.

89. Lee, J. -., Hon, M. -. and Cheng, G. -. (1987), "The continuous cooling transformation of carbon-manganese steel", *Scripta Metallurgica,* vol. 21, no. 4, pp. 521-526.

90. Krauss, G. and Thompson, S. W. (1995), "Ferritic microstructures in continuously cooled low-amd ultralow-carbon steels", *ISIJ International,* vol. 35, no. 8, pp. 937-945.

91. Keehan, E., Zachrisson, J. and Karlsson, L. (2010), "Influence of cooling rate on microstructure and properties of high strength steel weld metal", *Science and Technology of Welding and Joining,* vol. 15, no. 3, pp. 233-238.

92. Shi, Y. and Han, Z. (2004), "Effect of weld thermal cycle on microstructure and fracture toughness of simulated heat affected zone for a 800 MPa grade high strength low alloy steel", *J Mater Process Technol,* vol. 31, pp. 379-388.

93. Bott, I. S., Vieira, A. A. H., De Souza, L F G and Rios, P. R. (2010), "Microstructural evaluation of API 5L X80 pipeline steels submitted to different cooling rates", *Materials Science Forum.Vol.638-642,* vol. 638-642, pp. 3146-3151.

94. Howard, B. C. (1998), *Modern welding technology,* 4th ed, Prentice-Hall inc, New jersey.

95. Trevisan, R. E., Santos, N. F., Fals, H. C. and Santos, A. A. (2002), "Effect of interpass temperature on morphology, microstructure and microhardness of welded API 5L X65 steel", *Proceedings of the International Pipeline Conference, IPC,* Vol. A, Calgary, Alta, pp. 327.

96. Jones, J. E. and Luo, Y. (1990), *Welding: Theory and Practice,* Elsevier.

97. Rajad, D. (1992), "Heat effects of welding-temperature field, residual stress, distortion", *Springer-Verlag, USA,* , pp. 348.

98. API. (1220 L Street, N.W., Washington, D.C. 20005), (2007), *Specification for line pipe (ANSI/API Specification 5L)* (unpublished Standard), USA.

99. Lord, M. and Bhadeshia, H. K. D. H. (1998), "Scatter in steel weld metal tensile properties due to variations in the interpass temperature", *ASM Proceedings of the International Conference: Trends in Welding Research,* Pine Mountain, GA, pp. 870.

100. Lord, M. (1999), "Effect of interpass temperature on properties of high-strength weld metals", *Svetsaren, a Welding Review,* vol. 54, no. 1, pp. 53-58.

101. Porter, D. A. and Easterling, K. E. (2001), *Phase Transformations in metals and alloys,* 2nd ed, Nelson thornes, UK.

102. Navaching.com (2010)*, Continuous cooling transformation diagram*, available at: http://www.navaching.com/forge/forge.gifs/cctO1.jpg (accessed 7th July, 2010).

103. Thompson, S. W., Colvin, D. J. and Krauss, G. (1990), "Continuous cooling transformations and microstructures in a low-carbon, high-strength low-alloy plate steel", *Metall.Trans.A,* vol. 21A, no. 6, pp. 1493-1507.

104. Stalheim, D. G. and Muralidharan, G. (2007), "The role of continuous cooling transformation diagrams in material design for high strength oil and gas transmission pipeline steels", *Proceedings of the Biennial International Pipeline Conference, IPC,* Vol. 3 PART A, pp. 231.

105. LI, Z., WU, D., LV, H. -. and FANG, S. -. (2007), "Continuous cooling transformation behaviour of C-Si-Mn TRIP steel", *Journal of Iron and Steel Research International,* vol. 14, no. 5 SUPPL. 1, pp. 277-281.

106. Zhang, M., Li, L., Fu, R. Y., Krizan, D. and De Cooman, B. C. (2006), "Continuous cooling transformation diagrams and properties of micro-alloyed TRIP steels", *Materials Science and Engineering A,* vol. 438-440, no. SPEC. ISS., pp. 296-299.

107. García De Andrés, C., Caballero, F. G., Capdevila, C. and Álvarez, L. F. (2002), "Application of dilatometric analysis to the study of solid-solid phase transformations in steels", *Materials Characterization,* vol. 48, no. 1, pp. 101-111.

108. De Cock, T., Capdevila, C., Caballero, F. G. and De Andrés, C. G. (2006), "Interpretation of a dilatometric anomaly previous to the ferrite-to-austenite transformation in a low carbon steel", *Scripta Materialia,* vol. 54, no. 5, pp. 949-954.

109. Onsoien, M. I., M'hamdi, M. and Mo, M. (2009), "A CCT diagram for an offshore pipeline steel of X70 type", *Welding Journal,* vol. 88, no. Supplement, pp. 1-s-6-s.

110. Xiao, F., Liao, B., Ren, D., Shan, Y. and Yang, K. (2005), "Acicular ferritic microstructure of a low-carbon Mn-Mo-Nb microalloyed pipeline steel", *Materials Characterization,* vol. 54, no. 4-5, pp. 305-314.

111. Wang, W., Yan, W., Zhu, L., Hu, P., Shan, Y. and Yang, K. (2009), "Relation among rolling parameters, microstructures and mechanical properties in an acicular ferrite pipeline steel", *Materials and Design,* vol. 30, no. 9, pp. 3436-3443.

112. Niu, T., Yu, H., Kang, Y. and Long, M. (2008), "Research on the accurate control of initial and finishing cooling temperatures for X70 pipeline steels", *Materials Science Forum,* Vol. 575-578 PART 2, pp. 1038.

113. Fonda, R. W., Vandermeer, R. A. and Spanos, G. (1998), "Continuous cooling transformation diagrams for rich and lean compositional variants of an ultra-low carbon weld consumable", *ASM Proceedings of the International Conference: Trends in Welding Research,* pp. 197.

114. Prior, G. K. (1994), "Role of dilatometry in the characterisation of steels", *Metals forum,* vol. 18, pp. 265-276.

115. García De Andrés, C., Caballero, F. G. and Capdevila, C. (1998), "Dilatometric characterization of pearlite dissolution in 0.1C-0.5Mn low carbon low manganese steel", *Scripta Materialia,* vol. 38, no. 12, pp. 1835-1842.

116. Datta, D. P. and Gokhale, A. M. (1981), "Austenitization kinetics of pearlite and ferrite aggregates in a low carbon steel containing 0.15 wt pct C.", *Metallurgical transactions.A, Physical metallurgy and materials science,* vol. 12 A, no. 3, pp. 443-450.

117. De García Andres, C., Jiménez, J. A. and Álvarez, L. F. (1996), "Splitting phenomena occurring in the martensitic transformation of Cr13 and CrMoV14 Stainless steels in the absence of carbide precipitation", *Metallurgical and Materials Transactions A: Physical Metallurgy and Materials Science,* vol. 27, no. 7, pp. 1799-1805.

118. Nippes, E. F., Savage, W. F., Bastian, B. J., Mason, H. F. and Curran, R. M. (1955), "An investigation of the hot ductility of high temperature alloys", *Welding Journal,* vol. 34, no. 4, pp. 183s-196s.

119. Knorovsky, G. A., Robino, C. V., Dykhuizen, R. C. and MacCallum, D. O. (1998), "Dilatometry in the Gleeble: What Did You Really Measure?", *ASM Proceedings of the International Conference: Trends in Welding Research,* pp. 101.

120. Chen, Y. and Wang, Y. -. (2009), "Thermal and microstructure analysis software for GMAW girth welds of high strength pipelines", *Welding in the World,* vol. 53, no. SPECIAL ISSUE, pp. 189-194.

121. García De Andrés, C., Caballero, F. G., Capdevila, C. and Bhadeshia, H. K. D. H. (1998), "Modelling of kinetics and dilatometric behavior of non-isothermal pearlite-to-austenite transformation in an eutectoid steel", *Scripta Materialia,* vol. 39, no. 6, pp. 791-796.

122. Gamsjager, E., Svoboda, J. and Fischer, F. D. (2005), "Austenite-ferrite phase transformation in low-alloyed steels", *Computational Materials Science,* vol. 32, pp. 360-369.

123. Rath, B. B. and Pande, C. S. (2011), "An analytical description of overall phase transformation kinetics applied to the recrystallization of pure iron", *Acta Materialia,* vol. 59, pp. 7538-7545.

124. Zhao, J. Z., Mesplont, C. and Cooman, C. D. (2002), "Calculation of the phase transformation kinetics from a dilatation curve", *Journal of Materials Processing Technology,* vol. 129, pp. 345-348.

125. Zhao, J. Z., Mesplont, C. and Cooman, C. D. (2002), "Quantitative analysis of the dilatation during an isothermal decomposition of austenite", *Materials Science and Engineering A,* vol. 332, pp. 110-116.

126. Ishikawa, N., Okatsu, M., Endo, S., Kondo, J., Zhou, J. and Taylor, D. (2009), "Mass production and installation of X100 linepipe for strain-based design application", *Proceedings of the Biennial International Pipeline Conference, IPC,* Vol. 3, pp. 705.

127. Hamad, F., Collins, L. and Volkers, R. (2009), "Effects of GMAW procedure on the heat-affected zone (HAZ) toughness of X80 (GRADE 550) linepipe", *Proceedings of the Biennial International Pipeline Conference, IPC,* Vol. 3, pp. 553.

128. Krauss, G. and Marder, A. R. (1971), "The morphology of martensite in iron alloys", *Metallurgical Transactions,* vol. 2, no. 9, pp. 2343-2357.

129. Thomas, G. (1971), "Electron microscopy investigations of ferrous martensites", *Metallurgical Transactions,* vol. 2, no. 9, pp. 2373-2385.

130. Di Schino, A., Izquierdo, A. and Anelli, E. (2008), "Effect of chemical composition on hardenability and response to tempering of high strength low-C steels", *New Developments on Metallurgy and Applications of High Strength Steels, Buenos Aires 2008 - Proceedings of the International Conference on New Developments on Metallurgy and Applications of High Strength steels,* Vol. 1, Buenos Aires, pp. 583.

131. ZHANG, Y. -., ZHANG, H. -., LI, J. -. and LIU, W. -. (2009), "Effect of heat input on microstructure and toughness of coarse grain heat affected zone in Nb microalloyed HSLA steels", *Journal of Iron and Steel Research International,* vol. 16, no. 5, pp. 73-80.

132. Chen, Y. T., Guo, A. M., Wu, L. X., Zeng, J. and Li, P. H. (2006), "Microstructure and mechanical property development in the simulated heat affected zone of V treated HSLA steels", *Acta Metallurgica Sinica (English Letters),* vol. 19, no. 1, pp. 57-67.

133. Beidokhti, B., Koukabi, A. H. and Dolati, A. (2009), "Effect of titanium addition on the microstructure and inclusion formation in submerged arc welded HSLA pipeline steel", *Journal of Materials Processing Technology,* vol. 209, no. 8, pp. 4027-4035.

134. Penniston, C., Collins, L. and Hamad, F. (2009), "Effects of Ti, C and N on weld HAZ toughness of high strength line pipe", *Proceedings of the Biennial International Pipeline Conference, IPC,* Vol. 3, pp. 75.

135. Calvo, J., Jung, I. -., Elwazri, A. M., Bai, D. and Yue, S. (2009), "Influence of the chemical composition on transformation behaviour of low carbon microalloyed steels", *Materials Science and Engineering A,* vol. 520, no. 1-2, pp. 90-96.

136. Ishida, K. (1995), "Calculation of the effect of alloying elements on the Ms temperature in steels", *Journal of Alloys and Compounds,* vol. 220, no. 1-2, pp. 126-131.

137. Gilbert, A. and Owen, W. S. (1962), "Diffusionless transformation in iron-nickel, iron-chromium and iron-silicon alloys", *Acta Metallurgica,* vol. 10, no. 1, pp. 45-54.

138. Liu, C., Zhao, Z., Northwood, D. O. and Liu, Y. (2001), "A new empirical formula for the calculation of M_S temperatures in pure iron and super-low carbon alloy steels", *Journal of Materials Processing Technology,* vol. 113, no. 1-3, pp. 556-562.

139. Moeinifar, S., Kokabi, A. H. and Madaah Hosseini, H. R. (2010), "Influence of peak temperature during simulation and real thermal cycles on microstructure and fracture properties of the reheated zones", *Materials and Design,* vol. 31, no. 6, pp. 2948-2955.

140. Moeinifar, S., Kokabi, A. H. and Hosseini, H. R. M. (2011), "Role of tandem submerged arc welding thermal cycles on properties of the heat affected zone in X80 microalloyed pipe line steel", *Journal of Materials Processing Technology,* vol. 211, no. 3, pp. 368-375.

141. Moeinifar, S., Kokabi, A. H. and Hosseini, H. R. M. (2011), "Effect of tandem submerged arc welding process and parameters of Gleeble simulator thermal cycles on properties of the intercritically reheated heat affected zone", *Materials and Design,* vol. 32, no. 2, pp. 869-876.

142. Suzuki, S., Kamo, T. and Komizo, Y. (2009), "Influence of martensitic islands on fracture behaviour of high heat input weld HAZ", *Welding International,* vol. 23, no. 6, pp. 397-402.

143. Li, C., Wang, Y., Han, T., Han, B. and Li, L. (2011), "Microstructure and toughness of coarse grain heat-affected zone of domestic X70 pipeline steel during in-service welding", *Journal of Materials Science,* vol. 46, no. 3, pp. 727-733.

144. DNV. (Veritasveien 1, NO-1322 Høvik, Norway), (2007), *Offshore standard DNV-OS-F101 (Submarine pipeline systems)* (unpublished Standard), Norway.

145. Liratzis, H. (2007), *Tandem gas metal arc pipeline welding* (unpublished PhD. thesis), Cranfield University, Cranfield Press.

146. Hudson, M. G. (2004), *Welding of X100 linepipe* (unpublished PhD. thesis), Cranfield University, Cranfield Press.

147. Dynamic Systems Inc. (2012), *Gleeble 3500 System*, available at: http://www.gleeble.com/index.php/products/gleeble-3500.html (accessed June/19).

148. Dynamic Systems Inc. (2012), *The Gleeble newsletter (Spring 2001)*, available at: http://www.gleeble.com/images/Newsletters/SPRING2001.PDF (accessed June/19).

149. Dynamic Systems Inc. (2012), *The Gleeble newsletter (Summer 2000)*, available at: http://www.gleeble.com/images/Newsletters/SUMMER2000.PDF (accessed June/19).

150. OERLIKON (2012), *Pipe mills an Oerlikon market solutions*, available at: www.oerlikon-welding.com (accessed April/2012).

151. Bewick, A., (2011), *Submerged arc welding*, Lincoln Electric.

152. ASTM E8/E8M:2011. (2011), *Standard test methods for tension testing of metallic materials* (unpublished Standard), USA.

153. ASTM E23-07. (2008), *Standard test methods for notched bar impact testing of metallic materials* (unpublished Standards), USA.

154. BS 7448-1. (London), (1991), *Method for determination of $K_{IC,}$ critical CTOD and critical J values of metallic materials* (unpublished British Standard), British Standard Institute.

155. Mohrbacher, H. (2006), "The development of niobium microalloyed steel for the production of seamless tubes", *Metal:2006 15th International metallurgical and materials conference,* 23 -25th May, 2006, Červený zámek, Hradec nad Moravicí. Czech Republic, Czech Republic, pp. 1.

156. Anelli, E. and Colleluori, D. (2001), "Sour service X65 seamless linepipe for offshore special applications", *Proceedings of the Eleventh (2001) International Offshore and Polar Engineering Conference,* Vol. IV, 17-22 June, 2001, Norway, pp. 242.

157. Waldo, S. (2009), "Line pipe steel - treading the tightrope", *Essays Innovate,* vol. 3, pp. 62-64.

158. Graf, M., Schröder, J., schwinn, V. and Hulka, K. (2002), "Production of large diameter pipes grade X70 with high toughness using acicular ferrite microstructures", *International Conference on Application and Evaluation of High Grade Linepipes in Hostile Environments,* 8-9th November, 2002, Yokohama, Japan, pp. 1.

159. Hillenbrand, H., Graf, M. and Kalwa, C. (2001), "Development and production of high strength pipeline steels", *Niobium 2001,* 2-5th December, 2001, Orlando, Florida, USA, pp. 1.

160. Arafin, M. A. and Szpunar, J. A. (2011), "Effect of bainitic microstructure on the susceptibility of pipeline steels to hydrogen induced cracking", *Materials Science and Engineering A,* vol. 528, no. 15, pp. 4927-4940.

161. Tsuru, S. (1990), "Comparison of various TMCP steel manufacturing techniques", *Proceedings, International Conference on the Metallurgy, Welding, and Qualification of Microalloyed (HSLA) Steel Weldments, November 6-8, 1990,* 6-8 November, 1990, Houston Texas, USA, American Welding Society, 1990, pp. 105.

162. Liessem, A. and Erdelen-Peppler, M. (2004), "A critical view on the significance of haz toughness testing", *Proceedings of the Biennial International Pipeline Conference, IPC,* Vol. 2, pp. 1871.

163. Fonda, R. and Spanos, G., (2000), *Microstructural evolution in ultra-low-carbon steel weldments—Part I: Controlled thermal cycling and continuous cooling transformation diagram of the weld metal*, Springer Boston.

164. Yue, X., Lippold, J. C., Alexandrov, B. T. and Babu, S. S. (2012), "Continuous cooling transformation behavior in the CGHAZ of naval steels", *Welding journal suppliment,* vol. 91, pp. 67-s-75-s.

165. Andrews, K. W. (1965), "Empirical formulae for the calculation of some transformation temperatures", *Journal of the Iron and Steel Institute,* vol. 203, no. 7, pp. 721-727.

166. García De Andrés, C., Capdevila, C., Madariaga, I. and Gutiérrez, I. (2001), "Role of molybdenum in acicular ferrite formation under continuous cooling in a medium carbon microalloyed forging steel", *Scripta Materialia,* vol. 45, no. 6, pp. 709-716.

167. Thompson, S. W., Colvin, D. J. and Krauss, G. (1996), "Austenite decomposition during continuous cooling of an HSLA-80 plate steel", *Metallurgical and Materials Transactions A: Physical Metallurgy and Materials Science,* vol. 27, no. 6, pp. 1557-1571.

168. Krauss, G. (1993), "Steels: Heat treatment and processing principles", *Proceedings of the ASM international conference, Materials park, Ohio USA, 1993,* 1993, Materials Park, Ohio, ASM International, USA, pp. 169.

169. Kasuya, T., Yurioka, N. and Okumura, M. (1995), *Methods for predicting maximum hardness of HAZ and selecting necessary preheat temperature for steel welding,* 65, Nippon Steel Technical Report, Japan.

170. Adonyi, Y. (2006), ""Heat-affected zone characterization by physical simulations" An overview on the use of the Gleeble discusses the advantages and disadvantages of thermomechanical simulation", *Welding Journal,* , pp. 42-47.

171. Williams, J. G. (2007), "Advances in steels for high strength ERW linepipe application in Australia", *Materials Forum,* vol. 31, pp. 1-10.

172. Robert, W. M. (1999), *Principles of welding processes, Physics, Chemistry, and Metallurgy,* 1st ed, John Wiley & Sons, INC., Canada.

173. Han, S. Y., Shin, S. Y., Lee, S., Kim, N. J., Bae, J. -. and Kim, K. (2010), "Effects of cooling conditions on tensile and charpy impact properties of API X80 linepipe steels", *Metallurgical and Materials Transactions A: Physical Metallurgy and Materials Science,* vol. 41, no. 2, pp. 329-340.

174. Rojko, D. and Gliha, V. (2005), "Simulations of transformation kinetics in a multi-pass weld", *Materials and Manufacturing Processes,* vol. 20, no. 5, pp. 833-849.

175. Drayton, P. A. (1972), "An examination of the influence of process parameters on submerged arc welding", *Welding Research International,* vol. 2, no. 2, pp. 1.

176. Jackson, C. E. (1960), "The science of arc welding, Part II - consumable electrode welding arc", *Welding Journal,* vol. 39, no. 5, pp. 177-s.

177. Robinson, M. H. (1961), "Observations on electrode melting rates during submerged arc welding", *Welding Journal,* vol. 40, no. 11, pp. 503-s.

178. Widgery, D. J. (1979), "New ideas in submerged arc welding", *Trends in Steel and Consumables for Weld, Int Conf,* vol. 1, pp. 217-229.

179. Webster, S. E. and Bateson, P. H. (1989), "The significance of LBZ - A comparison of normalised and higher strength steels", *8th International conference on offshore mechanics and arctic engineering the Hague, 1989,* 19-23 March, 1989, Hague, pp. 613.

180. Francois, D. and Burdekin, F. M. (1999), "State of the art resume on significance of local brittle zones", *Welding Research Abroad,* vol. 45, no. 5, pp. 36-41.

181. Hashemi, S. H., Mohammadyani, D., Pouranvari, M. and Mousavizadeh, S. M. (2009), "On the relation of microstructure and impact toughness characteristics of DSAW steel of grade API X70", *Fatigue and Fracture of Engineering Materials and Structures,* vol. 32, no. 1, pp. 33-40.

182. Haze, T. and Aihara, S. (1988), "Influence of toughness and size of local brittle zone on HAZ toughness of HSLA steels", *Proceedings of the International Offshore Mechanics and Arctic Engineering Symposium,* Vol. 3, pp. 515.

183. Ritchie, R. O., Knott, J. F. and Rice, J. R. (1973), "On the relationship between critical tensile stress and fracture toughness in mild steel", *J. Mech. Phys. Solids,* vol. 21, pp. 395.

184. Bleck, W., Reisgen, U., Mokrov, O., Rossiter, E. and Rieger, T. (2010), "Methodology for thermo mechanical simulation and validation of mechanical weld-seam properties", *Advanced Engineering Materials,* vol. 12, no. 3, pp. 147-152.

185. Güngör. (ArcelorMittal Global R&D Gent / OCAS NV), (2011), *General description and usage of different etchants* (unpublished Report), .

186. Shin, S. Y., Hwang, B., Lee, S., Kim, N. J. and Ahn, S. S. (2007), "Correlation of microstructure and charpy impact properties in API X70 and X80 line-pipe steels", *Materials Science and Engineering A,* vol. 458, no. 1-2, pp. 281-289.

187. Shin, S. Y., Hong, S., Bae, J., Kim, K. and Lee, S. (2009), "Separation phenomenon occurring during the charpy impact test of API X80 pipeline steels", *Metallurgical and Materials Transactions A,* vol. 40A, pp. 2333.

188. Newman, M. (2008), *Experimental tandem GMAW in narrow gap X100 pipe material* (unpublished MSc. thesis), Cranfield University, Cranfield Press.

189. Girbo, A. A. (2011), *Study on the effect of oxygen content on the impact toughness of weld metal* (unpublished MSc thesis), Cranfield University, Cranfield University.

190. Norrish, J. (1992), *Advanced Welding processes,* IOP ltd, NY.

191. University of Wollongong. (Australia), (2001), *Welding processes and equipment 2* (unpublished lecture notes), Cranfield university.

192. BS 7448-2. (British Standard Institute), (1997), *Fracture mechanics toughness tests. Method for determination of KIc, critical CTOD and critical J values of welds in metallic materials* (unpublished British Standard), UK.

193. Devillers, L., Kaplan, D. and Testard, P. (1993), "Approach to predicting microstructures and toughness properties in heat affected zones of multipass welds of structural steels", *Welding Research Abroad,* vol. 40, no. 3, pp. 8-19.

194. Smith, R. A. (1989), "Aspects of the interaction between a fatigue crack a local brittle zone (LBZ)", *Proceedings of the International Offshore Mechanics and Arctic Engineering Symposium,* Vol. 3, pp. 705.

195. Pisarski, H. G. and Slatcher, S. (1993), "Assessment of the significance of LBZs in steels using a probabilistic model", *Proceedings of the International Conference on Offshore Mechanics and Arctic Engineering - OMAE,* Vol. 2, pp. 89.

196. Tronskar, J. P., Karlsen, A., Bratfos, H. and Hauge, M. (1992), "Probabilistic fracture mechanics analyses of a welded K-node: significance local brittle zones", *Proceedings of the International Offshore Mechanics and Arctic Engineering Symposium,* Vol. 2, pp. 105.

197. Bonnevie, E., Ferrière, G., Ikhlef, A., Kaplan, D. and Orain, J. M. (2004), "Morphological aspects of martensite-austenite constituents in intercritical and coarse grain heat affected zones of structural steels", *Materials Science and Engineering A,* vol. 385, no. 1-2, pp. 352-358.

198. Nuruddin, I. K. (2009), *An investigation on the toughness properties of welded pipeline steels* (MSc thesis), Cranfield University, Cranfield University.

199. ASM International (1987), *Fractography,* Vol. 12 ed, ASM International, USA.

200. Eroglu, M. and Aksoy, M. (2000), "Effect of initial grain size on microstructure and toughness of intercritical heat-affected zone of a low carbon steel", *Materials Science and Engineering A,* vol. 286, no. 2, pp. 289-297.

201. Lambert-Perlade, A., Gourgues, A. F., Besson, J., Sturel, T. and Pineau, A. (2004), "Mechanisms and modelling of cleavage fracture in simulated heat-affected zone microstructures of a high-strength low alloy steel", *Metallurgical and Materials Transactions A: Physical Metallurgy and Materials Science,* vol. 35, no. 13, pp. 1039-1053.

202. Taban, E. (2008), "Toughness and microstructural analysis of super duplex stainless steel joined by plasma arc welding", *Journal of Materials Science,* vol. 43, no. 12, pp. 4309-4315.

203. Gianetto, J. A., Shen, G., Tyson, W. R. and Glover, A. G. (1998), "Assessment of the Fracture Toughness of Pipeline Girth Welds", *ASM Proceedings of the International Conference: Trends in Welding Research,* pp. 916.

204. Matsuda, F., Fukada, Y., Okada, H., Shiga, C., Ikeuchi, K., Horii, Y., Shiwaku, T. and Suzuki, S. (1996), "Review of mechanical and metallurgical investigations of martensite-austenite constituent in welded joints in Japan", *Welding in the World, Le Soudage Dans Le Monde,* vol. 37, no. 3, pp. 134-154.

APPENDICES

Appendix A Welding Parameters

A.1 Submerged arc welding full welds

Cranfield UNIVERSITY

Welding Process	Submerged Arc Weld
Welding Position	1G
Material Grade	X65 (A)
Diameter	324 mm
Thickness	25.4 mm
Electrode Wire	Φ = 3.2 mm
Brand	Lincoln LNS 164
Batch	F1SW100600
Name	X65 (a) Weld 1
Preparation	Saw cut and machining
Backing System	No Backing bar
Cleaning Method	Wire Brush or Grinding
Flux	Lincoln 888
Batch	2.2
Welder: Ibrahim Nuruddin Katsina	

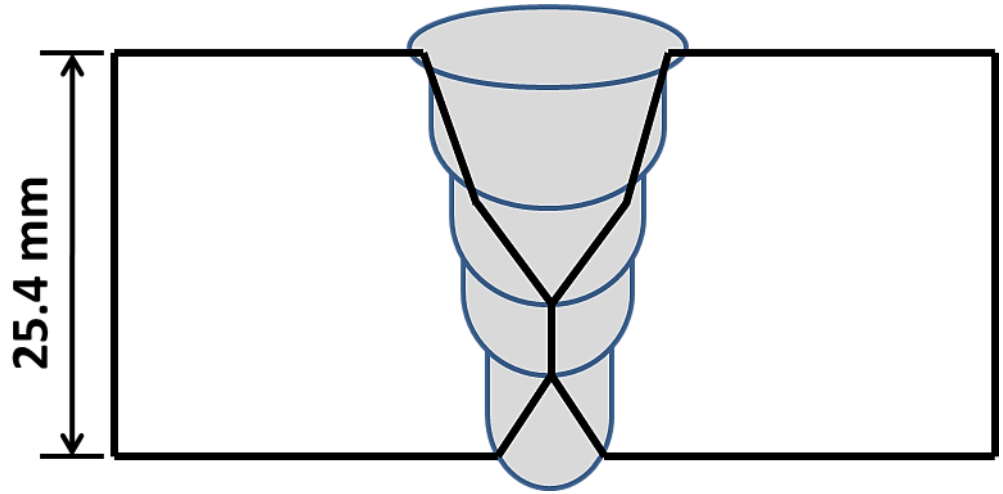

Pass	CTWD [mm]	Set Parameters			Recorded Parameters			Heat Input kJ/mm
		Travel Speed mm/min	Amps [I]	Volts [v]	WFS m/min	Amps [I]	Volts [v]	
Root Pass	22	400	500	22	2.13	414	22.4	1.37
Fill 1	22	400	550	26	-	-	-	2.15*
Fill 2	22	500	550	26	2.2	449	26.8	1.44
Cap	22	400	600	26	-	400	26	1.60
Internal pass	22	450	550	26	-	444	26	1.58

* The heat input was calculated using the set parameters not from the AMV data.

Cranfield UNIVERSITY

Welding Process	Submerged Arc Weld
Welding Position	1G
Material Grade	X65 (A)
Diameter	324 mm
Thickness	25.4 mm
Electrode Wire	Φ = 3.2 mm
Brand	Lincoln LNS 164
Batch	F1SW100600
Name	X65 (a) Weld 2
Preparation	Saw cut and machining
Backing System	No Backing bar
Cleaning Method	Wire Brush or Grinding
Flux	Lincoln 888
Batch	2.2
Welder: Ibrahim Nuruddin Katsina	

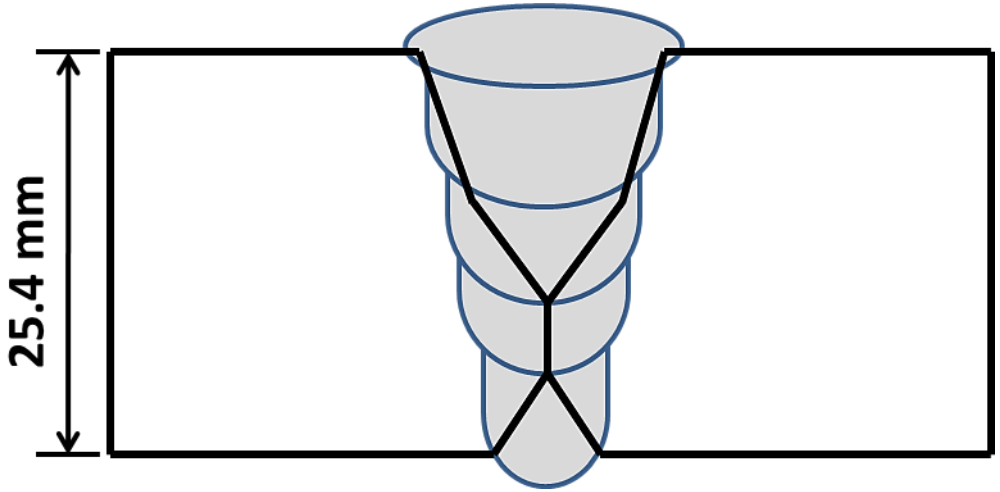

Pass	CTWD [mm]	Set Parameters			Recorded Parameters			Heat Input kJ/mm
		Travel Speed mm/min	Amps [I]	Volts [v]	WFS m/min	Amps [I]	Volts [v]	
Root Pass	22	400	500	22	2.10	403	22.8	1.37
Fill 1	22	450	550	26	2.17	441	26.8	1.57
Fill 2	22	450	550	26	2.17	437	26.8	1.56
Cap	22	400	600	26	2.56	459	26.7	1.84
Internal pass	22	450	550	26	2.08	419	26.4	1.47

Cranfield UNIVERSITY

Welding Process	Submerged Arc Weld
Welding Position	1G
Material Grade	X65 (A)
Diameter	324 mm
Thickness	25.4 mm
Electrode Wire	Φ = 3.2 mm
Brand	Lincoln LNS 164
Batch	F1SW100600
Name	X65 (a) Weld 3
Preparation	Saw cut and machining
Backing System	No Backing bar
Cleaning Method	Wire Brush or Grinding
Flux	Lincoln 888
Batch	2.2
Welder: Ibrahim Nuruddin Katsina	

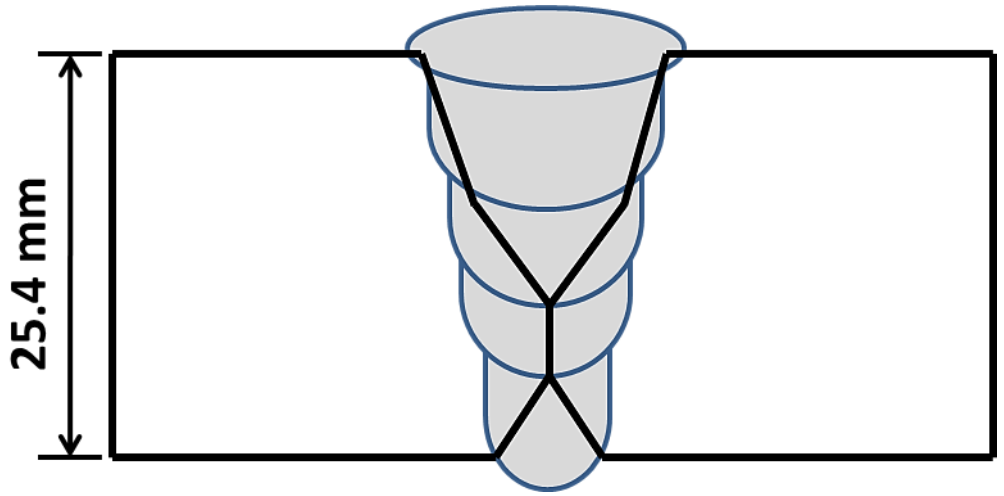

Pass	CTWD [mm]	Set Parameters			Recorded Parameters			Heat Input kJ/mm
		Travel Speed mm/min	Amps [I]	Volts [v]	WFS m/min	Amps [I]	Volts [v]	
Root Pass	22	400	500	22	2.10	437	22.8	1.48
Fill 1	22	450	550	26	2.2	531	26.8	1.89
Fill 2	22	450	550	26	2.16	508	27.2	1.81
Cap	22	400	600	26	2.52	519	26.6	2.07
Internal pass	22	450	550	26	2.07	476	26.8	1.69

Cranfield UNIVERSITY

Welding Process	Submerged Arc Weld
Welding Position	1G
Material Grade	X70
Diameter	1210 mm
Thickness	31mm
Electrode Wire	Φ = 3.2 mm
Brand	Lincoln LNS 164
Batch	F1SW100600
Name	X70 Weld 1
Preparation	Saw cut and machining
Backing System	No Backing bar
Cleaning Method	Wire Brush or Grinding
Flux	Lincoln 888
Batch	2.2
Welder: Ibrahim Nuruddin Katsina	

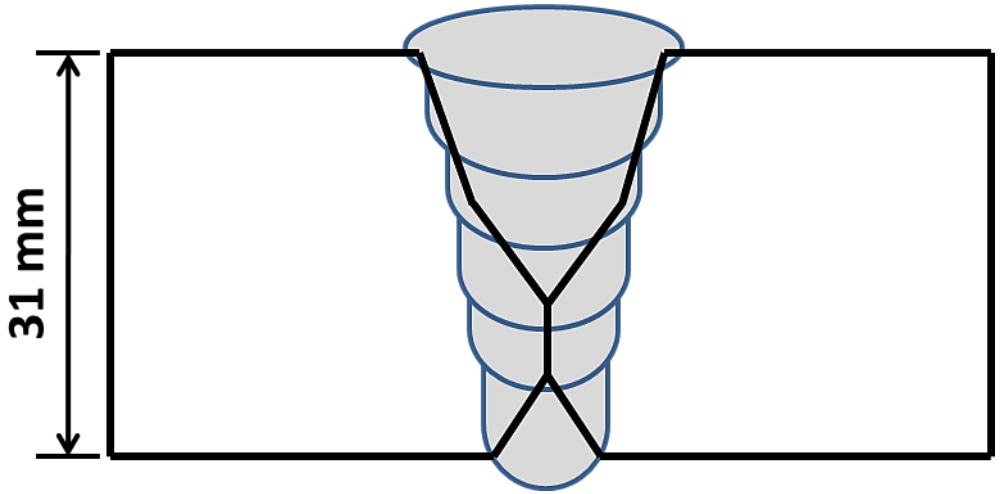

Pass	CTWD [mm]	Set Parameters			Recorded Parameters			Heat Input kJ/mm
		Travel Speed mm/min	Amps [I]	Volts [v]	WFS m/min	Amps [I]	Volts [v]	
Root Pass	22	400	500	26	1.49	510	26.6	2.03
Fill 1	22	400	600	28	1.91	610	28.8	2.63
Fill 2	22	400	600	28	1.91	611	28.4	2.60
Fill 3	22	400	600	28	2.38	603	28.1	2.55
Cap	22	400	600	28	1.93	610	28.7	2.99
Internal pass	22	400	600	26	1.98	610	26.5	2.16

Cranfield UNIVERSITY

Welding Process	Submerged Arc Weld
Welding Position	1G
Material Grade	X70
Diameter	1210 mm
Thickness	31mm
Electrode Wire	Φ = 3.2 mm
Brand	Lincoln LNS 164
Batch	F1SW100600
Name	X70 Weld 2
Preparation	Saw cut and machining
Backing System	No Backing bar
Cleaning Method	Wire Brush or Grinding
Flux	Lincoln 888
Batch	2.2
Welder: Ibrahim Nuruddin Katsina	

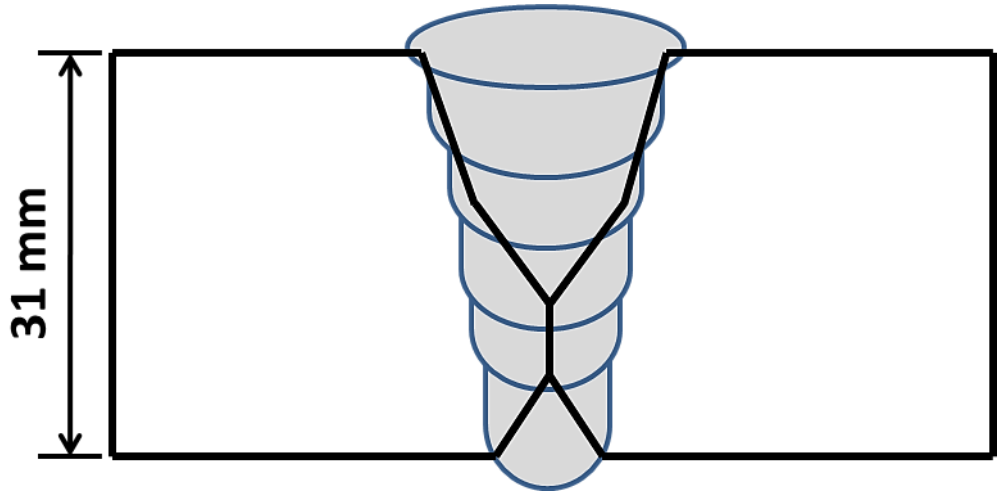

Pass	CTWD [mm]	Set Parameters			Recorded Parameters			Heat Input kJ/mm
		Travel Speed mm/min	Amps [I]	Volts [v]	WFS m/min	Amps [I]	Volts [v]	
Root Pass	22	400	500	26	1.48	505	26.6	2.00
Fill 1	22	400	600	28	1.94	610	28.8	2.63
Fill 2	22	400	600	28	1.94	614	28.8	2.64
Fill 3	22	350	600	28	1.96	611	28.8	3.00
Cap	22	350	600	28	1.95	610	28.8	3.00
Internal pass	22	450	550	26	1.69	561	26.3	1.96

Cranfield UNIVERSITY

Welding Process	Submerged Arc Weld
Welding Position	1G
Material Grade	X70
Diameter	1210 mm
Thickness	31mm
Electrode Wire	Φ = 3.2 mm
Brand	Lincoln LNS 164
Batch	F1SW100600
Name	X70 Weld 3
Preparation	Saw cut and machining
Backing System	No Backing bar
Cleaning Method	Wire Brush or Grinding
Flux	Lincoln 888
Batch	2.2
Welder: Ibrahim Nuruddin Katsina	

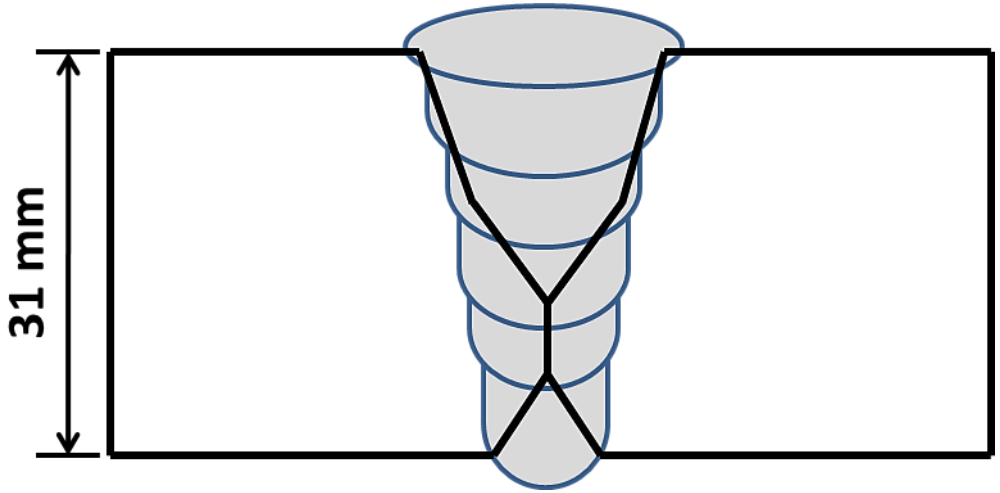

Pass	CTWD [mm]	Set Parameters			Recorded Parameters			Heat Input kJ/mm
		Travel Speed mm/min	Amps [I]	Volts [v]	WFS m/min	Amps [I]	Volts [v]	
Root Pass	22	400	500	26	1.88	406	26.5	1.61
Fill 1	22	400	600	28	2.38	565	28.7	2.43
Fill 2	22	400	600	28	2.41	544	28.7	2.34
Fill 3	22	350	600	28	2.48	544	28.0	2.60
Cap	22	350	600	28	2.50	550	28.0	2.70
Internal pass	22	450	550	26	2.21	507	26.7	1.80

Cranfield UNIVERSITY

Welding Process	Submerged Arc Weld
Welding Position	1G
Material Grade	X65 (B)
Diameter	1210 mm
Thickness	31mm
Electrode Wire	Φ = 3.2 mm
Brand	Lincoln LNS 164
Batch	F1SW100600
Name	X65 (b) Weld 1
Preparation	Saw cut and machining
Backing System	No Backing bar
Cleaning Method	Wire Brush or Grinding
Flux	Lincoln 888
Batch	2.2
Welder: Ibrahim Nuruddin Katsina	

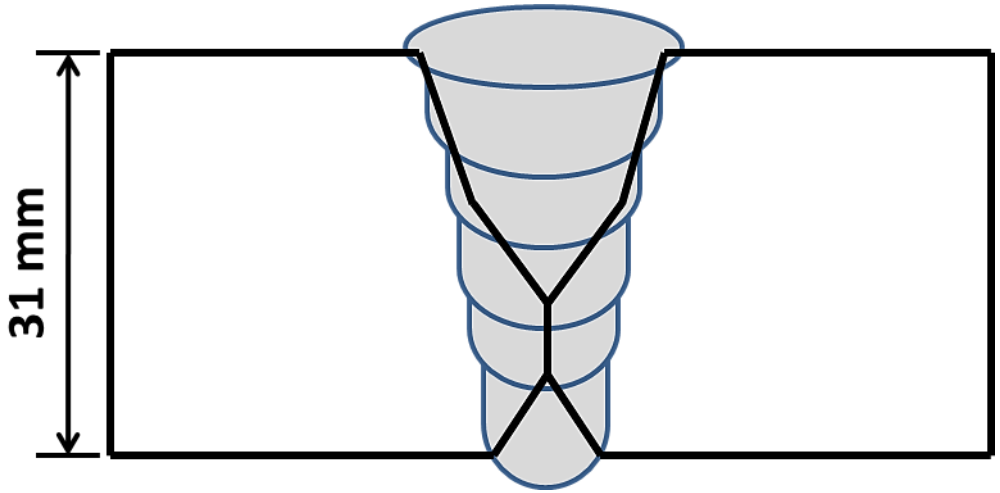

Pass	CTWD [mm]	Set Parameters			Recorded Parameters			Heat Input kJ/mm
		Travel Speed mm/min	Amps [I]	Volts [v]	WFS m/min	Amps [I]	Volts [v]	
Root Pass	22	400	500	26	1.93	493	26.6	1.96
Fill 1	22	400	600	28	2.47	593	28.9	2.56
Fill 2	22	400	600	28	2.53	590	28.8	2.54
Cap	22	350	600	28	2.82	592	28.8	2.97
Internal pass	22	450	500	26	1.77	381	27.0	1.75

Cranfield UNIVERSITY

Welding Process	Submerged Arc Weld
Welding Position	1G
Material Grade	X65 (B)
Diameter	1210 mm
Thickness	31mm
Electrode Wire	Φ = 3.2 mm
Brand	Lincoln LNS 164
Batch	F1SW100600
Name	X65 (b) Weld 2
Preparation	Saw cut and machining
Backing System	No Backing bar
Cleaning Method	Wire Brush or Grinding
Flux	Lincoln 888
Batch	2.2
Welder: Ibrahim Nuruddin Katsina	

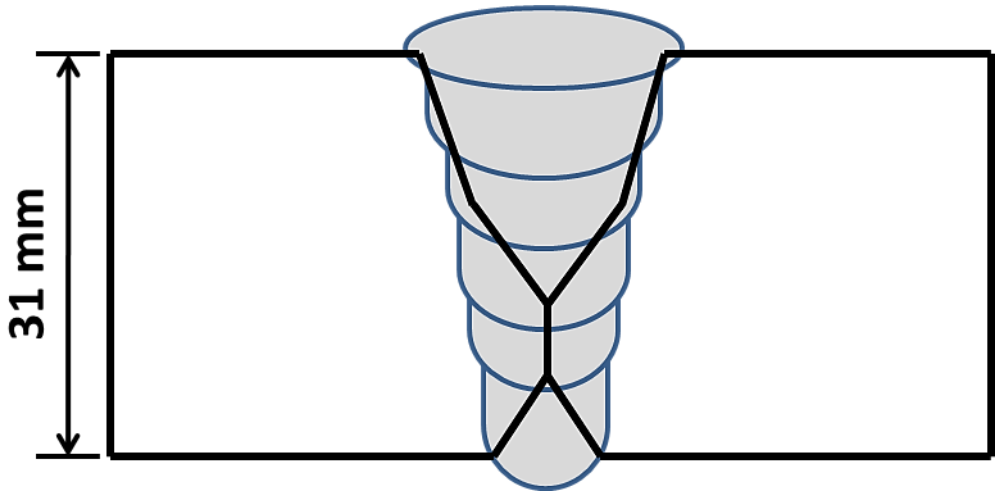

Pass	CTWD [mm]	Set Parameters			Recorded Parameters			Heat Input kJ/mm
		Travel Speed mm/min	Amps [I]	Volts [v]	WFS m/min	Amps [I]	Volts [v]	
Root Pass	22	400	500	26	1.92	495	26.6	1.97
Fill 1	22	400	600	28	2.44	516	28.7	2.22
Fill 2	22	400	600	28	2.49	522	28.7	2.25
Cap	22	350	600	28	2.52	520	28.7	2.56
Internal pass	22	450	500	26	1.88	445	26.8	1.58

Cranfield UNIVERSITY

Welding Process	Submerged Arc Weld
Welding Position	1G
Material Grade	X65 (B)
Diameter	1210 mm
Thickness	31mm
Electrode Wire	Φ = 3.2 mm
Brand	Lincoln LNS 164
Batch	F1SW100600
Name	X65 (b) Weld 3
Preparation	Saw cut and machining
Backing System	No Backing bar
Cleaning Method	Wire Brush or Grinding
Flux	Lincoln 888
Batch	2.2
Welder: Ibrahim Nuruddin Katsina	

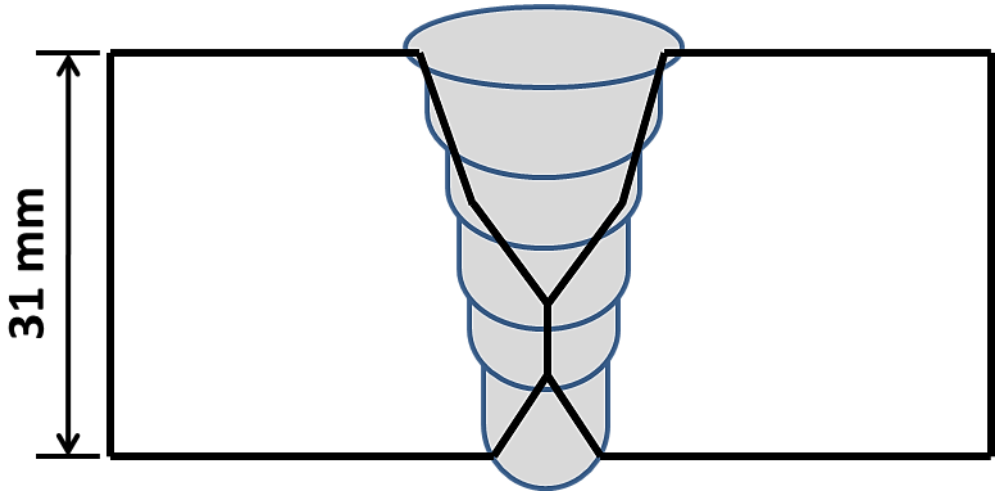

Pass	CTWD [mm]	Set Parameters			Recorded Parameters			Heat Input kJ/mm
		Travel Speed mm/min	Amps [I]	Volts [v]	WFS m/min	Amps [I]	Volts [v]	
Root Pass	22	400	500	26	1.98	436	26.6	1.73
Fill 1	22	400	600	28	2.50	517	28.8	2.23
Fill 2	22	400	600	28	2.57	520	28.8	2.24
Cap	22	350	600	28	2.50	520	28.8	2.55
Internal pass	22	450	500	26	1.83	427	26.4	1.49

A.2 Narrow groove Tandem MIG Weld Parameters

Cranfield UNIVERSITY

Welding Process	Tandem GMAW DC +ve
Welding Position	1G
Material Grade	X70
Diameter	1210 mm
Thickness	31mm
Electrode Wire	Φ = 1mm
Brand	Union MoNi
Batch	17691
Name	X70 Weld 1
Preparation	Saw cut
Backing System	X70 (a) Backing Strip
Cleaning Method	Wire Brush or Grinding
Shielding Gas	92.0% Ar- 8.0%CO2
Flow rate	30 L/min
Welder: Ibrahim Nuruddin Katsina	

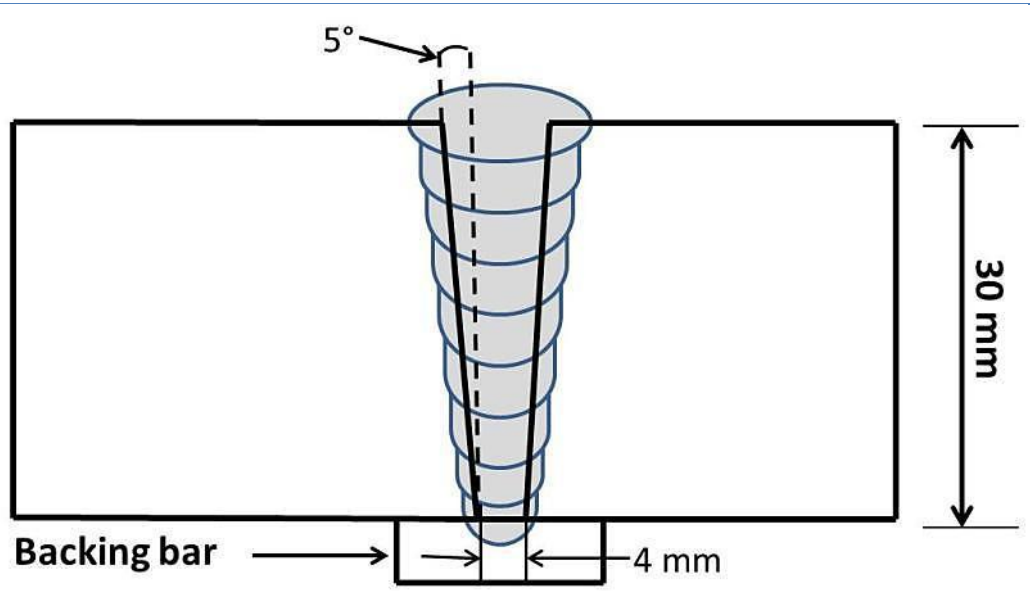

Pass	Travel Speed m/min	Lead			Trail			Oscillation		CTWD [mm]
		WFS m/min	Amps [I]	Volts [v]	WFS m/min	Amps [I]	Volts [v]	Freq. (Hz)	Osc. width	
Root Pass	0.9	11	179	20	11	184	21	350	90	13.5
Fill 1	0.8	11	179	21	11	184	22	350	135	13.5
Fill 2	0.8	11	177	21	11	183	22	350	190	13.5
Fill 3	0.75	11	173	23	11	176	21	350	225	13.5
Fill 4	0.7	11	168	21	11	181	22	350	250	13.5
Fill 5	0.7	11	166	22	11	173	23	350	270	13.5
Fill 6	0.6	11	168	21	11	179	22	350	290	13.5
Fill 7	0.6	11	169	22	11	174	21	350	320	13.5
Fill 8	0.6	11	166	22	11	175	22	350	350	13.5
Cap	0.6	11	169	23	11	174	21	350	30	13.5

Cranfield UNIVERSITY

Welding Process	Tandem GMAW DC +ve
Welding Position	1G
Material Grade	X70
Diameter	1210 mm
Thickness	31mm
Electrode Wire	Φ = 1mm
Brand	Union MoNi
Batch	17691
Name	X70 Weld 2
Preparation	Saw cut
Backing System	X70 (a) Backing Strip
Cleaning Method	Wire Brush or Grinding
Shielding Gas	92.0% Ar- 8.0%CO2
Flow rate	30 L/min
Welder: Ibrahim Nuruddin Katsina	

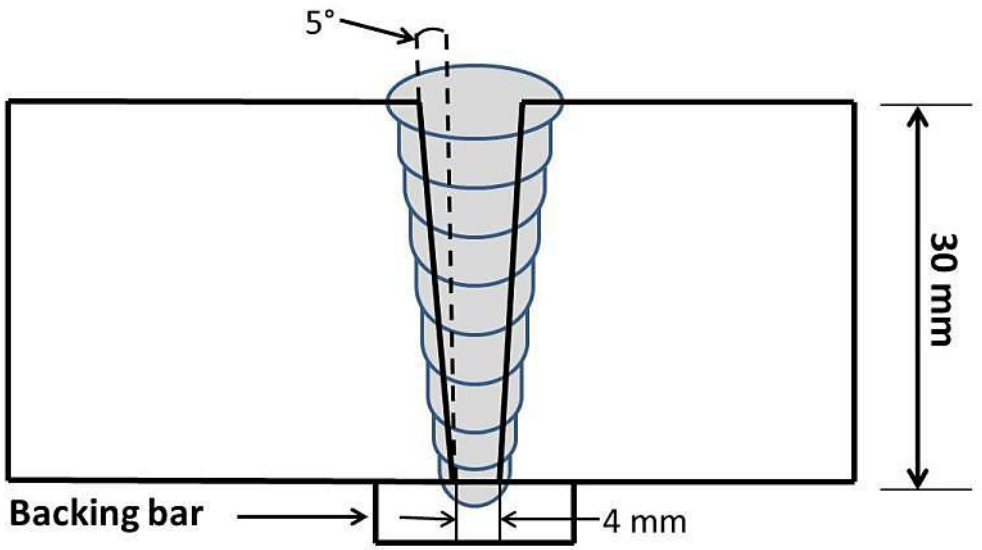

Pass	Travel Speed m/min	Lead			Trail			Oscillation		CTWD [mm]
		WFS m/min	Amps [I]	Volts [v]	WFS m/min	Amps [I]	Volts [v]	Freq. (Hz)	Osc. width	
Root Pass	0.9	11	179	20	11	184	21	350	90	13.5
Fill 1	0.8	11	179	21	11	184	22	350	135	13.5
Fill 2	0.8	11	177	21	11	183	22	350	190	13.5
Fill 3	0.75	11	173	23	11	176	21	350	225	13.5
Fill 4	0.7	11	168	21	11	181	22	350	250	13.5
Fill 5	0.7	11	166	22	11	173	23	350	270	13.5
Fill 6	0.6	11	168	21	11	179	22	350	290	13.5
Fill 7	0.6	11	169	22	11	174	21	350	320	13.5
Fill 8	0.6	11	166	22	11	175	22	350	350	13.5
Cap 1	0.6	11	169	23	11	174	21	350	305	13.5
Cap 2	0.8	11	177	21	11	183	22	350	350	13.5

Cranfield UNIVERSITY

Welding Process	Tandem GMAW DC +ve
Welding Position	1G
Material Grade	X100
Diameter	1321 mm
Thickness	22.9 mm
Electrode Wire	Φ = 1mm
Brand	Union MoNi
Batch	17691
Name	X100 Weld 1
Preparation	Saw cut
Backing System	X100 Backing Strip
Cleaning Method	Wire Brush or Grinding
Shielding Gas	92.0% Ar- 8.0%CO2
Flow rate	30 L/min
Welder: Ibrahim Nuruddin Katsina	

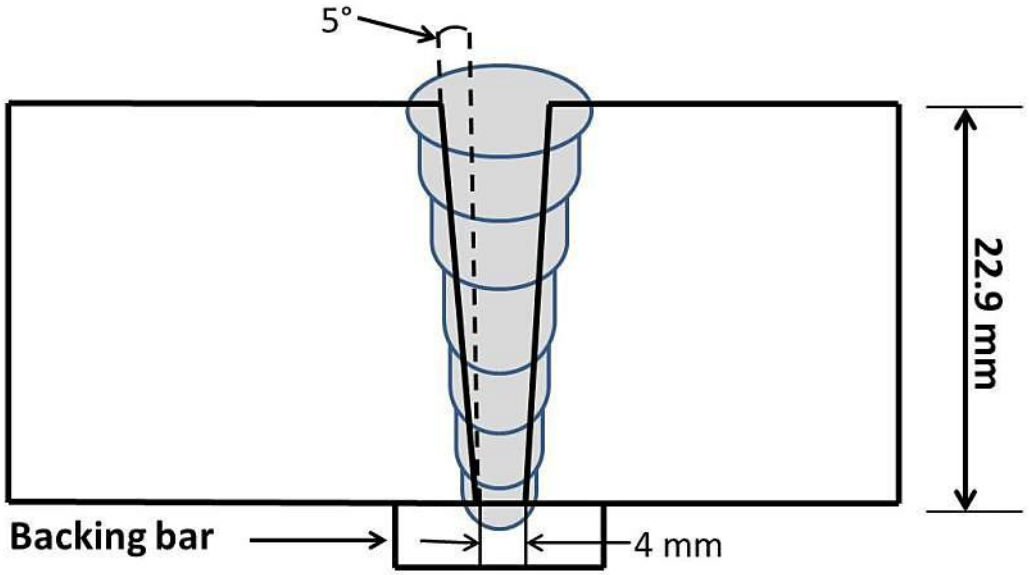

Pass	Travel Speed m/min	Lead		Trail		Oscillation		CTWD [mm]
		WFS m/min	Volts [v]	WFS m/min	Volts [v]	Freq. (Hz)	Osc. width	
Root Pass	0.7	8.5	22.7	11	22.7	350	120	13.5
Fill 1	0.7	9.5	22.9	11	22.9	350	150	13.5
Fill 2	0.7	10.4	23.3	11	23.3	350	200	13.5
Fill 3	0.7	11.4	24.1	11	24.1	350	240	13.5
Fill 4	0.7	12.4	24.9	11	24.9	350	280	13.5
Fill 5	0.7	13.3	25.6	11	25.6	350	320	13.5
Cap	0.6	14.5	26.5	11	26.5	400	400	13.5

Cranfield UNIVERSITY

Welding Process	Tandem GMAW DC +ve
Welding Position	1G
Material Grade	X100
Diameter	1321 mm
Thickness	22.9 mm
Electrode Wire	Φ = 1mm
Brand	Union MoNi
Batch	17691
Name	X100 Weld 2
Preparation	Saw cut
Backing System	X100 Backing Strip
Cleaning Method	Wire Brush or Grinding
Shielding Gas	92.0% Ar- 8.0%CO2
Flow rate	30 L/min
Welder: Ibrahim Nuruddin Katsina	

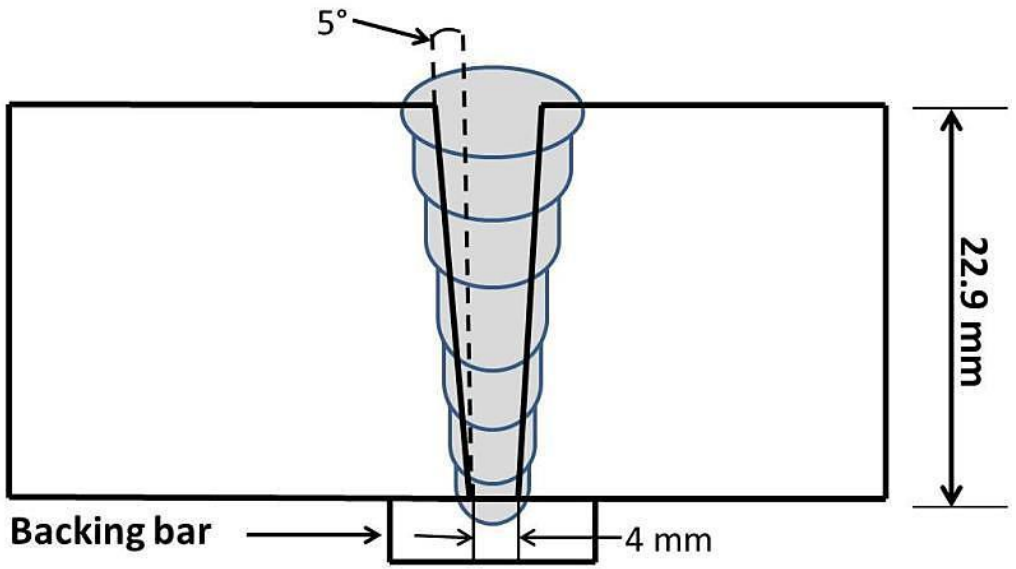

Pass	Travel Speed m/min	Lead		Trail		Oscillation		CTWD [mm]
		WFS m/min	Volts [v]	WFS m/min	Volts [v]	Freq. (Hz)	Osc. width	
Root Pass	0.7	8.5	22.7	8.5	22.7	350	120	13.5
Fill 1	0.7	9.5	22.9	9.5	22.9	350	150	13.5
Fill 2	0.7	10.4	23.3	10.4	23.3	350	200	13.5
Fill 3	0.7	11.4	24.1	11.4	24.1	350	240	13.5
Fill 4	0.7	12.4	24.9	12.4	24.9	350	280	13.5
Fill 5	0.7	13.3	25.6	13.3	25.6	350	320	13.5
Cap	0.6	14.5	26.5	14.5	26.5	400	380	13.5

Appendix B Gleeble experiments thermal cycles

B.1 X70 first trial

	X70	First Thermal Cycles			Second Thermal Cycles			Third Thermal Cycles				Charpy Impact Energy (J)				
No.	Heated at 500°C/s	Cooled at 50°C/s to	Cooled to (°C)	C R (°C/sec)	Heated at 500°C/s to	Cooled to (°C)	C R (°C/sec)	Heated at 500°C/s to	Cooled to (°C)	CR (°C/sec)	Quench	0°C	-20° C	-40° C	-60° C	-80° C
1	1250	800	200	25	800	200	25	-	-	-	No	299	299	7	73	-
2	1250	800	200	40	800	200	40	-	-	-	No	-	-	190	-	-
3	1250	800	100	40	800	100	40	-	-	-	No	-	-	-	39	-
4	1250	900	200	25	900	200	25	-	-	-	Air	-	256	39	-	-
5	1250	900	200	10	900	200	10	-	-	-	Air	-	-	279	54	-
6	1250	850	200	40	850	200	40	-	-	-	Air	-	-	264	-	-
7	1250	850	200	25	850	200	25	-	-	-	Air	-	-	245	222	-
8	1250	850	200	10	850	200	10	-	-	-	Air	-	-	299	208	-
9	1250	800	200	40	800	200	40	-	-	-	Air	-	-	295	-	-
10	1250	800	200	25	800	200	25	-	-	-	Air	-	299	116	-	-
11	1250	800	200	10	800	200	10	-	-	-	Air	-	-	299	217	-
12	1250	800	20	25	800	20	25	450	20	25	Air	-	-	299	277	-
13	1250	800	20	10	800	20	10	450	20	10	Air	-	-	299	239	-
14	1250	800	20	25	800	20	25	350	20	25	Air	-	-	238	233	-
15	1250	800	20	10	800	20	10	350	20	10	Air	-	-	256	40	-
16	1250	750	200	40	750	200	40	-	-	-	Air	-	-	-	251	-
17	1250	750	200	25	750	200	25	-	-	-	Air	-	-	225	217	-
18	1250	750	200	10	750	200	10	-	-	-	Air	-	-	248	229	-
19	PARENT METAL											-	218	190	208	167

B.2 X70 second experiment

	X70	First Thermal Cycles		Second Thermal Cycles		Third Thermal Cycles		Charpy Impact Energy		
No.	Heated @ 500°C/s	Cooled to 800°C. @ °C/s	Cooled to 200°C. @ °C/s	Heated @ 500°C/s	Cooled to 200°C. @ °C/s	Heated @ 500°C/s	Cooled to (200°C) @ °C/s	-40°C	-60°C	-80°C
1	1250	50	35	-	-	-	-	22 J	25 J	15 J
2	1000	50	35	-	-	-	-	249 J	38 J	76 J
3	1250	50	35	950	17.5	-	-	192 J	55 J	19 J
4	1250	50	35	950	20	-	-	180 J	12 J	8 J
5	1250	50	35	900	17.5	-	-	22 J	22 J	13 J
6	1250	50	35	900	20	-	-	61 J	24 J	25 J
7	1250	50	35	1000	17.5	-	-	25 J	20 J	7 J
8	1250	50	35	1000	20	-	-	18 J	10 J	16 J
9	1250	50	35	1000	20	450	5.5	31 J	10 J	7 J
10	1250	50	35	1000	20	350	5.5	20 J	13 J	10 J
11	1250	50	35	950	17.5	450	5.5	176 J	14 J	8 J
12	1250	50	35	950	17.5	350	5.5	38 J	25 J	13 J
13	1250	50	35	900	17.5	450	5.5	292 J	124 J	21 J
14	1250	50	35	900	17.5	350	5.5	292 J	14 J	10 J
15	1250	50	35	950	20	450	5.5	36 J	25 J	12 J
16	1250	50	35	950	20	350	5.5	12 J	8 J	8 J
17	1250	50	35	900	20	450	5.5	296 J	50 J	18 J

B.3 X65 (B) and X65 (A) Gleeble experiments

	X65 (B)	First Thermal Cycles		Second Thermal Cycles		Third Thermal Cycles		Charpy Impact Energy		
No.	Heated at 500°C/s to	Cooled to (800°C) at °C/s	Cooled to (200°C) at °C/s	Heated at 500°C/s to	Cooled to (200°C) at °C/s	Heated at 500°C/s to	Cooled to (200°C) at °C/s	-40°C	-60°C	-80°C
1	1250	50 (9s)	35 (17.14s)	-	-	-	-	244 J	48 J	11 J
2	1000	50 (9s)	35 (17.14s)	-	-	-	-	269 J	65 J	16 J
3	1250	50 (9s)	35 (17.14s)	750	20 (27.5s)	-	-	251 J	228 J	26 J
4	1250	50 (9s)	35 (17.14s)	800	20 (30.0 s)	-	-	115 J	44 J	66 J
5	1250	50 (9s)	35 (17.14s)	850	20 (32.5s)	-	-	238 J	225 J	12 J
6	1250	50 (9s)	35 (17.14s)	900	17.5 (40s)	-	-	246 J	187 J	15 J
7	1250	50 (9s)	35 (17.14s)	900	20 (35.0s)	-	-	34 J	189 J	11 J
8	1250	50 (9s)	35 (17.14s)	950	17.5 (42.857s)	-	-	244 J	12 J	13 J
9	1250	50 (9s)	35 (17.14s)	950	20 (37.5s)	-	-	256 J	71 J	16 J
10	1250	50 (9s)	35 (17.14s)	1000	17.5 (45.71s)	-	-	222 J	38 J	19 J
11	1250	50 (9s)	35 (17.14s)	1000	20 (40)	-	-	331 J	36 J	10 J
12	1250	50 (9s)	35 (17.14s)	1000	20 (40s)	450	5.5 (45.45s)	286 J	271 J	131 J
13	1250	50 (9s)	35 (17.14s)	1000	20 (40s)	350	5.5 (27.27s)	284 J	92 J	14 J

	X65 (A)	First Thermal Cycles		Second Thermal Cycles		Third Thermal Cycles		Charpy Impact Energy		
No.	Heated at 500°C/s to	Cooled to (800°C) at °C/s	Cooled to (200°C) at °C/s	Heated at 500°C/s to	Cooled to (200°C) at °C/s	Heated at 500°C/s to	Cooled to (200°C) at °C/s	-40°C	-60°C	-80°C
1	1250	50 (9s)	35 (17.14s)	-	-	-	-	63 J	28 J	15 J
2	1000	50 (9s)	35 (17.14s)	-	-	-	-	26 J	17 J	8 J
3	1250	50 (9s)	35 (17.14s)	750	20 (27.5s)	-	-	34 J	24 J	10 J
4	1250	50 (9s)	35 (17.14s)	800	20 (30.0 s)	-	-	36 J	14 J	13 J
5	1250	50 (9s)	35 (17.14s)	850	20 (32.5s)	-	-	38 J	15 J	11 J
6	1250	50 (9s)	35 (17.14s)	900	17.5 (40s)	-	-	23 J	26 J	9 J
7	1250	50 (9s)	35 (17.14s)	900	20 (35.0s)	-	-	17 J	14 J	10 J
8	1250	50 (9s)	35 (17.14s)	950	17.5 (42.857s)	-	-	15 J	14 J	11 J
9	1250	50 (9s)	35 (17.14s)	950	20 (37.5s)	-	-	16 J	13 J	9 J
10	1250	50 (9s)	35 (17.14s)	1000	17.5 (45.71s)	-	-	20 J	10 J	10 J
11	1250	50 (9s)	35 (17.14s)	1000	20 (40)	-	-	26 J	12 J	9 J
12	1250	50 (9s)	35 (17.14s)	1000	20 (40s)	450	5.5 (45.45s)	185 J	11 J	22 J
13	1250	50 (9s)	35 (17.14s)	1000	20 (40s)	350	5.5 (27.27s)	17 J	28 J	7 J

Appendix C MATLAB Programs

C.1 Thermal cycle curve fitting and differentiation program (Individual thermocouple control)

```
%CCT_plot_1.m

%The code below is from the PhD thesis of M G Hundson 2004
%The original filename was CCT_plot_MGH.m
%
%The matrix of data A should be a nx2 matrix, the first and
second colums
%representing time and data respectively.


%Modified - Harry Coules  2010 for Ibrahim Nuruddin
%The program now reads in data from a tab-delimited text
file (Without ANY headers!)
%generated by the thermocouple logger

disp('Which file contains the temperature data you wish to
analyse?');
filename = input('File must be tab-separated data from the
thermocouple logger, without headers.    ','s');

tc_name = input('Which thermocouple do you wish to use
(tc_1 - tc_16)?  ','s');

fid = fopen(filename);
C = textscan(fid,'%f %f %f %f %f %f %f %f %f %f %f %f %f %f
%f %f %f');
fclose(fid);

tc_time = C{1};
tc_1 = C{2};
tc_2 = C{3};
tc_3 = C{4};
tc_4 = C{5};
tc_5 = C{6};
tc_6 = C{7};
tc_7 = C{8};
tc_8 = C{9};
tc_9 = C{10};
tc_10 = C{11};
tc_11 = C{12};
tc_12 = C{13};
tc_13 = C{14};
tc_14 = C{15};
```

```
tc_15 = C{16};
tc_16 = C{17};

A = [tc_time,eval(tc_name)];


%clear all
close all
%clc

figure(11);
grid on;
plot(A(:,1),A(:,2),'r-');
hold on;
axis([0 140 0 1800]);
xlabel('Time (s)');
ylabel('Temperature (deg C)');

time0 = input('Enter time0 : ');
timeend = input('Enter timeend : ');
time = linspace(time0,timeend,10000);

%for LL=1:5

    grau=input('Enter order : ');
    [dummy,pos0]=min(abs(A(:,1)-time0));
    [dummy,posend]=min(abs(A(:,1)-timeend));

    coef = polyfit(A(pos0:posend,1),A(pos0:posend,2),grau);

    save('savefile','coef','-ASCII');
    plot_poly = polyval(coef,time);

    diff_poly = polyder(coef);
    plot_diff_poly = polyval(diff_poly,time);
    diff_diff_poly = polyder(polyder(coef));
    plot_diff_diff_poly = polyval(diff_diff_poly,time);

    for jj=1:grau+1
        disp(['coef(',num2str(jj),')=',num2str(coef(jj))]);
    end

    figure(11);
    plot(time,plot_poly);

    figure(12);
    sp_1 = subplot(2,1,1);
    subplot(sp_1);
    plot(time,plot_poly);
```

```
    axis([time0 timeend 0 1000]);
    grid on
    ylabel('T in deg C');
    xlabel('t in s');
    hold on;

    figure(12);
    sp_2 = subplot(2,1,2);
    subplot(sp_2);
    plot(time,plot_diff_poly);
    axis([time0 timeend -100 0])
    grid on
    ylabel('dT/dt (K/s)');
    xlabel('Time (s)');
    hold on;

    figure(13);
    plot(time,plot_diff_diff_poly);
    axis([time0 timeend -100 100]);
    grid on
    hold on;
    xlabel('Time (s)');
    ylabel('d^2T/dt^2');

%end
```

C.2 Thermal cycle curve fitting and differentiation program

```
%CCT_plot_2.m

%The code below is from the PhD thesis of M G Hundson 2004
%The original filename was CCT_plot_MGH.m
%
%The matrix of data A should be a nx2 matrix, the first and
second colums
%representing time and data respectively.


%Modified - Harry Coules  2011 for Ibrahim Nuruddin

%clear all
close all
%clc

figure(11);
grid on;
plot(A(:,1),A(:,2),'r-');
hold on;
axis([0 140 0 1800]);
xlabel('Time (s)');
ylabel('Temperature (deg C)');

time0 = input('Enter time0 : ');
timeend = input('Enter timeend : ');
time = linspace(time0,timeend,10000);

%for LL=1:5

    grau=input('Enter order : ');
    [dummy,pos0]=min(abs(A(:,1)-time0));
    [dummy,posend]=min(abs(A(:,1)-timeend));

    coef = polyfit(A(pos0:posend,1),A(pos0:posend,2),grau);

    save('savefile','coef','-ASCII');
    plot_poly = polyval(coef,time);

    diff_poly = polyder(coef);
    plot_diff_poly = polyval(diff_poly,time);
    diff_diff_poly = polyder(polyder(coef));
    plot_diff_diff_poly = polyval(diff_diff_poly,time);

    for jj=1:grau+1
```

```
        disp(['coef(',num2str(jj),')=',num2str(coef(jj))]);
    end

    figure(11);
    plot(time,plot_poly);

    figure(12);
    sp_1 = subplot(2,1,1);
    subplot(sp_1);
    plot(time,plot_poly);
    axis([time0 timeend 0 1000]);
    grid on
    ylabel('T in deg C');
    xlabel('t in s');
    hold on;

    figure(12);
    sp_2 = subplot(2,1,2);
    subplot(sp_2);
    plot(time,plot_diff_poly);
    axis([time0 timeend -100 0])
    grid on
    ylabel('dT/dt (K/s)');
    xlabel('Time (s)');
    hold on;

    figure(13);
    plot(time,plot_diff_diff_poly);
    axis([time0 timeend -100 100]);
    grid on
    hold on;
    xlabel('Time (s)');
    ylabel('d^2T/dt^2');

%end
```